Dynamics and Defects of Complex Crystals and Quasicrystals: Perspectives from Simple Model Systems

Von der Fakultät Mathematik und Physik
der Universität Stuttgart
zur Erlangung der Würde eines Doktors der
Naturwissenschaften (Dr. rer. nat.) genehmigte Abhandlung

Vorgelegt von

Michael Engel

aus Leinfelden-Echterdingen

Hauptberichter: Prof. Dr. Hans-Rainer Trebin
Mitberichter: Prof. Dr. Günter Wunner

Tag der mündlichen Prüfung: 17. März 2008

Institut für Theoretische und Angewandte Physik
Universität Stuttgart

2008

Für Meike und Anna

Contents

Abstract

Complex crystals and quasicrystals are ordered states of matter with very large or even infinite unit cells. Their particle dynamics and defects differ significantly from what is known for simple crystals: Local rearrangements – phason flips – and new types of dislocations are consequences of the structural complexity. In order to understand their behavior at an elementary level, we introduce three model systems in one and two dimensions. The systems are studied analytically and with numerical simulations.

(i) The structure factors of the *dynamic Fibonacci chain* are computed with high resolution. They show a characteristic broadening of the phonon dispersion relation. The particle motion in real space reveals soliton and breather modes, closely connected to phason flips.

(ii) Using a *tiling model for the intermetallic system AlPdMn*, experimental observations of metadislocations and the collective particle dynamics are explained. The Burgers vectors of stable dislocations are derived from energy considerations.

(iii) In the *Lennard-Jones-Gauss system* a surprising variety of two-dimensional complex crystals as well as a decagonal and two dodecagonal quasicrystals are grown. The particles reorder by phason flips at elevated temperatures. During annealing, the entropically stabilized quasicrystals undergo reversible phase transitions into complex crystals. Competing interparticle distances seem to favor structural complexity. With the Lennard-Jones-Gauss system the growth, equilibrium dynamics, and defects of quasicrystals and complex crystals can be studied in simulations for the first time.

Deutsche Zusammenfassung

Die vorliegende Arbeit beschäftigt sich mit komplexen Kristallen und Quasikristallen. Ziel ist es, deren Dynamik und Defekte anhand einfacher Modellsysteme zu verstehen. Der erste Teil führt die notwendigen theoretischen Grundlagen und die verwendeten numerischen Methoden ein. Im zweiten Teil werden die Modellsysteme sowie die mit analytischen Rechnungen und Simulationen erzielten Ergebnisse beschrieben.

Methoden und theoretischer Hintergrund.

Komplexe Kristalle sind geordnete Festkörperstrukturen mit großen Elementarzellen. Experimentell treten sie vor allem als intermetallische Phasen auf und enthalten typischerweise einige zehn bis einige tausend Atome pro Elementarzelle. Am unteren Ende stehen die Laves-Phasen mit 12 beziehungsweise 24 Atomen und am oberen Ende aktuell $YbCu_{4,5}$ mit 7448 Atomen. In den vergangenen Jahren wurden komplexe Kristalle auch in Hochdruckphasen von elementarem Bor und Mangan gefunden. Des Weiteren wurde beobachtet, dass sich bestimmte Makromoleküle und Kolloide spontan komplex anordnen können.

Viele Eigenschaften sind unabhängig von der konkreten Realisierung der komplexen Struktur. Im Allgemeinen kommen Teilchen (Atome, Kolloide, Proteine, etc.) einer Sorte aufgrund der großen Elementarzelle in unterschiedlichen lokalen Umgebungen vor. Das hat zur Folge, dass manche von ihnen energetisch günstiger koordiniert sind, während andere sich mit ungünstigen Konfigurationen abfinden müssen. Komplexe Kristalle treten genau dann auf, wenn die Gesamtenergie, die mit diesem Kompromiss verbunden ist, geringer ist als die Gesamtenergie eines einfachen Kristalls. Teilchen in energetisch günstigen Konfigurationen haben häufig hochsymmetrische Umgebungen, sogenannte *Cluster*, und möchten diese nur ungern verlieren. Dagegen sind Teilchen in ungünstigen Umgebungen flexibler und können durch Überwinden eines Potentialbergs in ein alternatives lokales Minimum wechseln. Diese spontanen, diskreten Umordnungen der Struktur werden *Phasonflips* genannt.

Den Grenzfall einer unendlich großen Elementarzelle bilden die *Quasikristalle*. Sie sind weitreichend geordnet, weisen aber keine Periodizität auf und treten häufig in Kombination mit komplexen Kristallen auf. Bis heute wurde eine Vielzahl von thermodynamisch stabilen Quasikristallen in binären und ternären Legierungen gefunden. Phasonflips treten in Quasikristallen ebenfalls auf. Aufgrund der fehlenden Translationssymmetrie ändern sie die mittlere Struktur nicht wesentlich und führen zu keiner Energieänderung. Sie werden daher zu *Phasonmoden* zusammengefasst. Die theoretische Beschreibung erfolgt mit Hilfe eines höherdimensionalen Konfigurationsraumes, genannt *Hyperraum*.

Es zeigt sich, dass komplexe Kristalle und Quasikristalle in eine endliche Anzahl von unterschiedlichen *Tiles* (Zellen) zerlegt werden können. Auf diese Weise wird das herkömmliche Konzept der Elementarzelle erweitert: Anstatt eines periodischen Gitters gibt es nun unterschiedliche Tiles, die wiederum periodisch (komplexer Kristall) oder aperiodisch (Quasikristall) angeordnet sind. Zusammen mit der Dekoration der Tiles beschreibt das resultierende *Tiling* (Parkettierung) die komplette Struktur.

Alle durch Phasonflips verbundenen möglichen Eckpunkte des Tilings bilden eine diskrete, aber dichte Menge. Jeder der Eckpunkte kann als ganzzahlige Linearkombination einer n-dimensionalen Basis geschrieben werden. Daher ist das (nicht notwendigerweise periodische) Tiling als diskrete *de Bruijn-Fläche* in ein n-dimensionales periodisches Gitter im Hyperraum eingebettet. Beliebige Tilings werden als Schnitte durch den Hyperraum beschrieben. Anregungen des phasonischen Freiheitsgrades entsprechen Deformationen der *Schnittfläche*. Ist umgekehrt die Schnittfläche vorgegeben, so kann das dazugehörige Tiling bestimmt werden. Eine Möglichkeit ist die *Auswahlmethode*: Der Hyperraum wird dazu durch die Wahl eines periodischen Gitters in Atomvolumina zerlegt. Die Zentren derjenigen Atomvolumina, die einen nichtleeren Schnitt mit der Schnittfläche haben, werden zur Konstruktion des Tilings verwendet. Diese neue Methode wurde speziell für Tilings mit Versetzungen entwickelt. Sie unterscheidet sich etwas von den üblicherweise verwendeten Methode.

Ideale Tilings entsprechen ebenen Schnitten. Abweichungen davon werden durch das Feld der *phasonische Verschiebung* $\boldsymbol{u}$ und deren Ableitung $\boldsymbol{\chi} = \boldsymbol{\nabla u}$, der *phasonischen Verzerrung*, beschrieben. Die freie Energiedichte F kann als Funktion der phasonischen Verzerrung geschrieben werden. Im Fall eines Quasikristalls unterscheidet man zwischen einem *locked state*-Verhalten mit $F \sim |\boldsymbol{\chi}|$ und einem *unlocked state*-Verhalten mit

$F \sim \chi^2$. Ein locked state-Verhalten wird erhalten, wenn der Quasikristall der energetische Grundzustand bei $T = 0$ ist. Das unlocked state-Verhalten entspricht einem Ensemble von *Random-Tilings* (Zufallsparkettierungen) mit einer im thermischen Gleichgewicht fluktuierenden Schnittfläche. Ein Random-Tiling Quasikristall weist daher bei endlicher Temperatur eine gewisse Unordnung der Tiles auf. Die daraus resultierende Entropie stabilisiert das Random-Tiling.

Herkömmliche *Versetzungen* können in Quasikristallen nicht existieren, da letztere keine Translationssymmetrie aufweisen. Es ist jedoch im Hyperraum möglich, Versetzungen mit Hilfe eines verallgemeinerten Volterra-Prozesses zu konstruieren. Das führt dazu, dass der Burgersvektor der Versetzung aus einer phononischen und einer phasonischen Komponente besteht. Die phononische Komponente deformiert die Tiles, die phasonische Komponente ordnet sie um. Ein analoges Verfahren ist auch für komplexe Kristalle möglich und führt dort zu Partialversetzungen. Umgekehrt kann jede Partialversetzung durch Wahl eines passenden Burgersvektor im Hyperraum beschrieben werden. Die Bewegung der Versetzung, die mit Hilfe des Hyperraums verstanden werden kann, ist zwangsläufig mit Umordnungen, das heißt Phasonflips verbunden.

Die *Stukturfaktoren* sind wichtige Observable für die Dynamik von Atomen in Festkörpern. Sie können experimentell in Röntgen- und Neutronenstreuversuchen gemessen werden. Man unterscheidet zwischen dem kohärenten, dem inkohärenten und dem statischen Strukturfaktor. Der kohärente und der inkohärente Strukturfaktor sind proportional zur fouriertransformierten Dichte-Dichte-Korrelations- beziehungsweise Autokorrelationsfunktion. Der statische Strukturfaktor ist proportional zum Beugungsbild. Aus dem Mermin-Wagner-Theorem ist bekannt, dass es keine weitreichende Ordnung in einer oder in zwei Dimensionen geben kann. Das bedeutet, es gibt keine scharfen Bragg-Peak, sondern nur Peaks mit endlicher Breite.

Für die im zweiten Teil folgenden Simulationen werden meist *Molekulardynamik*, aber auch *Monte Carlo-Verfahren* verwendet. Um große Teilchenzahlen über längere Zeiträume simulieren zu können, ist allerdings eine Beschränkung auf klassische Paarpotentiale notwendig. Die Simulationen werden mit einem selbstentwickelten C-Programm und einer *interaktiven Java-Visualisierung* durchgeführt. Im Laufe der Simulation können jederzeit das Potential sowie die thermodynamischen Parameter geändert werden. Dies ist wichtig, um für das Lennard-Jones-Gauß-System (siehe unten) die Abhängigkeit der Kristallstruktur von der Potentialform zu bestimmen.

Simulationen und Ergebnisse.

Drei unterschiedliche Modellsysteme werden vorgestellt: (i) die dynamische Fibonacci-Kette, (ii) Tilingmodelle für komplexe intermetallische Phasen in AlPdMn und (iii) das zweidimensionale Lennard-Jones-Gauß-System.

Es ist wichtig, den Einfluss der Dimensionalität der Modellsysteme auf die Teilchendynamik zu berücksichtigen. So ist es zum Beispiel nicht ohne Weiteres möglich, die allgemeine Theorie der Strukturfaktoren auf ein oder zwei Dimensionen zu übertragen, da die darin verwendete Phononzerlegung auf dem Langzeitverhalten von Korrelationsfunktionen beruht, die in Dimensionen kleiner drei divergieren. In der Literatur über niedrigdimensionale Systeme scheint zumindest der dynamische Strukturfaktor in seiner Allgemeinheit bisher noch nicht behandelt zu sein. Um den Einfluss der Dimensionalität zu verstehen, werden daher die Strukturfaktoren für die einfachsten Fälle berechnet: eine harmonische Kette und ein harmonisches Quadratgitter. Es zeigt sich, dass in niedrigdimensionalen Systemen eine Verallgemeinerung der Phononzerlegung möglich ist. Die dreidimensionalen Ergebnisse werden dahingehend erweitert, dass die Peaks im inkohärenten und statischen Strukturfaktor und die Phonondispersionsrelation im dynamischen Strukturfaktor gemäß einer sogenannten Formfunktion verbreitert sind. Die Formfunktion entspricht einer Lorentzkurve in einer Dimension und (meist) einer algebraischen Divergenz in zwei Dimensionen.

Die dynamische Fibonacci-Kette

Die Fibonacci-Kette ist eine quasiperiodische Anordnung von kurzen und langen Teilchenabständen und somit ein einfaches eindimensionales Modell eines Quasikristalls. An ihr soll der Einfluss der Quasiperiodizität sowie der Phasonflips auf die Strukturfaktoren untersucht werden. Dazu werden Molekulardynamiksimulationen für vier unterschiedliche Ketten durchgeführt: die harmonische periodische Kette (HPC), die harmonische Fibonacci-Kette (HFC), die dynamische Fibonacci-Kette (DFC) und die asymmetrische Fibonacci-Kette (AFC). Die Wechselwirkung zwischen benachbarten Teilchen ist gegeben durch ein harmonisches Potential (HFC), ein symmetrisches Doppelmuldenpotential (DFC) oder ein asymmetrisches Doppelmuldenpotential (AFC).

Die HPC dient zur Überprüfung des Algorithmus. Es zeigt sich, dass die

Strukturfaktoren vollständig mit den Ergebnissen der analytischen Rechnungen übereinstimmen. Im Fall der quasiperiodischen Kette (HFC) tritt wie erwartet ein dichtes Spektrum von Peaks im statischen Strukturfaktor sowie von Dispersionsrelationen im dynamischen Strukturfaktor auf. Der Einfluss von Phasonflips (DFC) ist in erster Linie eine zusätzliche Verbreiterung der Peaks und der Dispersionsrelationen. Leider lässt sich die Verbreiterung nur schwer von der intrinsischen (dimensionsbedingten) Verbreiterung trennen. Das asymmetrische Potential (AFC) führt zur Abspaltung von dispersionslosen optischen Phononmoden im dynamischen Strukturfaktor, wie auch im Experiment beobachtet.

Bei Verwendung der anharmonischen Potentiale besteht die Teilchenbewegung einerseits aus Phononschwingungen innerhalb der Potentialmulden und andererseits aus Phasonflips über den dazwischenliegenden Potentialberg hinweg. In der Simulation zeigt sich, dass Phasonflips bevorzugt zusammen mit lokalisierten Phononmoden auftreten. (Letztere sind eine Folge der Niedrigdimensionalität.) Falls die Kette durch Stöße lokal angeregt wird, bilden sich neuartige Solitonmoden und diskrete Breather, die sich dadurch auszeichnen, dass sie ausschließlich durch das Auftreten von Phasonflips stabilisiert werden.

Tilingmodelle für komplexe intermetallische Phasen in AlPdMn

Im Phasendiagramm des intermetallischen System AlPdMn tritt eine Vielzahl von komplexen Phasen auf. Die ternären Al-reichen Phasen können in zwei Klassen eingeteilt werden: die Ξ-Phasen und die T-Phasen. Beide bestehen aus Clustersäulen, die gemäß zweidimensionalen Tilings, den Clustertilings, angeordnet sind. Im Fall der Ξ-Phasen sind die Clustertiles Hexagone oder Kombinationen eines Pentagons mit einem Nonagon. Letztere werden als Phasonlinien bezeichnet. Die Phasonlinien sind wiederum in Ebenen, den Phasonebenen angeordnet. Der Grund für die Bezeichnung 'Phason-' liegt darin, dass sich Phasonlinien senkrecht zum Gleichgewichtsverlauf der Phasonebenen per Phasonflips bewegen können.

Es wird gezeigt, das die Clustertilings durch Rautentilings ersetzt werden können. Dies erlaubt eine vereinfachte Beschreibung des strukturellen Aufbaus der Ξ-Phasen. Da das Hyperraummodell für die zweidimensionalen Rautentilings dreidimensional ist, folgt, dass genau ein Phasonfreiheitsgrad existiert. Dieser beschreibt die Bewegung der Phasonlinien und gleichzeitig die Deformation der Phasonebenen. Je nach Orientierung der

Schnittfläche im Hyperraum werden Tilings mit unterschiedlichen Anordnungen der Phasonlinien beschrieben. Die Untersuchung zeigt, dass zwei ganzzahlige Parameter ausreichen, um alle möglichen einfachen Tilings der Ξ-Phasen zu klassifizieren. Der erste Parameter bestimmt den mittleren Abstand der Phasonebenen, der zwei Parameter deren Orientierung. Ein analoges Vorgehen ist für die T-Phasen möglich.

Die Elastizitätstheorie von einfachen Kristallen kann in den Hyperraum erweitert werden. In der freien elastischen Energie treten dann phononische und phasonische Terme wie auch eine Phonon-Phason-Kopplung auf. Dies überträgt sich auf die Energie einer Versetzung. Die phononische Komponente verursacht eine Deformation der Tiles und die phasonische Komponente deren Umordnung. Anhand von einfachen energetischen Überlegungen werden die Burgersvektoren mit den geringsten Versetzungsenergien bestimmt. Dazu wird als experimentelles Ergebnis verwendet, dass die phasonischen elastischen Konstanten um Größenordnungen kleiner sind als die phononischen. (Das bedeutet es kostet weniger Energie, Tiles umzuordnen als sie zu verformen.) Die Tilings der Versetzungen werden mit Hilfe der Auswahlmethode berechnet. Die Anordnungen der daraus erhaltenen Clusterpositionen stimmen vollständig mit den zuvor im Experiment gefundenen Ergebnissen überein. Aufgrund der Größe der Versetzungsanordnung ($> 10\,\mathrm{nm}$) und ihres Einflusses auf die Phasonebenen werden diese Versetzungen als Metaversetzungen bezeichnet. Eine Metaversetzung vom Typ m erzeugt durch ihre Bewegung $2F_m$ neue Phasonebenen. (F_m ist das m-te Element der Fibonacci-Folge.) Metaversetzungen treten häufig in komplizierten Netzwerken auf.

Das zweidimensionale Lennard-Jones-Gauß-System

Vorhergehende Untersuchungen haben gezeigt, dass es durchaus möglich ist Random-Tiling Quasikristalle in Simulationen mit Paarpotentialen zu stabilisieren. (Bisher ist keine Simulation bekannt, die zu einem perfekten Quasikristall geführt hat.) Die bekanntesten Modelle sind das Dzugutov-Potential in drei Dimensionen und das binäre System mit Lennard-Jones-Wechselwirkungen in zwei Dimensionen. Die damit erhalten Quasikristalle sind allerdings recht klein, und Simulationen über lange Zeiträume sind notwendig, um in die Nähe des thermischen Gleichgewichts zu gelangen. Der Grund dafür ist, dass die Systeme zu lange in metastabilen stark ungeordneten Zwischenstrukturen verbleiben. Es wurde daher versucht, Poten-

tiale zu finden, die ebenfalls Quasikristalle stabilisieren, aber gleichzeitig lokal flexibel genug sind, um problemlos Kristallisation zu ermöglichen.

Als geeignet erweist sich dazu das Lennard-Jones-Gauß Potential, das meist die Form einer Doppelmulde hat. Es besteht aus einem abstoßenden Potentialwall und dazugehöriger erster Mulde, gegeben durch ein Lennard-Jones-Potential, sowie einer zweiten Mulde, gegeben durch eine negative Gaußkurve. Die Gaußkurve besitzt drei Parameter: die Position der Mulde r_0, ihre Tiefe ϵ und Breite σ. Je nach Wahl der Parameter werden unterschiedliche Strukturen stabilisiert. Die Simulationen werden mit Molekulardynamik unter Verwendung eines Thermostaten und eines Barostaten ($P = 0$) mit offenen oder periodischen Rändern durchgeführt. Es werden kleine Systeme mit 1024 Teilchen und große Systeme mit 10 000 Teilchen verwendet.

Das Phasendiagramm bei $T = 0$ wird in Abhängigkeit der Potentialparameter bestimmt. Dazu dienen in einem ersten Schritt Abkühlsimulationen. Aus der Schmelze startend wird die Temperatur langsam erniedrigt. Am Ende bildet sich in der Regel ein Polykristall heraus, dessen Struktur einfach visuell bestimmt wird. Nach 5000 Abkühlsimulationen auf einen feinen Parametergitter in der r_0-ϵ-Ebene zeigt sich, dass das Phasendiagramm überraschend kompliziert ist. Außer einfachen hexagonalen Phasen und einem Quadratgitter tauchen auch komplexere Phasen mit bis zu 13 Teilchen pro Elementarzelle sowie ein dekagonaler Quasikristall (Dec) und ein dodekagonaler Quasikristall (Dod I) auf. Später wird sich herausstellen, dass noch ein weiterer dodekagonaler Quasikristall (Dod II) stabilisiert wird. Um das exakte Phasendiagramm zu berechnen, werden Relaxationen durchgeführt. Dazu wird eine Menge von potentiellen Grundstrukturen verwendet, die Teststrukturen, die entweder direkt aus den Abkühlsimulationen erhalten wurden, Variationen davon sind oder aus sonstigen Gründen als Grundzustände in Frage kommen. Für jede von ihnen wird ein defektfreies, ideales Tiling bei $T = 0$ relaxiert und dessen Energie bestimmt. Der Vergleich ergibt den exakten energetischen Grundzustand innerhalb der Menge der Teststrukturen. Es zeigt sich, dass die Ergebnisse der Abkühlsimulationen recht gut mit denjenigen der Relaxationen übereinstimmen, mit einer Ausnahme: Die Quasikristalle sind nicht stabil bei $T = 0$. Der energetische Grundzustand ist stattdessen jeweils ein komplexer Kristall mit ähnlicher lokaler Struktur, ein sogenannter Approximant. Jeder der drei Quasikristalle wird nun zusammen mit seinem Approximanten im Detail untersucht.

Die dekagonale Phase Dec entspricht einem stochastischen Tübinger Tiling (Random-Tiling). Das Wachstum aus der Schmelze erfolgt in einem Phasenübergang erster Ordnung. Dabei expandiert das Volumen des Systems, was als anomale thermische Expansion bezeichnet wird. Die stabilsten gebundenen lokalen Umgebungen sind Dekagon-Tiles. Sie tauchen in geringer Konzentration schon in der Schmelze auf, sind aber charakteristisch für Dec. Selbst bei einem großen System mit 10 000 Teilchen kann das thermische Gleichgewicht erreicht werden. Der resultierende hochgeordnete Quasikristall weist eine Vielzahl von scharfen Peaks im Beugungsbild und in der radialen Verteilungsfunktion und damit (algebraisch) weitreichende Ordnung auf. Die Dynamik ist von Phasonflips geprägt, die verteilt über das System und zeitlich unkorreliert auftreten.

Wie aus dem Phasendiagramm bekannt, ist Dec nur bei hohen Temperaturen stabil. Unterhalb der kritischen Temperatur T_C, die bei ca. 60% der Schmelztemperatur liegt, tritt ein Phasenübergang zum Approximanten Xi auf. Er entspricht einer dichtgepackten periodischen Anordnung der Dekagone. Der Phasenübergang lässt sich auch im Hyperraum beschreiben: Dazu wird die mittlere Orientierung der de Bruijn-Fläche in Abhängigkeit der Temperatur bestimmt. Die Orientierung entspricht der mittleren phasonischen Verzerrung $\boldsymbol{\chi}$ des Tilings, welcher ein Ordnungsparameter des Phasenübergangs ist. Oberhalb T_C verschwindet $\boldsymbol{\chi}$, darunter ist ein kontinuierlicher Anstieg zu beobachten. Die Berechnung der Energieabhängigkeit $E(\boldsymbol{\chi})$ zeigt, dass der Approximant Xi in der Tat der energetische Grundzustand ist.

Im Falle des dodekagonalen Quasikristalls Dod I erfolgt das Wachstum ebenfalls über einen Phasenübergang erster Ordnung Die thermische Expansion ist dabei wiederum anomal. Nahe der Schmelztemperatur ist eine einfache hexagonale Phase stabil. Der Übergang zur dodekagonalen Phase wird durch phononische Instabilitäten ausgelöst. Im Gleichgewicht entspricht die Struktur von Dod I einem Random-Tiling des Quadrat-Dreiecks-Tilings. Anders als in Dec können Phasonflips nur in Kombination mit speziellen Defekttiles, den Shield-Tiles auftreten. Der zugrunde liegende Mechanismus wird als Zipper (Reißverschluss) bezeichnet. Entlang der Trajektorien der Zipper ordnet sich der Kristall um. Es handelt sich dabei aber nicht um Leerstellendiffusion. Da der Zippermechanismus langsamer als die Phasonflips in Dec ist, weist das Tiling von Dod I eine größere Unordnung als das Tiling von Dec auf. Bei geeigneten Potentialparametern wurde allerdings auch ein vollständiger Übergang zum Approximanten Sig

gefunden. Die dazu notwendigen Umstrukturierungen kommen ausschließlich durch Zipper zustande.

Ein weiterer dodekagonaler Quasikristall Dod II wurde gefunden. Seine lokalen Teilchenanordnungen sind mit Dec verwandt, da das Tiling unter anderem aus Pentagonen aufgebaut ist. Interessanterweise bilden die Mittelpunkte der Pentagone wieder ein Quadrat-Dreiecks-Tilings. Daher kann Dod II als eine inflationierte Version von Dod I angesehen werden. In der Nähe der Schmelztemperatur ist das einfache Quadratgitter stabil, bei mittleren Temperaturen Dod II und bei niedrigen Temperaturen der Approximant Pen2. Das Wachstum von Dod II aus dem Quadratiling erfolgt in einem Phasenübergang erster Ordnung und mit normaler thermischer Expansion. Während des Übergangs von Dod II zu Pen2 werden in einem Zwischenschritt periodische Superstrukturen beobachtet Diese zeichnen sich durch Satelliten-Peaks im Beugungsbild ab. Mit fortschreitender Simulationsdauer wächst die Gitterkonstante der Superstruktur. Aufgrund der Größe ihrer Superzelle – sie umfasst mehrere hundert Teilchen – gehören die Pen2 Superstrukturen zu den komplexesten geordneten Strukturen, die bisher in Simulationen von einfachen Modellsystem aufgetreten sind.

Zusammenfassend lässt sich sagen: Mit dem hier vorgestellten Lennard-Jones-Gauß-System ist es erstmals möglich, das Wachstum, Phasenumwandlungen, die Gleichgewichtsdynamik und Defekte von komplexen Kristallen und Quasikristallen in Simulationen zu untersuchen. Die hier vorgestellten Ergebnisse ermöglichen eine Vielzahl weiterführender Arbeiten.

Part I.

Methods and theoretical background

Chapter 1.

Introduction

1.1. Structural complexity

A look at the periodic table reveals that the crystal structure of many elements is simple. This is especially true for metals, whose ground states with few exceptions are either body-centered cubic (bcc), face-centered cubic (fcc), or hexagonal closed-packed (hcp) [36, 93]. Similar structurally simple crystals are frequently found in mesoscopic or macroscopic systems. Examples are certain types of globular proteins [148], monodisperse colloidal particles [181], and bubble rafts on liquid surfaces yielding two-dimensional close-packed hexagonal and three-dimensional layered crystals [18].

Let us assume that the interaction in a system of identical particles (atoms, colloids, proteins, etc.) can be described with an effective pair potential. If the potential has a single minimum only, simple and close-packed crystals are almost inevitably observed at low temperatures. This is the case for noble gas atoms, which interact in a good approximation with a Lennard-Jones potential [169], but also for hard-sphere colloids crystallizing under gravity [138]. On the other hand, potentials which have a more complicated radial dependence can – but not automatically do – lead to more complex structures. Metals for example are well described with isotropic potentials, which have a strongly repulsive core plus a decaying oscillatory Friedel term [63]. As we will see below, this leads to the tendency to abandon simple crystal structures given appropriate conditions. Of course structural complexity also increases considerably in polydisperse systems, e.g. by mixing two or more elements, using colloids of different sizes, or branching polygons with different chain lengths.

How can structural complexity be understood from bottom-up? It is instructive to study the energy ground states for finite portions of the system – more or less spherical clusters – as a function of the particle number N. The structure of small clusters ($N < 200$ in three dimensions, $N < 30$ in two dimensions) is often quite different from the bulk crystal

($N \to \infty$) [37]. This is the case because the particle arrangement of small clusters is usually not compatible with periodicity. If certain clusters are energetically much more favorable compared to such local configurations, which are compatible with periodicity, then some of the clusters are preserved also in the bulk, and the space in-between is filled with additional particles. If, on the other side, these clusters are energetically only slightly favorable or the filling particles have a comparably high energy, it will be more advantageous to form a different, usually simpler structure. For example, in a monodisperse Lennard-Jones system icosahedral coordination frequently occurs in small clusters [131, 176].[1] However, in the bulk not icosahedral clusters, but the hcp crystal eventually appears [169]. Preserving the icosahedrons would cost too much energy. In general there is a competition between local lowest-energy configurations and the necessity of spatial continuity.

Structural complexity can imply the loss of long-range order. In this case, the system is in an amorphous state. Although frequently observed in experiment, the amorphous state usually is only metastable. For example metallic glasses have to be cooled rapidly[2] to suppress crystallization. Long-range ordered complex structures are either periodic with large unit cells or quasiperiodic. With respect to their physical properties, quasicrystals [84] can be seen as complex crystals with infinite unit cells. Both are intermediate to simple crystals and amorphous solids.

Complex crystals and quasicrystals are long-range ordered structures characterized by the following particular features [175]: *(i) Large or infinite unit cells containing a high number of particles. (ii) The particles are arranged in clusters with a multitude of different coordination polyhedra. (iii) Inherent chemical and configurational disorder.* The systems we are interested in, have one additional feature: *(iv) The particle interactions are well described with effective pair potentials.* The latter excludes most non-metals, because they interact with strong angular dependent covalent bonds. There is no fixed bound of how big the unit cells have to be for a crystal to be called complex. The following criterion can be used as a guideline: The lattice constants of a complex crystal should be larger than the range of its interaction potentials. This means that their unit cells are stabilized by geometric constraints.

[1] The icosahedron has the highest symmetry of all coordination polyhedra. The distance from the center to a vertex is only 5% smaller than the distance between two vertices.
[2] The slowest critical cooling rates are in the order of one Kelvin per second [61].

What we do not understand under structural complexity is the complexity of the particles themselves (in case of colloids, polymers, etc.). In general there should be a hierarchy between the forces stabilizing the particles and the interparticle forces.

1.2. Experimental realizations of complex crystals

Complex crystals in alloys have a long tradition. *James B. Friauf* solved the crystal structure of the magnesium compounds $MgCu_2$ and $MgZn_2$ already in 1927 [57, 58]. However, in recognition of extensive work by *Fritz Laves* and coworkers [104, 105, 179] this and one other related phase ($MgNi_2$) are collectively called the Laves phases. They turned out to be very common amongst binary alloys. The Laves phases are part of a larger class of intermetallic compounds – the packing dominated or Frank-Kasper phases [55, 56], which are characterized by high density and can be understood as tetrahedral packings of spheres [159, 161]. The Frank-Kasper principle requires that solely coordination polyhedra with 12, 14, 15, or 16 vertices appear. Pentagonal Frank-Kasper phases with predominantly icosahedral coordination polyhedra (coordination number CN 12) can be distinguished from hexagonal ones with predominantly CN 14 (hexagonal antiprism plus two caps) and mixtures of the two [3]. Whereas Laves-phases are pentagonal, an example for a hexagonal Frank-Kasper phase is the technologically important[3] σ-phase [160].

After the improvement of X-ray technology, reliable structure determinations of increasingly complex crystals came into reach. In 1957, *Gunnar Bergman*, *John L. T. Waugh*, and *Linus Pauling* solved the structure of $Mg_{32}(Al,Zn)_{49}$ with 162 atoms per unit cell [12]. It is a bcc packing of icosahedral 104 atom clusters. Together with the Mackay cluster [116], named after *Alan L. Mackay*, this Bergman cluster is today known to be the basic building block of many icosahedral quasicrystals and complex crystals with very large unit cells [101]. Both can be understood as a succession of shells with icosahedral symmetry as shown in Fig. 1.1. In many elemental metals and multi-component alloy systems they constitute the lowest-energy configurations.

With the discovery of quasicrystals in 1984 [156], most researchers who previously studied structurally complex alloy phases turned to the new

[3]The formation of the σ-phase crystallites leads to embrittlement of alloy steals.

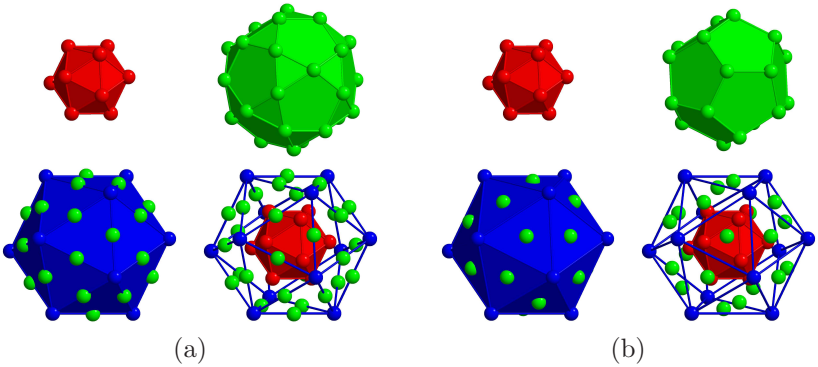

Figure 1.1: (a) The three inner shells of the Mackay cluster: icosahedron (red), icosidodecahedron (green), icosahedron (blue) containing 55 atoms. (b) First three shells of the Bergman cluster: icosahedron (red), dodecahedron (green), icosahedron (blue) containing 45 atoms.

field of aperiodic order. Only recently in the framework of an European Network of Excellence (NoE), "Complex Metallic Alloys" (CMAs), which was started in 2005, the focus of the community partially switched back again. The goal of the NoE is to drive forward the understanding of CMAs and survey potential technological applications. In a first, joint effort, the light-weight structure β-Mg_2Al_3 with 1168 atoms per unit cell, first solved by *Sten Samson* in 1965 [152], has been reevaluated, and its physical properties thoroughly measured [52]. Further work on several different families of alloy phases with typically several tens up to several thousands of atoms per unit cell is currently under way.

Today, it is established that structural complexity is not restricted to alloys. Over the last couple of years, complex phases have been observed in various physical systems on increasing length scales. First of all, complex ground states are found in a few elemental metals under ambient conditions, most notably in manganese. α-manganese has cubic symmetry with 58 atoms per unit cell [17]. Complex phases are quite common in many metals at high pressures [120]. The phase β-boron with 105 atoms per unit cell, thermodynamically stable at high temperatures, is built from icosahedrons located on a rhombohedral lattice [36].

Recently, different kinds of macromolecules have been observed to self-

assemble into complex crystals and quasicrystals. We discuss three systems: (i) Under appropriate experimental conditions tree-like molecules (dendrons) forming spherical micelles arrange to a dodecagonal quasicrystal [183]. The average separation of the micelles is nearly 10 nm, which is almost two orders of magnitude larger compared to few Ångstroms in metallic alloys. (ii) T-shaped molecules can be designed in such a way that they self-organize into nanoscale liquid crystalline honeycombs based on polygons with any chosen number of sides [23]. The resulting two-dimensional arrangements of cylinders have local pentagonal or dodecagonal order. (iii) Similarly, ABC-star polymers form cylindrical columns according to the two-dimensional σ-phase [68]. Random orderings of quadratic and triangular columns resemble dodecagonal quasicrystals. In all these systems, the interaction is well modeled with effective pair potentials. Due to the size of the molecules, multi-body contributions can be neglected.

On an even larger length scale, binary mixtures of colloids can lead to complex crystals. Recently, micron-sized plastic and glass particles have been found to form at least 12 new structures [107]. With various kinds of opposingly charged nanoparticles more than 15 crystals were observed [157]. Complex structures of colloids also have natural examples. Opals consist of spheres of silica dispersed in a solid solution of hydrated calcium carbonate. In the 1970s, it was discovered that Brazilian opals are made up of two different sizes of particles that form the AB_{13} structure, whose unit cell contains more than 100 particles (see the discussion in [30]). Colloidal self-assembly is currently a fast evolving field and new results emerge continuously.

1.3. A short history of quasiperiodic order

Historically, solids have been divided into two classes: amorphous structures and crystalline (morphous) structures. Whereas an amorphous solid is not ordered – the atoms are arranged only in some types of locally favorable configurations – a crystal is a regular, periodic pattern.[4] The idea that order in nature is necessarily achieved via periodicity goes back to the 18th century, when *René-Just Haüy* began formulating the mathematical theory of crystallography [67]. The equivalence of both concepts was

[4]The current definition of a crystal is given in the International Tables of Crystallography, Volume A [65], section 8.1.

widely believed to be true. Only in the last 25 years the notion of order in physics was expanded to include quasicrystals.[5] Nevertheless, examples of quasiperiodically ordered patterns were known to mathematicians for a long time (at least to a small group of people), but not attributed physical relevance.

The investigation of ordered patterns without periodicity is spread over centuries and cultures. The oldest reported appearances can be observed in the architecture of the medieval Islamic world. Probably by trial and error, *Islamic scientists* discovered highly symmetrical two-dimensional patterns (tilings) built from a special set of equilateral polygons (tiles). The tenth Century Arabic mathematician *Mohammed Abu'l-Wafa Al-Buzjani* introduced the use of tiles of so-called 'kite' and 'dart' shape. Between the 13th and 15th century, Arabian scientists developed a practical method, which made use of self-similar transformations to construct decagonal tilings [114, 118]. Ornaments with quasicrystal patterns have been found as decorations for shrines and mosques in Turkey, Iraq, Afghanistan, Iran, and India (Fig. 1.2(a)).

The German artist *Albrecht Dürer* became interested in the geometry of the plane through his investigations of perspective in art. In 1525 he made use of regular pentagons to produce tilings in which the gaps (or 'frustrations') were filled by rhombuses [28].[6] At the beginning of the 17th century, *Johannes Kepler* investigated the appearance of symmetry in the sciences as known at his time. By his study of two-dimensional infinite patterns he knew that triangles, squares, and hexagons can fill space without gaps, but not so e.g. pentagons or decagons. However, inspired by the earlier findings of Dürer, Kepler noticed that there was an alternative way if one is ready to accept a compromise [91]:

> *If you really wish to continue the pattern, certain irregularities must be admitted, two decagons must be combined, two sides being removed from each of them. As the pattern is continued outwards five-cornered forms appear repeatedly. [...] So as it progresses this five-cornered pattern continually introduces something new. The structure is very elaborate and intricate.*

The resulting tiling (Fig. 1.2(b)) has been much commented on (see [22]).

[5] The definition of quasicrystals will be given in Sec. 2.4.

[6] Many more examples of fivefold symmetry in nature, art, and mathematics can be found in [66].

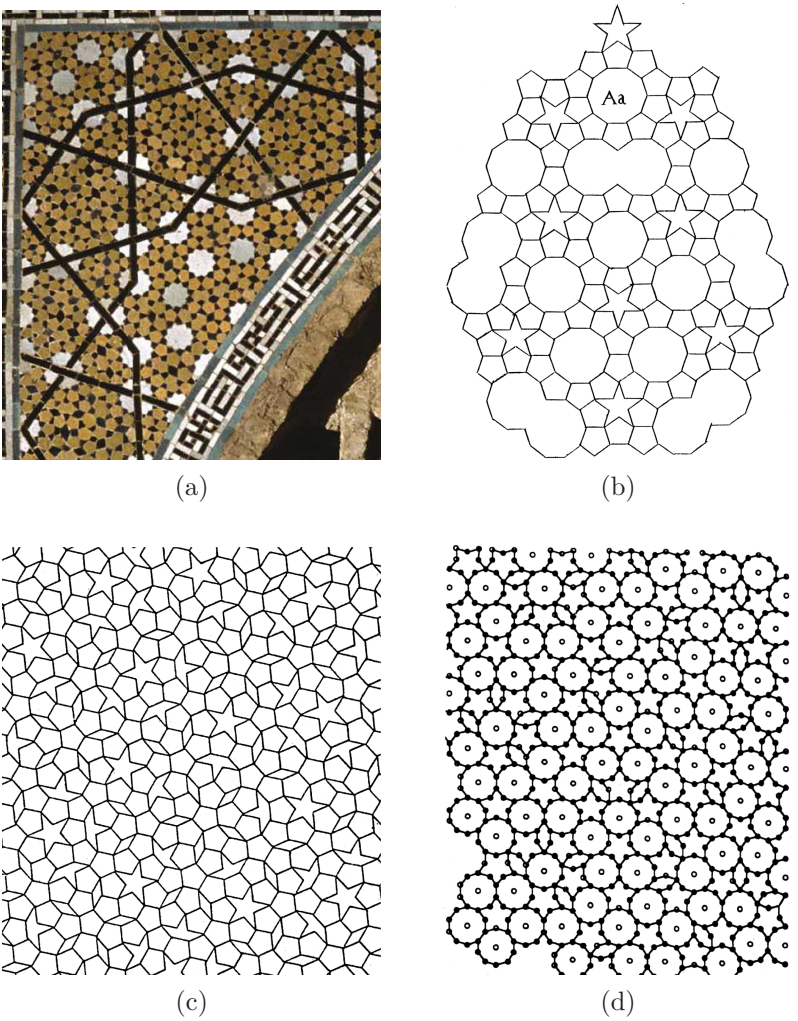

Figure 1.2: (a) Pattern on a spandrel from the Darb-i Imam shrine, Isfahan, Iran (1453) [114]. (b) One of Kepler's drawings (1619) [91]. (c) The pentagon tiling as presented by Penrose (1974) [136]. (d) Tiling observed in an electron microscopy image of a decagonal Al-Mn-Pd phase (1998) [158].

350 years later *Roger Penrose* "wanted to design something interesting for someone who was in hospital to look at" [136]. What he found was a "definite rule whereby one could continue [a configuration of pentagons and similar shapes] to arbitrary size", which made him "feel that the pattern has a certain esthetic appeal". The tiling, today called the pentagon tiling was born (Fig. 1.2(c)). Later a modification lead to a structurally identical tiling of only two different types of rhombic tiles, known as the Penrose tiling [137] (Fig. 1.3). Similar tilings and an extension to three dimensions were first described by *Robert Ammann*, a mail sorter for a post office and amateur mathematician.[7] A common feature was the composition of a few different types of tiles, which were fitted according to simple matching rules to fill all of space. However, the construction was still a bit tricky. In 1981, *Nicolaas G. de Bruijn* found a possibility to project the Penrose tiling from a higher-dimensional space [32]; an easy formalism, which simplified the construction significantly. One year later, *Alan L. Mackay* showed by the help of an optical transform that the Fourier transform of the Penrose tiling has the 'forbidden' five-fold symmetry [117]. In retrospect, these last mathematical discoveries were exactly in time to prepare the experimental observation to come two years afterwards.

The discovery of a "metallic phase with long-range orientational order and no translational symmetry" in 1984 by *Dan Shechtman*, *Ilan Blech*, *Denis Gratias*, and *John W. Cahn* [156] came as a big surprise to many researchers. Within months it initiated an enormous amount of experimental and theoretical work. At the beginning several publications tried to explain the new discovery using conventional concepts[8], but it was soon realized that these quasicrystals [109] did not fit into the known scheme of crystallography. The debate was silenced after high-resolution electron microscopy images clearly showed the aperiodicity (Fig. 1.2(d)). Nevertheless, modified theoretical models where quickly successful in explaining essential structural features of the quasicrystals [166]. The first model [109] was published only one month after the original discovery. Until today all models are characterized by the use of a higher-dimensional configuration space from which the quasicrystal is constructed via projection, cut, or some other dimension-reducing technique.

[7] After reading an announcement by science writer Martin Gardner [59] of new work by Roger Penrose, Ammann wrote a letter to Gardner describing his own discoveries. This started a series of correspondence lasting for several years [155].

[8] One example is the twined crystal theory by Nobel laureate Linus Pauling [135].

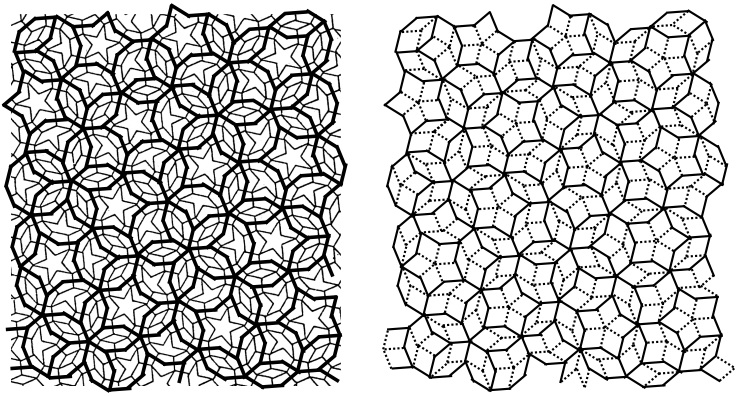

(a) (b)

Figure 1.3: (a) The HBS (hexagon, boat, star) tiling is obtained by connecting the centers of the pentagons in the pentagon tiling. (b) By introducing additional vertices the Penrose (rhomb) tiling (see also Fig. 3.3) is obtained. It is built from obtuse (ob) and acute (ac) rhombs: $H \mapsto 1 \times \mathrm{ob} + 2 \times \mathrm{ac}$, $B \mapsto 3 \times \mathrm{ob} + 1 \times \mathrm{ac}$, $S \mapsto 5 \times \mathrm{ob}$. The decomposition of the H-tile is ambiguous: It is done in such a way as to maximize the number of five-stars built from ob-tiles.

So, does this mean that aperiodic order is identical to quasicrystals? The answer is: It depends on the definition of order. There is an ongoing controversy on how to best define order (and crystallinity) [168]. Certainly crystals, quasicrystals, and modulated crystals[9] should be regarded as ordered, see Fig. 1.4. The opposite is not so clear. Today, there is no generally accepted mathematical criterion that could be used to distinguish order from disorder. From the experimental point of view the current vague understanding of order seems to be adequate and works quite well for the existing solid state systems.

1.4. Theoretical structure modeling

The most important tool for describing simple crystals is the notion of a unit cell. By applying the Bloch theorem the problem of treating an

[9] A modulated crystal has an incommensurable modulation of the chemistry or the positions of the atoms [34].

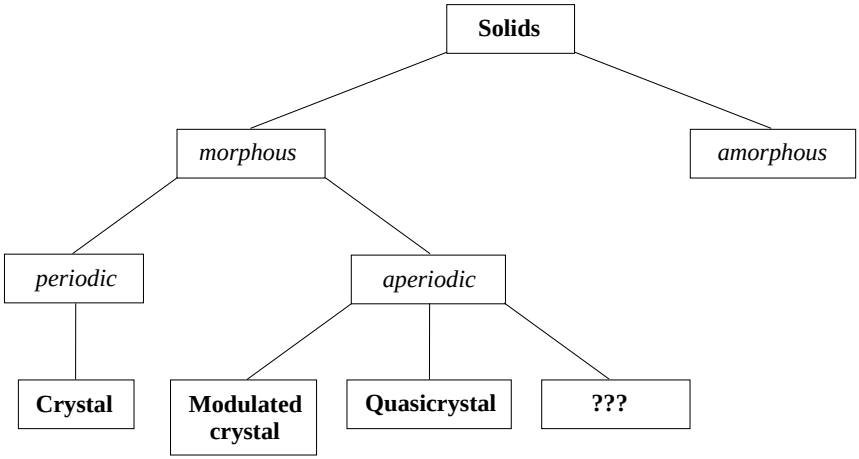

Figure 1.4: Classification of solids. At the moment there is no generally accepted definition of order. Structures on the left side would be regarded more ordered than structures on the right side.

infinite number of particles in the bulk is reduced to the study of particles inside one or a few unit cells.[10] Although complex phases on first sight seem much more complicated, there is still a possibility to simplify their theoretical description. Investigations of complex crystals have shown that certain local particle coordinations appear repeatedly inside the unit cell. Some of them are symmetric or stand out in another way – they are called clusters. Connecting one type of clusters generates a basic framework of the structure in the form of a tiling. In general the tiling is built from a finite number of different tiles, which can be arranged in various ways resulting in different phases. The physical properties of complex phases are influenced by three length scales: the interparticle distances, the tile sizes[11], and the unit cell dimensions.

The tiling model is especially useful for quasicrystals. Consider the vicinity of a particle inside a sphere of radius r. In all quasicrystals found up

[10] The study of particle dynamics or defects in simulations makes it necessary to expand the simulation box to several unit cells.

[11] The tile size is typically similar to the cluster diameter, if the clusters touch along the tile edges.

to date, there are for every radius r only a finite number of different local configurations. Therefore the tiling describing a quasicrystal will be built up by finitely many tile types only. Although often several choices for the clusters are possible, it is a priori not obvious what characterizes those which should be used to construct the tiling. Yet, highly symmetric ones like the Mackay- or Bergman-cluster have proven to be well-suited in many cases. The existence of a tiling description of quasicrystals follows directly from the study of their diffraction patterns: Similarly as in crystals, where the lattice of the Bragg peaks allows the identification of the unit cell, their positions in quasicrystals are determined solely by the tiling. A variation of the tile decoration does not change the positions of the Bragg peak, but only their intensity ratios.

The tiling substructure is of central importance for the dynamics and defects of complex phases. New dynamical modes in complex crystals are local rearrangements of the particles by discrete phason flips, which lead to changes of the tiling and an enhanced flexibility of the structure. They form so-called phason degrees of freedom, unknown for simple crystals. Defects appear either as defect tiles[12], possibly including vacancies or interstitials, and new types of dislocations combining regular strain with phason flips. Furthermore, the movement of dislocations and large-scale rearrangements of the tiling can generate phase transformations, induced either by mechanical stress or by a change of temperature and pressure.

We note that the description of phason flips and tile rearrangements within the tiling model is only possible, if it is thermodynamically robust. This means that the tiling should not be broken easily, e.g. by defects. In other words, the tiles themselves have to be somehow stabilized energetically, and the clusters or coordinations used for the construction of the tiling need to have low energies compared to the rest of the structure. Nevertheless, it is safe to say that the stabilization of the tiling substructure is currently not well understood and subject to controversies and discussions [73].

1.5. Outline

The thesis is split into two parts: In the first part we introduce the necessary methods and theoretical background. We begin by extending conven-

[12] Defect tiles have higher energy and do not appear in the ground states.

tional crystallography from simple periodic systems to general tiling models. This is done by making use of higher-dimensional spaces (chapter 2) and is the basis for modeling complex crystals and quasicrystals. All tilings needed are presented in chapter 3. They are one- and two-dimensional. After the discussion of the static structure, we come to dynamics and defects in chapter 4. Of special interest are phason flips and partial dislocations. Characteristic functions of the correlated particle motion are the structure factors. As main numerical tools we use molecular dynamics and (in a few places) Monte Carlo simulations (chapter 5). They are implemented using an own code, which allows to run the simulations interactively. An efficient analytic method for calculating tilings from a higher-dimensional model with and without phason fluctuations and dislocations is the iterative selection method.

The model systems and results follow in the second part. Three different model systems are examined:

(i) Because the conventional theory for the structure factors is available for three-dimensional systems with few exceptions only, we generalize it to the case of analytically solvable harmonic lattices in one and two dimensions (chapter 6). The structure factors are then extracted from simulations for various one-dimensional chains to see the influence of quasiperiodicity and anharmonicity. Furthermore, the particle motion in real space is studied in chapter 7.

(ii) The intermetallic system AlPdMn is interesting due to the occurrence of several quasicrystals and complex metallic alloys in the phase diagram. Metadislocations and phason flips are a consequence of structural complexity. We explain experimental observations using simple tiling models in chapter 8.

(iii) The Lennard-Jones-Gauss potential is a family of double-well functions parametrised by the position, depth, and width of the second well. If applied to a system of identical particles in two dimensions, it has a surprisingly rich phase behavior with interesting particle dynamics as shown in chapter 9.

We finish with a short summary in chapter 10.

Chapter 2.

Higher-dimensional crystallography

To describe the structure of quasicrystals and complex crystals an extension of the conventional crystallography is necessary. We introduce the basic techniques using higher-dimensional configuration spaces. Most of the theory in this chapter is well-known with the exception of a new tiling construction method called selection method [45].

2.1. Crystals and their symmetries

In a d-dimensional crystal a general position $\boldsymbol{x}$ can be uniquely written as

$$\boldsymbol{x} = \boldsymbol{x}_0 + \sum_{i=1}^{d} a_i \boldsymbol{t}_i, \tag{2.1}$$

where the linearly independent vectors $\boldsymbol{t}_i$ are the basis of a lattice Γ with coefficients $a_i \in \mathbb{Z}$. The residual vector $\boldsymbol{x}_0 = \sum_i \lambda_i \boldsymbol{t}_i$, $0 \leq \lambda_i < 1$ lies inside a parallelepiped spanned by the $\boldsymbol{t}_i$. All possible $\boldsymbol{x}_0$ form a unit cell Z of the crystal. An alternative choice for the unit cell is the *Voronoi cell*, which consists of the points $\boldsymbol{x}_0$ with $|\boldsymbol{x}_0| \leq |\boldsymbol{t} - \boldsymbol{x}_0|$ for all $\boldsymbol{t} \in \Gamma$. The unit cell is decorated with atoms and will often contain only a few atoms, but as we will see later it can also include many more. The full crystal is the periodic continuation of the unit cell.

A *symmetry* is an Euclidean transformation, which leaves the crystal invariant. In other words, a symmetry maps atom positions onto each other. The transformation consists of an orthogonal matrix $\mathcal{T}$ representing a distance preserving transformation, and a translation $\boldsymbol{t} \in \Gamma$. The operation on an arbitrary vector $\boldsymbol{x}$ is given by

$$\{\mathcal{T}, \boldsymbol{t}\}\boldsymbol{x} = \mathcal{T}\boldsymbol{x} + \boldsymbol{t} \tag{2.2}$$

with the product of two transformations

$$\{\mathcal{T}_1, \boldsymbol{t}_1\}\{\mathcal{T}_2, \boldsymbol{t}_2\} = \{\mathcal{T}_1\mathcal{T}_2, \mathcal{T}_1\boldsymbol{t}_2 + \boldsymbol{t}_1\}. \tag{2.3}$$

n	1	2	3	4	5	6	7	8	9	10
$\Phi(n)$	0	1	2	2	4	2	6	4	6	4
n	11	12	13	14	15	16	17	18	19	20
$\Phi(n)$	10	4	12	6	6	8	16	6	18	6

Table 2.1: The additive Euler totient function Φ (see [74]). A symmetry of order n can be found in d-dimensional crystals only if $d \geq \Phi(n)$.

A symmetry is called of order n, if $\{\mathcal{T}, \boldsymbol{t}\}^n = \{1, \mathbf{0}\}$, which is equivalent to $\mathcal{T}^n = 1$. In three dimensions an orthogonal matrix $\mathcal{T}$ is a rotation of angle θ, possibly followed by an inflection at the origin. It has trace $\pm(1+2\cos\theta)$. By using the lattice basis $\boldsymbol{t}_i$, the matrix $\mathcal{T}$ will have only integer entries, this means $2\cos\theta \in \mathbb{Z}$. The result is known as the *crystallographic restriction*: Rotational symmetries of a three-dimensional crystal are limited to the orders 2, 3, 4, and 6. Especially, there are no fivefold axes or higher than sixfold symmetry axes.

A generalized version of the crystallographic restriction for higher dimensions can be formulated by the use of an additive version of Euler's totient function, Φ (Tab. 2.1): A d-dimensional crystal can have a symmetry of order n if $d \geq \Phi(n)$. Fivefold, eightfold, tenfold and twelvefold symmetries require $d \geq 4$. For proofs see the references [74, 154].

2.2. The reciprocal lattice

Diffraction experiments are ideally suited to study the structure and dynamics of crystals. Either X-rays, electrons, or neutrons with wavelength close to the interatomic distances can be used. Electrons feel the influence of both the atomic nuclei and the surrounding electrons. In comparison, X-rays interact with the spatial distribution of the valence electrons, while neutrons are scattered by the atomic nuclei through the strong nuclear forces. In all cases, the interaction is described locally by the scattering power $\rho(\boldsymbol{x})$, which we will simply call the *distribution of matter* in the following.[1] The incoming plane wave with wave vector $\boldsymbol{q}_{\text{in}}$ is scattered to an

[1] By this we mean: $\rho(\boldsymbol{x})$ is the distribution of matter responsible for the scattering. The following considerations do not depend on the choice of ρ, as long as it is peaked at the position of the atoms.

outgoing wave vector $\boldsymbol{q}_{\text{out}}$. Non-energy resolved diffraction experiments measure the *diffraction image* (also known as static structure factor or scattering intensity) $S(\boldsymbol{q}) = |\rho(\boldsymbol{q})|^2$ as a function of the transferred wave vector $\boldsymbol{q} = \boldsymbol{q}_{\text{out}} - \boldsymbol{q}_{\text{in}}$. $\rho(\boldsymbol{q})$ is the Fourier transform of $\rho(\boldsymbol{x})$,

$$\rho(\boldsymbol{q}) = \int \mathrm{d}^d\boldsymbol{x}\; e^{-\mathrm{i}\boldsymbol{q}\cdot\boldsymbol{x}}\rho(\boldsymbol{x}). \tag{2.4}$$

Using (2.1), the spatial integral can be decomposed into a integral over the unit cell and a sum over the lattice,

$$\rho(\boldsymbol{q}) = \sum_{\boldsymbol{t}\in\Gamma} e^{-\mathrm{i}\boldsymbol{q}\cdot\boldsymbol{t}} \int_Z \mathrm{d}^d\boldsymbol{x}_0\; e^{-\mathrm{i}\boldsymbol{q}\cdot\boldsymbol{x}_0}\rho(\boldsymbol{x}_0). \tag{2.5}$$

This will be non-zero in case of constructive interference of the outgoing waves, which for ideal crystals at zero temperature can only be satisfied by wave vectors on the reciprocal lattice Γ^*, given by

$$\Gamma^* = \{\boldsymbol{Q} \mid \boldsymbol{Q}\cdot\boldsymbol{t} \in 2\pi\mathbb{Z} \text{ for all } \boldsymbol{t}\in\Gamma\}. \tag{2.6}$$

$\rho(\boldsymbol{q})$ is singular on the reciprocal lattice. The singular points are called *Bragg peaks*.

Let us assume that the crystal and thus the distribution of matter is invariant under the transformation $\{\mathcal{T}, \boldsymbol{t}\}$, i.e.

$$\rho(\boldsymbol{x}) = \rho(\{\mathcal{T}, \boldsymbol{t}\}\boldsymbol{x}). \tag{2.7}$$

After applying the Fourier transform we obtain

$$\rho(\boldsymbol{q}) = e^{\mathrm{i}(\mathcal{T}\boldsymbol{q})\cdot\boldsymbol{t}}\rho(\mathcal{T}\boldsymbol{q}) \tag{2.8}$$

and $S(\boldsymbol{q}) = S(\mathcal{T}\boldsymbol{q})$. In this way the symmetries of the crystal are mapped on symmetries of the diffraction image. The reverse mapping is also possible with an exception: The inversion $\mathcal{I}$ and the compositions $\mathcal{I}\circ\mathcal{T}$ are always symmetries of the diffraction image, even if they are not symmetries of the crystal.

2.3. Hyperspaces for tilings

A *tiling* is a space-filling with an infinite number of building blocks, the *tiles*. We assume that: (1) The tiles are bounded by planar sides, which

means they are line segments in one dimension, polygons in two dimensions, and polyhedra in three dimensions. (2) There is only a finite number of *prototiles*, and every tile is a translated copy of one of the prototiles. The second condition is known as *finite local complexity. Such tilings are the simplest extension of periodic lattices.* Since there is only a finite number of prototiles, every vector connecting two vertices of the tiling is an integer multiple of a finite number n of vectors,

$$\boldsymbol{t} = \sum_{i=1}^{n} a_i \boldsymbol{t}_i. \tag{2.9}$$

We assume that n is minimal and there are at least two prototiles. Then it is easily seen that this expansion is unique with $n > d$, and the $\{\boldsymbol{t}_i \mid i = 1, \ldots, n\}$ form an *integer tiling basis*. Although the $\boldsymbol{t}_i$ are not linearly independent over the real numbers, they can be embedded as a real basis in a n-dimensional space, called *hyperspace*, where they form a lattice, the *hyperlattice*. Using this basis, the tiling vertices can be *lifted* into the hyperspace as a subset of the hyperlattice, called the *de Bruijn surface*. Conversely, a point in hyperspace can be *lowered* to the *tiling space* E. The lowering is described by the *lowering operator* $\mathcal{L} = (\boldsymbol{t}_1 \ \boldsymbol{t}_2 \ \cdots \ \boldsymbol{t}_n)$. Two hyperspace points are lowered to the same point in E, if their difference lies in the orthogonal complement $E^\perp$.

As a basic example we study a one-dimensional tiling consisting of two tiles: a short tile S and a long tile L. In the two-dimensional hyperspace with the square hyperlattice the L-tile corresponds to the horizontal, and the S-tile to the vertical basis vector of the lattice. Every tiling of L and S can be lifted unambiguously to a de Bruijn surface in the form of a staircase as shown in Fig. 2.1. Conversely any such staircase running strictly from bottom left to top right can be lowered to a tiling of L- and S-tiles.

One method to construct tilings with a uniform distribution of a finite number of prototiles is the *selection formalism* [45].[2] We need: (i) the n-dimensional hyperspace plus hyperlattice, (ii) a unit cell of the hyperlattice[3], called the atomic volume, (iii) a lowering operator $\mathcal{L}$ (or alternatively a tiling basis $\{\boldsymbol{t}_i \mid i = 1, \ldots, n\}$ in E), (iv) a *phason*[4] *displacement*

[2] There are tilings with a finite number of prototiles, which cannot be constructed with the selection formalism, e.g. the square-triangle tiling in Sec. 3.5.

[3] The canonical choice for the atomic volume is the Voronoi cell of the hyperlattice.

[4] The name "phason" originates from the theory of modulated crystals. Therein the pha-

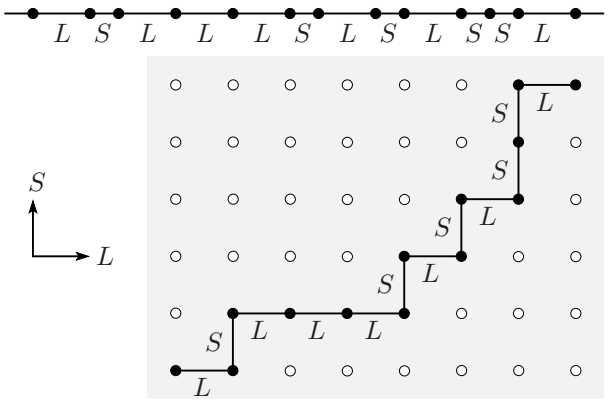

Figure 2.1: The one-dimensional tiling $LSLLLSLSLSSL$ of L- and S-tiles can be lifted to a staircase on the square lattice in a two-dimensional hyperspace.

$\boldsymbol{u}^\perp : E \to E^\perp$. The phason displacement parameterizes the *cut space* E_C:

$$\boldsymbol{x} \mapsto \boldsymbol{x} \oplus \boldsymbol{u}^\perp(\boldsymbol{x}), \quad E \to E_C \subset E \oplus E^\perp. \tag{2.10}$$

For the application of the selection formalism we first append the atomic volume to each hyperlattice point. Next we select those atomic volumes, which are cut by E_C. Finally the hyperlattice points corresponding to the selected atomic volumes are lowered on E. For the one-dimensional tiling with a square as atomic volume this is demonstrated in Fig. 2.2. In a more elaborated version of the selection formalism several atomic volumes per unit cell can be used in the construction process.

The selection formalism allows the control of two tiling parameters: (i) The lowering operator $\mathcal{L}$ determines the tile shapes. It is kept constant, if one is interested in tilings built from the same prototiles. (ii) The phason displacement and thus the cut space E_C determines the arrangement of the tiles. The lifting of a tiling into the hyperspace can be used to reconstruct the phason displacement $\boldsymbol{u}^\perp(\boldsymbol{x})$ of a tiling. Note that $\boldsymbol{u}^\perp(\boldsymbol{x})$ is only defined up to a small displacement inside the atomic volumes, which is irrelevant for the construction.

son corresponds to a change of the modulation phase, which is a continuous symmetry operation [34]. The term has been used first by Overhauser in 1971 [132].

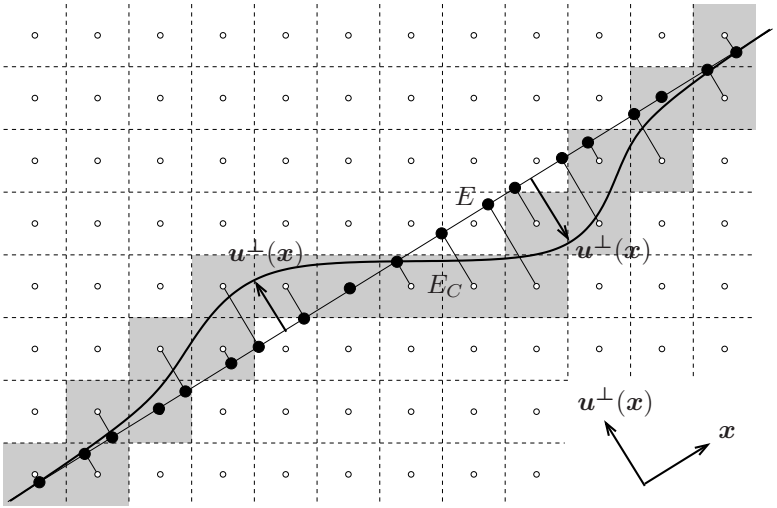

Figure 2.2: The selection formalism for a spatially varying phason displacement $\boldsymbol{u}^\perp(\boldsymbol{x})$. The hyperlattice points selected by E_C are lowered on E. The phason displacement induces discrete phason flips.

2.4. Construction of quasicrystals

A solid is called *quasiperiodic*, if it has a dense, but discrete set of Bragg peaks, which can be indexed with a finite number n of vectors $\boldsymbol{t}_i^*$, greater than the space dimension (Fig. 2.3(a)). $\rho(\boldsymbol{q})$ is then given by

$$\rho(\boldsymbol{q}) = \sum_{\boldsymbol{Q}\in\Gamma^*} S_{\boldsymbol{Q}}\delta(\boldsymbol{Q}-\boldsymbol{q}) \tag{2.11}$$

with $\Gamma^* = \{\sum_{i=1}^n a_i\boldsymbol{t}_i^* \mid a_i \in \mathbb{Z}\}$, $n > d$. Although the points in Γ^* do not form a lattice, they can be obtained as the projection with the projection operator $\mathcal{P}$ of a hyperlattice in an n-dimensional space, the hyperspace. This separates the hyperspace in $E \oplus E^\perp$, where E is the physical space of the atoms and $E^\perp$ an internal space. We can now find a function $\rho(\boldsymbol{q}, \boldsymbol{q}^\perp)$ in hyperspace with Bragg peaks on the hyperlattice and $\mathcal{P}\rho(\boldsymbol{q}, \boldsymbol{q}^\perp) = \rho(\boldsymbol{q})$. The distribution of matter $\rho(\boldsymbol{x})$ is calculated from $\rho(\boldsymbol{q})$ using the hyper-

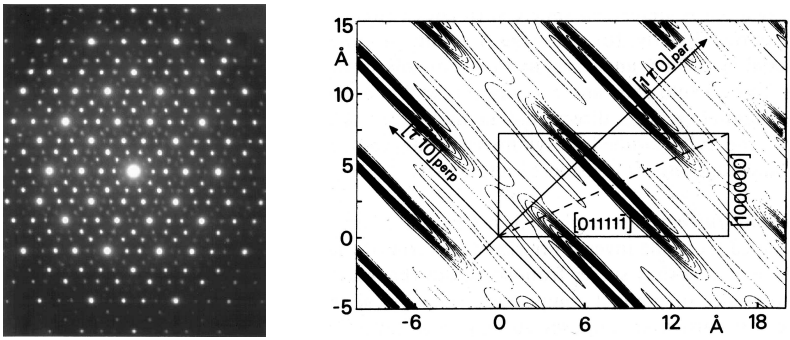

(a) (b)

Figure 2.3: (a) Diffraction image of an icosahedral quasicrystal in direction of a fivefold axis. Six vectors are needed to index the Bragg peaks. (b) Two-dimensional projection of the Li atom density for an icosahedral Al-Cu-Li quasicrystal in six-dimensional hyperspace as obtained from Fourier transform of the diffraction image. The atomic surfaces extend in the internal direction (perp), which is perpendicular to the physical direction (par) [84].

space in an intermediate step:

$$\rho(\boldsymbol{x}) = \int \frac{\mathrm{d}^d \boldsymbol{x}}{(2\pi)^d}\, e^{\mathrm{i}\boldsymbol{q}\cdot\boldsymbol{x}} \mathcal{P}\rho(\boldsymbol{q}, \boldsymbol{q}^\perp) = \rho(\boldsymbol{x}, \boldsymbol{0}). \tag{2.12}$$

Here $\rho(\boldsymbol{x}, \boldsymbol{x}^\perp)$ is the Fourier transform of $\rho(\boldsymbol{q}, \boldsymbol{q}^\perp)$. Since the latter has periodic support in hyperspace, $\rho(\boldsymbol{x}, \boldsymbol{x}^\perp)$ is a periodic function. The restriction on $\boldsymbol{x}^\perp = \boldsymbol{0}$ is called a cut. We have shown: *A quasiperiodic function is a planar cut of a periodic function.*

In a *quasicrystal*[5] the atoms are represented by *atomic surfaces* in hyperspace. These surfaces are sharply peaked in E, but extend along the direction of $E^\perp$, so that the cut dissects them along their narrow axis. As example, the calculation of the atomic surfaces from the experimental diffraction image is shown in Fig. 2.3(b).

The corresponding construction process is the *cut formalism*. We need: (i) the hyperspace plus hyperlattice, (ii) the position and orientation of the

[5]Every quasicrystal is quasiperiodic, but not every quasiperiodic solid is a quasicrystal. Examples for the latter are modulated crystals and random tilings (see Sec. 4.1.3).

physical space E, (iii) the decoration of one of the hyperlattice unit cell, i.e. the positions and shapes of the atomic surfaces. Furthermore, there are constraints on the shape of the atomic surfaces: The total number of atoms, electrons, etc. should not change upon a shifting of E in direction of $E^\perp$. At the end of one atomic surface (seen along $E^\perp$) always a new atomic surface has to begin. This is known as the *closeness condition* [89]. In case there are several atomic surfaces per unit cell, the tiles will be decorated with several atoms.

We explain the cut formalism using the two-dimensional model from the last section: We choose one atomic surface per unit cell given as the projection of a unit cell on $E^\perp$.[6] The atomic surfaces extending in $E^\perp$ are cut by E at the locations of the atoms as shown in Fig. 2.4. Note that the midpoints of those atomic surfaces, which are cut by E, form a staircase in the hyperlattice as indicated by the dashed line. A short distance S corresponds to a vertical part of the staircase, and a long distance L to a horizontal part.

The cut formalism and the selection formalism are closely related: On the one hand the projections of the atomic volumes on $E^\perp$ can be used as atomic surfaces, on the other hand the atomic surfaces can be expanded in the hyperspace to fill it without gaps. This shows that the cut formalism is equivalent to the selection formalism with $E_C = E$. From this we conclude: *A quasicrystal is a tiling with a finite number of decorated prototiles.*

The symmetry of a quasicrystal is defined as the symmetry of its diffraction image. It is found in the experiment that quasicrystals have symmetries which are forbidden by the crystallographic restriction (although there is no mathematical necessity for that). They have icosahedral, octagonal, decagonal, or dodecagonal order. The latter three are periodic in two dimensions and quasiperiodic in the third, i.e. a periodic stacking of quasiperiodic layers.

2.5. Phason flips and approximant tilings

If the selection formalism and the cut formalism are extended to describe two- and three-dimensional tilings, all of the concepts explained above for the one-dimensional chain will be generalized. Although in many cases the two formalisms can be used interchangeably, the selection formalism

[6] This is the again the canonical choice for the atomic surface.

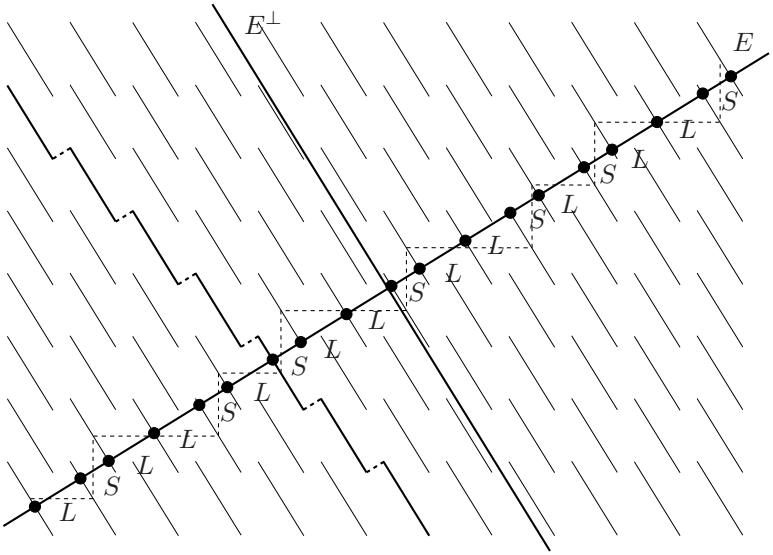

Figure 2.4: Cut formalism for the construction of a simple one-dimensional quasicrystal. The atomic surfaces are connected: A shifting of E in direction of $E^\perp$ does not change the number of atoms.

is more general: An arbitrary phason displacement is possible in the selection formalism, whereas only a constant or linear phason displacement is applicable in the cut formalism.[7] However, the cut formalism has a practical advantage: Only the atomic surfaces can be determined directly from the diffraction image, but not the atomic volumes. The cut formalism is typically used for the structure determination from diffraction experiments. The selection formalism is the formalism of choice for studying variations of the phason displacement, which plays a crucial role for the particle dynamics and defects.

The arrangement of the tiles is modified by applying a phason displacement $\boldsymbol{u}^\perp(\boldsymbol{x})$. This can be seen in Fig. 2.2: A variation of $\boldsymbol{u}^\perp(\boldsymbol{x})$ changes E_C and the selection of atomic volumes, and therefore the sequence of L

[7] A varying phason displacement in the cut formalism can lead to a violation of the closeness condition. An extreme case is a cut space which does not intersect any atomic surfaces at all.

and S. In the case of a small, local variation an exchange of a L- and a S-tile can occur, $LS \leftrightarrow SL$, which is called a *phason flip*. It is the elementary process for the tile dynamics. Every tile rearrangement is achieved by a sequence of phason flips. In general, if the d-dimensional tiling is constructed from a n-dimensional hyperspace, there are $n - d$ directions to apply a local phason displacement. One can say: The tiling has $n - d$ *phason degrees of freedom*. If for some reason phason flips are not possible (see Sec. 3.5), then one or several of the phason degrees of freedom are *not excitable*.

Whereas local variations of $\boldsymbol{u}^{\perp}(\boldsymbol{x})$ do not modify the average number densities of the tiles, this is necessarily achieved with global variations. If we describe the variations by the *phason strain tensor*

$$\chi_{ij} = \frac{\mathrm{d}u_i^{\perp}}{\mathrm{d}x_j}, \tag{2.13}$$

then a tiling will be termed a *perfect tiling*, if $\chi = \text{const}$, a *random tiling* (see also Sec. 4.1.3), if $\chi \neq \text{const}$, and an *approximant*, if the average $\langle\chi\rangle \neq 0$. Perfect tilings have a flat cut space and approximants a tilted one in spatial average. The tiling of the latter approximates the quasicrystal tiling and usually has a highly complex unit cell [60]. If the orientation of the cut space is rational with respect to the hyperlattice, the approximant will be a periodic tiling, otherwise it is a quasicrystal. Periodic approximants are complex crystals.

Chapter 3.

Some one- and two-dimensional tilings

After the extension of crystallography to include general tilings, we now study one- and two-dimensional examples, which will play a central role in the course of this work.

3.1. The Fibonacci chain

The *Fibonacci chain* is a one-dimensional quasicrystal built from particles arranged according to a sequence of two tiles: a large one with length L and a short one with length S. The tiling results from the successive application of the *inflation rule* $L \mapsto LS$, $S \mapsto L$ starting from a single L-tile:

$$\begin{aligned} &L \mapsto LS \mapsto LSL \mapsto LSLLS \mapsto \\ &LSLLSLSL \mapsto LSLLSLSLLSLLS \mapsto \dots \end{aligned} \tag{3.1}$$

After n inflation steps the number of L-tiles is F_{n+1} and the number of S-tiles F_n with the F_n given by $F_1 = F_2 = 1$ and $F_{n+1} = F_n + F_{n-1}$. These numbers are known as the *Fibonacci sequence*:

$$1, 1, 2, 3, 5, 8, 13, 21, 34, 55, 89, \dots \tag{3.2}$$

We summarize the inflation in an *inflation matrix*

$$\begin{pmatrix} N_L' \\ N_S' \end{pmatrix} = \begin{pmatrix} 1 & 1 \\ 1 & 0 \end{pmatrix} \begin{pmatrix} N_L \\ N_S \end{pmatrix}, \tag{3.3}$$

where N_L, N_S, N_L', N_S' are the numbers of L- and S-tiles at the n-th and $(n+1)$-th step of the inflation. The number densities per unit area n_L, n_S are obtained from the dominant eigenvector of the inflation matrix: $n_L = \tau^{-1}$, $n_S = \tau^{-2}$. Here $\tau = \frac{1}{2}(\sqrt{5}+1)$ is the *golden number*[1] and $n_L + n_S = 1$.

[1]The golden number satisfies the relation $\tau : 1 = (\tau + 1) : \tau$, i.e. $\tau^2 = \tau + 1$.

The tiling can be constructed from a two-dimensional hyperspace with the square hyperlattice as already introduced in the Secs. 2.3, 2.4 and Fig. 2.2. We now give an analytical formula for the Fibonacci chain. The choice of the planar cut space guarantees the most uniform distribution of L and S along the chain. Therefore we separate the position of the j-th particle in a periodic plus a discretely modulated part:[2]

$$x_j - x_0 = jS + \lfloor n_L j \rfloor (L - S) = \lceil n_S j \rceil S + \lfloor n_L j \rfloor L. \tag{3.4}$$

Here $\lfloor x \rfloor$ and $\lceil x \rceil$ are the floor and the ceil function, i.e. the largest integer less than or equal to x and the lowest integer not less than x. For $j \geq 1$ this gives $LSLLSLSLLSLLS\ldots$

The Fibonacci sequence and the golden number are closely related. We list some of their properties:

(i) $\tau^n = F_n\tau + F_{n-1}$

(ii) $(-\tau)^{-n} = F_{n+1} - F_n\tau$

(iii) $F_n = \frac{1}{5}\sqrt{5}(\tau^n - (-\tau)^{-n})$

(iv) $\lim\limits_{n\to\infty} \dfrac{F_n}{F_{n-1}} = \tau$

(v) $\dfrac{a\tau + b}{c\tau + d} = \dfrac{ac - bc - bd + \tau(bc - ad)}{c^2 - cd - d^2}$

(vi) $\cos(\frac{2\pi}{10}) = \frac{1}{2}\tau, \quad \sin(\frac{2\pi}{10}) = \frac{1}{2}\tau^{-1}\sqrt{\tau + 2},$
$\cos(\frac{2\pi}{5}) = \frac{1}{2}\tau^{-1}, \quad \sin(\frac{2\pi}{5}) = \frac{1}{2}\sqrt{\tau + 2}$

Especially due to the last property, the golden number is important for the geometry of the pentagon and the decagon.

3.2. Tripod tiling

The tripod tilings are the simplest two-dimensional tilings with at least two prototiles. They are constructed from a three-dimensional hyperspace with a cubic hyperlattice. Depending on the choice of the tiling basis $\{\boldsymbol{t}_i\}_{i=1}^3$

[2]The inflation rule can be seen using $j = j' + \lfloor j' n_L \rfloor$ in (3.4): $x_{j'} - x_0 = \lceil j' n_S \rceil L + \lfloor j' n_L \rfloor (L + S)$. The $(x_{j'})_{j'}$ form an deflated Fibonacci chain with tiles LS and L.

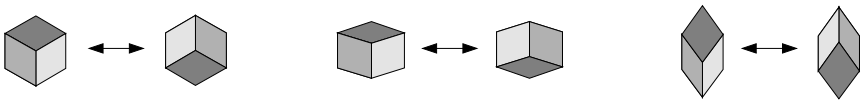

Figure 3.1: The phason flip of the tripod tiling. The dark gray rhomb is moved in the vertical direction.

three variants are distinguished. The lowering operator for the *three-star tripod tilings* is given by

$$\mathcal{L}_3 = \begin{pmatrix} -\cos(2\pi\frac{1}{3}) & 1 & -\cos(2\pi\frac{2}{3}) \\ -\sin(2\pi\frac{1}{3}) & 0 & -\sin(2\pi\frac{2}{3}) \end{pmatrix}, \tag{3.5}$$

whereas for the *obtuse five-star tripod tilings* and the *acute five-star tripod tilings*

$$\mathcal{L}_{\mathrm{ob}} = \begin{pmatrix} c_4 & 1 & c_1 \\ s_4 & 0 & s_1 \end{pmatrix}, \tag{3.6}$$

$$\mathcal{L}_{\mathrm{ac}} = \begin{pmatrix} -c_2 & 1 & -c_3 \\ -s_2 & 0 & -s_3 \end{pmatrix}. \tag{3.7}$$

with $s_i = \sin(2\pi\frac{i}{5})$ and $c_i = \cos(2\pi\frac{i}{5})$. The selected hyperlattice vertices form a two-dimensional staircase surface (Fig. 3.2(a)), from which the tilings are constructed with the lowering operators (Fig. 3.2(b)–(d)). There are three prototiles, whose shapes are determined by the tiling basis. Their arrangement depends on the choice of the cut plane and thus the phason displacement. Note that the tilings can be visualized (with some practice) by imagining Fig. 3.2(a) as a staircase surface in three dimensions. The black rhombs serve as guides to the eye: They are mapped on each other by the lowering operators. The three-star tilings are built from three congruent rhombs, the five-star tiling from obtuse rhombs (smallest interior angle 72°) and acute rhombs (36°), known as the *Penrose rhombs*.

There is only one type of phason flip in the tripod tilings (Fig. 3.1), which moves the rhomb spanned by $\boldsymbol{t}_1$ and $\boldsymbol{t}_3$ (shown in dark gray) past the other two rhombs. By successive phason flips the dark gray rhomb can slide in the vertical direction.

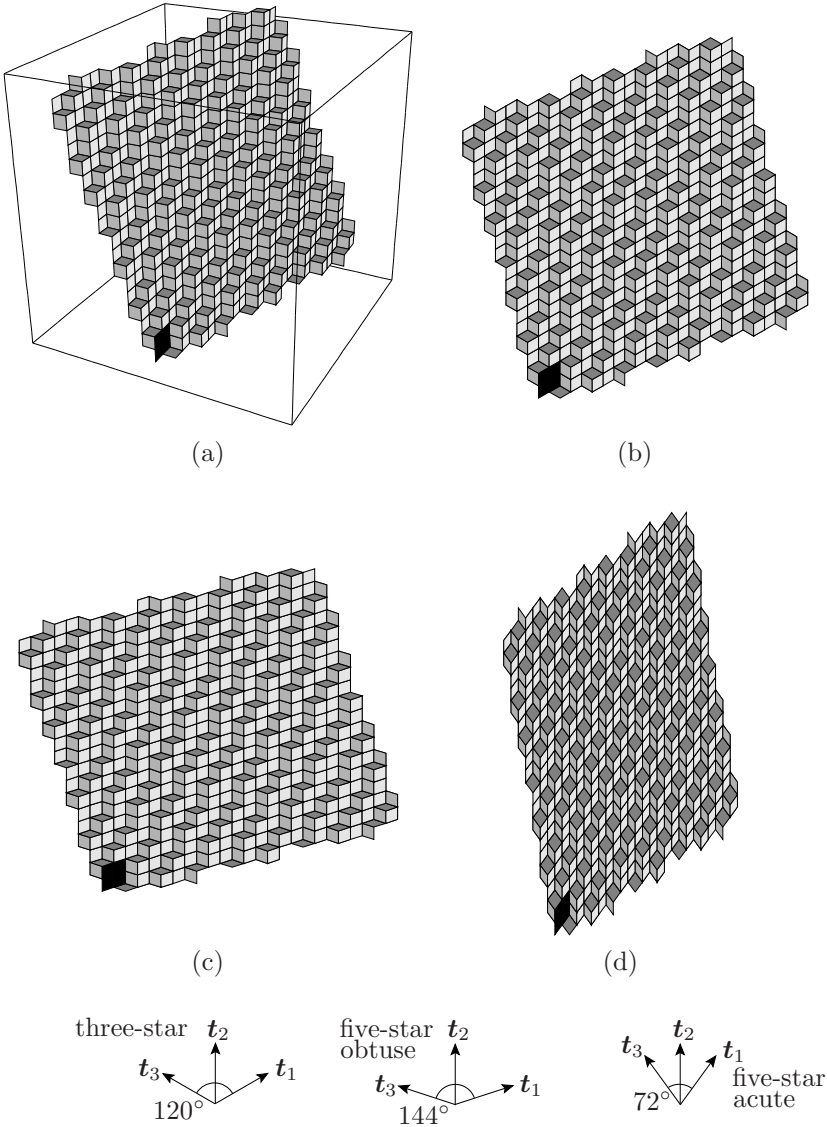

Figure 3.2: The staircase surface (a) is lowered to a three-star (b), obtuse (c) and acute (d) five-star tiling using the basis vectors shown at the bottom.

3.3. Penrose tiling

The five-star tripod tilings are approximants of the *Penrose tiling*. It is constructed from a five-dimensional hypercubic lattice $\mathbb{Z}^5$, which has a tenfold symmetry given by

$$D_{10} = \begin{pmatrix} 0 & 0 & 0 & 0 & -1 \\ -1 & 0 & 0 & 0 & 0 \\ 0 & -1 & 0 & 0 & 0 \\ 0 & 0 & -1 & 0 & 0 \\ 0 & 0 & 0 & -1 & 0 \end{pmatrix}. \tag{3.8}$$

Under the operation of D_{10} the hyperspace is decomposed into three invariant subspaces $U = \langle \boldsymbol{u} \rangle$, $V = \langle \boldsymbol{v}_1, \boldsymbol{v}_2 \rangle$, $W = \langle \boldsymbol{w}_1, \boldsymbol{w}_2 \rangle$ with

$$\begin{aligned} \boldsymbol{u} &= (1,\ 1,\ 1,\ 1,\ 1) \\ \boldsymbol{v}_1 &= (1,\ c_1,\ c_2,\ c_3,\ c_4) \\ \boldsymbol{v}_2 &= (0,\ s_1,\ s_2,\ s_3,\ s_4) \\ \boldsymbol{w}_1 &= (1,\ c_2,\ c_4,\ c_1,\ c_3) \\ \boldsymbol{w}_2 &= (0,\ s_2,\ s_4,\ s_1,\ s_3) \end{aligned} \tag{3.9}$$

If we choose for the lowering operator $\mathcal{L}_{\mathrm{Pen}}$ the projection on either V or W (and no phason displacement), then the tenfold symmetry will be preserved and the Penrose tiling is obtained. It is built from ten prototiles, five obtuse rhombs and five acute rhombs. The Penrose tiling is shown in Fig. 3.3. Note that there is again an inflation symmetry with inflation matrix

$$\begin{pmatrix} N'_{\mathrm{ob}} \\ N'_{\mathrm{ac}} \end{pmatrix} = \begin{pmatrix} 2 & 1 \\ 1 & 1 \end{pmatrix} \begin{pmatrix} N_{\mathrm{ob}} \\ N_{\mathrm{ac}} \end{pmatrix}. \tag{3.10}$$

The inflation matrix of the Penrose tiling is the squared inflation matrix of the Fibonacci chain. Therefore the number densities are transferred: $n_{\mathrm{ob}} = \tau^{-1}$, $n_{\mathrm{ac}} = \tau^{-2}$. From the area ratio of the tiles, $\tau : 1$, the area densities are calculated: $a_{\mathrm{ob}} = \frac{1}{5}(2+\tau) \approx 0.724$, $a_{\mathrm{ac}} = \frac{1}{5}(3-\tau) \approx 0.276$.

The phason flips of the Penrose tiling are of two types: Obtuse and acute flips. They appear in five different orientations.

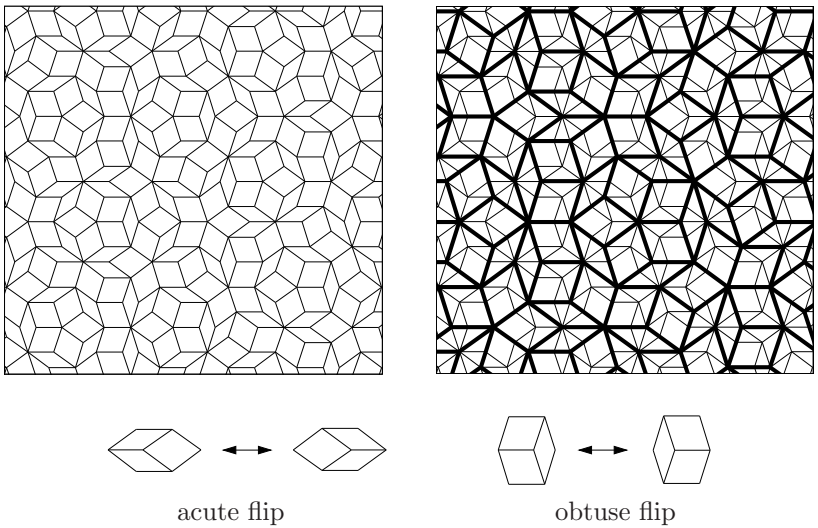

Figure 3.3: The Penrose tiling is built from obtuse and acute rhombs and has tenfold symmetry. It exhibits an inflation symmetry (scale factor τ).

3.4. Tübingen tiling

The hyperspace dimension for the Penrose tiling is not minimal. According to the crystallographic restriction (Sec. 2.1), tilings with tenfold symmetry can be constructed in a four-dimensional hyperspace. We start from the Penrose tiling and remove the superfluous one-dimensional subspace U by restricting the hyperlattice to $V \oplus W$. As a result[3] we obtain the basis matrix of the Tübingen tiling[4]:

$$B = \begin{pmatrix} 1-c_1 & c_1-c_2 & c_2-c_1 & c_1-1 \\ -s_1 & s_1-s_2 & -s_2+s_1 & -s_1 \\ 1-c_2 & c_2-c_1 & c_1-c_2 & c_2-1 \\ -s_2 & s_2+s_1 & s_1+s_2 & -s_2 \end{pmatrix}. \tag{3.11}$$

[3]Consider the right side of (3.9) as an (orthogonal) 5×5 matrix. Subtract columns 1 and 2, 2 and 3, 4 and 5, 5 and 1 to obtain the sublattice in $V \oplus W$. Discard the first row (projection) and use the relations $c_3 = c_2$, $c_4 = c_1$, $s_3 = -s_2$, $s_4 = -s_1$.

[4]The Tübingen tiling has been studied first at the university Tübingen [6]. In the original version different prototiles with triangular shapes were used.

The hyperlattice is identical to the root-lattice A_4.[5] The columns of B are the hyperlattice basis vectors in the canonical basis. B can be considered the transformation from the hyperlattice basis L to the canonical basis C. The tenfold symmetry operators (3.8) in these bases are

$$D_{10,L} = \begin{pmatrix} 0 & 1 & 0 & -1 \\ -1 & 1 & 0 & 0 \\ 0 & 1 & 0 & 0 \\ 0 & 1 & -1 & 0 \end{pmatrix} \tag{3.12}$$

and

$$D_{10,C} = BD_{10,L}B^{-1} = \begin{pmatrix} -c_1 & s_1 & 0 & 0 \\ -s_1 & -c_1 & 0 & 0 \\ 0 & 0 & -c_2 & s_2 \\ 0 & 0 & -s_2 & -c_2 \end{pmatrix}. \tag{3.13}$$

Therefore the first two and the second two rows of B span invariant subspaces. They are the V and W from (3.9). For the lowering operator $\mathcal{L}_{\mathrm{TTT}}$ we choose the first two rows of B, and the Voronoi cells as atomic volumes. The prototiles of the Tübingen tiling (see Fig. 3.4) have five different shapes: (D)ecagon, (U)-tile, (N)onagon, (H)exagon, and (P)entagon. There is again an inflation symmetry: The vertices of the deflated tiling (deflation = inflation^{-1}) are positioned at the centeres of the D-tiles. A quick count gives the inflation matrix

$$\begin{pmatrix} N'_D \\ N'_U \\ N'_N \\ N'_H \\ N'_P \end{pmatrix} = \begin{pmatrix} 5 & 5 & 3.5 & 2 & 1.5 \\ 3 & 2 & 1 & 0 & 0 \\ 4 & 4 & 3 & 2 & 1 \\ 3 & 3 & 2 & 1 & 1 \\ 30 & 28 & 19 & 10 & 7 \end{pmatrix} \begin{pmatrix} N_D \\ N_U \\ N_N \\ N_H \\ N_P \end{pmatrix}, \tag{3.14}$$

from which the eigenvector of the dominant eigenvalue τ^6 yields the number densities

$$(n_D,\, n_U,\, n_N,\, n_H,\, n_P) = \frac{1}{3\tau^5}(\tau^3,\, 1,\, 2\tau,\, \tau^2,\, 2\tau^5). \tag{3.15}$$

[5] Root lattices are highly symmetrical lattices. Historically, they have been introduced to classify semi-simple Lie algebras.

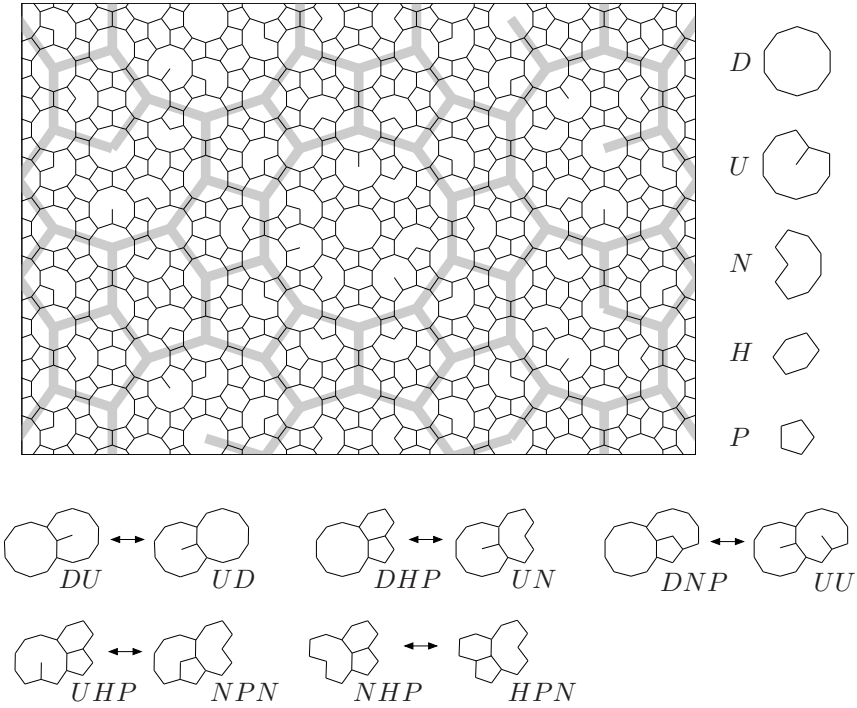

Figure 3.4: The Tübingen tiling has tenfold symmetry and is built from 28 prototiles in five different shapes: (D)ecagon (1×), (U)-tile (10×), (N)onagon (10×), (H)exagon (5×), and (P)entagon (2×). The deflated tiling is also shown.

The area densities are calculated using the tile areas with the result

$$(a_D,\, a_U,\, a_N,\, a_H,\, a_P) = \frac{1}{5\tau^5}(5\tau+10,\, 8\tau-9,\, \tau+7,\, \tau+2,\, 10\tau+5)$$
$$= (0.326,\, 0.071,\, 0.155,\, 0.065,\, 0.382). \qquad (3.16)$$

Interestingly, the smallest tile (P) consumes the largest area. Together with the D-tiles they cover more than 70%.

There are five possibilities for phason flips in the Tübingen tiling as shown in Fig. 3.4. However only the phason flips $DU \leftrightarrow UD$ and $NHP \leftrightarrow HPN$ do not change the tile types. The others lead to the tile arrangements UN, UU, and NPN, which are not observed in the original tiling.

Tiling	tiling dimension	hyperspace dimension	hyper-lattice	atomic volume
Fibonacci	1	2	$\mathbb{Z}^2$	square
Tripod	2	3	$\mathbb{Z}^3$	cube
Penrose	2	5	$\mathbb{Z}^5$	hypercube
Tübingen	2	4	A_4	Voronoi cell
Square-triangle	2	4	D_4	—

Table 3.1: The tilings introduced in this section, ordered roughly by the complexity of the construction process.

3.5. Square-triangle tiling

Not all quasicrystals can be constructed from a simple decoration of the hyperspace. Examples where this is not possible are tilings built from squares (Sq) and equilateral triangles (Tr). In contrast to the previous tilings, the *square-triangle tilings* [165] do not have phason flips. This means that the selection formalism or the cut formalism cannot be applied to square-triangle-tilings.[6] Perfectly ordered dodecagonal tilings are best described by an inflation rule as shown in Fig. 3.5. The inflation matrix is

$$\begin{pmatrix} N'_{\mathrm{Sq}} \\ N'_{\mathrm{Tr}} \end{pmatrix} = \begin{pmatrix} 7 & 16 \\ 3 & 7 \end{pmatrix} \begin{pmatrix} N_{\mathrm{Sq}} \\ N_{\mathrm{Tr}} \end{pmatrix} \tag{3.17}$$

leading to the number densities $n_{\mathrm{Sq}} = \sqrt{3}/(4+\sqrt{3})$, $n_{\mathrm{Tr}} = 4/(4+\sqrt{3})$ and equal area densities $a_{\mathrm{Sq}} = a_{\mathrm{Tr}}$.

Notice that at the vertices of the deflated tiling, dodecagonal clusters consisting of twelve triangles and six squares are found. These clusters have an external twelve-fold symmetry. However, since the corresponding 30° rotation cannot be split up into elementary phason flips, all six vertices around the cluster center would have to move collectively, which is very unlikely to happen. The phason degrees of freedom of the square-triangle-tilings are not excitable.

[6] A perfect square-triangle tiling could in principle be constructed with a fractally shaped atomic surface [5]. However there seems to be no easy way to extend such an atomic surface to an atomic volume, and therefore it cannot be used for approximants or phason flips.

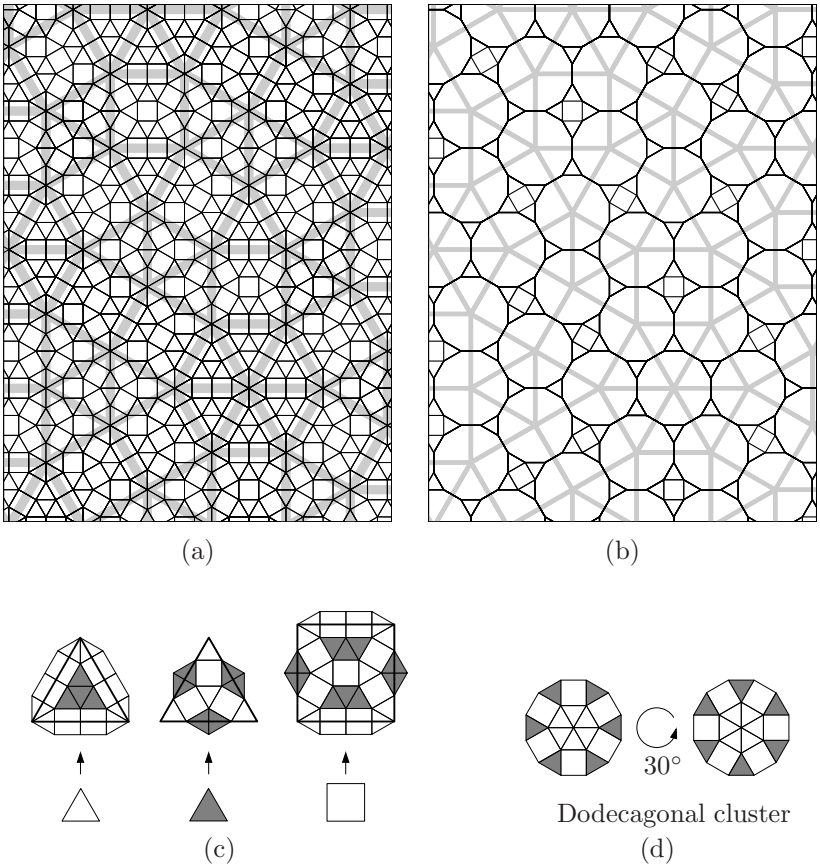

Figure 3.5: (a) Square-triangle tiling with twelve-fold symmetry. The deflated tiling is shown in light gray. (b) The vertices of the deflated tiling are dodecagonal clusters. (c) The inflation rule used to generate the tiling. It distinguishes two types of triangles [134]. (d) A collective rotation of the inner vertices in the dodecagonal cluster by 30° does not affect the outside of the cluster.

Chapter 4.

Particle dynamics and defects

At finite temperature the particles are not at rest, but move around their local equilibrium positions determined by the interaction potentials, and – on the long scale – diffuse through the system. Hence, the lattice and tiling description introduced in chapter 2 is only a static idealization, which will now be extended to include dynamics and defects.

4.1. Phason modes and elasticity

The elementary modes in higher-dimensional crystals are phonons and phason flips (Sec. 2.5). Whereas phonons propagate freely through the system, phason flips are local and instantaneous events, correlated weakly in time. Only the positions of the flips are correlated by the underlying tiling structure, since they are restricted to a discrete set of locations. Mapped to hyperspace this means that although the de Bruijn surface is fluctuating locally, on a mesoscopic level it remains continuous. It is important to point out that phason flips are not topological defects.

In the literature, large scale fluctuations of the de Bruijn surface are called phason modes [7, 88, 108]. Similarly to phonons, phason modes are introduced in the form of plane waves. However phason modes do not propagate, but move stochastically by phason flips. A special case is the global translation of the de Bruijn surface, corresponding to a phason mode with long wave length. For a quasicrystal the translation is an internal symmetry. Because of the non-periodicity and the closeness condition, long wave length phasons do not change global physical properties of the tiling. In contrary, for a periodic tiling a translation of the de Bruijn surface leads to a different decoration of the unit cell and thus is no symmetry operation.

In quasicrystals, phasons modes are connected with many physical properties. Examples are elastic deformations [31], dislocations [149, 162], diffusion [13, 87], and phase transformations [167]. Indications for phason flips [1, 41] have recently been observed by in situ transmission electron

microscopy. For the physics behind phason modes two theories are discussed in the literature [72, 80]: (i) The unlocked state, which attributes phason modes with elastic free energy in the form of a continuum model, (ii) the locked state emphasizing the discreteness of phason flips.

4.1.1. Unlocked state

In the unlocked state, the theory of elasticity is assumed to be extendible to the phason degrees of freedom. In classical elasticity, the state of a solid is uniquely characterized by a continuous displacement field $\boldsymbol{u}(\boldsymbol{x})$ attributing to each position $\boldsymbol{x}$ a displacement vector $\boldsymbol{u}$. Since uniform displacements do not alter the physical properties, only the gradient $\boldsymbol{\nabla u}$ has significance, which can be separated in a symmetric and an antisymmetric part. The analysis shows that the antisymmetric part only leads to local rotations, whereas the symmetric part, the strain tensor $\boldsymbol{\epsilon} = (\boldsymbol{\nabla u})^S$, is connected to volume and shape changes. In linear elasticity, the elastic free energy density is written as a quadratic form (with the Hooke tensor C_{ijkl}):

$$F = \tfrac{1}{2} C_{ijkl} \epsilon_{ij} \epsilon_{kl}. \tag{4.1}$$

The concept is extended to hyperspace $E \oplus E^\perp = \mathbb{R}^d \oplus \mathbb{R}^{n-d}$ by writing a general displacement as $\boldsymbol{u}(\boldsymbol{x}) + \boldsymbol{u}^\perp(\boldsymbol{x})$. Additionally, the phason displacement $\boldsymbol{u}^\perp$ (Sec. 2.3) is necessary. The elastic free energy density is now a function of the phonon strain $\boldsymbol{\epsilon} \in \mathbb{R}^{d\times d}$ and the phason strain $\boldsymbol{\chi} \in \mathbb{R}^{d\times(n-d)}$ with

$$\epsilon_{ij} = \frac{1}{2}(\partial_i u_j + \partial_j u_i), \tag{4.2}$$

$$\chi_{ij} = \partial_i u_j^\perp, \tag{4.3}$$

$$\boldsymbol{\eta} = \begin{pmatrix} \boldsymbol{\epsilon} \\ \boldsymbol{\chi} \end{pmatrix}. \tag{4.4}$$

Note that $\boldsymbol{\chi}$ is not symmetrized, because its two indices refer to different spaces. Both strains are collected in the strain tensor $\boldsymbol{\eta} \in \mathbb{R}^{d\times n}$. The elastic free energy density includes phonon-phonon elastic constants (identical to the classical case) phason-phason elastic constants, and phonon-phason coupling constants:

$$F = \tfrac{1}{2} C_{i\alpha k\beta} \eta_{i\alpha} \eta_{k\beta}. \tag{4.5}$$

4.1.2. Locked state

Assume that there is a Hamiltonian with a perfect tiling as sole energetic ground state at $T = 0$. Each phason flip leads to an energy penalty. The energy of a given tiling close to the perfect tiling is proportional to the number of phason flips necessary to transform the tiling into the perfect tiling. Furthermore this number is proportional to the average phason strain. If we summarize the unlocked state behavior as $F \sim \chi^2$, i.e. the elastic energy is quadratic in the phason strains, then the locked state predicts $F \sim |\chi|$. Hence the elastic energy is a non-analytic function of the phason strains. No phason elastic theory exists in the locked state.

For periodic tilings, the locked state emerges very naturally, since phason flips always lead to a deviation from periodicity. However for quasicrystals, the situation is much more complex. It is not clear, how a local Hamiltonian could enforce a perfect tiling. At least for two-dimensional quasicrystals, the locked state has been shown in a recent work [99] to be unlikely. If a locked state existed in a three-dimensional quasicrystal, it would appear at low temperature. At high temperature, the activation energy necessary for phason flips is available and a transition to the unlocked state occurs [72]. With increasing temperature, entropy will finally win against energy in the struggle to minimize the free energy $F = E - TS$.

4.1.3. Random tiling

Whereas the locked state describes perfect tilings, the unlocked state corresponds to random tilings. A random tiling is the ensemble of all tilings that are obtained from a given set of prototiles within certain restrictions. The tilings can transform into another via thermally activated phason flips. In thermal equilibrium, the de Bruijn surface fluctuates with temperature depending amplitudes. As a result, a random tiling quasicrystal will show a lot of disorder. Nevertheless, the random tiling has in average all the properties of quasicrystals. For example, it has (algebraic) long-range order (see Sec. 4.5), and its diffraction image shows non-crystallographic symmetry. However, the disorder leads to additional diffuse scattering.

The random tiling is stabilized by entropy, in contrast to the perfect tiling, which is stabilized by energy. In fact, the quadratic dependence of the free energy is explained by Henley's random tiling hypotheses [72]: (i) The entropy density is maximum for an average phason strain of zero.

(ii) The entropy increases quadratically with the average phason strain. The hypotheses have been proven for simple systems [72] and verified numerically for some complex systems [86, 171, 172].

It is important to note that in two dimensions thermal roughening of the de Bruijn surface occurs at all $T > 0$ [172].

4.2. New types of partial dislocations

Topological defects of periodic crystals are defects in the displacement field $\boldsymbol{u}$, called dislocations. They are characterized by a lattice vector $\boldsymbol{b}$ known as Burgers vector. Dislocations are $d-2$-dimensional defects – lines in three dimensions and points in two dimensions. The Burgers vector is obtained from circular integrals of the displacement field around discs S_1 cutting the dislocation line in three dimensions, or surrounding the dislocation core in two dimensions:

$$\boldsymbol{b} = \oint_{S_1} \mathrm{d}\boldsymbol{u}. \tag{4.6}$$

If we assume as an approximation that the crystal is elastically isotropic, then in the linear theory of elasticity the elastic energy of dislocations is proportional to the square of the Burgers vector [77].

As shown in [162], the extension of dislocations to higher dimensions is straightforward. Dislocations in quasicrystals and complex crystals are uniquely specified by a Burgers vector, which is a lattice vector of the hyperlattice and can again be obtained from a Burgers circuit in physical space when using the tiling basis. However, the appearance of higher-dimensional dislocations is quite different from regular dislocations in simple crystals. Since the Burgers vector now has both – a phonon component $\boldsymbol{b}^{\parallel} = \mathcal{L}\boldsymbol{b}$ and a phason component $\boldsymbol{b}^{\perp} = (\mathbb{1} - \mathcal{L})\boldsymbol{b}$ (where $\mathcal{L}$ is the lowering operator introduced in Sec. 2.3), the effect of a dislocation on a tiling is two-fold: The phonon component leads to the usual straining of the tiling around the dislocation core, but the phason component generates additional rearrangements of particles. The creation, as well as the motion of dislocations are accompanied by phonons and phason flips.

Using the conventional language of dislocation theory, this means that the dislocation is a partial dislocation – in contrast to a regular dislocation, whose (phonon component of the) Burgers vector is a lattice vector. It is one of the advantages of the hyperspace formalism that partial dislocations

appear naturally. In fact, every partial dislocation can be constructed from the hyperspace, which is also directly seen from the construction mechanism in chapter 2. In the theory of elasticity for the unlocked state one finds that the elastic energy of a partial dislocation has phonon, phason, and coupling components. By (i) approximating the phasonic degree as continuous[1], and (ii) assuming isotropy in the strain fields we get for the dislocation energy:

$$E = c_{\text{phon}}(\boldsymbol{b}^{\parallel})^2 + c_{\text{phas}}(\boldsymbol{b}^{\perp})^2 + 2c_{\text{coupl}}\boldsymbol{b}^{\parallel}\boldsymbol{b}^{\perp}. \tag{4.7}$$

The materials properties c_{phon}, c_{phas}, and c_{coupl} depend on the phonon elastic, phason elastic, and coupling constants, of the crystal. Since the energy change of the system by phason flips is relatively low, phason elastic and coupling constants are much smaller than the phonon elastic constants, and we can assume

$$c_{\text{phas}}, c_{\text{coupl}} \gg c_{\text{phon}}. \tag{4.8}$$

For a confirmation of these relations see the discussion in Sec. 8.4. Hence physical relevant dislocations will have small phonon components of the Burgers vectors. The minimization of the dislocation energy implies an optimization of the ratio $b^{\parallel} : b^{\perp}$.

4.3. Examples

4.3.1. Elasticity of decagonal quasicrystals

The number of independent elastic constants depends on the symmetry of the (quasi)crystal. As an example we study the Tübingen tiling (Sec. 3.4). The dimension of the tiling is $d = 2$ and of the hyperspace $n = 4$. There are 7 independent strains in $\boldsymbol{\eta}$. In the hyperspace basis given by (3.11) the symmetry-adapted basis of the strain matrix is [98]:

$$\begin{aligned}\mathcal{B} = \Bigg\{ &\frac{1}{\sqrt{2}}\begin{pmatrix} 1 & 0 \\ 0 & 1 \\ 0 & 0 \\ 0 & 0 \end{pmatrix}; \frac{1}{\sqrt{2}}\begin{pmatrix} 1 & 0 \\ 0 & -1 \\ 0 & 0 \\ 0 & 0 \end{pmatrix}, \frac{1}{\sqrt{2}}\begin{pmatrix} 0 & 1 \\ 1 & 0 \\ 0 & 0 \\ 0 & 0 \end{pmatrix}; \\ &\frac{1}{\sqrt{2}}\begin{pmatrix} 0 & 0 \\ 0 & 0 \\ 1 & 0 \\ 0 & -1 \end{pmatrix}, \frac{1}{\sqrt{2}}\begin{pmatrix} 0 & 0 \\ 0 & 0 \\ 0 & 1 \\ 1 & 0 \end{pmatrix}; \frac{1}{\sqrt{2}}\begin{pmatrix} 0 & 0 \\ 0 & 0 \\ 1 & 0 \\ 0 & 1 \end{pmatrix}, \frac{1}{\sqrt{2}}\begin{pmatrix} 0 & 0 \\ 0 & 0 \\ 0 & 1 \\ -1 & 0 \end{pmatrix} \Bigg\}.\end{aligned} \tag{4.9}$$

[1]This is good approximation if the phason strain is not too big.

In this basis, a general strain is written as

$$\eta = \{\epsilon_1; \epsilon_{2,1}, \epsilon_{2,2}; \chi_{1,1}, \chi_{1,2}; \chi_{2,1}, \chi_{2,2}\} \tag{4.10}$$

with one one-dimensional and three two-dimensional invariant subspaces. The elastic free energy density consists of a phonon, phason, and coupling term:

$$F_{\text{phon}} = \tfrac{1}{2}\lambda_1 \boldsymbol{\epsilon}_1^2 + \tfrac{1}{2}\lambda_2 \boldsymbol{\epsilon}_2^2, \tag{4.11}$$

$$F_{\text{phas}} = \tfrac{1}{2}\lambda_3 \boldsymbol{\chi}_1^2 + \tfrac{1}{2}\lambda_4 \boldsymbol{\chi}_2^2, \tag{4.12}$$

$$F_{\text{coupl}} = \lambda_5 \boldsymbol{\epsilon}_2 \cdot \boldsymbol{\chi}_1, \tag{4.13}$$

with two phonon elastic constants λ_1, λ_2, two phason elastic constants λ_3, λ_4, and one coupling constant λ_5.

4.3.2. Dislocations in Laves phases

One of the simplest materials class with a high structural flexibility are the Laves phases (see Sec. 1.2). They are binary metallic alloys built from small and large atoms with a size ratio of about 1.3. The prototiles of the Laves phases are parallelepipeds as shown in Fig. 4.1(a). All of its faces are identical rhombs with an internal angle of 60° formed by the small atoms (red). The long diagonal is subdivided by the big atoms (yellow) in a ratio 3 : 2 : 3. In the projection along one of the prototile axes the internal angle is 71° (Fig. 4.1(b)). There are several possibilities to tile space. In all of them, the parallelepiped occurs in maximal two different orientations. Two of them are the C15- and the C14-phase. Another possibility is C36, which is a stacking of period four. C15 is a parallel, and C14 an alternating arrangement of the two prototiles (Fig. 4.1(c) - (d)). The small atoms form a tetragonal network including voids, which are filled with big atoms.[2]

In projection, the Laves phases are described by two-dimensional tilings, which are variants of the obtuse tripod tiling (Sec. 3.2). Dislocations with low energies have Burgers vectors with small phonon components. Using the basis of Fig. 3.2 we find a partial dislocation with

$$\boldsymbol{b} = (-1, 1, -1), \qquad b^{\parallel} = 0.38. \tag{4.14}$$

[2]Note that although the two-dimensional tiling is unique, this is not the case for the three-dimensional structure. There are several distinct possibilities for the tiling.

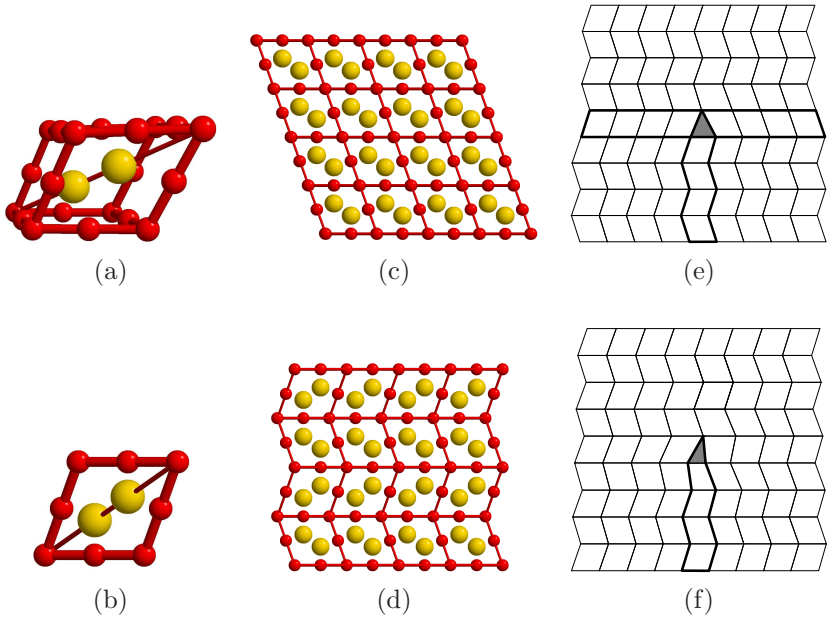

Figure 4.1: Prototile of the Laves phases (a), projected along one of its basis vectors (b). The C15-phase is a parallel arrangement (c), and the C14-phase an alternating one (d). A partial dislocation (e) is energetically favourable compared to a regular dislocation (f).

Compared to a regular dislocation with Burgers vector

$$\boldsymbol{b} = (0, 1, 0), \qquad b^{\parallel} = 1.0 \tag{4.15}$$

the phonon strain generated by the partial dislocation is much lower, which is directly seen in the tiling shown in Figs. 4.1(e)–(f). The additional stacking fault generated by the dislocation movement in the horizontal direction (the glide plane) is attributed to the phason component of the Burgers vector.

Partial dislocations[3] are the sole dislocations experimentally observed in the Laves phases. Recently, electron microscopy investigations allowed the

[3]In the literature they are also known as Shockley partials [77].

direct observation of the dislocation cores [24] confirming the tiling picture in Fig. 4.1(e). Since the tilings of Laves phases are simple, the description of their dislocations is possible without the help of higher-dimensional space. However as soon as the tiling is getting more complicated, the hyperspace method has to be applied.

4.4. Structure factors and correlation functions

The structure factors are characteristic functions for the motion of atoms in ordered and disordered media. They are typically determined with neutron diffraction experiments. In the following derivation we follow the textbook by Squires [164].

4.4.1. Scattering experiments

An incoming plane wave of neutrons with wave vector $\boldsymbol{q}$ is scattered at a target. The outgoing neutrons are energy resolved and counted by a detector covering the area $\mathrm{d}S = r^2\mathrm{d}\Omega$. This gives the partial differential cross section $\mathrm{d}^2\sigma/\mathrm{d}\Omega\mathrm{d}E'$.

In quantum mechanics, the scattering process is a transition from the state $|\boldsymbol{q}, \lambda\rangle$ and energy E into a state $|\boldsymbol{q}', \lambda'\rangle$ and energy E'. The parameters λ and λ' characterize the state of the scattering system. With Fermi's golden rule we have

$$\left(\frac{\mathrm{d}^2\sigma}{\mathrm{d}\Omega\mathrm{d}E'}\right)_{\lambda\to\lambda'} = \frac{q'}{q}\left(\frac{m}{2\pi\hbar^2}\right)^2 |\langle\boldsymbol{q}', \lambda'|V|\boldsymbol{q}, \lambda\rangle|^2\ \delta(E_\lambda - E'_\lambda + E - E'). \tag{4.16}$$

The interaction between the neutrons and the system is given by the potential V. Since the scattering occurs with the nuclei at position $\boldsymbol{x}_i$, the Fermi pseudopotential is a good approximation: $V(\boldsymbol{x}) = \sum_{i=1}^{N} b_i\delta(\boldsymbol{x} - \boldsymbol{x}_i)$. b_i depends on the nuclide type only. After the transition to Fourier space and some further calculations [164] the following result is obtained:

$$\frac{\mathrm{d}^2\sigma}{\mathrm{d}\Omega\mathrm{d}E'} = \frac{N}{4\pi}\frac{q'}{q}\frac{1}{2\pi\hbar}\left[\sigma S(\boldsymbol{q}, \omega) + \sigma_\mathrm{i} S_\mathrm{i}(\boldsymbol{q}, \omega)\right], \tag{4.17}$$

where ω is defined by $\hbar\omega = E - E'$. The material constants σ and σ' are determined by the nuclear composition of the system. Furthermore, the

coherent and incoherent structure factors are given by[4]

$$S(\boldsymbol{q},\omega) = \frac{1}{2\pi N}\int e^{-\mathrm{i}\omega t}\sum_{j,l}\left\langle e^{-\mathrm{i}\boldsymbol{q}\cdot\boldsymbol{x}_j(t)}e^{\mathrm{i}\boldsymbol{q}\cdot\boldsymbol{x}_l(0)}\right\rangle \mathrm{d}t, \tag{4.18}$$

$$S_{\mathrm{i}}(\boldsymbol{q},\omega) = \frac{1}{2\pi N}\int e^{-\mathrm{i}\omega t}\sum_{l}\left\langle e^{-\mathrm{i}\boldsymbol{q}\cdot\boldsymbol{x}_l(t)}e^{\mathrm{i}\boldsymbol{q}\cdot\boldsymbol{x}_l(0)}\right\rangle \mathrm{d}t. \tag{4.19}$$

The angle brackets denote an average, which can be either a time average or an ensemble average.[5] Both functions are symmetric about $\boldsymbol{q} = 0$. The static structure factor is the integral of the coherent structure factor:

$$S(\boldsymbol{q}) = \int S(\boldsymbol{q},\omega)\,\mathrm{d}\omega = \frac{1}{N}\sum_{j,l}\left\langle e^{-\mathrm{i}\boldsymbol{q}\cdot\boldsymbol{x}_j(0)}e^{\mathrm{i}\boldsymbol{q}\cdot\boldsymbol{x}_l(0)}\right\rangle. \tag{4.20}$$

Depending on the setup, all structure factors are obtained from scattering experiments: (i) The coherent structure factor $S(\boldsymbol{q},\omega)$ is studied via coherent inelastic neutron scattering or alternatively via inelastic X-ray scattering. It allows the determination of the phonon dispersion relations. (ii) The incoherent structure factor $S_{\mathrm{i}}(\boldsymbol{q},\omega)$ can be measured in quasielastic neutron scattering. Neutrons are exclusively used here, due to the necessity of a high energy resolution. (iii) The static structure factor $S(\boldsymbol{q})$ is the usual non-energy resolved diffraction image $I(\boldsymbol{q}) = |\rho(\boldsymbol{q})|^2$ for $\rho(\boldsymbol{x}) = n(\boldsymbol{x})$, measured with either X-rays or neutrons.[6] It is used for the determination of the atomic structure.

4.4.2. Correlation functions

To see the relation to the atom dynamics, we write the number density of the d-dimensional system as a sum of delta functions positioned along the atom trajectories $\boldsymbol{x}_l(t)$, $n(\boldsymbol{x},t) = \sum_{l=1}^{N}\delta(\boldsymbol{x}-\boldsymbol{x}_l(t))$ and introduce

[4] The coherent structure factor $S(\boldsymbol{q},\omega)$ is also called '(total) scattering function', 'response function', or 'dynamic(al) structure factor'. The incoherent structure factor $S_{\mathrm{i}}(\boldsymbol{q},\omega)$ is alternatively known as 'incoherent scattering function' and 'self part of the structure factor'.

[5] Here and in the following the system is in thermal equilibrium. We assume ergodicity. Boundary or surface effects do not play a role.

[6] The diffraction image has been introduced in Sec. 2.2. In different contexts, the Fourier transformed density $\rho(\boldsymbol{q})$ is also called structure factor, which might sometimes lead to confusion.

the time dependent density correlation function and the density-density autocorrelation function as

$$\begin{aligned} G(\boldsymbol{x},t) &= \frac{1}{N}\int \langle n(\boldsymbol{x}',t)n(\boldsymbol{x}+\boldsymbol{x}',0)\rangle \ \mathrm{d}^d\boldsymbol{x}' \\ &= \frac{1}{N}\sum_{j,l}\langle \delta(\boldsymbol{x}-\boldsymbol{x}_j(t)+\boldsymbol{x}_l(0))\rangle\,, \end{aligned} \tag{4.21}$$

$$G_{\mathrm{a}}(\boldsymbol{x},t) = \frac{1}{N}\sum_{l}\langle \delta(\boldsymbol{x}-\boldsymbol{x}_l(t)+\boldsymbol{x}_l(0))\rangle\,. \tag{4.22}$$

The coherent and incoherent structure factors (4.18), (4.19) are the space-time Fourier transforms of the correlation functions (4.21), (4.22). The static structure factor (4.20) is the Fourier transform of $G(\boldsymbol{x}) = G(\boldsymbol{x},0)$.

Another important property to study is the vibrational density of states (DOS) $D(\omega)$. The DOS per particle is proportional to the Fourier transform of the velocity autocorrelation function [62]:

$$D(\omega) = \frac{2}{NkT}\frac{1}{2\pi}\int e^{-\mathrm{i}\omega t}\mathrm{d}t\ \sum_l m_l\langle \boldsymbol{v}_l(t)\cdot\boldsymbol{v}_l(0)\rangle, \tag{4.23}$$

and normalized to

$$\int_0^\infty D(\omega)\mathrm{d}\omega = d. \tag{4.24}$$

By interchanging the Fourier transform and two time derivatives we can alternatively write

$$D(\omega) = \frac{2}{NkT}\frac{\omega^2}{2\pi}\int e^{-\mathrm{i}\omega t}\mathrm{d}t\ \sum_l m_l\langle \boldsymbol{x}_l(t)\cdot\boldsymbol{x}_l(0)\rangle. \tag{4.25}$$

After a Taylor expansion of the exponentials in (4.19), a connection to the incoherent structure factor for monodisperse systems ($m_l = m$) is found:

$$D(\omega) = \frac{2m}{kT}\lim_{q\to 0}\frac{\omega^2}{q^2}S_{\mathrm{i}}(q,\omega), \quad \omega \neq 0. \tag{4.26}$$

4.4.3. Influence of phonons and phason modes

To get a feeling for the influence of phonons and phason modes on the structure factors, we begin with discussing some special cases. At $T = 0$

all the atoms are at rest and sit in their (local) equilibrium positions.[7] The static structure factor (4.20) is a sum of delta peaks positioned at the reciprocal lattice vectors. Furthermore, the coherent and incoherent structure factors are very simple: $S(\boldsymbol{q},\omega) = \delta(\omega)S(\boldsymbol{q})$ and $S_{\mathrm{i}}(\boldsymbol{q},\omega) = \delta(\omega)$.

A single phonon with frequence ω' and wave vector $\boldsymbol{q}'$, related by the dispersion relation $\omega' = \omega'(\boldsymbol{q})$, is written as

$$\boldsymbol{x}_j(t) = \boldsymbol{x}_j(0) + A\cos(\omega' t - \boldsymbol{q}' \cdot \boldsymbol{x}_j(0)). \tag{4.27}$$

After expanding the exponentials with $\boldsymbol{x}_j(t) - \boldsymbol{x}_j(0)$ appearing in (4.18)–(4.20) in a Taylor series, the main effect of the phonon on the coherent structure factor is found to be a peak at $\omega = \omega'$, $\boldsymbol{q} = \pm\boldsymbol{q}'$. Hence there is a contribution along the phonon dispersion relation in the ω-$\boldsymbol{q}$-plane. As we will later see (chapter 6), the interaction of several phonons leads to higher harmonics and a continuous broadening of the peaks for all structure factors, which is the more pronounced the stronger the phonon fluctuations present in the system, i.e. the lower the dimension. In general, dimensionality plays a very important role.

Not much is known about the relation between phason modes and the structure factors in one and two dimensions. Only for three dimensional solids, the broadening is well studied, where it is usually called diffuse scattering. In lowest approximation and close to the Bragg peaks (in the hydrodynamic regime, see Sec. 6.2), the shape and width of the diffuse scattering is determined by the elastic constants only. For the static structure factors, this can be transfered to quasicrystals. Here, phason modes lead to an additional diffuse scattering, and the peak shapes are now described by using the phason elastic constants as shown by Jarić and Nelson [85]. In contrast to the phonon diffuse scattering, the phason diffuse scattering is much stronger and highly anisotropic.

Theoretically, the effect of phason modes on the (in)coherent structure factor has not yet been studied in detail. Note that if we use the assumption that the dynamics of phason flips is slow on the time scale of a typical scattering event, or if the phason flips cannot occur, e.g. at low temperatures, then phason modes are static. Since the effect on all structure factors therefore is mainly the peak broadening, no additional features besides the peaks along the dispersion relations will be present in quasicrystals.

[7] Of course, a low temperature the classical approximation is no longer valid. For an exact treatment, zero point vibrations play a role.

4.5. Long-range order and low dimensions

Because the model systems used in this work are one- and two-dimensional, the influence of dimensionality on the dynamics has to be taken into account. In general, long-range order characterizes physical systems in which remote portions exhibit correlated behavior. This is seen with correlation functions. Here, we need to take a look at the correlation of the function $\rho(\boldsymbol{x})$ introduced in Sec. 2.2, which describes the distribution of matter:

$$G(\boldsymbol{x}, \boldsymbol{x}') = \langle \rho(\boldsymbol{x}) \rho(\boldsymbol{x}') \rangle. \tag{4.28}$$

Due to the translational symmetry of the Hamilton function, the correlation function C only depends on the difference $\boldsymbol{x} - \boldsymbol{x}'$. Furthermore, a spatial average is applied:

$$G(\boldsymbol{x}) = \lim_{V \to \infty} \frac{1}{V} \int_V \mathrm{d}^d \boldsymbol{x}' \; \langle \rho(\boldsymbol{x} - \boldsymbol{x}') \rho(\boldsymbol{x}') \rangle. \tag{4.29}$$

With the average value $\langle \rho \rangle = \lim_{V \to \infty} \frac{1}{V} \int_V \mathrm{d}^d \boldsymbol{x} \; \rho(\boldsymbol{x})$, long-range order is defined as the behavior of $G'(\boldsymbol{x}) = G(\boldsymbol{x}) - \langle \rho \rangle^2$ in the limit $|\boldsymbol{x}| \to \infty$:[8]

- Long-range order: $G'(\boldsymbol{x})$ does not decay to 0 (keeps oscillating).
- Algebraic long-range order[9]: $G'(\boldsymbol{x})$ decays to 0 algebraically.
- Short-range order: $G'(\boldsymbol{x})$ decays to 0 exponentially.

The dimensionality of the system has an important impact on long-range order and the existence of thermodynamic phases: In all dimensions, a gas (short-range order) is found at high temperatures. However, the low-temperature behavior is different. In three dimensions, first a liquid, and then an ordered solid (crystal, quasicrystal) is usually obtained during slow cooling. Rapid cooling leads to an amorphous solid (undercooled liquid). Whereas liquid and amorphous solid do not have long-range order, the ordered solid has of course long-range order. In two dimensions, also liquid, ordered solid, and amorphous solid are found. However, the solid

[8] By the definition, long-range order could vary for different directions of $\boldsymbol{x}$, but for our purpose this will not occur.

[9] Also known as quasi-long-range order. Since quasi-longe-range order has nothing to do with quasicrystals we do not use this term.

has only algebraic long-range order. This follows from the work by Mermin and Wagner [121, 122], who showed that long-range order is not possible in one and two dimensions.[10] In one dimension, a liquid appears at low temperatures, but only short-range order and therefore no ordered solid exists. An amorphous state is not possible.

In many respects, two- and three-dimensional systems behave similar, whereas one-dimensional systems are quite different. An important reason is that the separation of a liquid or solid in two halves costs a fixed amount of energy in one dimension independent of the system size (only one bond is broken), whereas in two dimensions the energy increases linearly and in three dimensions with the square of the system size. This means droplets of liquid or pieces of solid do not gain energy by growth in one dimension and coarsening is not energetically favored. Additionally, neighbors are fixed in one dimension. Voids cannot exist, diffusion is absent.

[10] Nevertheless there is directional long-range order in two dimension [121] as revealed by a calculation of $\langle[\rho(\boldsymbol{x}+\boldsymbol{x}_0)-\rho(\boldsymbol{x})]\cdot[\rho(\boldsymbol{x}'+\boldsymbol{x}_0)-\rho(\boldsymbol{x}')]\rangle$. Here $\boldsymbol{x}_0$ is a fixed vector, e.g. a basis vector of the lattice.

Chapter 5.

Numerical methods

For the numerical study of our model systems we use molecular dynamics and Monte Carlo simulations. After the discussion of these methods, we introduce the customized simulation package, which has been written for the present thesis. It consists of a fast simulation module and an interactive visualization module. Various observables can be extracted from the simulation data. Additionally, an efficient algorithm to calculate tilings with or without dislocations (iterative selection algorithm) is addressed.

5.1. Effective interaction potentials

On a microscopic level, the interaction of atoms and electrons is correctly described by the many-body Schrödinger equation. However, since the state of a system with n particles is represented by a $3n$-dimensional wave function, a direct solution is not feasible for more than a few atoms and electrons. For periodic crystals, the problem simplifies significantly by the use of the Bloch theorem. It implies that the wave function is a linear combination of a countable number of basis functions. The Born-Oppenheimer approximation separates the dynamics of the nuclei and the electrons plus considering the nuclei as classical particles. Additionally, the Hohenberg-Kohn theorems [78] show that for the electronic part of the Schrödinger equation, it suffices to study the electron density only: The first of these demonstrates the existence of a one-to-one mapping between the ground state electron density and the ground state wavefunction of a many-particle system. The second one proves that the ground state density minimizes the total electronic energy of the system.

An efficient implementation of the density functional theory through the Car-Parrinello method [21] makes use of the interatomic forces calculated from the self-consistent Kohn-Sham equations [97]. This combines ab initio calculations with finite-temperature computer simulations and allows

to study systems with up to several hundreds of atoms, which also includes some complex crystals with not too big unit cells. Yet, the number of time steps accessible for large systems is limited. When dealing with the dynamics of complex crystals and when exploring phenomena, where periodic boundary conditions are hardly applicable, the power of even massively parallel computer systems is still not sufficient. Therefore classical effective interaction potentials are necessary for large-scale and long-time simulations. These potentials in the ideal case mimic the forces between the atoms in a way to reproduce all relevant physical properties. One general method to obtain such potentials is force matching, which uses an appropriately chosen set of parameterized potentials to optimize the misfit between 'ideal' values for the forces, elastic constants, potential energies, etc. obtained from ab initio calculations and the ones reproduced from the classical potentials [49]. Force matching has been applied to complex metallic alloys in a recent thesis by Peter Brommer [19].

Within the limitations of the Born-Oppenheimer approximation, the motion of atoms can be fully described using a general multi-body potential $V(\boldsymbol{x}_1, \ldots, \boldsymbol{x}_N)$, which splits up into a sequence of two-body, three-body, etc. interactions. In the absense of an external potential:

$$V(\boldsymbol{x}_1, \ldots, \boldsymbol{x}_N) = \sum_{i,j} V(|\boldsymbol{x}_i - \boldsymbol{x}_j|) + \sum_{i,j,k} V(x_{ij}, x_{ik}, \theta_{ijk}) + \ldots \qquad (5.1)$$

Fortunately, contributions of higher terms rapidly decrease, and it is often sufficient to consider pair interactions, $V(|\boldsymbol{x}_i - \boldsymbol{x}_j|)$, only.[1]

The particle trajectories are obtained from the numerical solution of Newton's equations

$$\frac{\mathrm{d}\boldsymbol{p}_i}{\mathrm{d}t} = \boldsymbol{F}_i = -\boldsymbol{\nabla}_i V(\boldsymbol{x}_1, \ldots, \boldsymbol{x}_N), \qquad (5.2)$$

$$\frac{\mathrm{d}\boldsymbol{x}_i}{\mathrm{d}t} = \frac{\boldsymbol{p}_i}{m_i}, \qquad (5.3)$$

which can be done either via integration (molecular dynamics) or with statistical (Monte Carlo) methods.

[1] In metals, the influence of the electron gas is sometimes taken into account by including an embedding energy of the atoms as a function of the local electron density. This so-called embedded atom method (EAM [29]) is meant to mimic certain aspects of density functional theory.

5.2. Molecular dynamics simulations

In molecular dynamics (MD) simulations Newton's equations of motions are solved by a numerical integrator subject to requirements like high precision, stability, time-reversal symmetry and therefore energy and momentum conservation. The conditions are met by the relatively simple expressions of the Verlet and the leap-frog algorithms. In the Verlet algorithm the Taylor expansions of $\boldsymbol{x}_i(t+\delta t)$ and $\boldsymbol{x}_i(t-\delta t)$,

$$\boldsymbol{x}_i(t+\delta t) = \boldsymbol{x}_i(t) + \delta t\ \dot{\boldsymbol{x}}_i(t) + \frac{1}{2}(\delta t)^2\ddot{\boldsymbol{x}}_i(t) + \ldots, \tag{5.4}$$

$$\boldsymbol{x}_i(t-\delta t) = \boldsymbol{x}_i(t) - \delta t\ \dot{\boldsymbol{x}}_i(t) + \frac{1}{2}(\delta t)^2\ddot{\boldsymbol{x}}_i(t) - \ldots, \tag{5.5}$$

are added such that the odd powers of δt vanish and the velocities do not appear explicitly:

$$\boldsymbol{x}_i(t+\delta t) = 2\boldsymbol{x}_i(t) - \boldsymbol{x}_i(t-\delta t) + (\delta t)^2\ddot{\boldsymbol{x}}_i(t) + \ldots \tag{5.6}$$

with $\ddot{\boldsymbol{x}}_i(t) = \boldsymbol{F}_i(t)/m$. The algorithm is correct to order $(\delta t)^4$ and time-reversible as it is centered. For the iteration the particle positions are needed at two times, t and $t-\delta t$. A modification is the half-step leap-frog algorithm:

$$\boldsymbol{x}_i(t+\delta t) = \boldsymbol{x}_i(t) + \delta t\ \dot{\boldsymbol{x}}_i(t+\frac{1}{2}\delta t), \tag{5.7}$$

$$\dot{\boldsymbol{x}}_i(t+\frac{1}{2}\delta t) = \dot{\boldsymbol{x}}_i(t-\frac{1}{2}\delta t) + \delta t\ \boldsymbol{a}_i(t). \tag{5.8}$$

Here, the second order equation is replaced by two first order ones, in which also the velocities have become independent degrees of freedom. Inserting (5.7) and (5.8) into the centering procedure (5.6) shows that the leap-frog scheme is algebraically equivalent to Verlet. With the leap-frog integrator we can simulate the microcanonical NVE ensemble, where particle number N, volume V and energy E are kept constant. For other ensembles, like the canonical NVT ensemble, or the NPT ensemble, one must apply numerical thermostats and barostats.

Temperature and pressure control can be achieved with suitable modifications of the equations of motion. Specifically, for a thermostat a (positive or negative) friction term is added, and for a barostat the box and all

coordinates are rescaled. In this work we use a generalized Nosé-Hoover thermostat and barostat, which correctly reproduce the isothermal-isobaric partition function. The modified equations of motion for a simulation of N particles in d dimensions with N_f degrees of freedom[2] then read as follows [119, 174]:

$$\dot{\boldsymbol{p}}_i = \boldsymbol{F}_i - \left(1 + \frac{d}{N_f}\right)\frac{p_\epsilon}{W}\boldsymbol{p}_i - \frac{p_\xi}{Q}\boldsymbol{p}_i, \tag{5.9}$$

$$\dot{\boldsymbol{x}}_i = \frac{\boldsymbol{p}_i}{m_i} + \frac{p_\epsilon}{W}\boldsymbol{x}_i, \tag{5.10}$$

$$\dot{V} = \frac{dVp_\epsilon}{W}, \tag{5.11}$$

$$\dot{p_\xi} = N_f kT - (N_f + 1)kT_{\text{ext}} + \frac{p_\epsilon^2}{W}, \tag{5.12}$$

$$\dot{p_\epsilon} = d\,V(P - P_{\text{ext}}) + d\,kT - \frac{p_\xi}{Q}p_\epsilon. \tag{5.13}$$

Here p_ξ and p_ϵ are the thermostat and barostat momentum. Their values are determined by the deviation of the actual temperature and pressure from the desired values T_{ext} and P_{ext}. The actual temperature and pressure are computed from the coordinates and momenta:

$$T = \frac{1}{N_f k}\sum_{i=1}^{N}\frac{\boldsymbol{p}_i^2}{m_i}, \tag{5.14}$$

$$P = \frac{1}{dV}\left[\sum_{i=1}^{N}\frac{\boldsymbol{p}_i^2}{m_i} + \sum_{i=1}^{N}\boldsymbol{x}_i \cdot \boldsymbol{F}_i\right]. \tag{5.15}$$

Good starting values for the thermostat and barostat masses are $Q = N_f kT\tau_T^2$ and $W = (N_f + d)kT_{\text{ext}}\tau_P^2$, with the time constants τ_T and τ_P chosen suitably to ensure the best possible coupling of p_ξ and p_ϵ to the other degrees of freedom. If only a thermostat is needed, p_ϵ is set identically zero (and thus $\tau_P = \infty$).

Furthermore, boundary conditions of the simulation have to be fixed. One can apply open boundaries or enclose the system in a hard box. In most instances periodic boundary conditions are chosen. They allow to simulate an infinite system by packing it into a periodically repeated array of unit cells. Thus one avoids the influence of surfaces.

[2] $N_f = dN$, if there are no additional constraints like e.g. chemical bonding in polymers.

5.3. Metropolis-Monte Carlo simulation

Monte Carlo (MC) methods refer, in a very general sense, to simulations of an arbitrary system which use a computer algorithm explicitly dependent on a series of (pseudo)random numbers. The name, which derives from the famous Monaco casino district, emphasizes the importance of randomness, or chance, in the method. MC is particularly important when systems have a large number of degrees of freedom and quantities of interest, such as thermal averages, cannot be computed exactly.

The MC approach to investigate the dynamics of a multi-particle system is completely different from (and in a way much simpler than) the MD approach. In the Metropolis algorithm [123] Newton's equations of motion are not solved directly, but its (non-)equilibrium statistics are reproduced by a random walk in configuration space. The walk is designed so that its points are distributed according to the required probability distribution. At each step a random trial move from the current position in configuration space is selected. Such a single MC trial move typically consists of a random particle displacement inside a sphere around the particle position. The iteration over all particles is called a MC sweep. A trial move is then either accepted or rejected according to a simple probabilistic rule. In this way it is possible to gradually explore the accessible configuration space of the problem.

Let us now derive the rule used to decide whether a trial move is accepted or not. The equilibrium probability distribution in the canonical ensemble for the temperature T in configuration space is given by

$$\rho(\boldsymbol{x}_1, \ldots, \boldsymbol{x}_2) = Z^{-1} e^{-V(\boldsymbol{x}_1, \ldots, \boldsymbol{x}_N)/kT} \tag{5.16}$$

with the partition function

$$Z = \int \mathrm{d}^d \boldsymbol{x}_1 \cdots \mathrm{d}^d \boldsymbol{x}_N \; e^{-V(\boldsymbol{x}_1, \ldots, \boldsymbol{x}_N)/kT}. \tag{5.17}$$

In momentum space it is purely Gaussian

$$\rho(\boldsymbol{p}_1, \ldots, \boldsymbol{p}_N) = \prod_{i=1}^{N} \left(\frac{2\pi}{m_i kT} \right)^{d/2} \exp\left(\frac{-\boldsymbol{p}_i^2}{2m_i kT} \right) \tag{5.18}$$

and isotropic (for a single particle). The momentum part is independent of the position $\boldsymbol{X} = (\boldsymbol{x}_1, \ldots, \boldsymbol{x}_N)$ in configuration space. The acceptance

probability $W(\boldsymbol{X}_i \to \boldsymbol{X}_f)$ of the trial move depends on the difference of potential energy $\Delta E = E_f - E_i$ between final (f) and initial (i) state and is derived from the condition of detailed balance, which postulates equal transition rates in thermodynamic equilibrium:

$$\rho(\boldsymbol{X}_i)W(\boldsymbol{X}_i \to \boldsymbol{X}_f) = \rho(\boldsymbol{X}_f)W(\boldsymbol{X}_f \to \boldsymbol{X}_i). \tag{5.19}$$

It is fulfilled by the choice

$$W(\boldsymbol{X}_i \to \boldsymbol{X}_f) = \min(1, e^{-\Delta E/kT}). \tag{5.20}$$

Constant pressure simulations in the NPT ensemble can also be studied by introducing additional MC trial steps, rescaling the simulation box volume ΔV and all particle coordinates. The energy change ΔE is replaced by $\Delta E' = (P - NkT/V)\Delta V + \Delta E$.

5.4. Interactive simulation and visualization

There are many implementations of MD and MC simulations available in various programming languages. One example is the IMD (ITAP Molecular Dynamics) program [150] developed at the Institute of Theoretical and Applied Physics. Nevertheless, we use an own code, which has several reasons: (i) With foreign code the simulation, data evaluation, and visualization would be necessarily separated, which makes work inflexible. (ii) For the study of the Lennard-Jones-Gauss system (chapter 9) it is helpful to directly control the simulation parameters during a simulation run.[3] A goal of the new implementation was to include this as a key feature. (iii) It is not very time-consuming[4] to write an own (single processor) simulation code.

The simulation package developed for the thesis allows interactive simulations.[5] The layout consists of two modules: a visualization module and a simulation module as shown in Fig. 5.1. The visualization module is programmed in the Java language – therefore called INJAVIS (INteractive

[3] At least for one- and two-dimensional systems, modern computers are fast enough to watch and manipulate the simulation in real time. Maybe in a few years interactive simulations will become feasible for three dimensional systems.

[4] ..., but very instructive!

[5] The simulation package can be downloaded from the internet at `http://www.itap.physik.uni-stuttgart.de/~mengel/`

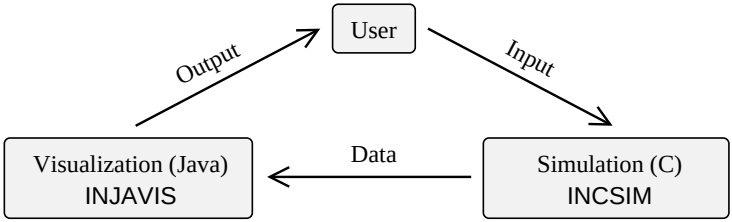

Figure 5.1: Layout of the interactive simulation package: The simulation is set up via user input and graphically displayed on the computer screen, which allows real-time control of the simulation parameters.

JAva VISualization) –, because Java is platform independent and handles graphics output easily. Furthermore an existing graphics application from the author's diploma thesis [43] could be used as starting point. The visualization essentially handles a set of graphics objects. Each of them is an array of vertex points in three-dimensional space, either a particle (one vertex), line (two vertices), or planar polygonal face (more than two vertices). The graphics objects are rendered as perspective projection on the screen including color shading effects, and can be rotated or translated via user input. An example output is shown in Fig. 1.1.

After the start of the visualization, the user loads an external simulation module, which can be for example MD or MC. The simulation modules are adapted for the specific system under investigation. They are programmed in C – and therefore called INCSIM (INteractive C SIMulation) – to optimize for execution speed. Since visualization and simulation are executed fully independent on the computer[6], they take advantage of the dual core architecture of modern computer processors and work in parallel. This way no processor time is lost by the visualization process. For the systems in chapters 7 and 9, the interactive simulation package is even a little bit faster than single processor IMD.

For communication between the two modules data is exchanged via internal pipes according to a fixed protocol. The visualization module sends the initial positions and particles types, as well as parameters received from the user (e.g. temperature, pressure, parameters for the interaction potential and thermo-/barostat, boundary conditions) as an input to the

[6]The simulation module is loaded by the visualization module as an external thread.

simulation module, which then outputs the updated positions and velocities of the particles and thermodynamic variables (kinetic and potential energy, pressure, and volume).

Additionally, the data is saved to a file or processed further by either of the modules. Some information that can be extracted are:

- The radial distribution function: it is defined as the average density at distance r divided by the global average density: $g(r) = \rho(r)/\rho$.
- The density-density (auto-)correlation function, the vibrational density of states, and the structure factors, see Sec. 5.4.1.
- The diffraction image (static structure factor): the particle configuration is mapped onto a two-dimensional $2^n \times 2^n$ array representing the simulation box by putting Gaussians at the projected positions of the particles.[7] The diffraction image is the absolute square of the fast Fourier transform (FFT) of the array (Sec. 2.2).[8]
- The diffusion constant D: its calculation is possible from the average particle displacement at long times (d is the dimension of the system):

$$D = \frac{1}{2d} \lim_{t\to\infty} \frac{\mathrm{d}}{\mathrm{d}t} \left\langle (\boldsymbol{x}_i(t) - \boldsymbol{x}_i(0))^2 \right\rangle . \tag{5.21}$$

- The structure image in Bragg contrast: an area of the Fourier transformed particle configuration is cut out and transformed back with inverse FFT. The position and Burgers vector of dislocations can be determined with Bragg contrast (Sec. 5.4.2).

5.4.1. Structure factors from molecular dynamics

For the numerical calculation of the structure factors (Sec. 4.4) the exact particle trajectories are required. Hence MC cannot be used and we rely on MD simulations. After the positions and velocities of the particles have been equilibrated, the equations of motion are integrated with MD for the simulation time T_{sim}. It is important to not control the particles by a thermostat, a barostat or in any other way after the simulation has been started.

[7] Otherwise the discreteness of the array introduces rounding errors.
[8] For an array size of 2^n the FFT algorithm is fastest.

According to (4.18)-(4.20) we must compute a fourfold sum: two sums over the particle number N and two over the time T_{sim}.[9] For the sake of clarity the averaging over the MD runs is suppressed in the following notation. We introduce a more compact notation by defining $f_j(\boldsymbol{q},t) = e^{\mathrm{i}\boldsymbol{q}\cdot\boldsymbol{x}_j(t)}$. Let us assume tentatively that $f_j(\boldsymbol{q},t)$ is periodic in time with period T_{sim} and in space with period L. Then the equations (4.18)–(4.20) are greatly simplified:

$$S(\boldsymbol{q},\omega) = \frac{1}{2\pi N T_{\mathrm{sim}}} \left\| \int e^{-\mathrm{i}\omega t} \sum_j f_j(\boldsymbol{q},t)\,\mathrm{d}t \right\|^2, \tag{5.22}$$

$$S_{\mathrm{i}}(\boldsymbol{q},\omega) = \frac{1}{2\pi N T_{\mathrm{sim}}} \sum_j \left\| \int e^{-\mathrm{i}\omega t} f_j(\boldsymbol{q},t)\,\mathrm{d}t \right\|^2, \tag{5.23}$$

$$S(\boldsymbol{q}) = \frac{1}{N T_{\mathrm{sim}}} \int \left\| \sum_j f_j(\boldsymbol{q},t) \right\|^2 \mathrm{d}t. \tag{5.24}$$

Since only two sums are left, the algorithm is numerically efficient. Furthermore, a fast Fourier transform is used for the time integrals. Note that the vibrational density of states (4.23) is obtained by substituting $f_j(\boldsymbol{q},t)$ by $\boldsymbol{x}_l(t)$ in (5.23).

It is left to discuss the periodicity conditions. The spatial periodicity follows, if periodic boundaries are used in the simulation. In the one-dimensional case an additional problem arises: Because there is no amplitude decrease of moving phonon waves in one dimension, a chain acts like a ring and excitations goes round during the simulation. To avoid such a behavior, which would lead to unwanted correlations, we limit the maximum simulation time by the quotient of the length of the chain and the sound velocity c to $T_{\max} = L/c$.

The functions $f_j(\boldsymbol{q},t)$ are not periodic in time. To handle the resulting discontinuity for the Fourier transform, we multiply $f_j(\boldsymbol{q},t)$ with a window function to enforce artificial smoothness. The window function has to decrease fast enough – both in direct and Fourier space – towards the boundaries of the system. We use a normalized broad Gaussian function.

[9] By assuming ergodicity, the thermal average $\langle\rangle$ is replaced by a time average $(T_{\mathrm{sim}})^{-1}\int \mathrm{d}t$ and additionally by an average over several independent MD runs. The latter average is crucial, because without it a speckle pattern is observed as a consequence of the fluctuations in a single MD sample.

Its width is chosen as large as possible with the constraint that the Gaussian has decayed to a small enough value at the interval boundaries. The effect is a smoothing of the structure factors by convolution with a narrow Gaussian. The exact value of the width has no influence on the results.

5.4.2. Bragg contrast imaging of dislocations

Given a configuration of particles: how can dislocations be found and their Burgers vector determined? For simple crystals this is done by direct inspection of the particle configuration, but for quasicrystals and complex crystals dislocations are not easily visible. In order to identify the dislocations, diffraction in the so-called Bragg contrast are simulated. We explain the method with the help of an example.

In Figs. 5.2(a)–(b) a simulation snapshot of an MD simulation at elevated temperature is shown. There is only one type of particles, interacting with the other particles by a Lennard-Jones potential. The ground state is a hexagonal lattice. We calculate the structure factor of the configuration, Fig. 5.2(c). One of the Bragg peaks and its image under inversion are chosen for the Bragg contrast. All the information outside two small circles around these Bragg peaks (indicated in the figure) is discarded by setting the structure factor to zero. After inverse Fourier transforming the filtered structure factor, a lattice fringe image is obtained, Fig. 5.2(d). Discontinuities in the lattice fringe image – inserted half lines – are identified as dislocations. From several Bragg contrast images of different Bragg peaks $\boldsymbol{Q}$, the Burgers vector $\boldsymbol{b}$ of the dislocation can be extracted. The dislocation is visible in Bragg contrast, if (and only if) $\boldsymbol{Q} \cdot \boldsymbol{b} \neq \boldsymbol{0}$. The method is transferred to tilings by substituting $\boldsymbol{Q}$ and $\boldsymbol{b}$ with higher-dimensional vectors. It has been applied successfully in studying dislocations in icosahedral quasicrystals with electron microscopy [20, 126, 180].[10]

5.5. The iterative selection algorithm

5.5.1. Perfect tilings

As introduced in Sec. 2.3, tilings of quasicrystals and approximants with arbitrary phason strain are calculated with the selection formalism by de-

[10] In electron microscopy, Bragg contrast is done by inserting an off-center aperture into the back focal plane of the objective lens, called dark-field technique.

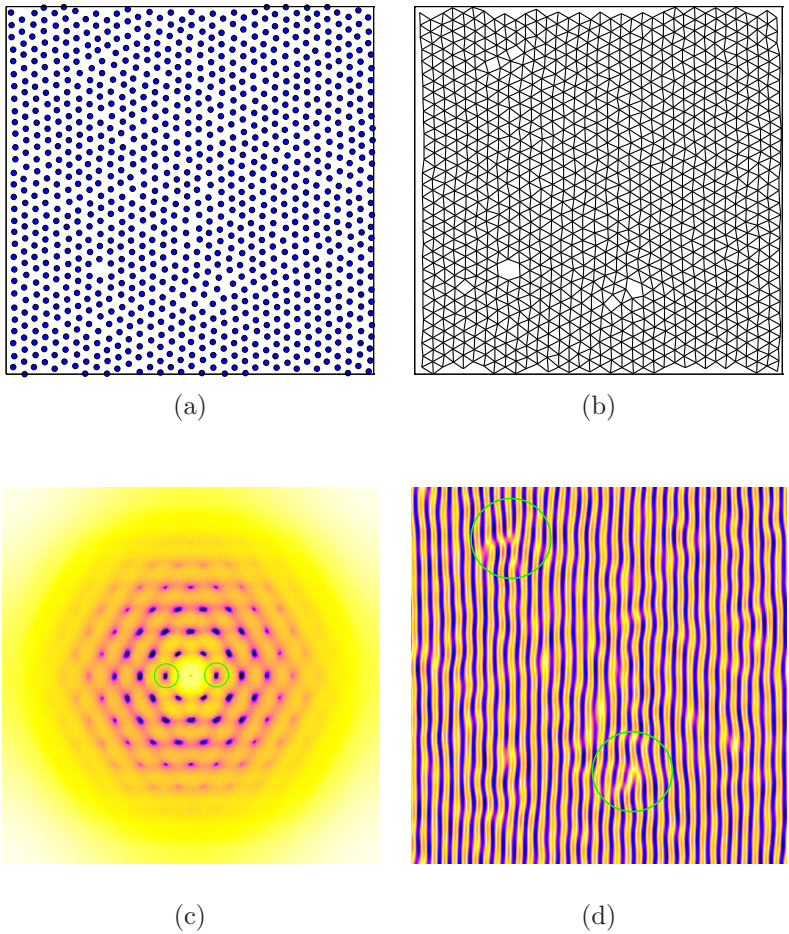

Figure 5.2: (a) MD simulation with the Lennard-Jones potential at 60% melting temperature. (b) Tiling connecting nearest neighbors. (c) Diffraction image showing sixfold symmetry. (d) Bragg contrast to identify the two dislocations present in the system.

termining all the atomic volumes which are selected by the the cut space. The straightforward way would be to decide, whether n-dimensional cells (the atomic volumes) are cut by a d-dimensional non-planar space. This leads to a system of non-linear equations. Furthermore the algorithm scales with the dimension of the hyperspace and not with the dimension of the physical space. However, one can take advantage of the fact that the atomic volumes fill the hyperspace without gap and apply an iterative algorithm, which we call the iterative selection algorithm. Here we explain it for the two-dimensional Penrose tiling with $d = 2$, $n = 5$, the hyperlattice $\mathbb{Z}^5$, and a hypercube as atomic volume, but it is also used without problems for other two- or three-dimensional tilings.

First, let us recapitulate what is given: (i) From the phason displacement we obtain a parametrization of the cut space E_C in hyperspace, see (2.10). (ii) Each point in hyperspace is associated with an atomic volume, and thus with a hyperlattice point, i.e. with a set of five integers for the Penrose tiling. Together, this means there is a discontinuous map $\boldsymbol{\mu} : E_C \to \mathbb{Z}^5$, which partitions the cut space in a discrete set of cells with constant $\boldsymbol{\mu}$. The partitioning is called a grid, see Fig. 5.3. For a perfect Penrose tiling, the grid lines are parallel and straight, but they will be bent in the general case. The calculation of the tiling is rephrased in the following way: Determine the set of values $M = \{\boldsymbol{\mu}(\boldsymbol{x}) \mid \boldsymbol{x} \in E_C\}$. The tiling is then the lowering of the hyperlattice points M. Note that the values $\boldsymbol{\mu}$ of neighboring cells only differ by ± 1 in one component.

In the grid formalism [32], the tiling is calculated by intersecting each pair of grid lines and determining the values of $\boldsymbol{\mu}$ for the cells containing the intersection as a vertex. For a perfect tiling this leads to a simple system of linear equations. In the general case, the equations are non-linear. The following iterative algorithm is more efficient than solving each of the non-linear equations separately:

(i) Initialization: Choose a rectangle $R = \{\boldsymbol{x}_1, \boldsymbol{x}_2, \boldsymbol{x}_3, \boldsymbol{x}_4\}$ in E_C, which will be used as the domain for calculating the tiling. $M = \emptyset$.

(ii) Iteration with rectangle R: Add the values $\boldsymbol{\mu}(\boldsymbol{x}_i)$ for $\boldsymbol{x}_i \in R$ to M.

a) Is $|\boldsymbol{\mu}(\boldsymbol{x}_1) - \boldsymbol{\mu}(\boldsymbol{x}_2)| > 1$ or $|\boldsymbol{\mu}(\boldsymbol{x}_3) - \boldsymbol{\mu}(\boldsymbol{x}_4)| > 1$? If yes, split the rectangle into $R_1 = \{\boldsymbol{x}_1, \boldsymbol{x}_{12}, \boldsymbol{x}_3, \boldsymbol{x}_{34}\}$, $R_2 = \{\boldsymbol{x}_{12}, \boldsymbol{x}_2, \boldsymbol{x}_{34}, \boldsymbol{x}_4\}$. Start (ii) with both $R = R_1$ and $R = R_2$. Return.

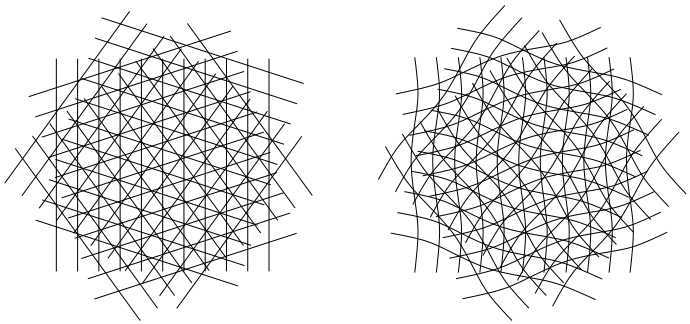

Figure 5.3: (a) The 5-grid of the perfect Penrose tiling. (b) For non-linear phason strains the grid lines will be wavy or bent.

b) Is $|\boldsymbol{\mu}(\boldsymbol{x}_1) - \boldsymbol{\mu}(\boldsymbol{x}_3)| > 1$ or $|\boldsymbol{\mu}(\boldsymbol{x}_2) - \boldsymbol{\mu}(\boldsymbol{x}_4)| > 1$? If yes, split the rectangle into $R_3 = \{\boldsymbol{x}_1, \boldsymbol{x}_2, \boldsymbol{x}_{13}, \boldsymbol{x}_{24}\}$, $R_4 = \{\boldsymbol{x}_{13}, \boldsymbol{x}_{24}, \boldsymbol{x}_3, \boldsymbol{x}_4\}$. Start (ii) with both $R = R_3$ and $R = R_4$. Return.

c) No further iteration necessary. Return.

(iii) Termination: Calculate the tiling by lowering the points M.

In the algorithm we used $\boldsymbol{x}_{ij} = (\boldsymbol{x}_i + \boldsymbol{x}_j)/2$ and $|\boldsymbol{\mu}| = \sum_{i=1}^{5} |\mu_i|$. 'The cells corresponding to $\boldsymbol{x}_i$ and $\boldsymbol{x}_j$ are identical' is equivalent to $|\boldsymbol{\mu}(\boldsymbol{x}_i) - \boldsymbol{\mu}(\boldsymbol{x}_j)| = 0$. 'The cells share a common side' is equivalent to $|\boldsymbol{\mu}(\boldsymbol{x}_i) - \boldsymbol{\mu}(\boldsymbol{x}_j)| = 1$. The idea is simple: Successively refine a network of rectangles $\{\boldsymbol{x}\}$, until each cell has been hit by at least one of their vertices. The iteration stops for a rectangle, if there is at most one intersection of grid lines inside it.

5.5.2. Tilings with dislocations

The iterative selection formalism is especially useful for calculating tilings with dislocations.[11] To do so, one has to impose an additional displacement on the cut plane. The easiest way to do it, is to assume elastic isotropy.

[11] An alternative is the extended grid formalism [14, 35].

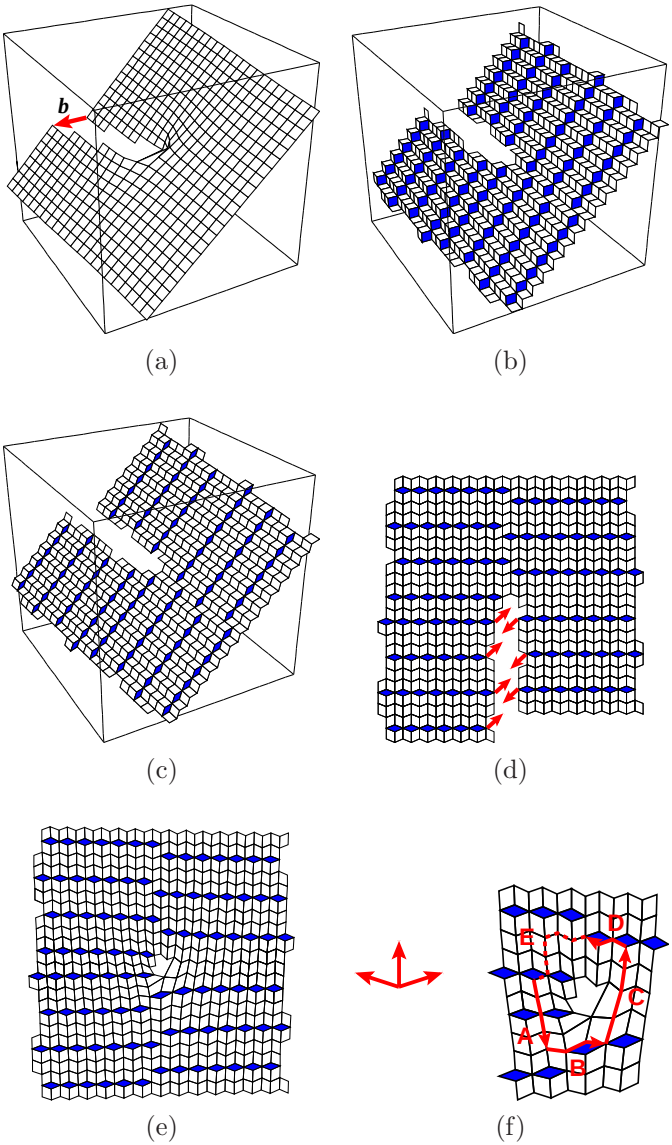

Figure 5.4: Construction of a dislocation in the tripod tiling (see text).

This leads to a displacement field of the form:

$$\boldsymbol{u}(x,y,z) = \arccos\left(\frac{x}{\sqrt{x^2+y^2}}\right)\frac{\boldsymbol{b}}{2\pi}. \tag{5.25}$$

The dislocation is assumed to run in z-direction. Here $\boldsymbol{b}$ is the Burgers vector of the dislocations, which is sitting in the origin. With the new cut space the selection formalism is applied as usual.

As an example, we demonstrate the calculation of a dislocation in the two-dimensional obtuse tripod tiling, which has a three-dimensional hyperspace and thus allows an easy visualization of the construction process (see also Sec. 2.3). The cut plane obtained with the additional displacement field is shown in Fig. 5.4(a). It is singular at the dislocation position and has a discontinuity along a radial line with a 'jump vector' $\boldsymbol{b}$. The cut plane selects those hyperlattice points whose atomic volumes (unit cubes around the hyperlattice points) are cut by the cut plane, Fig. 5.4(b). After lowering the selected hyperlattice points on the physical space, a gap remains, Fig. 5.4(c),(d). Note that up to now only the phason part of the displacement field has been accounted for. By closing the gap in an isotropic manner (distributing the phonon strain isotropically around the dislocation core), the final tiling with dislocation is obtained, Fig. 5.4(e).[12] The Burgers vector is checked by conducting a Burgers circuit, Fig. 5.4(f): Since the paths A and C, as well as B and D cancel, the Burgers vector is equal to path E. In the basis introduced in Sec. 3.2: $\boldsymbol{b} = (-3,-2,1)$.

[12] For demonstration purposes, the dislocation has a large phonon strain. Because of this, the dislocation would of course be physically unfavourable.

Part II.

Simulations and results

Chapter 6.

Structure factors of harmonic lattices

In order to see the influence of dimensionality on the correlation functions and structure factors, we discuss the exactly solvable orthogonal lattice in d dimensions. The structure factors are shown to consist of peaks at the reciprocal lattice vectors or along the dispersion relation, which are broadened in dimensions $d < 3$. The broadening is given by shape functions. We collect the results on the shape functions from the literature and give a simple derivation (correcting a minor mistake in the literature on the two dimensional case). The full structure factors far from the reciprocal lattice vectors are calculated by extending the phonon expansion to one and two dimensions, which as far as we know has not been done in the literature.

This chapter is not directly related to structural complexity and can be skipped on the first reading. We prepare the notations and theoretical background for the one-dimensional chains in the next chapter.

6.1. Model system

The orthogonal lattice is a linear chain ($d = 1$), a square lattice ($d = 2$), and a cubic lattice ($d = 3$). The system has lattice constant a, periodic boundaries and contains N particles with equilibrium positions $\boldsymbol{R}_l$. Each particle is permanently coupled to its $2d$ nearest neighbors with a harmonic pair interaction given by the potential $V(\boldsymbol{x}) = D\boldsymbol{x}^2/2$. The Hamiltonian has the form

$$\mathcal{H} = \sum_{l=1}^{N} \frac{\boldsymbol{p}_l^2}{2m} + \frac{1}{2} \sum_{j \text{ nn } l} V(\boldsymbol{x}_j - \boldsymbol{x}_l - \boldsymbol{R}_{jl}), \tag{6.1}$$

where the second sum runs over all nearest neighbors, and the vectors connecting their equilibrium positions, $\boldsymbol{R}_{jl} = \boldsymbol{R}_j - \boldsymbol{R}_l$, is a basis vector of the lattice.

The displacement from the equilibrium position $\boldsymbol{u}_l(t) = \boldsymbol{x}_l(t) - \boldsymbol{R}_l$ is in general expressed as a linear combination of normal phonon modes with amplitudes $\boldsymbol{\alpha_Q}$ and wave vectors $\boldsymbol{Q}$ within the first Brillouin zone:

$$\begin{aligned}\boldsymbol{u}_l(t) = \frac{1}{\sqrt{N}} \sum_{\boldsymbol{Q}\neq\boldsymbol{0}} [\boldsymbol{\alpha_Q} \exp(i[\omega_{\boldsymbol{Q}} t - \boldsymbol{Q}\cdot\boldsymbol{R}_l]) + \\ \boldsymbol{\alpha}^*_{\boldsymbol{Q}} \exp(i[-\omega_{\boldsymbol{Q}} t + \boldsymbol{Q}\cdot\boldsymbol{R}_l])].\end{aligned} \tag{6.2}$$

Wave vector and frequency are related according to the dispersion relation

$$\omega_{\boldsymbol{Q}} = 2\omega_0[\sin^2(Q_1 a/2) + \ldots + \sin^2(Q_d a/2)]^{1/2}. \tag{6.3}$$

Here $\omega_0 = (D/m)^{1/2}$ is the eigenfrequency of a single particle. The total energy of the system is

$$E[\boldsymbol{\alpha}] = \sum_{\boldsymbol{Q}\neq\boldsymbol{0}} \frac{1}{2} m\omega^2_{\boldsymbol{Q}} |\boldsymbol{\alpha_Q}|^2. \tag{6.4}$$

Let us come back to the structure factors. For harmonic interactions, the equations (4.18)–(4.20) can be transformed into[1]

$$S(\boldsymbol{q}) = \sum_{l=1}^{N} e^{\mathrm{i}\boldsymbol{q}\cdot\boldsymbol{R}_{l1}} \exp\left(-\tfrac{1}{2d}\boldsymbol{q}^2\sigma_l^2(0)\right) \tag{6.5}$$

$$S(\boldsymbol{q},\omega) = \frac{1}{2\pi}\int e^{-\mathrm{i}\omega t} \sum_{l=1}^{N} e^{\mathrm{i}\boldsymbol{q}\cdot\boldsymbol{R}_{l1}} \exp\left(-\tfrac{1}{2d}\boldsymbol{q}^2\sigma_l^2(t)\right)\,\mathrm{d}t, \tag{6.6}$$

$$S_{\mathrm{i}}(\boldsymbol{q},\omega) = \frac{1}{2\pi}\int e^{-\mathrm{i}\omega t} \exp\left(-\tfrac{1}{2d}\boldsymbol{q}^2\sigma_0^2(t)\right)\,\mathrm{d}t \tag{6.7}$$

with the displacement correlations

$$\sigma_l^2(t) = \langle[\boldsymbol{u}_l(t) - \boldsymbol{u}_0(0)]^2\rangle. \tag{6.8}$$

As a side remark we mention the Fourier transform of (6.6) and (6.7):

$$G(\boldsymbol{x},t) = \left(\frac{d}{2\pi}\right)^{d/2} \sum_{l=1}^{N} \frac{a}{\sigma_l(t)} \exp\left(-d\frac{(\boldsymbol{x}-\boldsymbol{R}_{l1})^2}{2\sigma_l^2(t)}\right), \tag{6.9}$$

$$G_{\mathrm{a}}(\boldsymbol{x},t) = \left(\frac{d}{2\pi}\right)^{d/2} \frac{a}{\sigma_0(t)} \exp\left(-d\frac{\boldsymbol{x}^2}{2\sigma_0^2(t)}\right). \tag{6.10}$$

[1] We use the following relation first derived by Bloch for harmonic interactions [164]: If Q is a linear sum of positions or momenta, then $\langle \exp Q\rangle = \exp\left(\frac{1}{2}\langle Q^2\rangle\right)$.

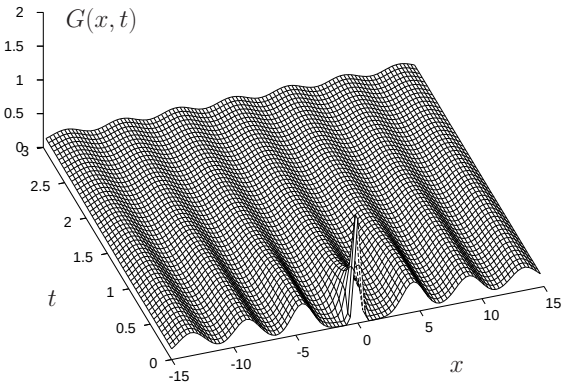

Figure 6.1: Density-density correlation function $G(x,t)$ of the harmonic chain for $kT/m\omega_0^2 = 0.06$. The Gaussians are centered at integer multiples of $a \approx 4.47$. $G(x,t)$ decays exponentially with x and t reflecting the fact that the one-dimensional chain has short-range order.

The position correlation function $G(\boldsymbol{x},t)$ is a sum of Gaussians with width $\sigma_l^2(t)$ centered at the equilibrium positions of the particles (Fig. 6.1). The autocorrelation function $G_\mathrm{a}(\boldsymbol{x},t)$ corresponds to the central peak at $\boldsymbol{x}=0$.

We now try to solve the integrals in (6.5)–(6.7). The problem consists of calculating and Fourier transforming the functions $\exp(-\frac{1}{2d}\boldsymbol{q}^2\sigma_l^2(t))$. In the canonical ensemble[2] and with (6.2) we get:

$$\sigma_l^2(t) = \frac{kT}{Nm}\sum_{\boldsymbol{Q}\neq\boldsymbol{0}}\frac{2-2\cos(\omega_{\boldsymbol{Q}}t-\boldsymbol{Q}\cdot\boldsymbol{R}_{l1})}{\omega_{\boldsymbol{Q}}^2}. \tag{6.14}$$

[2]The average of A in the canonical ensemble is given by

$$\langle A\rangle = Z^{-1}\int \mathcal{D}\boldsymbol{\alpha}\, e^{-E[\boldsymbol{\alpha}]/kT}A \tag{6.11}$$

with the partition function $Z=\int\int \mathcal{D}\boldsymbol{\alpha}\, e^{-E[\boldsymbol{\alpha}]/kT}$. Using (6.4), this leads to Gaussian integrals with the results

$$\langle \boldsymbol{\alpha}_{\boldsymbol{Q}}\boldsymbol{\alpha}^*_{\boldsymbol{Q}'}\rangle = \delta_{\boldsymbol{Q},\boldsymbol{Q}'}\frac{kT}{Nm\omega_{\boldsymbol{Q}}^2}, \tag{6.12}$$

$$\langle \boldsymbol{\alpha}_{\boldsymbol{Q}}\boldsymbol{\alpha}_{\boldsymbol{Q}'}\rangle = \langle \boldsymbol{\alpha}^*_{\boldsymbol{Q}}\boldsymbol{\alpha}^*_{\boldsymbol{Q}'}\rangle = 0. \tag{6.13}$$

In the limit $N \to \infty$, the sum is replaced by an integral:

$$\sigma_l^2(t) = \frac{kT}{m}\left(\frac{a}{2\pi}\right)^d \int_{-\frac{\pi}{a}}^{\frac{\pi}{a}} \cdots \int_{-\frac{\pi}{a}}^{\frac{\pi}{a}} \mathrm{d}^d\boldsymbol{Q}\, \frac{2-2\cos(\omega_{\boldsymbol{Q}}t)\cos(\boldsymbol{Q}\cdot\boldsymbol{R}_{l1})}{\omega_{\boldsymbol{Q}}^2}. \quad (6.15)$$

Since the numerator behaves like Q^{-2} for small Q the integral is unproblematic at small Q. Furthermore, for large t and l the nominator is zero already at a small Q-values and the integral eventually becomes large.

As we will find out in the course of the next sections, the calculation of the structure factors is not possible without approximations. Even if the $\sigma_l^2(t)$ were known exactly, exponentiating and Fourier transforming them would be impossible. In the following we proceed in two steps: (i) The continuum limit $l, t \to \infty$ is studied, which covers low frequency, long wave length phonons, (ii) which are then coupled to the other phonons via the generalized phonon expansion. We will see that the long wavelength phonons are also responsible for the peak broadening in the structure factors.

6.2. The continuum limit

In the limit $l, t \to \infty$ the equation (6.15) is dominated by the small $\boldsymbol{Q}$-region.[3] Hence dispersion does not play a role and the simplified assumption of the Debye phonon gas is valid. The phonon dispersion is chosen to be isotropic and linear, $\omega_{\boldsymbol{Q}} = \omega_0 a|\boldsymbol{Q}| = cQ$. After introducing spherical coordinates, the upper integration limit of the radial variable is given by the equality of the cubic integration volumes with the volume V_d of the d-sphere.

During the integration over the angular variables, the scalar product $\boldsymbol{Q}\cdot\boldsymbol{R}_{l1}$ has to be taken into account.[4] This gives for (6.15) with $s = Q/a$

[3] Note that the characteristic distances and the characteristic time scale of the system are coupled via the sound velocity $c = \omega_0 a$.

[4] For the angular integral we use an identity for $J_0(x)$, the 0-th Bessel function of the first kind [2]:

$$\int_0^{2\pi} e^{\mathrm{i}x\cos(\phi)}\,\mathrm{d}\phi = \int_0^{2\pi} \cos(x\cos(\phi))\,\mathrm{d}\phi = 2\pi J_0(x). \quad (6.16)$$

and $\sigma^2 = kT/m\omega_0^2$:

$$d = 1: \qquad \sigma_l^2(t) = \sigma^2 \int_0^{\pi} \mathrm{d}s \, \frac{2 - 2\cos(s\omega_0 t)\cos(sl)}{\pi s^2}, \tag{6.17}$$

$$d = 2: \qquad \sigma_l^2(t) = \sigma^2 \int_0^{2\sqrt{\pi}} \mathrm{d}s \, \frac{1 - \cos(s\omega_0 t) J_0(sR_{l1}/a)}{\pi s}, \tag{6.18}$$

$$d = 3: \qquad \sigma_l^2(t) = \sigma^2 \int_0^{(6\pi^2)^{1/3}} \mathrm{d}s \, \frac{1 - \cos(s\omega_0 t) J_0(sR_{l1}/a)}{2\pi}. \tag{6.19}$$

The limit $l \to \infty$ is identical to $a \to 0$. It leads to a system without distinguished length scale and is known as continuum or hydrodynamic limit. Instead of $\sigma_l^2(t)$, we write $\sigma^2(r,t)$ with $r = |\boldsymbol{R}_{l1}|$. For $d = 1$ and $d = 3$ the calculation of $\sigma^2(r,t)$ can be done directly[5]. The case $d = 2$ is more difficult [177]. Up to a constant of order unity one obtains:

$$d = 1: \qquad \sigma^2(r,t) = \sigma^2 \begin{cases} |r|/a, & |r| > c|t| \\ \omega_0|t|, & |r| \le c|t| \end{cases}, \tag{6.20}$$

$$d = 2: \qquad \sigma^2(r,t) = \frac{\sigma^2}{\pi} \begin{cases} \ln(|r|/a), & |r| > c|t| \\ \ln(\omega_0|t|), & |r| \le c|t| \end{cases}, \tag{6.21}$$

$$d = 3: \qquad \sigma^2(r,t) = \sigma^2 \left(3/4\pi\right)^{1/3}. \tag{6.22}$$

The results for the one- and two-dimensional cases are surprising, because $\sigma^2(r,t)$ has sharp bends at $r = \pm ct$ as shown in Fig. 6.2. The reason is that phonon prefer to propagate with the sound velocity.[6] Approaching the continuum limit, the wave front is getting sharper and sharper. In general, $\sigma^2(r,t)$ is split up into two parts: a static part, already present at $t = 0$ and constant up to $ct = r$, and a time-dependent part appearing at $ct > r$. Only the latter induces causality. In three dimensions the propagating wave front also forms, but quickly disappears with increasing time and distance as seen in the figure.

[5] The calculation is done with the computer algebra program MAPLE.

[6] The peculiar way a local displacement propagates in a harmonic chain was studied by Erwin Schrödinger in one of his first papers [153] published in 1914. It is still very nice to read even today.

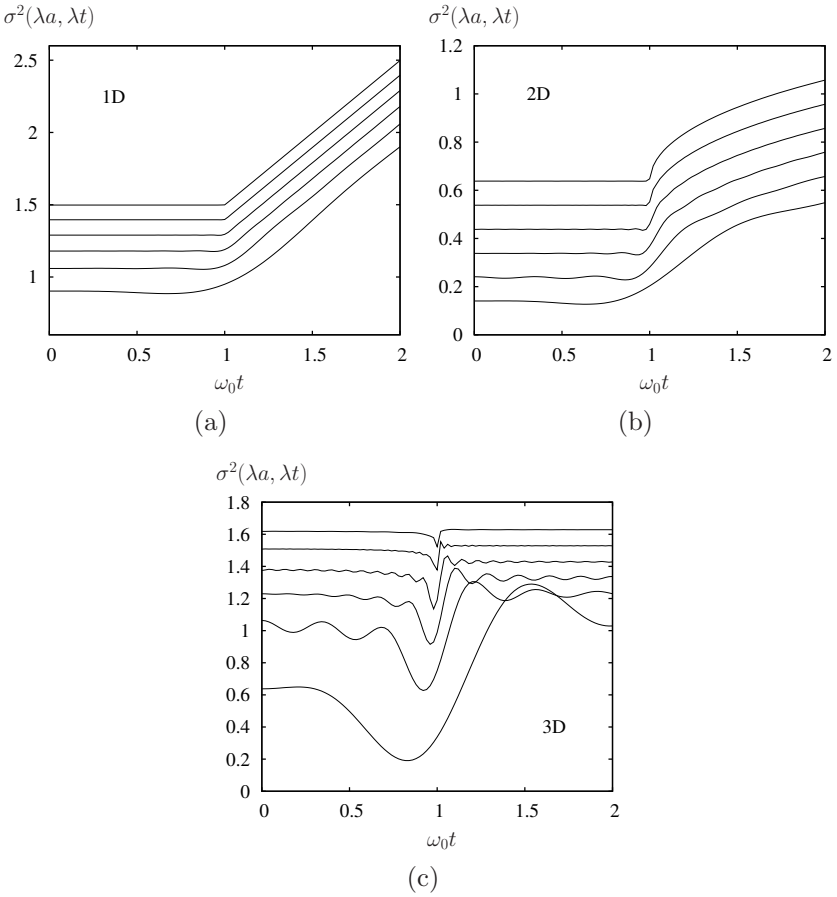

Figure 6.2: Numerical evaluation of the integrals (6.17)–(6.19). The plots show the displacement correlation function $\sigma^2(\lambda a, \lambda t)$ for (a) $d = 1$, (b) $d = 2$ and (c) $d = 3$ using the scaling factors $\lambda = 2, 5, 10, 20, 50, 100$ (from bottom to top). In the continuum limit $\lambda \to \infty$ a sharp bend appears at $\omega_0 t = 1$ for $d \leq 2$. The curves have been vertically scaled and translated in a way to converge for large λ. An additional vertical offset of 0.1 per curve has been added for better visual separation.

6.3. Shape functions

The structure factors are defined as the Fourier transforms of the exponential functions $\exp(-\boldsymbol{q}^2\sigma_l^2(t)/2d)$ appearing in (6.5)–(6.7). As a first step to calculate them, we determine the so-called shape functions:

$$\Gamma(\boldsymbol{q};\boldsymbol{Q}) = \frac{1}{a^d}\int e^{\mathrm{i}\boldsymbol{q}\cdot\boldsymbol{r}} \exp\left(-\tfrac{1}{2d}\boldsymbol{Q}^2\sigma^2(r,0)\right)\,\mathrm{d}^d\boldsymbol{r}, \tag{6.23}$$

$$\Gamma(\omega;\boldsymbol{Q}) = \frac{1}{2\pi}\int e^{-\mathrm{i}\omega t} \exp\left(-\tfrac{1}{2d}\boldsymbol{Q}^2\sigma^2(0,t)\right)\,\mathrm{d}t \tag{6.24}$$

$$\Gamma(\boldsymbol{q},\omega;\boldsymbol{Q}) = \frac{1}{2\pi a^d}\int e^{-\mathrm{i}\omega t}\int e^{\mathrm{i}\boldsymbol{q}\cdot\boldsymbol{r}} \exp\left(-\tfrac{1}{2d}\boldsymbol{Q}^2\sigma^2(r,t)\right)\,\mathrm{d}^d\boldsymbol{r}\,\mathrm{d}t. \tag{6.25}$$

Compared to (6.5)–(6.7), the particle sums have been replaced by integrals and the $\boldsymbol{q}$-vector in the integrand by $\boldsymbol{Q}$. Note that the shape functions only depend on $q = |\boldsymbol{q}|$ and $Q = |\boldsymbol{Q}|$. Later we will assume that $q \ll Q$.

Linear chain Using (6.20) one gets:

$$\exp(-\tfrac{1}{2}Q^2\sigma^2(r,t)) = \exp\left(-\frac{Q^2\sigma^2}{4a}(|ct-r|+|ct+r|)\right). \tag{6.26}$$

By the solution of the Fourier transform one obtains with $\kappa = Q^2\sigma^2/2a$:

$$\Gamma(q;Q) = \frac{2\kappa/a}{q^2+\kappa^2}, \tag{6.27}$$

$$\Gamma(\omega;Q) = \frac{\kappa/\pi c}{(\omega/c)^2+\kappa^2}, \tag{6.28}$$

$$\Gamma(q,\omega;Q) = \frac{2\kappa^2/\pi ac}{[(q+\omega/c)^2+\kappa^2][(q-\omega/c)^2+\kappa^2]}. \tag{6.29}$$

$\Gamma(q;Q)$ and $\Gamma(\omega;Q)$ are Lorentzians with width κ. $\Gamma(q,\omega;Q)$ is a product of two Lorentzians following the linearized dispersion relation.

Square lattice The dynamic behavior of the square lattice is the most difficult one amongst the harmonic lattices. This might be surprising at first, but after a second thought one realizes that two dimensions is the borderline between long-range order and short-range order. Therefore something special might be going on. Historically, the static structure factor

[79, 83, 125] and the continuum limit of the coherent structure factors [124, 177] remained unsolved for quite some time.

From (6.21) we obtain the following power law:

$$\exp(-\tfrac{1}{4}Q^2\sigma^2(r,t)) = \left[\frac{|ct-r|+|ct+r|}{2a}\right]^{-A} \tag{6.30}$$

with $A = Q^2\sigma^2/2\pi$. The Fourier transform of the expression is difficult. To calculate the shape function $\Gamma(q;Q)$ we again use (6.16):

$$\Gamma(q;Q) = \frac{4\pi}{a^{2-A}}\int_a^\infty \frac{J_0(qr)}{r^{A-1}}\,\mathrm{d}r. \tag{6.31}$$

Contrary to what has been done in the literature [125, 177], the lower bound is not zero, but has to be a finite cutoff at the lattice constant a. Otherwise the integral (6.31) would diverge at $r = 0$ for $A \geq 2$. We obtain:

$$\Gamma(q;Q) = 4\pi \begin{cases} \dfrac{C}{(qa)^{2-A}}, & 0 < A < 2 \\ D - \ln(qa), & A = 2 \\ \dfrac{1}{A-2} - E(qa)^{A-2}, & 2 < A < 4 \\ \dfrac{1}{A-2} - \ln(qa)(qa)^2, & A = 4 \\ \dfrac{1}{A-2} - F(qa)^2, & A > 4 \end{cases} \tag{6.32}$$

with constants C, D, E, F. For $0 < A < 2$ the shape function diverges with exponent $2 - A$ and for $A = 2$ a logarithmic divergence appears. For $A > 2$ the divergence disappears, the exponent varies between 0 and 2. $A = 4$ is again special, since it is the transition to the region $A > 4$, where the exponent is constant equal 2. The transition from diverging to finite peak behavior is shown in Fig. 6.3.

The calculations of the other shape functions are similar. For $\Gamma(\omega;Q)$ the dimension of the integral changes, $2\pi r\,\mathrm{d}r \to \mathrm{d}t$, and thus the exponent is smaller. In (6.32) this leads to the substitution $A \to A - 1$. The critical points are $A = 1$ and $A = 3$. Finally, $\Gamma(q,\omega;Q)$ can be obtained with the help of approximations. The literature suggests for $A < 1$ [177]:

$$\Gamma(q,\omega;Q) \sim \frac{1}{|q^2 + \omega^2/c^2|^{1-A}}, \tag{6.33}$$

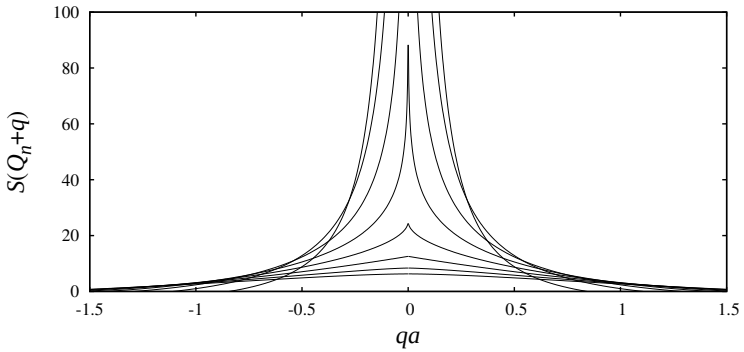

Figure 6.3: Shape function $\Gamma(q;Q)$ of the square lattice for different values of $A = Q^2\sigma^2/2\pi = 0.5,\ 1.0,\ 1.5,\ 2.0,\ 2.5,\ 3.0,\ 3.5,\ 4.0$. The fastest divergence appears here for $A = 0.5$, the broadest finite peak for $A = 4.0$.

although presumably the q-dependence is different from the ω-dependence. The expression for $A \geq 1$ is not known.

Cubic lattice Let us come to the most well-known case: For the cubic lattice, the shape functions are very simple. They are delta functions positioned at the origin:

$$\Gamma(q;Q) = (2\pi/a)^d \delta(q) W, \tag{6.34}$$

$$\Gamma(\omega;Q) = \delta(\omega) W, \tag{6.35}$$

$$\Gamma(q,\omega;Q) = (2\pi/a)^d \delta(q)\delta(\omega) W. \tag{6.36}$$

The Q dependence is put into the Debye-Waller factor

$$W = \exp\left(-\tfrac{1}{6}Q^2\sigma^2\left(\tfrac{3}{4\pi}\right)^{1/3}\right). \tag{6.37}$$

6.4. General formalism

Next we depart from the continuum model and study smaller distances and shorter times. Here, the assumption of linear dispersion is no longer valid. The idea found in the literature is to expand the terms $\exp(-\boldsymbol{q}^2\sigma_l^2(t)/2d)$

appearing in (6.5)–(6.7) in a Taylor series, which is then Fourier transformed term-wise [113, 164]. Although this works quite easy in three dimensions, care has to be applied in the general case, because $\sigma_l^2(t)$ diverges for $d \leq 2$. As far as we know, such an expansion has not yet been reported in the literature for low-dimensional system.

Combining (6.5)–(6.7) with (6.14), the structure factors are written as

$$S = \mathcal{F} \exp\left(-\frac{\boldsymbol{q}^2\sigma^2\omega_0^2}{dN} \sum_{\boldsymbol{Q}\neq\boldsymbol{0}} \frac{1-\cos(\omega_{\boldsymbol{Q}}t - \boldsymbol{Q}\cdot\boldsymbol{R}_{l1})}{\omega_{\boldsymbol{Q}}^2} \right). \tag{6.38}$$

Here S stands for one of the structure factors and $\mathcal{F}$ for a space, space-time, or time Fourier transform respectively. Note that we have to set $t = 0$ for the static structure factor and $\boldsymbol{R}_{l1} = \boldsymbol{0}$ for the incoherent structure factor.

The exponent in (6.38) is controlled by the dimensionless factor $\boldsymbol{q}^2\sigma^2$. For $\boldsymbol{q}^2\sigma^2 \gg 1$ only small times and distances contribute, and the cosine can be expanded to second order. In linear dispersion we get:

$$S = \mathcal{F} \exp\left(-\frac{\boldsymbol{q}^2\sigma^2}{2d}(t\omega_0 - R_{l1}/a)^2 \right). \tag{6.39}$$

For $\boldsymbol{q}^2\sigma^2 \gg 1$ the structure factors are simple Gaussians. Next we will discuss the more interesting limit $\boldsymbol{q}^2\sigma^2 \ll 1$. But before that: What is the physical meaning of the parameter $\boldsymbol{q}^2\sigma^2$? The wave vector $\boldsymbol{q}$ is of the order of the inverse lattice constant $1/a$. So $\boldsymbol{q}^2\sigma^2 = 1$ is identical to $kT = mc^2$, i.e. the average velocity of the particles represented by the temperature T is about equal to the sound velocity. Equivalently this means that the average fluctuation of the distance of neighboring atoms is about equal to the lattice constant a. According to the Lindemann criterion [111] generalized to low dimensions [9, 184], a system melts, if the average fluctuations are approximately an order of magnitude smaller than the lattice constant. Thus, for physically relevant situations $\boldsymbol{q}^2\sigma^2 < 1$ will be fulfilled and the structure factors are never close to Gaussian.

We assume $\boldsymbol{q}^2\sigma^2 \ll 1$ and write (6.38) as a product,

$$S = \mathcal{F}\left[\frac{1}{Z} \prod_{\boldsymbol{Q}\neq\boldsymbol{0}} \exp\left(\tau_{\boldsymbol{Q}}\right) \right], \tag{6.40}$$

using the coefficients

$$\tau_{\boldsymbol{Q}} = \frac{\boldsymbol{q}^2\sigma^2\omega_0^2}{dN}\frac{\cos(\omega_{\boldsymbol{Q}}t - \boldsymbol{Q}\cdot\boldsymbol{R}_{l1})}{\omega_{\boldsymbol{Q}}^2} \tag{6.41}$$

and the t- and r-independent normalization

$$Z = \prod_{\boldsymbol{Q}\neq\boldsymbol{0}} \exp\left(\frac{\boldsymbol{q}^2\sigma^2\omega_0^2}{dN}\frac{1}{\omega_{\boldsymbol{Q}}^2}\right). \tag{6.42}$$

After the exponentials in (6.40) are expanded in a Taylor series, which is converging because of $\boldsymbol{q}^2\sigma^2 \ll 1$, we collect the terms according to the number of $\tau_{\boldsymbol{Q}}$ factors:

$$S = \mathcal{F}\left[\frac{1}{Z}\left(1 + \sum_{\boldsymbol{Q}_1\neq\boldsymbol{0}} \tau_{\boldsymbol{Q}_1} + \sum_{\boldsymbol{Q}_1,\boldsymbol{Q}_2\neq\boldsymbol{0}} \tfrac{1}{2}\tau_{\boldsymbol{Q}_1}\tau_{\boldsymbol{Q}_2} + O(\tau_{\boldsymbol{Q}}^3)\right)\right]. \tag{6.43}$$

Since the $\tau_{\boldsymbol{Q}_1}$ are cosines, their Fourier transforms yield delta functions at $\boldsymbol{Q} = \pm\boldsymbol{Q}_1$, $\omega = \pm\omega_{\boldsymbol{Q}_1}$. Due to the occurrence of cosine products in higher terms delta functions at integer multiples of added or subtracted arguments appear. The peaks of the delta functions are at:

$$(\boldsymbol{Q},\omega) = \sum_i \pm n_i\left(\boldsymbol{Q}_1,\omega_{\boldsymbol{Q}_1}\right), \tag{6.44}$$

with $n_i \in \mathbb{Z}$. We call $(n_i)_i$ a partition of $\boldsymbol{Q}$, if (6.44) is fulfilled. Each delta function of a partition is weighted by the factor

$$c_{(n_i)_i} = \sum_i \frac{1}{n_i!\,2^{n_i}}\left(\frac{\boldsymbol{q}^2\sigma^2\omega_0^2}{dN\omega_{\boldsymbol{Q}}^2}\right)^{n_i}. \tag{6.45}$$

To calculate the structure factors for a given $\boldsymbol{Q}$ and ω, all possible partitions $(n_i)_i$ have to be found. Their respective weights are then summed up and finally normalized by Z. The approach is similar to a path integral formalism.

6.5. Phonon expansion

It would be easy to calculate the structure factors, if the 'coupling constants' $c_{(n_i)_i}$ were small: $\boldsymbol{q}^2\sigma^2\omega_0^2/2d\omega_{\boldsymbol{Q}}^2 < 1$.[7] Then only terms of low order in (6.43) contribute.[8] $\omega_{\boldsymbol{Q}}$ is arbitrarily small for infinite systems and thus the coupling is strong for small $\boldsymbol{Q}$, making the direct calculation tedious. However, one can expand the structure factors in a generalized phonon series

$$S = S_{\mathrm{el}} + \sum_{n=1}^{\infty} S_n. \tag{6.46}$$

6.5.1. Elastic term

Very close to the reciprocal lattice vectors $\boldsymbol{Q}_n$, i.e. $\boldsymbol{q} = \boldsymbol{Q}_n + \Delta\boldsymbol{q}$ with $\Delta\boldsymbol{q} \ll 2\pi/a$ and $\omega \ll \omega_0$, the structure factors are dominated by the long wave length modes. Therefore, the continuum model is directly applicable, and the structure factors are identical to the shape functions defined in (6.23)–(6.25):

$$S_{\mathrm{el}}(\boldsymbol{q}) = \Gamma(\Delta\boldsymbol{q}; \boldsymbol{Q}_n), \tag{6.47}$$

$$S_{\mathrm{el}}(\boldsymbol{q}, \omega) = \Gamma(\Delta\boldsymbol{q}, \omega; \boldsymbol{Q}_n), \tag{6.48}$$

$$S_{\mathrm{i,el}}(\boldsymbol{q}, \omega) = \Gamma(\omega; \boldsymbol{Q}_n). \tag{6.49}$$

The continuum limit is the zeroth order of the structure factors. Concerning neutron scattering experiments (Sec. 4.4), the elastic term is identified with elastic scattering, because it is associated with small momentum and energy transfer, in contrast to the rest which is called inelastic.

6.5.2. One-phonon term

Away from the reciprocal lattice vectors only few partitions $(n_i)_i$ contribute significantly to the structure factors. Because of

$$\left(\frac{\boldsymbol{q}^2\sigma^2\omega_0^2}{2d\omega_{\boldsymbol{Q}/2}^2}\right)^2 < \frac{\boldsymbol{q}^2\sigma^2\omega_0^2}{2d\omega_{\boldsymbol{Q}}^2}, \tag{6.50}$$

[7] The factor N^{-1} in (6.45) disappears with the transition towards an infinite system, which leads to the substitution of the sum by an integral.

[8] Using the analogy to path integrals, this is the case of weak coupling in quantum field theory, e.g. the electromagnetic interaction.

the lowest weights are obtained for partitions with a single large $\boldsymbol{Q}_{i_0} \approx \boldsymbol{q}$, $n_{i_0} = 1$ and the difference $\boldsymbol{q} - \boldsymbol{Q}_{i_0}$ is 'filled up' with smaller $\boldsymbol{Q}_i \ll \boldsymbol{q}$. The total weight is the multiplication of the weights for the two processes. For the weight of $\boldsymbol{Q}_{i_0}$ (6.45) is used. The weights of $\boldsymbol{q} - \boldsymbol{Q}_{i_0}$ are given by the shape functions. The one-phonon term is the sum over all possibilities:

$$S_1(\boldsymbol{q}) = \frac{\boldsymbol{q}^2\sigma^2}{2dN} \sum_{\boldsymbol{Q}\neq\boldsymbol{0}} \frac{\omega_0^2}{\omega_{\boldsymbol{Q}}^2} \Gamma(\boldsymbol{q} - \boldsymbol{Q}; \boldsymbol{Q}). \tag{6.51}$$

$$S_1(\boldsymbol{q}, \omega) = \frac{\boldsymbol{q}^2\sigma^2}{2dN} \sum_{\boldsymbol{Q}\neq\boldsymbol{0}} \frac{\omega_0^2}{\omega_{\boldsymbol{Q}}^2} \Gamma(\boldsymbol{q} - \boldsymbol{Q}, \omega - \omega_{\boldsymbol{Q}}; \boldsymbol{Q}). \tag{6.52}$$

$$S_{\mathrm{i},1}(\boldsymbol{q}, \omega) = \frac{\boldsymbol{q}^2\sigma^2}{2dN} \sum_{\boldsymbol{Q}\neq\boldsymbol{0}} \frac{\omega_0^2}{\omega_{\boldsymbol{Q}}^2} \Gamma(\omega - \omega_{\boldsymbol{Q}}; \boldsymbol{Q}). \tag{6.53}$$

In contrary to the usual theory [113, 164], the one-phonon term is not necessarily sharp, but broadened – with the characteristic line shape given by the shape function Γ. Nevertheless it corresponds to momentum and energy transfer in neutron scattering of $\Delta\boldsymbol{p} \approx \hbar\boldsymbol{Q}$ and $\Delta E \approx \pm\hbar\omega_{\boldsymbol{Q}}$ respectively. One can say: In a one-phonon scattering event, a phonon with wave vector and frequency within the range of the shape function from the dispersion relation is generated or annihilated.

6.5.3. Multi-phonon terms

The generalization to higher terms (two-phonon, etc.) is straight-forward. The n-th term of the structure factor is given by those partitions $(n_i)_i$ having exactly n large $\boldsymbol{Q}_i$. We introduce the dispersion function

$$D = \frac{\boldsymbol{q}^2\sigma^2\omega_0^2}{2d\,\omega^2} \left(\frac{a}{2\pi}\right)^d \int_{-\infty}^{\infty} \mathrm{d}\boldsymbol{Q}\, \delta(\boldsymbol{q} - \boldsymbol{Q})[\delta(\omega - \omega_{\boldsymbol{Q}}) + \delta(\omega + \omega_{\boldsymbol{Q}})], \tag{6.54}$$

where $\omega_{\boldsymbol{Q}} \approx \omega$ has been used, because Γ is a narrow peak centered at the origin. (6.54) is an integral of delta functions positioned along the dispersion relation. Away from the reciprocal lattice vectors, the n-phonon term can be written in the following short form:

$$S_n = S_{\mathrm{el}} * D * \ldots * D = \tfrac{1}{n} S_{n-1} * D. \tag{6.55}$$

The symbol $*$ denotes convolution. S_n is identified with n-phonon scattering. For $n \geq 2$ it does not correspond to sharp peaks but generates

a relatively homogeneous background proportional to $\boldsymbol{q}^2\sigma^2/\omega^2$ within the modified dispersion relation

$$\omega_{\boldsymbol{Q}} = 2n\omega_0\sqrt{\sin^2(Q_1 a/2n) + \ldots + \sin^2(Q_d a/2n)} \tag{6.56}$$

and a sharp decrease beyond. For example, the two-phonon scattering has momentum transfer $\Delta\boldsymbol{p} \approx \hbar(\boldsymbol{Q}_1 + \boldsymbol{Q}_2)$ and energy transfer $\Delta E \approx \hbar(\pm\omega_{\boldsymbol{Q}_1} \pm \omega_{\boldsymbol{Q}_2})$. Again note that the generalized phonon expansion is not valid close to the reciprocal lattice vectors. The regions of validity of the phonon expansion and the continuum limit are complementary.

We remark that most of the features found here are generic and similarly present also in other systems with the same dimensions, with or without harmonic interactions. Especially the peak shapes and the long time/large distance limit of the displacement correlation functions do not depend on the choice of system. However, the dispersion relation and thus the position and course of the peaks will of course strongly depend on the form of the interaction potentials. The influence of dimensionality is seen only in the shape of the peaks at the reciprocal lattice points and along the dispersion relation.

Chapter 7.

Dynamics of Fibonacci chains

In order to investigate the interplay of phonons and phason modes on an elementary level, we resort to various one-dimensional model systems. The main observables are the structure factors, which are extracted from molecular dynamics simulations. We compare the results for periodic and quasiperiodic, harmonic and anharmonic systems. By observing the particle motion in real space, new types of solitons and localized breathers are found.

Parts of the work in this chapter have been conducted in collaboration with Steffen Sonntag and Hansjörg Lipp, who in their diploma theses studied the structure factors [163] and real space excitations [112] of one-dimensional Fibonacci chains. Here we summarize and extend the work by focusing on the differences between the chain models. The results on the structure factors appeared in a joint publication [44].

7.1. Motivation

What is the influence of quasiperiodicity on the structure factors? Two basic effects play a role. One is static in nature and the other dynamic. Let us begin with the static one: The ideal quasiperiodic tiling has a diffraction image with a dense set of Bragg peaks located on a Fourier module with dimension bigger than the space dimension (Sec. 2.4). The number of peaks with a given intensity varies greatly and increases rapidly with decreasing intensity. Intrinsic structural disorder leads to additional diffuse scattering and modifies especially the intensity of the weak peaks. These effects are most easily studied with the static structure factor (i.e. the diffraction image) at low temperature, where they are not overlayed with dynamic effects of the atomic motion. Its investigation is necessary for structure determination and analyzing the statistics of (frozen in) defects, e.g. fluctuations of the de Bruijn surface. Because of static (mostly X-ray)

diffraction studies one can say that today, 25 years after their discovery, the structure of many quasicrystals is well understood.[1]

On the other side the dynamic influence of quasiperiodicity is the possibility of phason flips and phason modes (Sec. 4.1). These local rearrangements are much less understood than the static structure, because they are extremely hard to detect. Due to their stochastic nature, they have no clear signature in scattering experiments. Only under special conditions rearrangements of atom clusters are observable with electron microscopy [1, 41]. Although phason flips play a role in many physical properties (chapter 4), the atomic processes are not precisely known.

A motivation for the present study has been a series of experiments by Coddens and coworkers [25–27, 115], who showed that the signature of phason flips is found in quasielastic energy-resolved neutron scattering. They observed an anomalous q-dependence for icosahedral quasicrystals, which was interpreted as correlated simultaneous jumps of several atoms [26]. However the results are difficult to interpret and not yet fully understood. Other experiments measuring the coherent structure factors of icosahedral quasicrystals show well defined acoustic phonon modes at small wave-vectors [15] and dispersionless broad optic bands at larger wave vectors [16]. The cross-over between the two regions is very sharp.

Theoretically, phason flips have not been studied in detail. The reason is that in realistic three-dimensional models the flip frequency is too low. Furthermore, the flip frequency depends strongly on the structure model and the interactions chosen for the study. Therefore we decided to resort to toy models and for a start studied one-dimensional quasiperiodic chains with potentials allowing for phason flips. Later, we will extend some of the ideas to a similar two-dimensional model (chapter 9). As far as we know, this is the first attempt to study phason flips on an 'atomistic' scale including the full phonon dynamics.

The study of one-dimensional chains is also worthwhile from another point of view: The influence of dimensionality on the coherent structure factors and the extension of the phonon expansion to low-dimensional systems is not covered by the literature, and thus interesting in itself (chapter 6). Although structure factors play such a central role in the dynamics of solids, not much seems to be known about their exact forms for

[1] This was the consensus during a discussion at a conference in Tel Aviv (Israel), October 2007 celebrating the 25th anniversary of the quasicrystal discovery.

one-dimensional chains. Even for the simple harmonic periodic chain few articles exist [42, 54, 142, 182].

We note that up to now only partial calculations of the coherent structure factor of quasiperiodic model systems have been published. Amongst them are the perfect one-dimensional Fibonacci chain [4], Fibonacci chains disordered by static phason fields [130], and three-dimensional tilings [64]. In these studies the dynamical matrix is diagonalized, which is a purely analytic method and yields the phonon dispersion relations only. The results are highly structured excitation spectra with a hierarchical system of gaps [4]. The influence of anharmonicities, especially the dynamics of phason flips and the interplay with phonons has not been taken into account.

7.2. Model systems

We want to study chains of N identical particles of mass $m = 1$ with next-neighbor interactions. The Hamiltonian can be written in the form

$$\mathcal{H} = \sum_{j=1}^{N} \frac{p_j^2}{2} + V(x_j - x_{j+1} - a_j). \tag{7.1}$$

As a simple model for a quasiperiodic system we consider the well-known one-dimensional Fibonacci chain (Sec. 3.1). The dynamic Fibonacci chain (DFC) is defined by the choices $a_j \equiv a_0 = \tau^3$ for the equilibrium distances and $V(x) = x^4 - 2x^2$ for the interaction potential.[2] The latter is a double-well potential with minima at ± 1 and a potential hill of height $\Delta E = 1$ (Fig. 7.1). Because neighboring particles sit in either of the potential minima, the next-neighbor distances $L = a_0 + 1$ and $S = a_0 - 1$ are possible. They fulfill the constraint $L/S = \tau$ of the Fibonacci chain.

The DFC shows two types of elementary excitations: Phonon vibrations around the potential minima and phason flips interchanging L and S. At very low temperatures only phonons are excited. Phason flips have to be activated thermally. With its neighbors at rest, the potential hills of both neighbors are in perfect superposition. The activation energy of a particle for a phason flip is then $2\Delta E$. However, this value is lowered when the neighbors assist during the flip by moving collectively in a way to create a non-perfect superposition of the potential hills. Since the potential energy

[2]The choice of a_0 makes $V(x)$ a simple form. $\tau = (\sqrt{5}+1)/2$ is the golden number.

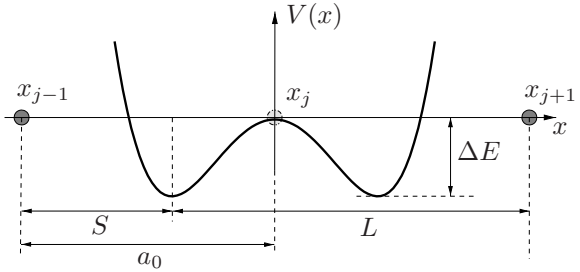

Figure 7.1: Double-well potential $V(x) = x^4 - 2x^2$ of the dynamic Fibonacci chain. The equilibrium distances S and L are energetically degenerate.

of a L and a S distance is energetically degenerate, the total potential energy of the chain is invariant under phason flips.

The occurrence of phason flips makes nonlinearity an intrinsic feature of the DFC and an analytic treatment of the dynamics impossible. To understand the influence of the nonlinearity, we study four model systems in this chapter with increasing dynamical complexity:

- Harmonic periodic chain (HPC):
  $V_{\mathrm{HPC}}(x) = 4x^2$ and $a_j = a = 2\sqrt{5}$.
- Harmonic Fibonacci chain (HFC):
  $V_{\mathrm{HFC}}(x) = 4x^2$ and $a_j = L$ or S according to the Fibonacci sequence.
- Dynamic Fibonacci chain (DFC):
  $V_{\mathrm{DFC}}(x) = x^4 - 2x^2$ and $a_j = \tau^3$.
- Asymmetric Fibonacci chain (AFC):
  $V_{\mathrm{AFC}}(x) = V_{\mathrm{DFC}} + \chi(x^2-1)^2(\epsilon x + x^2/2 - 1/2)$ and $a_j = \tau^3$ with parameters $\chi \in [0,1]$ and $\epsilon = \pm 1$.

The simplest system is of course the HPC, which is studied as reference system. The HFC consists of particles arranged on the Fibonacci chain, interacting with the same harmonic potentials as the HPC. It is used to observe the influence of quasiperiodicity, while leaving the potential unchanged. In the DFC Phason flips are possible, which alters the dynamics. In the case of the AFC the particles in the two potential minima have different eigenfrequencies. The parameters χ and ϵ determine the degree

of asymmetry. The potentials of the HPC, HFC, and DFC are chosen to be identical in harmonic approximation. The average particle distance a is the same for all four systems. For the Fibonacci chain the occurrence probabilities for L and S are given by τ^{-1} and τ^{-2}, hence $a = 2\sqrt{5}$.

In order to solve the equations of motions we use molecular dynamics (MD) simulations. The only external parameter of the simulation is the temperature T. We fix the Boltzmann constant at $k = 1$.

7.3. Structure factors

7.3.1. Harmonic periodic chain

The harmonic periodic chain (HPC) is used as reference system to test our algorithms. We begin with the static structure factor, which can be calculated analytically. From the literature [182] we get

$$\sigma_l^2(t) = \sigma^2 \left[l + \frac{1}{2} \int_0^{2\omega_0 t} J_{2l}(s)(2\omega_0 t - s)\,\mathrm{d}s \right]. \tag{7.2}$$

Inserting this in (6.5) gives a power series with the result

$$S(q) = \frac{\sinh(q^2\sigma^2/2)}{\cosh(q^2\sigma^2/2) - \cos(qa)}. \tag{7.3}$$

Close to the reciprocal lattice points at $q_n = 2\pi n/a$, the static structure factor is a Lorentzian with a rapidly increasing width for larger wave vectors given by (6.27). In Fig. 7.2 we compare the analytic result (7.3) with the MD simulation. Both are in perfect agreement over the full range of values (seven order of magnitude).

For the incoherent structure factor $S_{\mathrm{i}}(q,\omega)$ the phonon expansion gives an (elastic) Lorentzian peak $\Gamma(\omega - \omega'; Q)$ at $\omega = 0$, (6.28). To obtain the one-phonon part, we substitute the sum in (6.53) by an integral (note the transformation $Q \to \omega'$ in the integration variable):

$$S_{\mathrm{i},1}(q,\omega) = \frac{q^2\sigma^2}{\pi} \int_0^{2\omega_0} \mathrm{d}\omega' \frac{\omega_0^2}{\omega'^2} \frac{1}{\sqrt{(2\omega_0)^2 - \omega'^2}} \Gamma(\omega - \omega'; Q). \tag{7.4}$$

At very low temperatures, the shape function is $\Gamma(\omega - \omega'; Q) = \delta(\omega - \omega')$ and thus for $0 \ll \omega \leq 2\omega_0$:

$$S_{\mathrm{i},1}(q,\omega) = \frac{q^2\sigma^2}{\pi} \frac{\omega_0^2}{\omega^2\sqrt{(2\omega_0)^2 - \omega^2}}. \tag{7.5}$$

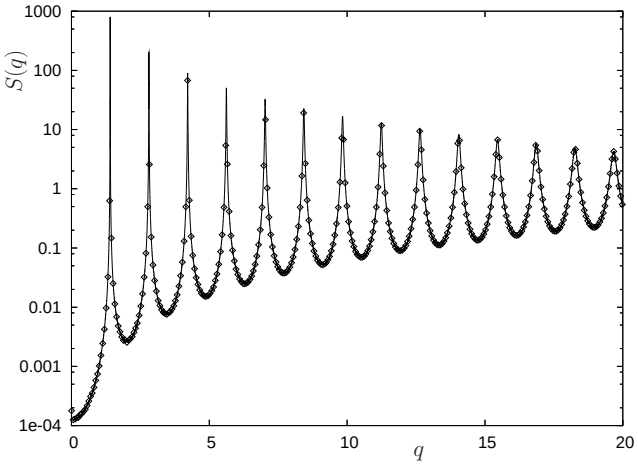

Figure 7.2: Static structure factor $S(q)$ of the HPC for the temperature $T = 0.02$. The symbols mark the data from MD simulation with 1000 particles, the line results from the analytic formula (7.3).

There is a diverging peak at $\omega = 2\omega_0$. The influence of temperature is a broadening by convolution with $\Gamma(\omega - \omega'; Q)$ making the peak finite. Unfortunately, higher phonon terms cannot be calculated analytically. The n-phonon term is a homogenous background proportional to q^2/ω^2 for ω-values with $2(n-1)\omega_0 \leq \omega \leq 2n\omega_0$ and a more or less (depending on the temperature) sharp edge at $\omega = 2n\omega_0$.

Since the variables T and q appear only as the combination q^2T in (6.7) and (7.2), it suffices to examine S_i at a fixed wave vector for different temperatures. We choose $q = \pi/a$ arbitrarily. The incoherent structure factor obtained from MD and the numerical integration of (6.7) are shown in Fig. 7.3 for a broad range of temperatures. At low temperatures the elastic peak is seen at $\omega = 0$, as well as the one-phonon peak, two-phonon edge, three-phonon edge, etc. at $\omega = 2\omega_0 \approx 5.7$, $\omega = 4\omega_0 \approx 11.3$, $\omega = 6\omega_0 \approx 17.0$. Note that the multi-phonon contributions decay rapidly (logarithmic scale). At higher temperatures the curve smoothes and approaches a Gaussian.

The coherent structure factor $S(q, \omega)$ is shown in Fig. 7.4. For a low temperature of $T = 0.01$ a one-phonon, two-phonon, and very weakly a

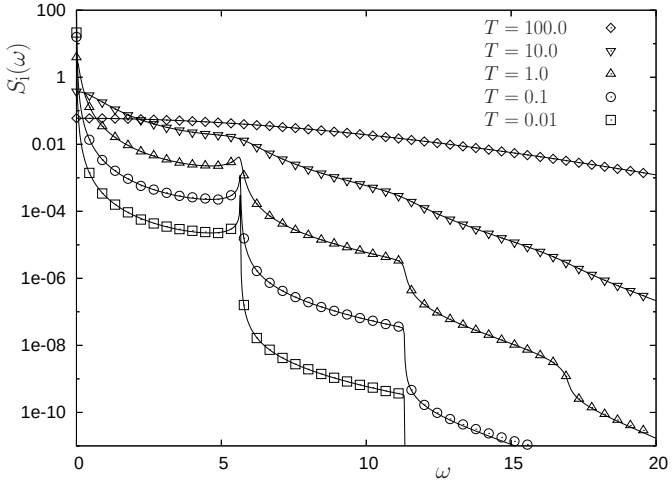

Figure 7.3: Incoherent structure factor $S_{\rm i}(q,\omega)$ of the HPC for $q = \pi/a$, and different temperatures. The symbols mark the data from MD simulations with 1000 particles, the lines the result from the numerical evaluation of the analytic formula (6.7). The peaks and edges are at integer multiples of $2\omega_0 = 2\sqrt{8}$.

three-phonon branch is observed. The one-phonon part has a Lorentzian line shape and follows the dispersion relation, broadening at higher q-values with width proportional to q^2T, (6.52). The multi-phonon branches follow the modified dispersion relations (6.56). In Fig. 7.4(b) the comparison of MD simulation (left side) and analytic formula (6.6) (right side) is shown. Since the temperature is higher than in Fig. 7.4(a), the one-phonon branch is broader. It is surprising that the accuracy of both calculation methods (12 orders of magnitude) is only limited by the internal floating point precision of the processor used.

For all structure factors the simulations and analytic formulas show perfect agreement. We conclude that MD simulations are well-suited for calculating the structure factors of the one-dimensional chains. Although we integrate the equations of motions with a good precision only on a short time scale using the simple Verlet-algorithm, the statistics extracted from the trajectories are correct. We proceed studying the Fibonacci chain in the next section.

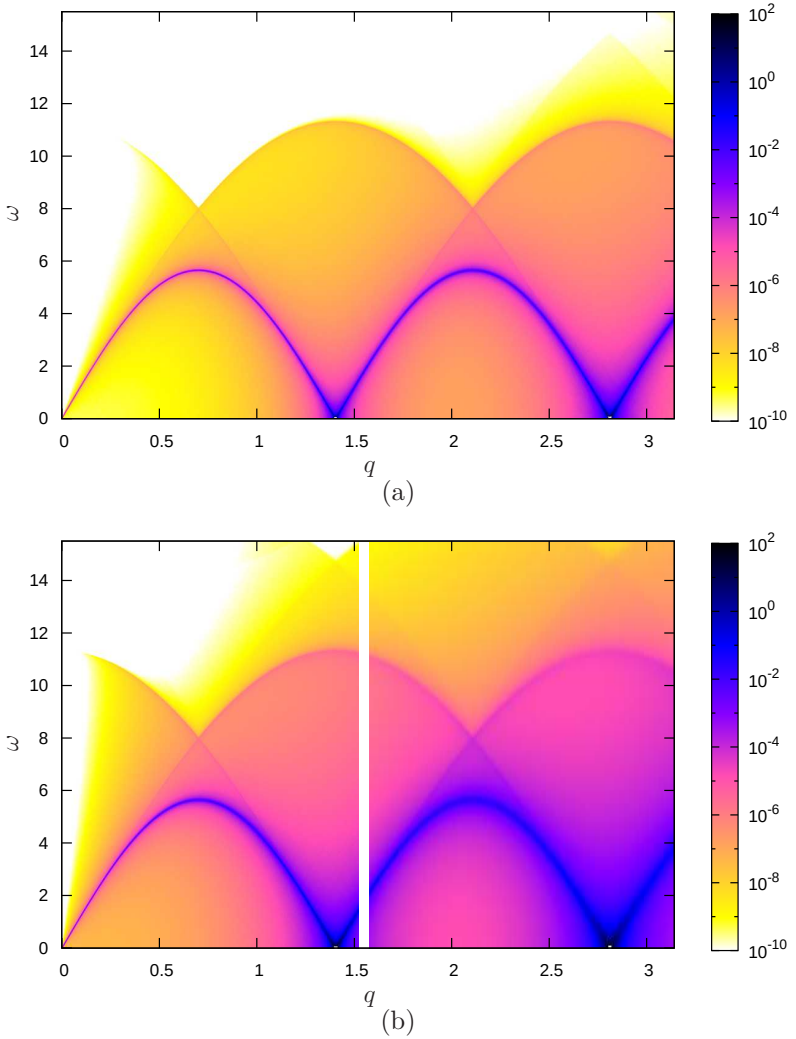

Figure 7.4: Coherent structure factor $S(q, \omega)$ of the HPC with 6500 particles from MD simulation. The temperatures are $T = 0.01$ (a) and $T = 0.1$ (b). One-phonon, two-phonon, and three-phonon branches are observed originating from the reciprocal lattice points $2\pi n/a$. In (b) the output from MD (left side) is compared to the numerical evaluation of (6.6) (right side).

7.3.2. Harmonic Fibonacci chain

The harmonic Fibonacci chain (HFC) is obtained by changing the interparticle equilibrium distances of the HPC to those the Fibonacci sequence with separations L and S (while leaving the interaction potential unchanged). In the static structure factor of the HFC (Fig. 7.2) Lorentzians are positioned at the reciprocal lattice points with varying intensity. At zero temperature (6.5) gives the Fourier transform of the static Fibonacci chain

$$S(q,\omega) = \delta(\omega) \sum_l e^{-iqR_l}, \tag{7.6}$$

which is well known [110]. It consists of a dense set of delta peaks at the reciprocal lattice points $q = \frac{2\pi}{a}(h + \tau h')$ with integers h, h'. The equilibrium positions of the particles are denoted by

$$R_l = \begin{cases} \sum_{j=1}^{l} a_j, & l > 0 \\ 0, & l = 0 \\ \sum_{j=l}^{-1} a_j, & l < 0 \end{cases}. \tag{7.7}$$

For a finite temperature $T = 0.02$, the static structure factor is shown in Fig. 7.5. In the region of small q-values a large number of narrow Lorentzians occur. With increasing q their width increases and the stronger ones hide the weaker ones. Comparing the position of the strong peaks and ignoring the change of their widths (and heights), it is found that parts of $S(q)$ are self-similar (deflation factor $\Delta q_1/\Delta q_2 = \tau^3$), which is typical for quasicrystals. It is interesting to note that there are regions with very few peaks. They are positioned around multiples of $q = \pi$ and correspond to a separation of $L - S = 2$ in real space.

Since the incoherent structure factor is a function of the single particle motion only, it does not depend on the equilibrium distances of the particles but only the interaction potential. Hence, the incoherent structure factor of the HPC and of the HFC are identical. For the coherent structure factor the interparticle distances become important. As shown in Fig. 7.6, $S(q,\omega)$ consists of many different branches all following the one-phonon dispersion relation. Relative to each other the branches are displaced in the q direction. They start at the reciprocal lattice points with the intensity of the respective elastic peak. Weak two-phonon branches are also found.

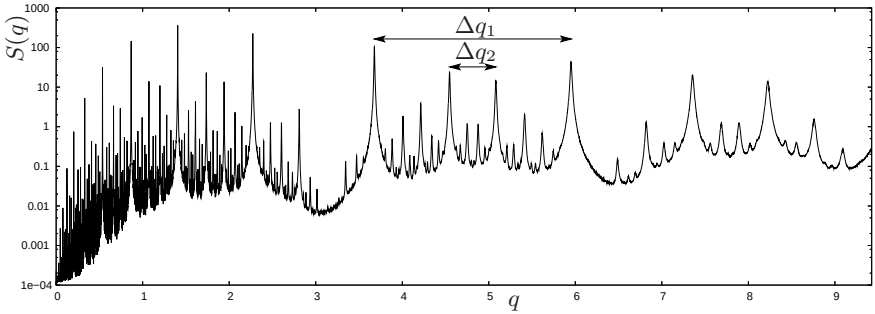

Figure 7.5: Static structure factor $S(q)$ of the HFC from a MD simulation with 2000 particles at the temperature $T = 0.02$.

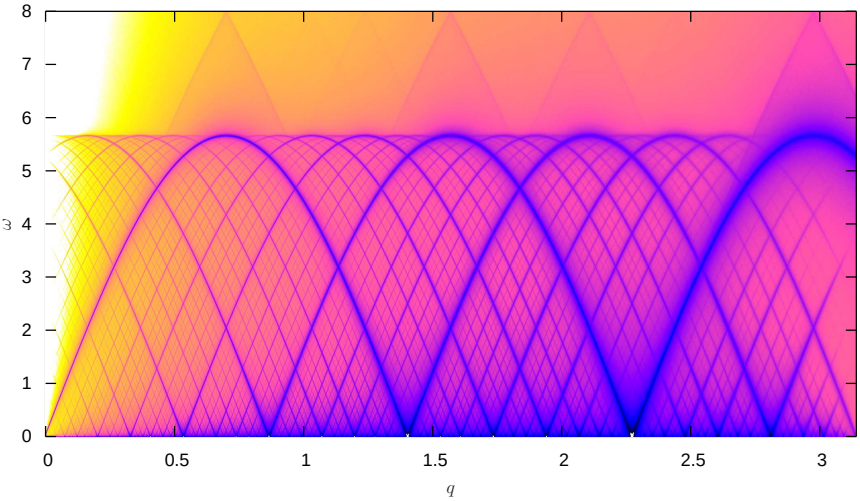

Figure 7.6: Coherent structure factor $S(q, \omega)$ of the HFC with 13000 particles for $T = 0.02$. It consists of a dense set of phonon branches starting from the reciprocal lattice points.

Towards $q = \pi$, all weak one-phonon branches vanish. Only the strong one starting from the elastic peak at $q = \tau q_0 \approx 2.27$ remains.

To understand the effect of quasiperiodic order on $S(q, \omega)$, we compare three situations in Fig. 7.7: (a) the HFC (over a larger q-range), (b) a periodic LS-chain (periodicity $L+S$), and (c) a randomized chain, which has the same occurrence frequencies of L and S as the HFC, but no preferred order of L and S. We draw several conclusions from the comparison: (i) The dispersion relation is determined by the average particle distance a only. It is the same in (a) and (c), but (slightly) different in (b). (ii) As expected, the positions of the reciprocal lattice points and the phonon branches is a consequence of the arrangement of L and S. Sharp peaks at the reciprocal lattice points are only observed in the case of long-range order, not in the randomized chain. (iii) The region with few phonon branches (multiples of $q = 2\pi/(L - S)$) are not characteristic for the quasicrystal. Around these regions the influence of (dis)order is only weak and the modulation of the phonon branch strengths is similar in (a)–(c). An explanation for this behavior is not known. (iv) There are vertical striped in the periodic LS-chain (Fig 7.7(b)), whose origin is also not understood.

7.3.3. Dynamic Fibonacci chain

MD simulations are the only possibility to obtain the structure factors with high accuracy for anharmonic chains.[3] The incoherent structure factors of the DFC and of the HFC/HPC differ remarkably as shown in Fig. 7.8. The comparison leads to the following conclusions: (i) At a fixed temperature, there are ω-ranges where the curve for the DFC lies below the curve for the HFC/HPC and vice versa. Since we have $\int S_{\mathrm{i}}(q, \omega)\, \mathrm{d}\omega = 1$, the area between the two curves vanishes. (ii) At very low T and $\omega < 2\omega_0 \approx 5.7$ the curves of the DFC and the HFC/HPC are indistinguishable in logarithmic scale except for two small bumps. The bumps are a consequence of the anharmonicity of the interaction potential and unrelated to the phason flips. At larger ω values the multi-phonon edges have different heights. (iii) Above $T = 0.1$ the one-phonon peak and the multi-phonon edges in the curves for the DFC broaden and weaken considerably faster than in the curves for the HFC/HPC. They disappear at $T = 1.0$. (iv) No additional

[3] There are analytic approaches like e.g. the Mori formalism [127, 128], which makes use of projection operators and leads to continued fractions [140–142]. In general, analytic methods are extremely laborious and converge slowly.

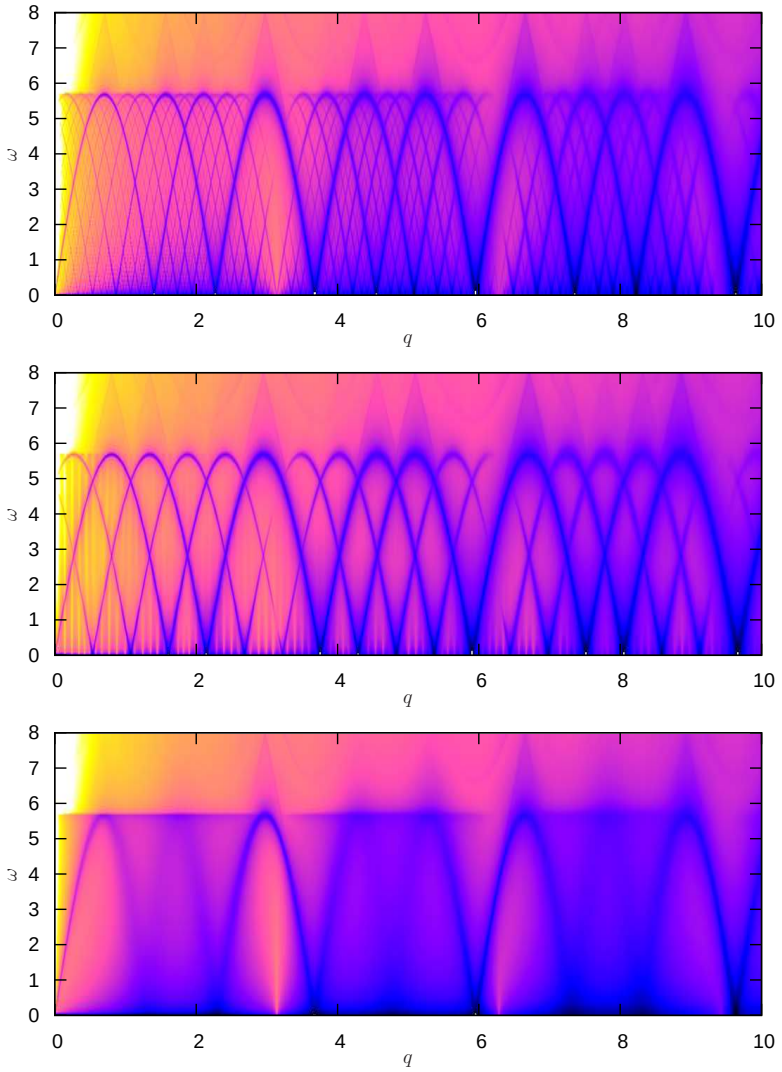

Figure 7.7: The influence of quasiperiodicity is seen by comparing $S(q, \omega)$ for (from top to bottom) (a) the HFC, (b) a periodic LS-chain, and (c) a randomized chain of L and S next-neighbor distances.

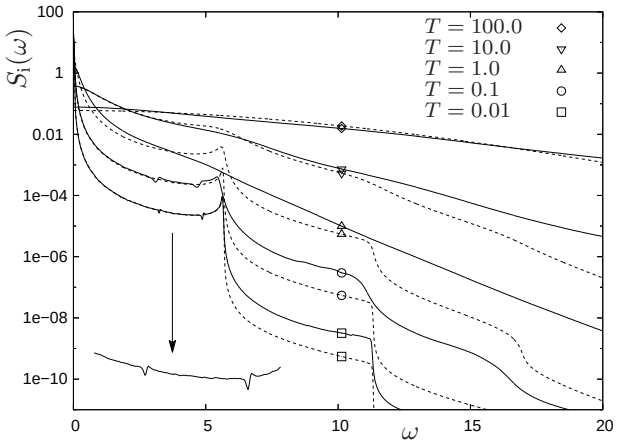

Figure 7.8: Incoherent structure factor $S_i(q, \omega)$ of the DFC (solid) and the HFC/HPC (dashed) for $q = \pi/a$.

peaks or edges occur at any temperature.

Similar conclusions hold for the coherent structure factor. $S(q, \omega)$ for the DFC looks similar to $S(q, \omega)$ for the HFC except that the branches broaden more quickly with temperature. To compare the broadening, we examine a cut through $S(q, \omega)$ at $\omega = 1.0$. Three cuts at $T = 0.05$, 0.2, and 0.3 are shown in Fig. 7.9. A one-phonon branch is located inside the cut resulting in a peak with approximate Lorentzian line shape as indicated by the fits in the figure. Only for low temperatures the line shape deviates from a Lorentzian, which is seen at the base of the peak for $T = 0.05$. The width of the Lorentzians is shown as a function of temperature in Fig. 7.10. In the case of the HFC the width increases linearly with temperature as expected for harmonic interactions (Sec. 6.3).[4] For the DFC the increase is exponential and can be explained by thermal activation of phason flips contributing significantly to the broadening.

There is one aspect of the DFC that has been ignored up to now. Due

[4]At low temperatures there is a deviation from linearity. This is an artefact from the calculation method. As explained in Sec. 5.4.1 the structure factor is convoluted with a Gaussian to compensate for the finite simulation time. The observed offset is generated by the (narrow) Gaussian. The convolution with the Gaussian is also responsible for the fact that the cuts in Fig. 7.9 at low temperature, deviate from Lorentzian shape.

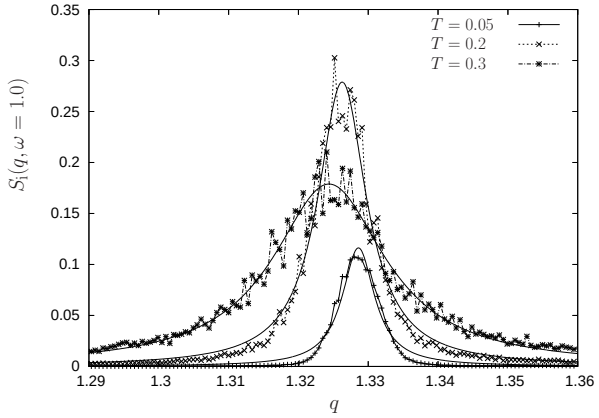

Figure 7.9: Cuts through $S(q, \omega)$ of the DFC for $\omega = 1.0$. The solid curves are fits with Lorentzians.

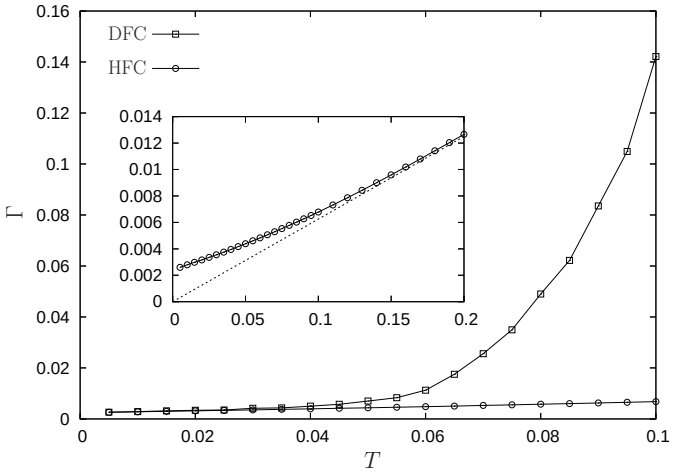

Figure 7.10: Width of the Lorentzian peak of Fig. 7.9 as a function of temperature for the HFC (inset) and the DFC.

to the phason flips, the original perfect quasiperiodic long-range order is slowly destroyed. With increasing simulation time the chain becomes randomized. Although this has no effect on the incoherent structure factor, the coherent structure factors will finally look like Fig. 7.7(c). Most of the details in $S(q,\omega)$ are then lost by the randomization process: The branches will become strongly broadened. However, the time scale necessary for the randomization process is too long to lead to a strong influence even in the case of the longest simulations reported here. For the calculations of the structure factors the randomization can be neglected.

7.3.4. Asymmetric Fibonacci chain

In the asymmetric Fibonacci chain (AFC) the particles interact with the potential $V_{\mathrm{AFC}} = V_{\mathrm{DFC}} + \Delta V$ (Fig. 7.11). The additional term is given by

$$\Delta V(x) = \chi(x^2-1)^2(\epsilon x + x^2/2 - 1/2) \tag{7.8}$$

with the parameters $\chi \in [0,1]$ and $\epsilon = \pm 1$. The potential has been chosen in such a way that the positions of the minima at $x = \pm 1$ are left invariant and the curvature is changed to $V''_{\mathrm{AFC}}(\pm 1) = 8(1 \pm \epsilon\chi)$. In harmonic approximation a particle will perform vibrations with three different eigenfrequencies depending on the next-neighbor configuration SS, SL, LS, or LL. For $\epsilon = 1$ we have $\omega_{\mathrm{LL}} > \omega_{\mathrm{LS}} = \omega_{\mathrm{SL}} > \omega_{\mathrm{SS}}$ and for $\epsilon = -1$ it is $\omega_{\mathrm{LL}} < \omega_{\mathrm{LS}} = \omega_{\mathrm{SL}} < \omega_{\mathrm{SS}}$. The sign change of ϵ corresponds to a mirror operation of V_{AFC} about $x = 0$.

The coherent structure factor for $\chi = 0.1, 0.3, 0.5$ and $\epsilon = \pm 1$ is shown in Fig. 7.12. Band gaps of different widths appear and broaden with increasing values for χ. They are positioned at the frequencies where one-phonon branches intersect each other. Empirically it is observed, that the stronger the bands, the deeper are the gaps. Their positions and widths are different for $\epsilon = 1$ and $\epsilon = -1$. For $\epsilon = 1$ three large and several smaller gaps appear, whereas for $\epsilon = -1$ only one very large, one medium, and several small gaps are found. The band gaps are a consequence of the coexistence of different eigenfrequencies resulting from the asymmetry of the potential. Analogously, band gaps appear in periodic systems with several particles per unit cell and distinct eigenfrequencies.

The gaps are seen more clearly in the density of states (DOS) $D(\omega)$. For comparison we give the DOS of a harmonic chain (HPC or HFC), which

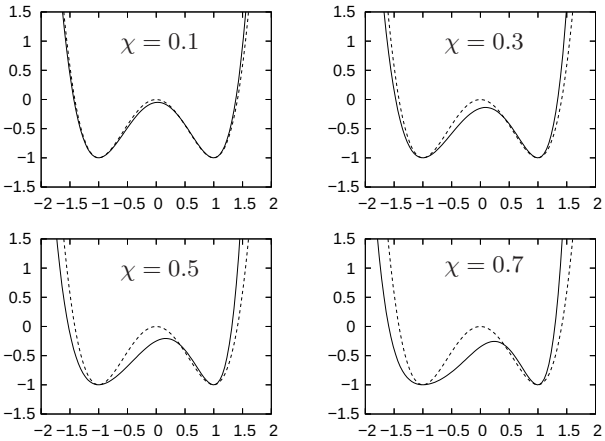

Figure 7.11: Interaction potential $V_{\mathrm{AFC}}(x)$ of the AFC for different values of the parameter χ and $\epsilon = 1$. V_{DFC} is shown with dashed lines.

is obtained from (4.26) and (7.5). It has the simple form

$$D(\omega) = \begin{cases} \dfrac{2}{\pi\sqrt{4\omega_0^2 - \omega^2}}, & 0 < \omega < 2\omega_0 \\ 0, & \omega > 2\omega_0 \end{cases} . \tag{7.9}$$

It can be checked that the DOS of the harmonic chain fits well to the DOS of the AFC for $\epsilon = 0.0$, except for small bumps that originate from the anharmonicity of the potentials. In Fig. 7.12 the DOS of the AFC for different values of χ and ϵ are drawn. The band gaps appear at the same frequencies and have the same widths as in the coherent structure factor.

7.4. Particle motion in real space

7.4.1. Thermal equilibrium

In order to observe the phason flips directly, we study the particle motion in real space. This is done by plotting the particle trajectories as a function of time and the spatial/temporal distribution of the total energy per particle. We begin with the well-known HPC. In Fig. 7.13(a) the particle positions $x_j(t)$ are shown as a function of time. Each particle trajectory

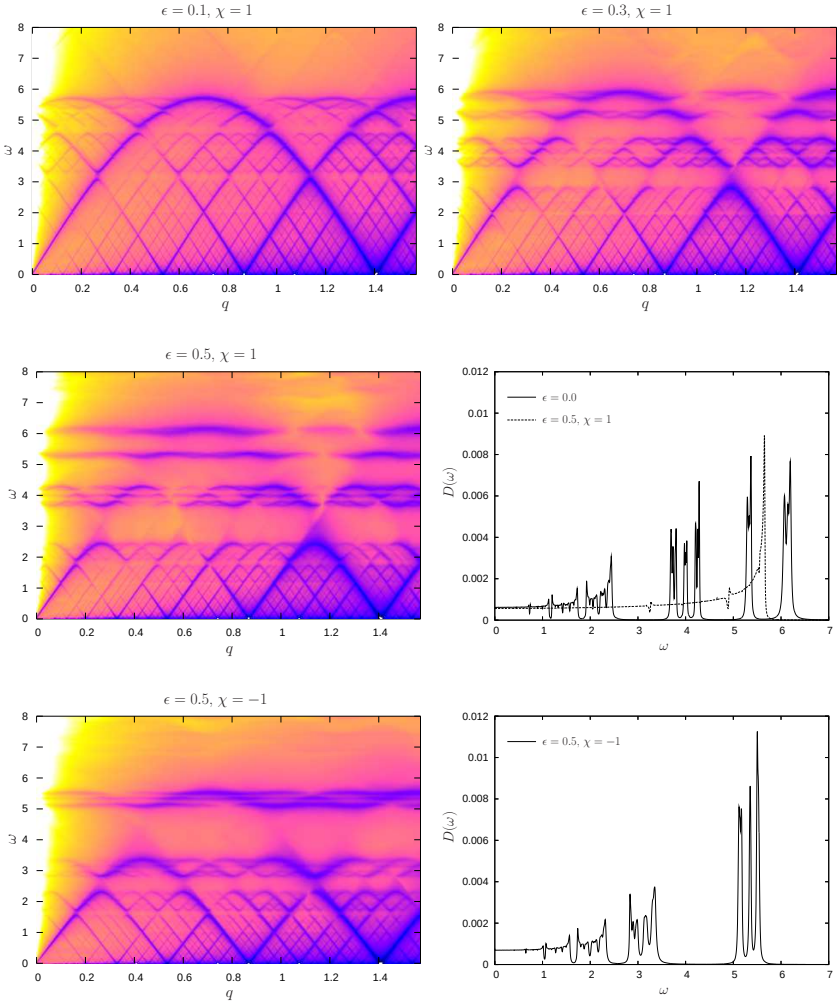

Figure 7.12: Coherent structure factor of the AFC and DOS for different values of χ and ϵ. MD simulations with 6500 particles at $T = 0.01$. Band gaps are characteristic for coexisting eigenfrequencies.

corresponds to one horizontal line.[5] Since the particles move only a little bit around their equilibrium positions, nothing interesting is happening. Next we plot the total energy as a function of time and particle index j. Dark color means higher energy. From Fig. 7.13(b) it is found that the dynamics is dominated by localized modes propagating over long distances. These modes (appearing as straight lines in the figure) correspond to the propagating wave fronts of Sec. 6.2. As we have already discussed there, localized phonons are characteristic for one-dimensional systems.

In the DFC the particle motion is more intricate since additionally phason flips can occur. At the temperature $T = 0.3$ many of them are observed in real space (Fig. 7.13(c)). We mark a flip from L to S with a black diamond and a flip from S to L with a blue triangle. Often a $L \to S$ change and a $S \to L$ change lie close to each other and the sequences LS and SL are interchanged, but this is not always the case. The DFC is flexible enough to compensate for a single flip by slow collective movements of larger parts of the chain via long wave-length phonons.[6] It is also found that the distribution of flips is not uniform. The energy distribution, Fig. 7.13(d) is more irregular than for the HPC. Localized phonons are found, but they propagate with various velocities while fluctuating a lot. This is a direct visual depiction of phonon scattering due to the anharmonicity of the DFC. Thus the fact that the phonons have a finite life time, explains the strong peak broadening in the structure factors. Furthermore, the phason flips are bound to the localized phonons. As shown in Fig. 7.13(e) flips usually occur at positions where the total energy is high, which is understandable from the fact that phason flips require a minimum energy to overcome the potential hill. This energy is provided by the phonon modes.

In the literature on the Fibonacci chain a phason flip is understood as the exchange of a L and a neighboring S particle distance. As we learned above, this is not what is necessarily happening in the DFC. In the following we denote as phason flip every change of L or S. The temperature dependence of the average phason flip frequency ω_{flip} is shown in Fig. 7.14. Phason flips start to appear at about $T = 0.1$. At low T the average phason flip frequency increases exponentially corresponding to a thermal

[5] In order to avoid finite size effects, the simulated chain is bigger than the narrow sections shown in the figures.

[6] Again the fact that many long wave-length phonons are present in one-dimensional systems (as compared to higher dimensions) plays an important role.

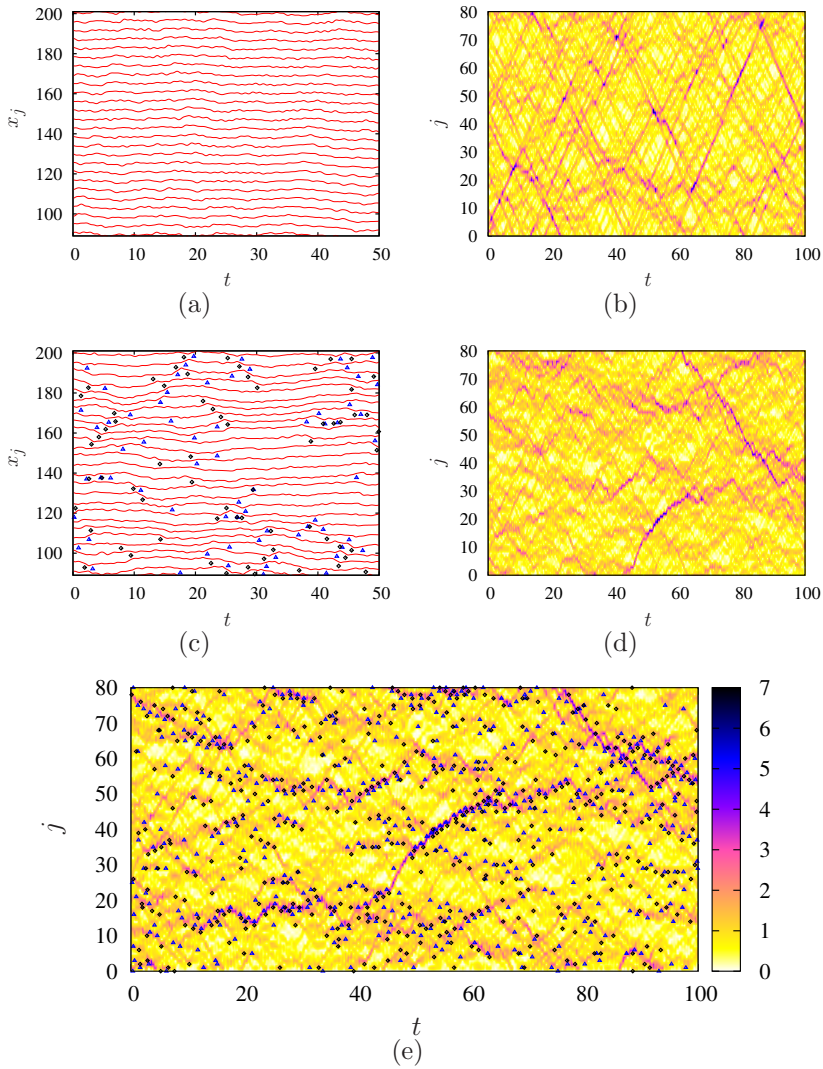

Figure 7.13: Particle motion in the HPC (a) and the DFC (c), (e), as well as the total energy distribution (b), (d) as a function of time t, position x_j, and particle index j. The temperature is $T = 0.3$. Phason flips are marked.

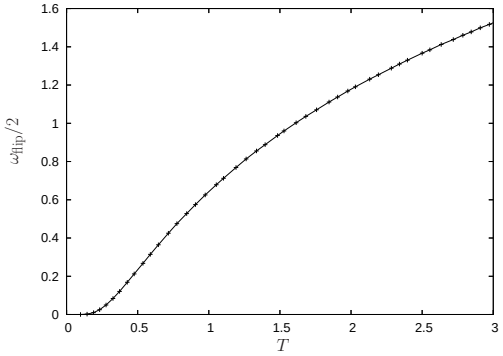

Figure 7.14: Average phason flip frequency as a function of the temperature T. In the temperature range of the figure: $\omega_{\rm flip} \leq \omega_0 \approx 2.83$.

activation process. Additionally, the flip frequency is low compared to the characteristic frequency ω_0. At higher temperatures $T > 0.4$ the average phason flip frequency saturates. However, temperatures close to or above $T = 1.0$ are not physically relevant (see the discussion in Sec. 6.4).

7.4.2. Local excitations

Next, we investigate the response of the chain to local excitations. All particles start on their equilibrium positions with zero velocity. Then at time t_0, one particle j_0 is 'kicked' by setting $v_j(t_0) = v_0\delta_{j,j_0}$.[7] For the HPC this is done in Fig. 7.15(a), (b). The excitation propagates outward uniformly. Although a small fraction of the energy travels faster than $c = a\omega_0$ (not seen in the figure) the main front arrives with the sound velocity. The energy distribution is almost uniform over all particles within the Mach (sound) cone.[8]

We change the potential from $V(x) = 4x^2$ (HPC) to $V(x) = 4x^2 + x^4$ (adding an anharmonic term) without modifying the equilibrium positions of the particles. An excitation in the resulting anharmonic periodic chain (APC) is seen in Fig. 7.15(c), (d). The energy propagation for velocities

[7] A local excitation in the particle positions $u_j(t_0) = u_0\delta_{j,j_0}$ leads to similar results.
[8] The particle trajectories $x_j(t)$ can be solved analytically. They are linear combinations of Bessel functions of the first kind [153].

$v \leq c$ is similar to the HPC, but additionally two fast localized modes propagating with $v = \pm v_0 > c$ are observed. These fast modes advancing the phonon front are identified as kink solitons. They are typical for one-dimensional anharmonic mechanical systems [147]. Although the potential is anharmonic, the energy propagation within the Mach cone is similar to the harmonic case.

In the DFC (Fig. 7.15(e), (f)) the response to the excitation is totally different. The fact that the motion of a particle under a double-well interaction is quite complex[9], leads to different competing dynamical phenomena. Surprisingly, energy propagation is not uniform at all. Most of the energy is concentrated in localized modes, which occur as two types: Kink solitons like in the APC and discrete breathers[10], which are stationary (or slowly moving) standing waves [53]. Contrary to solitons, neighboring particles in breathers have a phase difference close to π. In the vicinity of both – solitons and breathers – phason flips occur. In principle this allows the identification of the modes by depicting the flip positions. A more or less uniform phonon background (light colors) slowly builds up, but it takes a long time for the energy to distribute uniformly.

In Fig. 7.16 we examine another, stronger local excitation in more detail. Shortly after the excitation (1) a breather is formed. It moves slowly through the chain (2) and emits three solitons (3)–(5) losing some energy. The remaining breather continues for a short time (6) and then finally decays by decomposing into lower-energy phonon waves (7). In the long time limit the energy distributes over all particles and contributes to thermal equilibrium. Phason flips in Fig. 7.16 are constrained almost uniquely to solitons and breathers. Solitons propagate with different velocities depending on their energy.

By varying the excitation strength and excitation shape function, we can generate single solitons and breathers. As seen in Fig. 7.17(a), solitons usually pass each other with only little interaction. However it is also found that solitons are not stable. They continuously radiate phonons, therefore losing energy during propagation and slowing down. A soliton cannot exist with energy under a certain minium threshold and will eventually decay.

[9] One can distinguish between (near) harmonic motion in each of the wells, which is getting anharmonic and slower (!) with increasing amplitude, and then for large amplitudes the flip motion over the potential hill.

[10] Breathers also exist in the APC if excited appropriately, although we do not show that here.

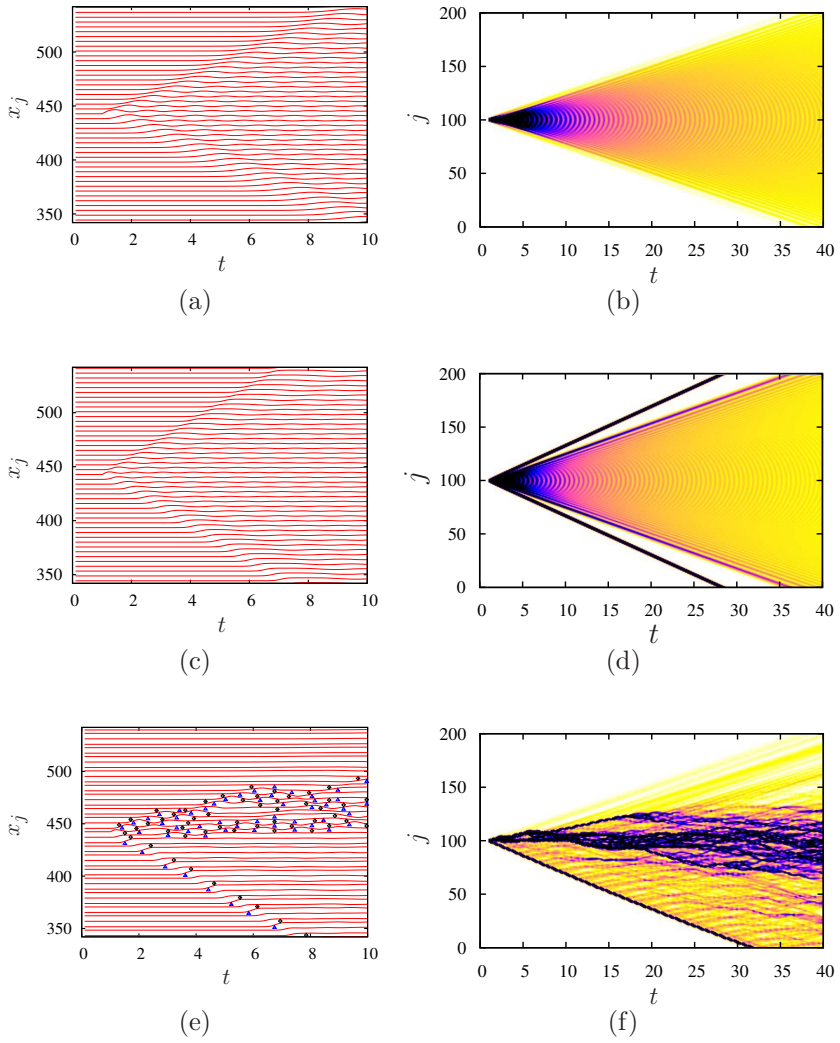

Figure 7.15: Propagation of a local excitation in the HPC (a), (b), the APC (c), (d), and the DFC (e), (f). Solitons are straight dark lines, breathers are irregular. Note the different scales of the axes.

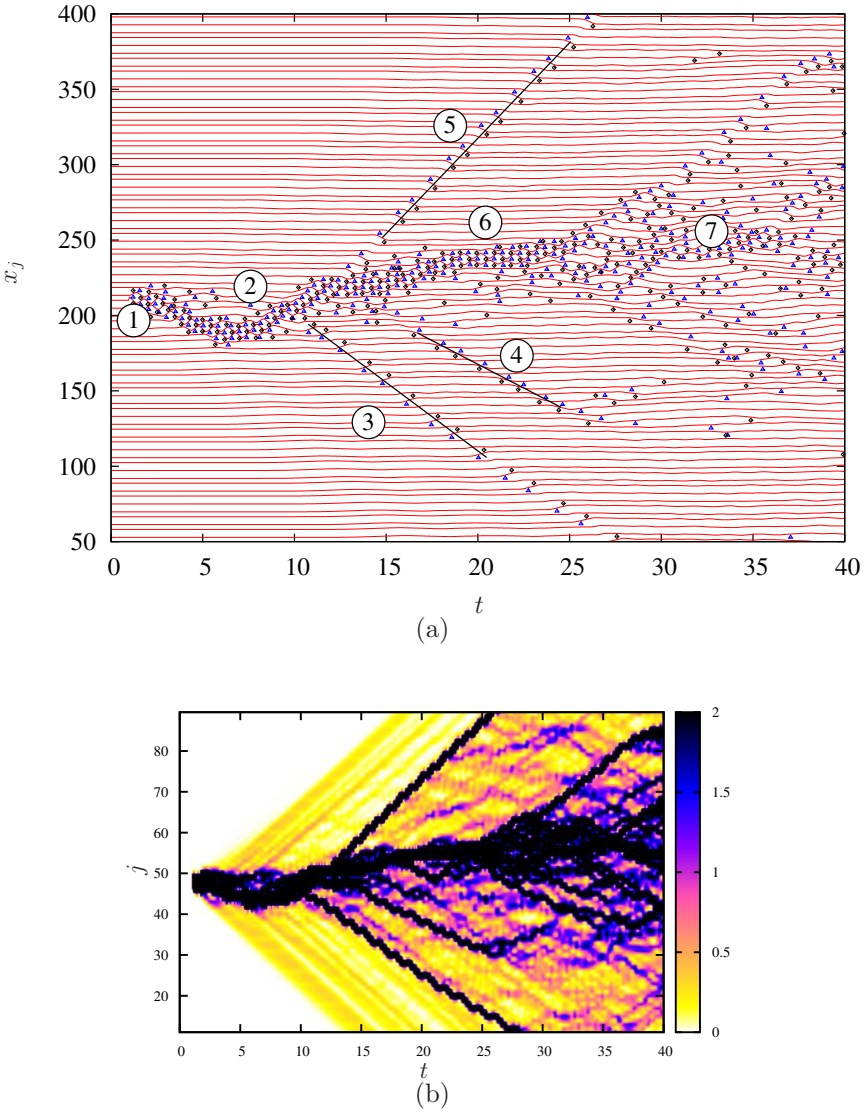

Figure 7.16: Propagation of a strong local excitation in the DFC. The particle trajectories (a) and the energy distribution (b) are shown.

Similar results hold for breathers. In Fig. 7.17(b) a stationary one is shown. After radiating phonons for some time, it disappears at $t = 80$.

Note that the mathematical notion of soliton and breather is reserved for localized modes that do not decay in time. So, strictly speaking our modes are not ideal solitons/breathers. However, compared to the characteristic time of the system, ω_0^{-1}, both are stable and thus we adopt the naming. Especially in the case of high amplitude modes or in periodic chains (e.g. the periodic LS-chain), solitons and breathers are stable over very long times. Fur further details and some analytic solutions of the equation of motions we refer to the diploma thesis of Lipp [112].

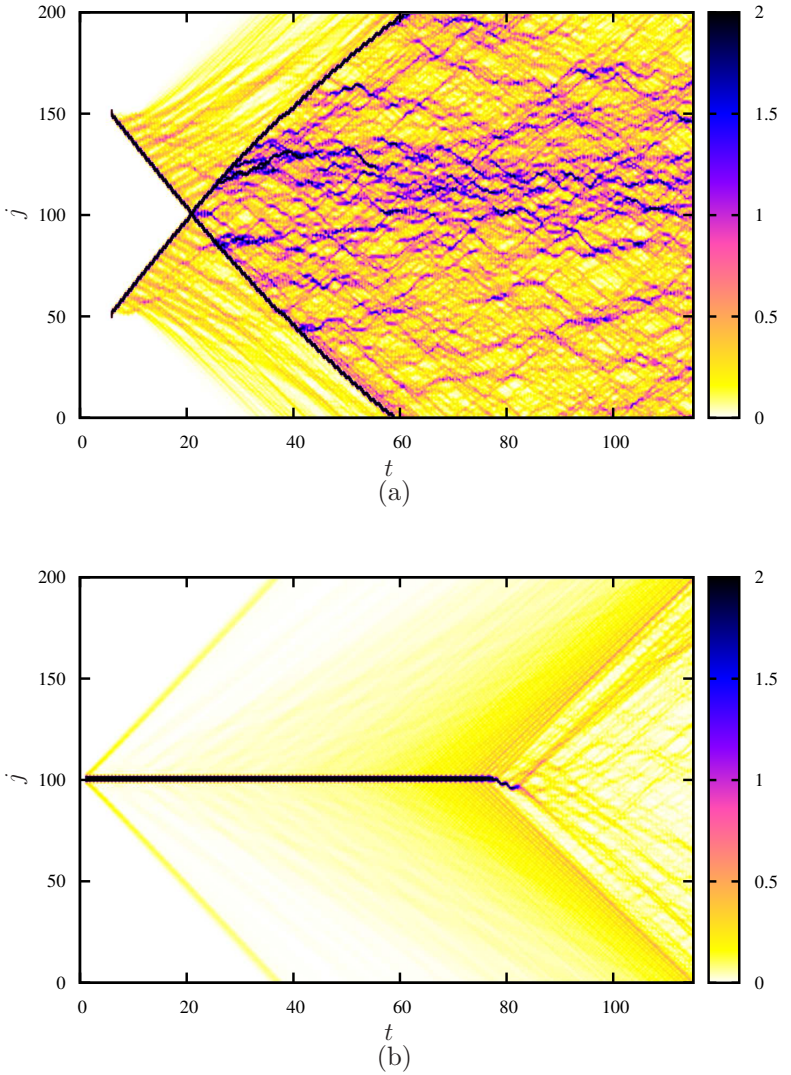

Figure 7.17: (a) Interaction of two solitons, (b) a stationary breather. Both modes radiate phonons.

Chapter 8.

Metadislocations and phason flips in AlPdMn

The ternary intermetallic system AlPdMn is interesting, because it contains a high number of complex metallic alloy compounds (CMAs). We classify the occurring CMAs (Ξ-phases and T-phases) and show the effect of structural complexity on their dislocations and phason dynamics. Because of the large unit cells of CMAs, regular dislocation mechanisms cannot take place and new types of dislocations occur. The role of the phason degree of freedom is discussed.

The results presented here are an extension and generalisation of parts of the author's diploma thesis [43]. They have appeared in two publications [45, 46]. Another one [70] is currently in press. Most of the experiments mentioned in the text and all electron microscopy images shown have been made by Michael Feuerbacher and Marc Heggen at the Forschungszentrum Jülich. The investigation of AlPdMn phases and their metadislocations is part of the EU Network of Excellence "Complex Metallic Alloys".

8.1. Phase diagram of AlPdMn

The ternary alloy system AlPdMn has been of great interest in the last years. The reason is the thermodynamic stability of various CMAs, which can be grown as single crystals with high perfection and which have interesting physical properties. In Fig. 8.1 we present a phase diagram of AlPdMn along the liquid-solid equilibrium and in the Al-rich corner [94]. It consists of two parts: The projection of the liquidus phase fields in Fig. 8.1(a) identifies the primary solidifying phases at a given composition. Furthermore the solubility domains of solid phases in equilibrium with the melts are shown in grey in Fig. 8.1(b). They represent the compositions of the primary solidifying phases. The arrows point in direction of decreasing temperatures and correspond to eutectic lines (single arrow) and peritectic lines (double arrow). Most of the phases grow off-stoichiometrically.

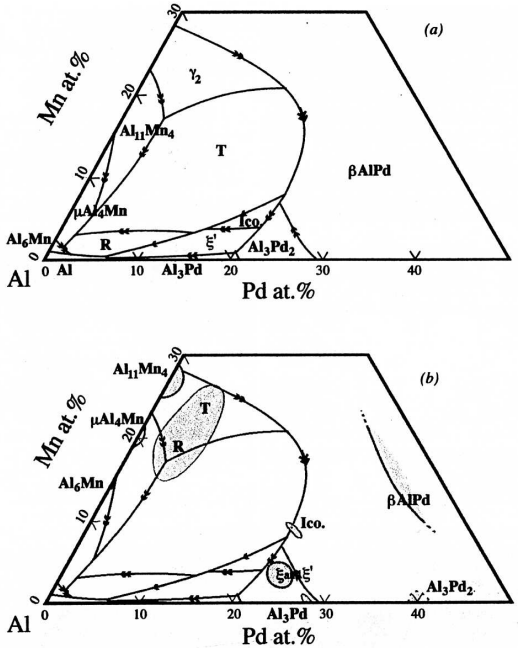

Figure 8.1: Projection of the liquidus phase fields in the Al-rich region of the AlPdMn system. The grey areas are the compositions of the solid phases [94].

In the region of small Pd and small Mn content, several binary AlPd- and AlMn-phases with minor solubility of the third element are found. There is an icosahedral quasicrystal i-AlPdMn (Ico. in Fig. 8.1), which however will not play a role in this work. Furthermore, there are two classes of true ternary phases: The 1.6 nm-phases (ξ, ξ', ...) and the 1.2 nm-phases (R, T, ...). The classes consist of a decagonal quasicrystal[1] and its approximants. The members of each class have in common one of the lattice constants, which is 1.6 nm and 1.2 nm respectively. By transferring the tiling structure of the decagonal quasicrystals to their approximants, a simplified cluster description is obtained. We now discuss the phases with regard to the cluster tiling.

[1]The decagonal quasicrystals do not appear in Fig. 8.1, since they are not obtained from the melt.

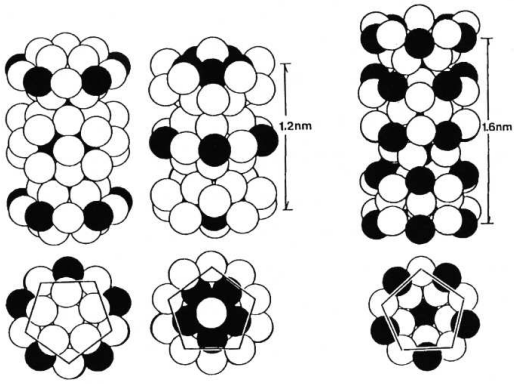

Figure 8.2: Cluster columns are the basic building blocks of the decagonal quasicrystals with 1.2 nm (left) and 1.6 nm periodicity (right). The black circles are Pd or Mn atoms, the white circles are Al atoms. Below, the projections along the five-fold symmetry axis is shown. [170].

8.1.1. The 1.6 nm-phases

The 1.6 nm-phases are approximants of a decagonal quasicrystal $d_{1.6}$-AlPdMn with lattice a constant of 1.6 nm in the periodic direction. Since $d_{1.6}$-AlPdMn can only be obtained by rapid quenching, it is not thermodynamically stable. Its structure is well described by the atomic model of Sun and Hiraga [170], which is built by clusters arranged in a two-step hierarchy. In the first step the clusters are stacked on top of each other forming cluster columns as shown in Fig. 8.2. The clusters are so-called Pseudo-Mackay clusters, closely related to the ideal Mackay-cluster as shown in Fig. 1.1. In the next step the columns (viewed in direction of their axis) are arranged on the vertices of the Tübingen tiling (introduced in Sec. 3.4). It is reproduced on the right side of Fig. 8.3(a). Most of the atoms are part of the cluster columns. The few remaining ones are filling atoms. All approximants of $d_{1.6}$-AlPdMn inherit the cluster column framework, but vary the positions of the cluster columns, and thus can be described by a two-dimensional tiling approximating the Tübingen tiling.

It is found in experiment that of all possible approximants only few are actually observed in thermodynamic equilibrium. The most impor-

tant ones are shown in Fig. 8.3(a). They are built from the nonagon- (N), hexagon- (H), and pentagon-tile (P) only: A parallel arrangement of H-tiles gives the ξ-phase ($\approx$ 160 atoms per unit cell[2]), an alternating arrangement the ξ'-phase ($\approx$ 320 atoms), and an arrangement with N- and P-tiles the ξ'_2-phase ($\approx$ 1480 atoms). ξ' is a variation of ξ and has the same ideal stoichiometry. ξ'_2 is a superstructure of ξ'. The basic length in the tiling is the tile edge, which is $l_{1.6} = 0.78\,\mathrm{nm}$. From this value and the tiling representations, the unit cell dimensions of the approximants can be calculated. For comparison, we show high-resolution transmission electron microscopy (HRTEM) images of the phases ξ' and ξ'_2 in Fig. 8.4. The images have been obtained by with an Cs-corrected[3] Philips CM 200 electron microscope. The pseudo-Mackay cluster columns sitting at the tile vertices are clearly visible either as bright spots (right side) or as ring contrasts representing the pseudo-Mackay clusters (left).

8.1.2. The 1.2 nm-phases

The decagonal quasicrystal $d_{1.2}$-AlPdMn with a lattice constant of 1.2 nm in the periodic direction is also metastable at room temperature, but thermodynamically stable at elevated temperatures around 1000 K [10]. An atomic model has been introduced by Hiraga and Sun [76]. Similarly to the 1.6 nm decagonal phase, $d_{1.2}$-AlPdMn is built by cluster columns (Fig. 8.2). However, the arrangement of the cluster columns is different: The tiling of $d_{1.2}$-AlPdMn (shown on the right side of Fig. 8.3(b)) consists of four tiles: decagons (D), stars (S), boats (B), and hexagons (H). Note that the edge length of the tiling is smaller for the 1.2 nm phases: $l_{1.2} = 0.66\,\mathrm{nm}$. There is a close connection to a HBS tiling (Fig. 1.3(a)): by combining a boat and two hexagons a decagon is obtained. If this substitution is done repeatedly, the HBS-tiling is turned into a tiling of the 1.2 nm decagonal phase. The process is ambiguous. In fact, the structure of the decagonal phases is very flexible and can rearrange locally via phason flips.

Experimentally important approximants are built from the hexagon and boat. The simplest ones are the R-phase ($\approx$ 78 atoms per unit cell), which is a parallel arrangement of H'-tiles only, and the T-phase ($\approx$ 156 atoms), an alternating arrangement. The T_2-phase ($\approx$ 720 atoms) is a

[2]The values for the atoms per unit cell are upper bounds. Many atomic sites are partially occupied, which lowers the number of atoms.

[3]Spherical aberration corrected

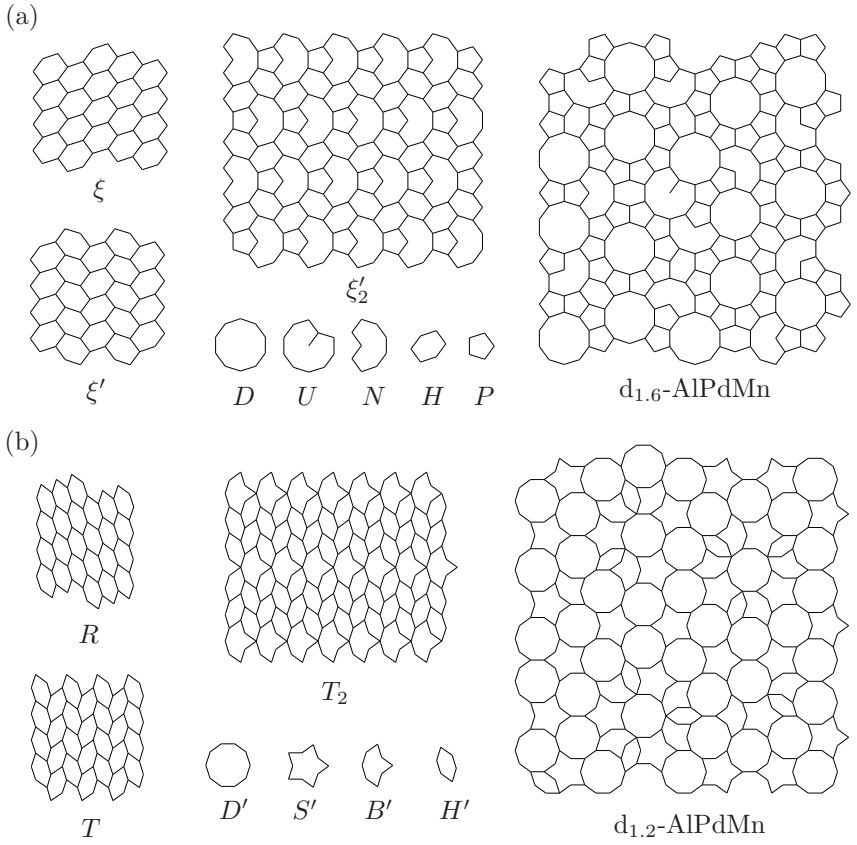

Figure 8.3: Cluster tilings of some 1.6 nm- (a) and some 1.2 nm-phases (b). The vertices of the tilings are the positions of the cluster columns viewed along the column axis. The edge lengths of the tiles are $l_{1.6} = 0.78\,\text{nm}$ and $l_{1.2} = 0.66\,\text{nm}$.

superstructure of T, but has not been observed experimentally yet. Further structural details of the 1.6 nm-phases and the 1.2 nm-phases like the exact atomic positions and an elaborated hyperspace model (decoration of the hyperlattice with atomic surfaces) are found in the thesis of Lara Beraha [11]. For the study of dislocations the cluster tiling as presented here suffices. Its decoration can be neglected.

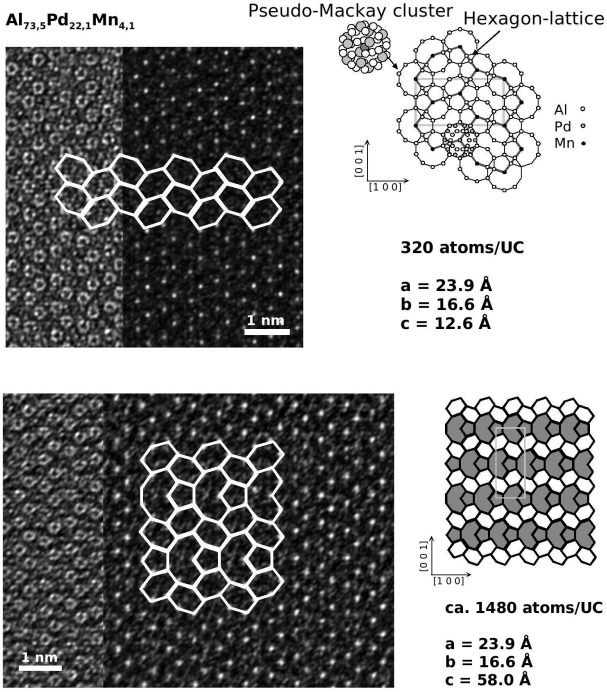

Figure 8.4: HRTEM images of the ξ'-phase (top) and the ξ'_2-phase (bottom). For the left and right parts of the microscopy images different contrast settings were applied [69].

8.2. Tilings models

8.2.1. Substitution tilings

In the case of the 1.6 nm phases, those approximants (of all possible approximants of the decagonal quasicrystals) are relevant for the experiments, which are built solely from the three prototiles $H1$, $H2$ (H in two orientations) and $PL1$, $PL2$ (a combination of N and P in two orientations, Fig. 8.5(a)). The latter one, PL, is called a phason line.[4] PL is really a 'line' because it extends perpendicular to the tiling plane along the cluster

[4]The reason for the term 'phason' will become clear later.

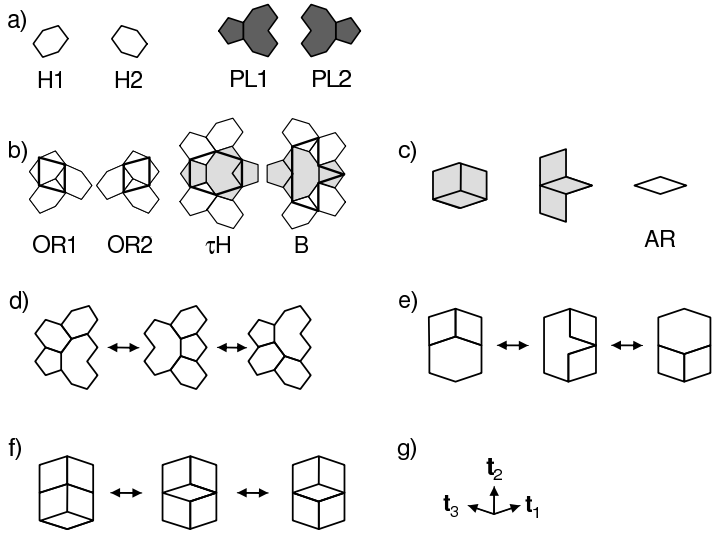

Figure 8.5: (a) Prototiles of the Ξ-phases. (b) The prototiles are substituted by the tiles $OR1/OR2$, H, and B. (c) H and B can be further decomposed into obtuse rhombs $OR1/OR2$ and acute rhombs AR. Phason flips can be formed in the cluster tiling (d), the tiling using the tiles $OR1/OR2$, τH, and B (e), and the tripod tiling (f). The basis for the tripod tiling (g).

columns. Since rearrangements of the tiles occur frequently (they do not cost much energy), the following question arises: What periodic tilings can be built from the tiles $H1$, $H2$, $PL1$, and $PL2$? This is most easily answered with the help of alternative tilings, which are now introduced.

Because the prototiles H and PL have an even number of vertices (6 and 12), the vertices can be divided into two disjoint sets[5]. By connecting the next-neighbors of one of those sets a substituted tiling is obtained: $H1/H2$ are substituted by the obtuse rhombs $OR1/OR2$, $PL1$ is substituted by a τ-inflated hexagon τH, and $PL2$ is substituted by a boat-shaped tile B (Fig. 8.5(b)).[6] The substitution is area-preserving and reversible. The tiles B and τH are further decomposed into a combination of $OR1$, $OR2$, and an acute rhomb AR (Fig. 8.5(c)). At the end, the cluster tiling is

[5]In other words: The cluster tiling with the prototiles in Fig. 8.5(a) is bipartite.
[6]The boat-shaped tile is different from the boat in HBS tilings.

substituted by a tiling using only obtuse and acute rhombs, $OR1$, $OR2$, and AR. This is the obtuse tripod tiling (see Sec. 3.2), for simplicity called just tripod tiling. The substitution of the tile τH by $OR1$, $OR2$, and AR, however, is not reversible as the back transformation is ambiguous. We will make use of both the cluster tiling and the tripod tiling.

In the phases under investigation local rearrangements of cluster columns are possible. These can be represented in the cluster tiling by an exchange and movement of $PL1$- and $PL2$-tiles (Fig. 8.5(d)) involving a correlated rearrangement of atomic clusters columns. This is a phason flip and the only possible phason flip of the system.[7] The fact that phason flips are closely related to changes in the PL-tiles is the reason for naming them 'phason' lines. Phason flips can also be described using the tiles $OR1$, $OR2$, B, and τH (Fig. 8.5(e)) and the tripod tiling (Fig. 8.5(f)). In terms of the tripod tiling, the distinction between $PL1$- and $PL2$-tiles is not possible. Accordingly, the substitution of the second and third tiling of Fig. 8.5(d) and (e) leads to equivalent tripod tilings.

8.2.2. Classification of Xi-phases

We now study periodic tripod tilings with a uniform distribution of the AR-tiles by making use of the hyperspace methods introduced in chapter 2. We then transfer the results to the cluster tilings, which leads to the phase family called Ξ-phases. The tilings under investigation are characterized by a planar cut space through the three-dimensional cubic hyperlattice (Sec. 3.2). For the projection we use the hyperlattice basis shown in Fig. 8.5(g). The cut space is spanned by two vectors. Let us choose the following ones:

$$\boldsymbol{e}_1 = \begin{pmatrix} 1 \\ 2+m \\ 1 \end{pmatrix}, \qquad \boldsymbol{e}_2 = \begin{pmatrix} 1 \\ n \\ -1 \end{pmatrix}. \tag{8.1}$$

An index pair $(m, n) \in \mathbb{Z}^2$ gives a periodic approximant, because $\boldsymbol{e}_1$ and $\boldsymbol{e}_2$ are hyperlattice vectors. The tilings with small values of m, n are shown in Fig. 8.6. $OR1$- and $OR2$-tiles are depicted white and AR-tiles grey. Each phase is uniquely characterized by the arrangement of the AR-tiles, which

[7] since the hyperspace is three-dimensional (for two-dimensional tilings), there is potentially only one phason degree of freedom in the system.

form a lattice. The lattice constants and their interior angle of the unit cell are

$$e_1/\lambda = \tau + 1 + m, \tag{8.2}$$

$$e_2/\lambda = \sqrt{n^2 + 2 + \tau}, \tag{8.3}$$

$$\tan(\phi) = \frac{\sqrt{2+\tau}}{n}, \tag{8.4}$$

with a length λ, which has the value $\lambda = 1.23\,\mathrm{nm}$ for the AlPdMn-phases. The number of the $H1$-, $H2$-, and PL-tiles per unit cell[8] is $\#(H1) = m+n$, $\#(H2) = m-n$, and $\#(PL) = 2$. A direct consequence are the restrictions $m \geq 0$ and $|n| \leq m$. Tilings with a sign change in m are related by a vertical mirror operation. Those with $n = 0$ have orthorhombic symmetry, the others are monoclinic.

Reversing the substitution, we obtain the cluster tilings in Fig. 8.7. We term the family of these tilings as the Ξ-phases, because they generalize the phases ξ, ξ', and ξ'_n. Note that the phason lines (PL-tiles) are arranged in planes called phason planes. In the orthorhombic phases the phason planes are horizontal, whereas they are tilted in the monoclinic phases. The tilt is stronger with larger n. On the other hand m describes the average distance between two phason planes. The ξ'- and the ξ-phase, consisting of H-tiles only, can be expressed in terms of the present classification as the limit of an infinite distance between the phason planes, i.e. by the indices $(m, 0)$ and $(m, \pm m)$ for $m \to \infty$, respectively. The phase ξ'_2 is identical to $(2, 0)$. The phases $(m, 0)$ appear most often in the literature. For historical reasons there are other notations for them: The phases $(2m-2, 0)$ are known as ξ'_m and ϵ_{16+6m}, the ξ'-phase is known as ϵ_6 [70].

Given a general tiling the indices m, n fitting the tiling in the best way possible are determined by counting the relative densities of the tile types:

$$m = \frac{\#(H1) + \#(H2)}{\#(PL)}, \qquad n = \frac{\#(H1) - \#(H2)}{\#(PL)}. \tag{8.5}$$

It should be noted that the phases of the present classification scheme represent 'simple' phases built with the tiles $H1$, $H2$, $PL1$, and $PL2$, which can be described by two translation vectors connecting PL-tiles. This directly results in the uniform distribution of straight phason lines. However,

[8] The number of $PL1$- and $PL2$-tiles is not invariant under phason flips.

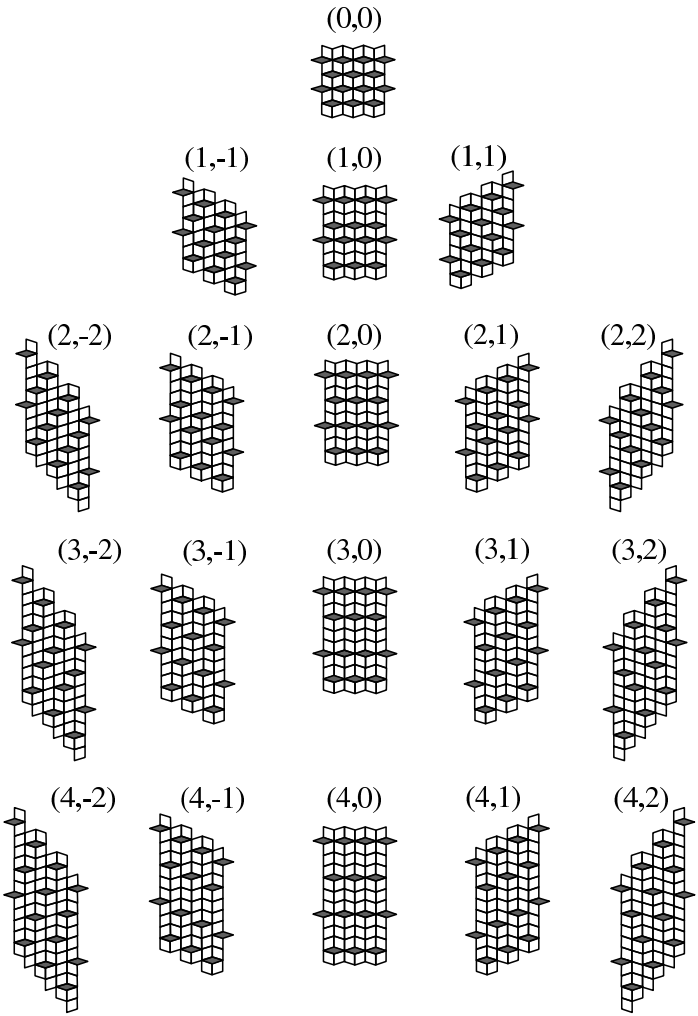

Figure 8.6: Tripod tilings for cut planes spanned by the vectors (8.1). The indices are (m, n) with $m \geq 0$ and $|n| \leq m$.

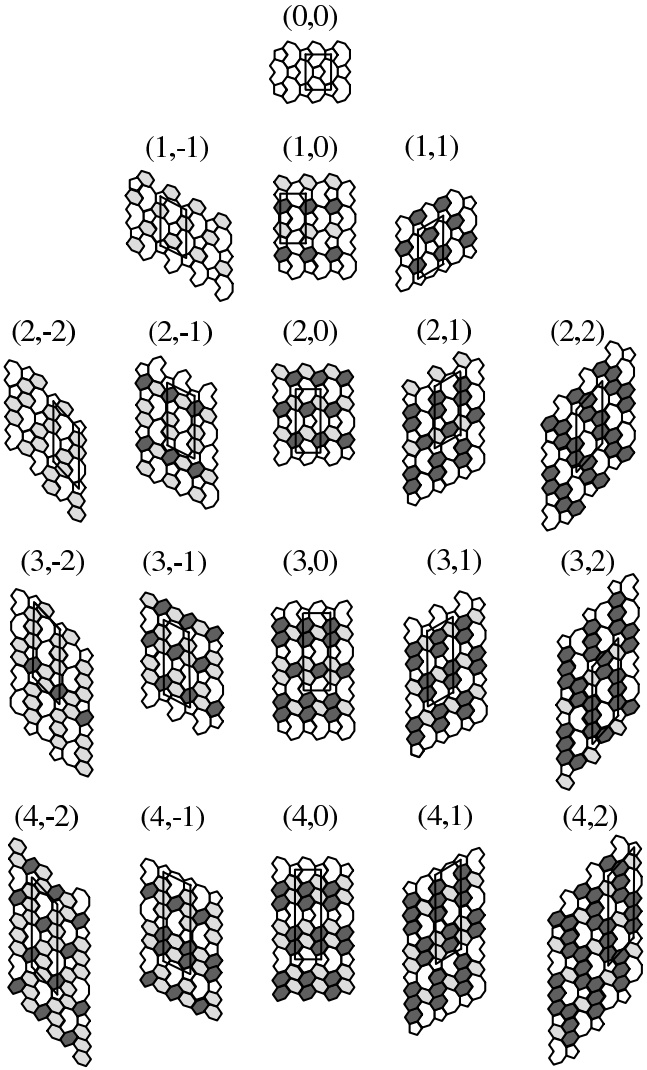

Figure 8.7: The cluster tilings of the Ξ-phases obtained from the tilings in Fig. 8.6.

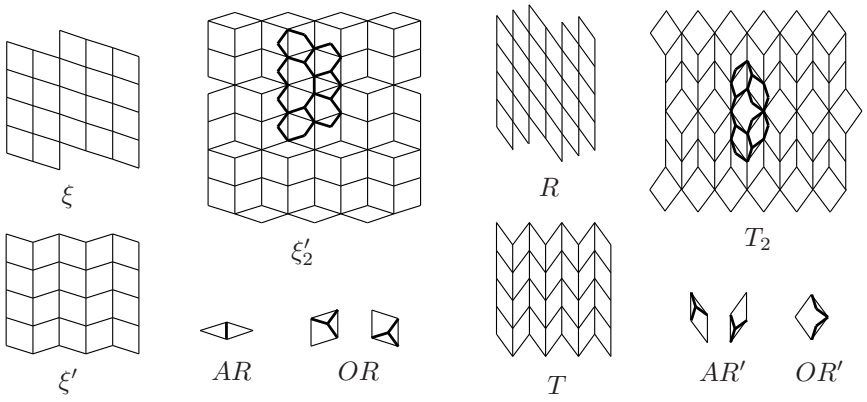

Figure 8.8: Substitution of the cluster tiling by obtuse tripod tilings for the Ξ-phases (left) and acute tripod tilings for the T-phases (right).

more complex periodic phases using H and PL-tiles can be constructed, e.g. by the creation of super-cells of the presented simple phases.

The Ξ-phases are not restricted to the system AlPdMn, but also occur in related systems. Hiraga [75] studied decagonal and approximants by high-resolution electron microscopy in AlPd(Cr, Co, Fe). He observed modulated-type structures, which can be classified with our scheme. The areas shown in figure 11 of Hiraga's work can be identified as the phases $(3,1)$, $(2,-1)$, $(2,0)$, and $(0,0)$. Further examples will be given below.

8.2.3. Tripod tilings for T-phases

An analog substitution procedure is possible for 1.2 nm-phases. We show the result for the phases T, R, and T_2 in Fig. 8.8. The H'-tiles are now substituted by acute rhombs AR', and the B'-tiles by an obtuse rhomb OR'. Using the rhomb tiles, a close similarity to the Ξ-phases is observed: Under the substitution $OR \to AR'$, $AR \to OR'$ a Ξ-phase is transformed into a 1.2 nm-phase. All of the 1.2 nm-phases obtained in this way form the family of T-phases. Since the classification of the T-phases is fully analogous to the one for the Ξ-phases, we do not repeat it here. In the cluster tiling, the phason lines of the T-phases are the B'-tiles.

8.3. Energy considerations

We now apply the general theory of Sec. 4.2. As shown in Sec. 5.5.2 a dislocation can be introduced into the tiling by a generalized Volterra process using a discontinuity in the cut plane. It is uniquely characterised by the Burgers vector, which for the tripod tilings of the Ξ- and the T-phases is a translation vector of the hyperlattice (=cubic lattice): $\boldsymbol{b} = (b_1, b_2, b_3)$, $b_i \in \mathbb{Z}$. The Burgers vector splits up into a phonon component $\boldsymbol{b}^{\parallel} = \mathcal{L}\boldsymbol{b}$ and a phason component $\boldsymbol{b}^{\perp}$. The lowering operator is either $\mathcal{L}_{\rm ob}$ from (3.6) for the Ξ-phases or $\mathcal{L}_{\rm ac}$ from (3.7) for the T-phases.

Since low energy dislocations are those with small phonon components, we use the minimization of $b^{\parallel}$ to determined the physically relevant, stable ones. The calculation gives:

$$\boldsymbol{b}^{\parallel}_{\Xi} = \mathcal{L}_{\rm ob}\boldsymbol{b} = \begin{pmatrix} b_2 + \frac{1}{2}\tau^{-1}(b_1 + b_3) \\ \frac{1}{2}\sqrt{2+\tau}(b_3 - b_1) \end{pmatrix}, \tag{8.6}$$

$$\boldsymbol{b}^{\parallel}_{T} = \mathcal{L}_{\rm ac}\boldsymbol{b} = \begin{pmatrix} b_2 - \frac{1}{2}\tau(b_1 + b_3) \\ \frac{1}{2}\tau^{-1}\sqrt{2+\tau}(b_3 - b_1) \end{pmatrix}. \tag{8.7}$$

In both cases $b^{\parallel}$ is small, if $b_1 = b_3$ and $b_2 = -\tau^{-1}b_1$ for $\boldsymbol{b}_{\Xi}$ and $b_2 = \tau b_1$ for $\boldsymbol{b}_{\rm T}$. Here, we approximate the golden number τ^{-1} by the fractions F_{m-1}/F_m of Fibonacci numbers and τ by the fractions F_{m+1}/F_m respectively. Finally, the Burgers vectors of stable dislocations are:

$$\boldsymbol{b}_{\Xi} = (-F_m, F_{m-1}, -F_m), \tag{8.8}$$

$$\boldsymbol{b}_{T} = (F_m, F_{m+1}, F_m). \tag{8.9}$$

In the following we will call a dislocation with such a Burgers vector a metadislocation of type m.

The second entry of the phonon component is zero: $\boldsymbol{b}^{\parallel} \parallel [1, 0]$. With the properties of the Fibonacci numbers (Sec. 3.1) we get

$$b^{\parallel}_{\Xi} = b^{\parallel}_{T} = F_{m-1} - \tau^{-1}F_m = F_{m+1} - \tau F_m = (-\tau)^{-m}. \tag{8.10}$$

The phason component depends on the hyperspace model. In order to make the results comparable with the literature, we have to use the Katz-Gratias model [90] with a six-dimensional hyperspace. Although originally developed for the icosahedral AlPdMn quasicrystal, the Katz-Gratias

model can also be applied to the Ξ- and the T-phases.[9] Because we only need the result in the following, we skip the derivation [46]. The phason component is

$$b_{\Xi}^{\perp} = b_{T}^{\perp} = (-\tau)^{m-3}. \tag{8.11}$$

Both, $b^{\parallel}$ and $b^{\perp}$, are identical for the Ξ- and the T-phases. The reason for this is the fact that $\boldsymbol{b}_{\Xi}$ and $\boldsymbol{b}_{T}$ correspond to the same six-dimensional Burgers vector in the Katz-Gratias model.

By substituting (8.10) and (8.11) into the equation for the elastic energy of dislocations (4.7), one has:

$$E = \left[c_{\mathrm{phon}}\tau^{-2m+3} + c_{\mathrm{phas}}\tau^{2m-3} + 2c_{\mathrm{coupl}}\right]\tau^{-3}. \tag{8.12}$$

There is a minimum at the ratio of the phonon and phason elastic constants

$$\frac{c_{\mathrm{phon}}}{c_{\mathrm{phas}}} = \tau^{4m-6}. \tag{8.13}$$

This determines the Burgers vector with lowest energy for given values of c_{phon} and c_{phas}. On the other hand, by determining the statistics of Burgers vectors observed in experiment conclusions about the magnitude of c_{phas} are possible. Note that c_{phon} is directly accessible to experiments via the (conventional) elastic constants.

8.4. Comparison with experiment

In Fig. 8.9, two metadislocations of type 4 are shown in the phase $(4, 0)$ of the obtuse and the acute tripod tiling. They have been calculated using the iterative selection algorithm. In the centers of the two sub-figures, the dislocation core is visible as a triangle. The main effect of the dislocation on the tiling is a strong bending of the phason planes, which in the original tiling without a dislocation have been straight and horizontal (see Fig. 8.8). Additionally, six new phason planes originate from the triangular shaped dislocation core to the left. There is also a small deformation of the rhombs near the dislocation core due to the phonon strain, however it is too small to be seen by eye.

Metadislocations of other types look similar. The only difference is the number of new phason planes created at the dislocation core. By conducting a Burgers circuit we can determine their number. To see this we study

[9] This was shown in [11]. See also the author's diploma thesis [43].

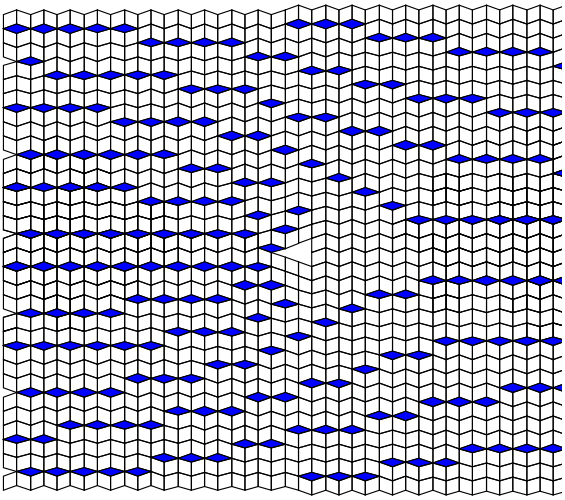

(a)

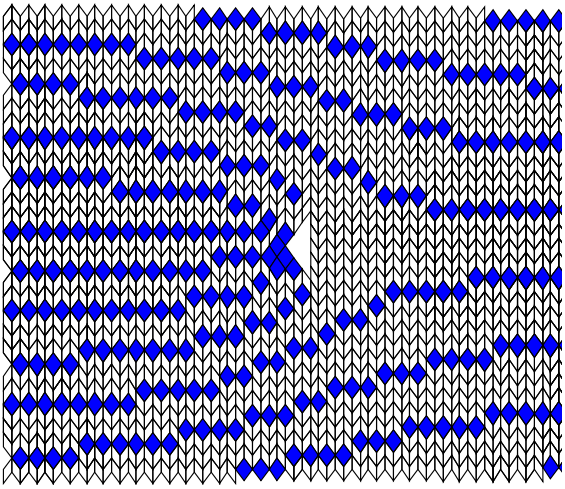

(b)

Figure 8.9: Type 4 metadislocation in the phase $(4, 0)$ of (a) the obtuse tripod tiling (ξ_3') and (b) the acute tripod tiling. Six new phason planes are inserted from the left, ending at the triangular shaped dislocation core.

three basic Burgers vectors: $(0,1,0)$, $(1,0,-1)$, and $(1,0,1)$. All others can be written as integer linear combinations. Let us imagine a Volterra process with these three vectors. In the case of the obtuse tripod tiling the first one inserts a horizontal zig-zag line of the two OR-tiles, the second one inserts two rows of OR-tiles, and the third one inserts two phason planes. This shows: A general dislocation with Burgers vector (b_1, b_2, b_3) results in $b_1 + b_3$ new phason planes starting from the dislocation core. For a metadislocation of type m it means: There are $2F_m$ new phason planes, e.g for $m = 4$: $2F_m = 6$.

For comparison we show a HRTEM image of the metadislocation of Fig. 8.9(a) in Fig. 8.10(a). Under the contrast settings chosen in the image the phason lines appear as dark contrast. Horizontal sequences of phason lines form phason planes, which are bent around the position of the dislocation. Again six phason planes originate from the dislocation core. Note the length scale on the HRTEM image: The metadislocation creates a modification of the tiling on a truly large scale of tens of nanometers, although the microscopic phonon component of the Burgers vector is only $b^{\parallel} = \tau^{-4}\lambda = 0.18\,\mathrm{nm}$. The phonon component is an order of magnitude bigger: $b^{\perp} = \tau\lambda = 2.0\,\mathrm{nm}$. Metadislocations can also be found in the ξ'-phase. The only difference is the absence of surrounding phason planes. In Fig. 8.10(b) we show such a type 4 metadislocation with the cluster tiling superimposed.

With HRTEM, metadislocations of types between $m = 2$ and $m = 6$ have been observed [69]. This means there are 2, 4, 6, 10, or 16 inserted phason planes. Furthermore, visual inspection reveals that the type 4 metadislocations are the most common ones. From (8.13) we get: $c_{\mathrm{phon}}/c_{\mathrm{phas}} = \tau^{-10} \approx 8 \cdot 10^{-3}$. MD simulations in a simple quasicrystal gave $c_{\mathrm{phon}}/c_{\mathrm{phas}} \approx 10 \cdot 10^{-3}$ [98]. In experiment the phason elastic constants are only measurable indirectly. For typical quasicrystals one has: $c_{\mathrm{phon}}/c_{\mathrm{phas}} = 10^{-3} \ldots 10^{-2}$, see the discussion in [40] and references therein. [40] also reports the first measurements of the phonon-phason coupling constant c_{coupl}, which is in the same order of magnitude as the phason elastic constants. This justifies the assumption in (4.8). One can say that observing metadislocations is a surprisingly simple method to study the (isotropically averaged) phason elastic constant.

Historically the naming 'meta'dislocations has been chosen, because the apparent effect of the dislocation on the tiling is a regular dislocation in the (large scale) 'meta'structure of the phason lines. After the experimental

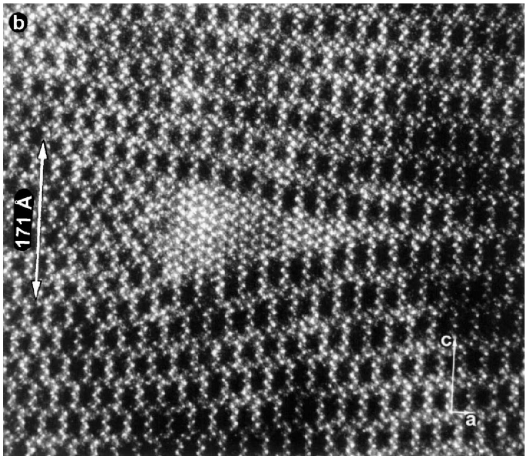

(a)

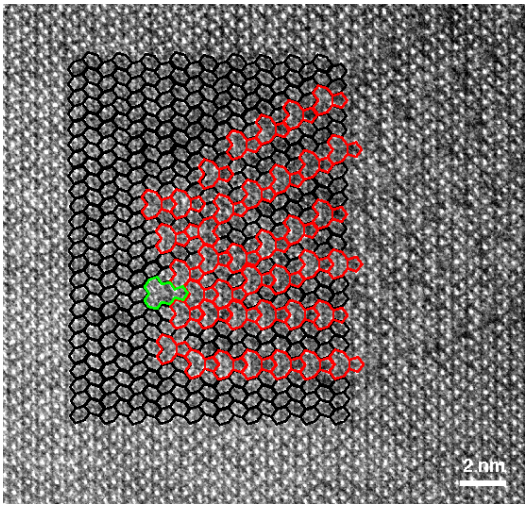

(b)

Figure 8.10: (a) HRTEM images of a metadislocation of type 4 in the ξ_2'-phase. The dark contrasts are phason lines [96]. (b) A metadislocation in the ξ'-phase. The cluster tiling fits the positions of the cluster columns at the white spots [69].

discovery in 1999 [96], the relationship to the underlying tiling was not immediately understood. Using the tiling model the rearrangement of clusters seen in HRTEM images is well explained.

8.5. Discussion

Here we present a selection of recent HRTEM images showing the wealth of features observed in connection with metadislocations in the system AlPdMn. We focus on theoretical aspects and clarify the role of the phason degree of freedom. All of the images in this section have been taken at the Ernst Ruska-Centre in Jülich. They are reproduced here from the original sources [8, 70, 71].

We begin with observations in the Ξ-phases. Fig. 8.11 shows two regions, where a lot of phason fluctuations are observed. Again the bright spots correspond to the pseudo-Mackay cluster columns. A cluster tiling representation of these areas using $H1$-, $H2$-, $PL1$-, and $PL2$-tiles can be made by connecting them. In Fig. 8.11(a) the unit-cell projection of the ξ_2'-phase is represented by a rectangle. Over large areas of the micrograph, however, the structure is disordered. Phason planes are not strictly oriented along the [100][10] direction, but show a wavy course due to mixing of $PL1$- and $PL2$-tiles within a single phason plane (e.g. regions 1 and 2). This observation can be explained by the occurrence of phason flips within a phason plane as shown in Fig. 8.5(d). In some areas the phason planes are inclined, i.e. a (101) translation can be found between neighbouring PL-tiles (arrows). Along the [001] direction a varying number of $H1$- and $H2$-tiles is observed between two PL- tiles, ranging from 0 to 3 (examples are indicated by circles). In Fig. 8.11(b) the average structure is $(3, 0)$ (see Fig. 8.7). In some areas even strong inclinations between PL-tiles are observed (arrow).

The fact that phason planes can start or end at the metadislocation core offers the possibility of a phase boundary between the phase ξ' without phason planes and a phase with phason planes. Indeed this is what has been found: In Fig. 8.12 a sequence of type 4 metadislocations (six phason planes) and type 5 metadislocations (ten phason planes) terminates all phason planes of ξ_2'. The joint appearance of two metadislocation types is not by accident. Since the phonon components of the Burgers vectors

[10] As basis vectors we use the orthorhombic unit cell of ξ'.

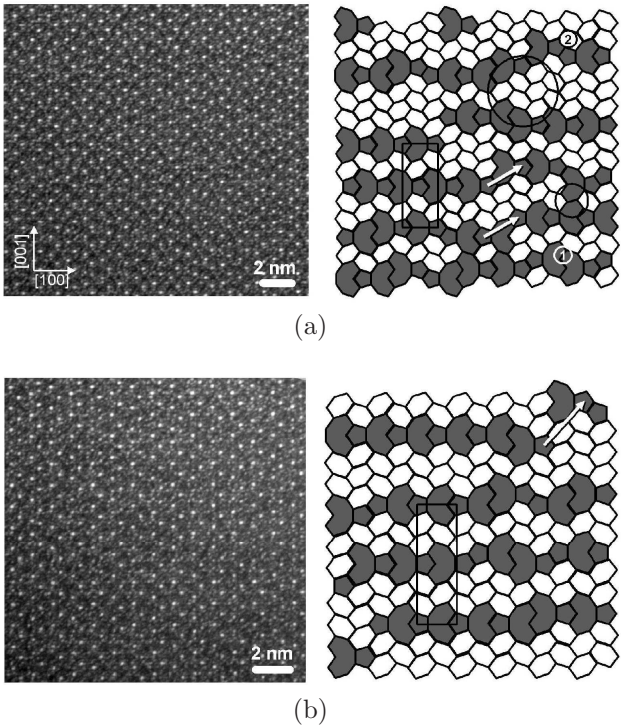

Figure 8.11: HRTEM images of Ξ-phases showing an average $(2,0)$-phase (ξ') (a) and $(3,0)$-phase (b) [70]. The corresponding cluster tilings are shown on the right-hand sides.

(8.10) of type 4 and type 5 point in opposite directions, their phonon elastic strains can cancel efficiently. A stacking of n type 4 and m type 5 metadislocations has a total Burgers vector of

$$b_{\text{total}} = \lambda\tau^{-5}(\tau n - m). \tag{8.14}$$

In Fig. 8.12 we count $n = 6$ and $m = 10$, which gives the very small value of $b_{\text{total}} = 0.032\,\text{nm}$. Perfect matching would be achieved by a ratio $m/n = \tau$.

Next we show in Fig. 8.13 a quite complicated arrangement of four metadislocations in the phase ξ_2' (labelled 1 to 4). They are connected to ξ'-phase regions (5 to 8). The reason for this is the disappearance of the

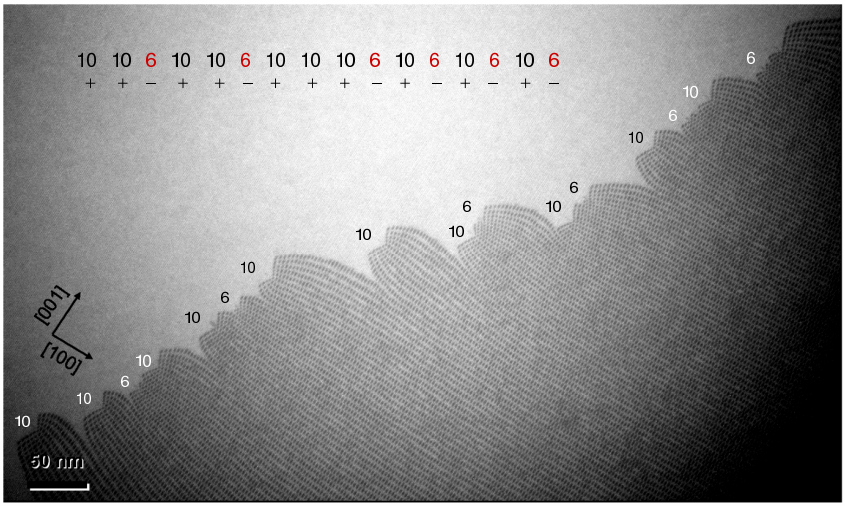

Figure 8.12: A sequence of metadislocations can form a phase boundary between ξ' (top) and ξ_2' (bottom). By combining type 4 and 5 metadislocations the total Burgers vector of the boundary can be made very small [71] (modified).

phason planes behind the dislocation core. It then takes some distance for the bent phason planes to fill the gap. In general phason planes have varying slopes (9). Some of them are indicated by black lines. Within areas of 10 to 20 nm in diameter various homogeneous local tiling structures are observed. The areas in the rectangles marked a, b, and c in Fig. 8.13 are enlarged at the bottom of the figure. The phases are $(2, 0)$ in (a), $(3, -1)$ in (b), and $(4, 1)$ in (c).

Furthermore a stacking fault (10) is observed in Fig. 8.13. Similar stacking faults have been reported previously [95]. A close inspection shows that its cluster tiling looks like Fig. 8.14(a). New tiles like the D-tile and various defect tiles (an X-shaped tile and an octagonal tile in between the H- and the N-tile) appear. However, the stacking fault disappears with the transition to the tripod tiling (Fig. 8.14(b)) indicating that its origin is connected with the ambiguity of the substitution. In fact there are exactly two possible ways to substitute the bipartite cluster tiling by the tripod tiling. On each side of the stacking fault one of the possibilities is realized.

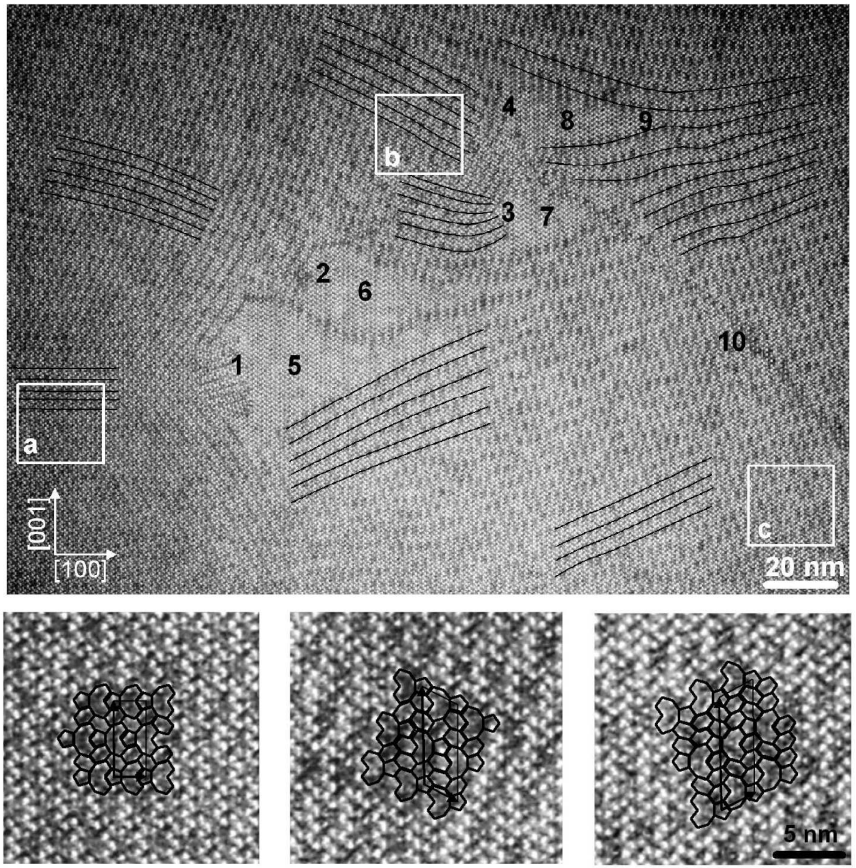

Figure 8.13: AlPdMn sample containing four metadislocations (1 to 4) connected to ξ'-phase regions (5 to 8). The course of some phason planes is exemplarily indicated by curved line elements (9). In addition, a stacking fault is observed (10). Enlarged images of the boxed regions are presented below. [70]

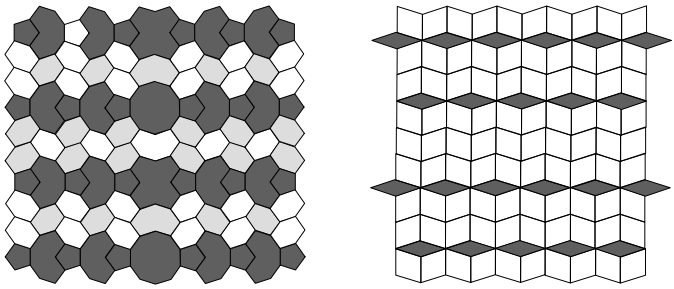

Figure 8.14: (a) Vertical stacking fault in the cluster tiling of the $(3, 0)$-phase. Defect tiles appear along the fault line. The stacking fault is not visible in the tripod tiling.

Thus there is only one type of stacking fault. Two of them annihilate automatically – a prediction which has no experimental verification yet. Note that stacking faults can again move via phason flips.

In Fig. 8.15 a complex arrangement of many metadislocations (types 3, 4, and 5) is shown. We make several observations: (i) Most of the Burgers vectors point in the same direction (to the top). This allows an efficient phonon strain transport [71]. (ii) The image strongly suggests that metadislocations move in direction of the phason planes creating them during their motion. Although it corresponds to dislocation climb that seems not to be a problem: Large tiling rearrangements are necessary during the motion anyway [43]. This also explains why metadislocations are only mobile at high temperatures above ca. 900K [51]. Only then, phason flips are thermally activated. (iii) In the regions marked with white ellipses, phason planes approach closely. An efficient attraction seems to favor a close distance. The possible origin of the attractive force is unknown.

We end the discussion of the Ξ-phases by noting that recently metadislocations in the ξ-phase of AlPdFe have been observed [50]. The tiling description is again applicable. It shows that the Burgers vectors of metadislocations in AlPdFe are identical to the Burgers vectors given for the AlPdMn-phases.

Finally we shortly mention the T-phases. Up to now, only few results are available for them. Both the T- and the R-phases are thermodynamically

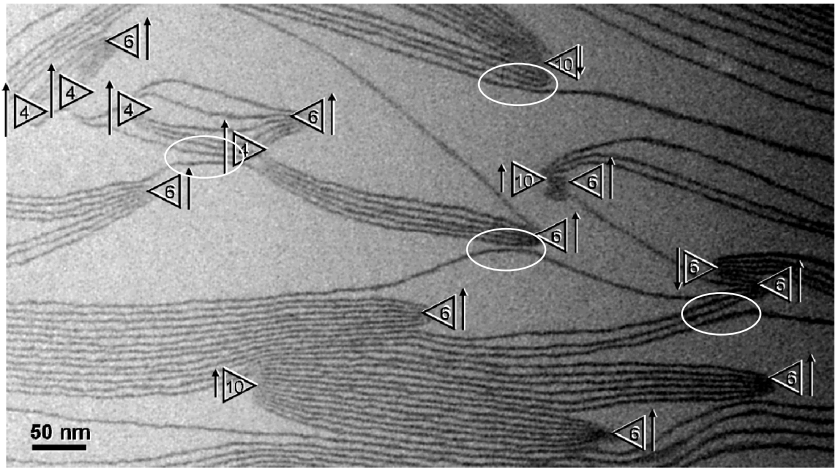

Figure 8.15: Complex metadislocation arrangement. Metadislocations with 4, 6, and 10 inserted phason planes occur. The image suggests an effective attraction between the phason planes (marked) [71] (modified).

stable [8]. During solidification they easily intergrow, forming lamellar structures (Fig. 8.16). Preliminary investigations show that dislocations similar to the metadislocations also exist in the T-phases [69], although the formation of phason planes is inhibited. Experiments clarifying this point are currently under way.

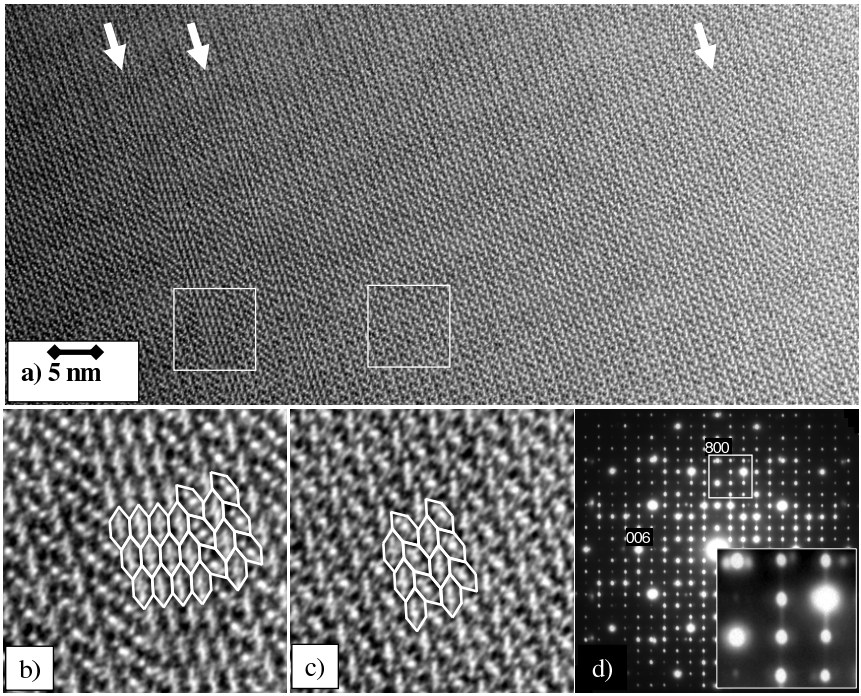

Figure 8.16: HRTEM image showing the coexistence of the T-phase and R-phase in $Al_{82.7}Mn_{12.0}Pd_{5.3}$. (a) The arrows mark stripes of the R-phase. (b), (c) Enlargements of the boxed areas. (d) The lamellar structure causes diffuse streaks in the electron diffraction pattern [8].

Chapter 9.

The Lennard-Jones-Gauss system

In this chapter we investigate the growth of quasicrystals and complex crystals with numerical simulations. For simplicity, we study a system of identical particles in two dimensions interacting with the Lennard-Jones-Gauss potential. To get an overview of the diversity of stabilized ground state structures, we calculate the phase diagram at $T = 0$. The equilibrium dynamics and solid-solid phase transformations of quasicrystals, simple and complex crystals are examined.

The results concerning the decagonal quasicrystal have appeared in two publications [47, 48]. As far as we know, the Lennard-Jones-Gauss system is the only system that allows to study both the growth of quasicrystals and their low temperature transition to approximants, i.e. complex crystals.

9.1. Model system

9.1.1. Previous models

The prerequisite for simulating crystal growth of a large number of particles on a computer is the use of effective pair potentials. Taking quantum mechanical effects into account is too slow on present-day computers.

The first simulations of a system with a quasicrystalline ground state were conducted independently by Lançon, Billard [103] and Widom et al. [178]. They used a binary system of small particles S (diameter 1) and large particles L (diameter τ) interacting with the Lennard-Jones (LJ) potential in two dimensions [102]. The LJ minima, as well as the composition were chosen to favor decagonal local symmetry. During annealing the formation of a random tiling with decagonal average symmetry was observed. Similarly, a dodecagonal quasicrystal was studied using a slight variation of the interaction potentials [106]. However, only in small samples (few hundreds of particles) single crystals were grown from the liquid. In large samples the decagonal symmetry is observed locally. After the formation of

seed crystals at the beginning of crystallization, the quasicrystal structure cannot ameliorate efficiently, because of the close packing of the particles and the high activation energy necessary for phason flips.

In 1992 Dzugutov introduced a new potential ('Dzugutov potential') [38]. His system was chosen monatomic to facilitate computation and to separate chemical from topological ordering. It is well-known that many common pair potentials like the Lennard-Jones (LJ) potential favor close-packed ground states. To force the formation of alternative structures, the Dzugutov potential is endowed apart from its LJ minimum with an additional maximum. Although the potential was originally tailored to lead to a glassy state [38], it stabilizes the σ-phase at low temperature [151]. Yet in annealing simulations, again quasicrystals were observed [39]. They were difficult to grow, because the dynamics in three dimensions is much slower than in two dimensions. The phase transformation to the σ-phase is too slow to be observed in simulations and the system gets stuck in the quasicrystal state. Later, similar potentials were used to demonstrate the formation of a dodecagonal quasicrystal in two dimensions [139].

In all simulations discussed here, the $T = 0$ ground state is periodic, although a random tiling quasicrystal forms first when cooling from the liquid. High temperature kinetics seems to favor the quasicrystal over related complex crystals. Due to the wealth of possible local configurations in quasicrystals, their formation is much easier than that of a periodic crystal, where each particle has its fixed position [92]. This might explain, why quasicrystals are often found in rapidly solidified intermetallic compounds.

There is one detail, which is common to all the systems: Each of them gives rise to two competing nearest neighbor equilibrium distances. In the case of the Dzugutov potential, neighboring particles can either be separated by the distance given by the potential minimum, or by a distance beyond the maximum. Separations in-between are strongly disfavored. In the case of the binary systems, the two distances are specified by the size ratio of the components. We now investigate in detail the connection between a pair of competing equilibrium distances and structural complexity.

9.1.2. Lennard-Jones-Gauss potential

For our model we combine the advantages of the systems above by looking for two-dimensional monatomic systems. Here, simulations are least time consumptive. It only remains to choose an appropriate interaction poten-

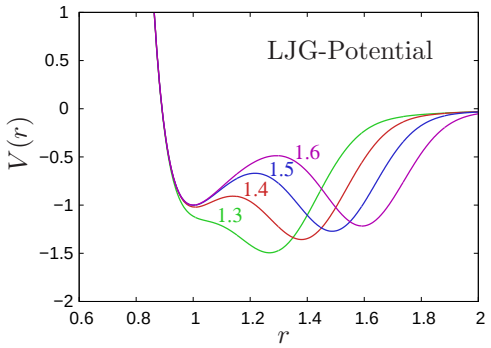

Figure 9.1: LJG-potential for $\sigma^2 = 0.02$, $\epsilon = 1.1$, and $r_0 = 1.3$ (Hex2 in Fig. 9.2), 1.4 (Sqa), 1.5 (Pen), 1.6 (Hex1).

tial. In general, the relation between a potential and its energy ground state is a fundamental problem of physics. It can be approached by two methods: The direct method starts from a given parametrized set of potentials and studies the resulting structures as a function of the parameters (and temperature/pressure). An example is the hard core plus linear ramp model with the ramp slope as single parameter, which has been demonstrated to show a density anomaly during cooling and a disorded quasicrystal state [81]. The inverse method tries to find an appropriate potential that stabilizes a given structure via optimization [143]. It was used recently by Rechtsman et al. to find potentials for various lattices like the honeycomb lattice in two dimensions [144] or the cubic and diamond lattices in three dimensions [145, 146]. We apply the direct method to a potential of the form

$$V(r) = \frac{1}{r^{12}} - \frac{2}{r^6} - \epsilon \exp\left(-\frac{(r-r_0)^2}{2\sigma^2}\right), \tag{9.1}$$

which we denote Lennard-Jones-Gauss (LJG) potential. For most values of the parameters, $V(r)$ is a double-well potential with the first minimum given by the LJ-term and the second well by a Gaussian, centered at position r_0, of depth ϵ and width σ (Fig. 9.1).

We note that the general form of pair potentials in metals consists of a strongly repulsive core plus a decaying oscillatory (Friedel) term [63, 129]. Classical potentials fitted to reproduce ab-initio forces typically show a

similar behavior [19]. A LJG-potential can be understood as such an oscillatory potential, cut off after the second minimum. We consider the LJG-system as a first, simple approximation for complex metallic alloys. Of course it might also be interesting to compare the applicability of double-well potentials for the growth of quasicrystals in solutions of macromolecules or in colloids as mentioned in the introduction (Sec. 1.2).

9.2. Phase diagram at zero temperature

We determine the energy ground state of the LJG-system as a function of the potential parameters σ^2, ϵ, and r_0. The results are presented in a zero temperature (and zero pressure) phase diagram. We proceed in two steps. First, candidate ground state structures are obtained from annealing simulations. Next, a defect free sample of each candidate is relaxed with a conjugate gradient algorithm. The stable structures (within the candidates) are the ones with the lowest potential energies. The obtained phase diagram is exact within the set of candidate structures.

9.2.1. Annealing simulations

Simulations are carried out by solving the equations of motion with molecular dynamics (MD) as introduced in Sec. 5.2. Open boundary conditions and a thermostat for temperature control in the NVT ensemble are used. The simulation box is chosen big enough to ensure that the system crystallizes in one droplet in the middle of the box. Thus, we effectively simulate at pressure $P = 0$. A cut-off is applied to the LJG-potential at $r = 2.5$. The time step in the simulation is $\Delta t = 0.01$. We perform 5000 annealing simulations with 1024 particles using parameters located on a fine grid: The position and depth of the second minimum are $r_0 \in [1.11, 2.10]$, $\Delta r_0 = 0.01$ and $\epsilon \in [0.1, 5.0]$, $\Delta\epsilon = 0.1$, respectively. The width of the second minimum is fixed at $\sigma^2 = 0.02$.

We automate the calculation by successively moving through parameter space in the ϵ-r_0-plane. In each run we start the simulation in a random configuration. The temperature of the system is increased, until either the liquid phase or gas phase is reached, which can be checked by measuring the momentary diffusion constant $D(t)$ of the system given by (5.21). $D(t)$ rapidly increases at the transition temperature.[1] Then, the temper-

[1] The procedure gives no exact value for the melting temperature, but an upper bound.

ature is lowered linearly over $2 \cdot 10^6$ MD steps.[2] This is enough to reach a well-ordered polycrystalline state in all cases, and in many cases even a single crystal. Afterwards we look at the sample and analyze its structure. Usually, the crystallized phase can be identified by visual inspection. Additionally, calculating the diffraction image helps. If two crystal structures are observed in different grains – which often happens close to the phase boundary –, we search for the largest grain.

The phase observation regions are displayed in Fig. 9.2. We found a decagonal quasicrystal (Dec), which is a random tiling based on the Tübingen tiling (Sec. 3.4) and built from the basic tiles (P)entagon, (H)exagon, (N)onagon, (U)-tile, (D)ecagon, as well as a dodecagonal random tiling quasicrystal (Dod), which is based on the square-triangle tiling (Sec. 3.5) and built from the basic tiles (Sq)are, (Tr)iangle, (Sh)ield. Furthermore, there are hexagonal phases with nearest neighbor distance close to 1.0 (Hex1) and close to r_0 (Hex2), a square lattice (Sqa), a phase built from pentagons and hexagons (Pen), a lattice of alternating obtuse rhombs (Rho), and finally a honeycomb lattice (Hon). For each phase a tiling of the unit cell is shown.[3] The two hexagonal phases are connected around the phase Sqa. Across the line between C and the phase Sqa there is a rapid increase in the hexagonal lattice constant, but no singularity. The results of Fig. 9.2 of course depend strongly on the total time steps used for the annealing simulations. Longer simulations will in general lead much closer to the energy ground state than faster ones.

As an example, we show in Fig. 9.3 the results of the annealing runs for two parameter sets. In the top the Sqa-phase (left) and the Pen-phase (right) are observed. For Pen we applied an algorithm to color the tiles according their shape. Most of the tiling is filled by the pentagons in cyan. Below, the diffraction images and the radial distribution functions $g(r)$ are shown. The Sqa-phase is a single crystal with sharp peaks. The Pen-phase is still highly disordered.

Solid-solid phase transformations are problematic in the search for the ground state, since they are often too slow to be observed in annealing simulations. Therefore we switch to relaxation simulations. This allows to check which parts of the phase observation regions are only metastable.

[2] The time, necessary for a simulation with n MD steps, is proportional to the number of particles N. On a single core of an Opteron processor: $10^{-6} nN$ seconds.
[3] Further details of the tilings can be found in Tab. 9.2.

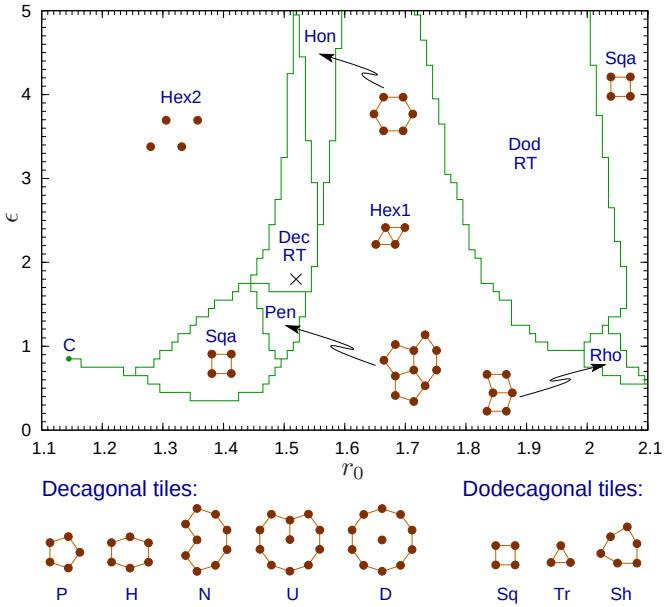

Figure 9.2: Phase observation regions in annealing simulations as a function of the potential parameters ϵ and r_0. Tilings of the unit cells are shown. The quasicrystal tiles are: (P)entagon, (H)exagon, (N)onagon, (U)-tile, (D)ecagon, (Sq)are, (Tr)iangle, (Sh)ield.

9.2.2. Numerical relaxation

The phases resulting from the annealing simulations are potential energy ground states. Further possibilities are periodic approximants, which we construct from the tiles in Fig. 9.2. The choice of approximants is restricted by the following observations at low temperature:[4] (i) The D-tiles have lowest energy and their number is maximized. (ii) The Sh-tiles and two neighboring Sq-tiles are avoided. Together, the approximants and the phases from annealing simulations – 25 of them in total – are used as initial structures for numerical relaxation. Each structure is set up as an ideal single crystal of ca. 1000 particles. By running the MD simulation at very low temperature (less than 10^{-3} of the melting temperature), the particle

[4] Justifications and further details will be given in the subsequent sections.

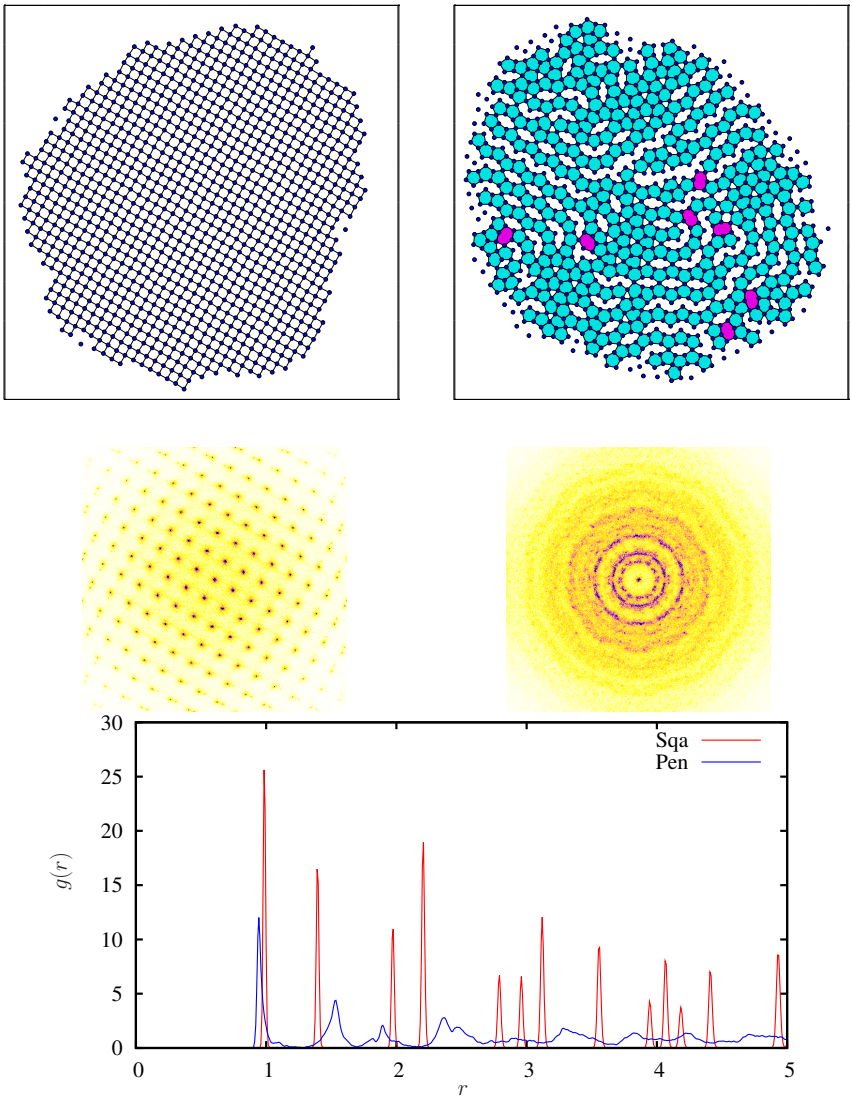

Figure 9.3: Final configuration after two annealing simulations for the parameters $\sigma^2 = 0.02$, $\epsilon = 1.1$, $r_0 = 1.4$ (Sqa, left) and $r_0 = 1.5$ (Pen,right). Diffraction images and radial distribution functions $g(r)$ are shown.

positions are relaxed into the lowest energy configuration. Additionally, the *NPT* ensemble is used to automatically adjust the simulation box dimensions.

In the phase diagram shown in Fig. 9.4 several complex crystals[5] are stable: the phases Pen and Pen2, the decagonal approximants Xi and Xi2, and the dodecagonal approximant Sig. The structure of Pen2 differs from Pen by a small displacement. The three pentagons appearing in the unit cell are deformed. Note that the elongated hexagon of Pen can be decomposed into the triangle of Pen2 and a further deformed pentagon. Xi is a periodic stacking involving *D*-tiles. Xi2 is identical to the cluster tiling of the ξ'-AlPdMn phase as introduced in Fig. 8.3. Sig is the two-dimensional σ-phase. A detailed discussion of the phases will follow in the next sections. The phase diagram in Fig. 9.4 matches quite well the phase observation regions in Fig. 9.2.

The phase diagram in Fig. 9.4 deviates slightly from the one presented in Fig. 3 of [47]. Therein two additional dodecagonal approximants appear, but not the phases Pen2 and Xi2. The reason is an improvement of the computer code for the relaxation procedure. The new phase diagram of Fig. 9.4 is more accurate. The relative changes in potential energy are few tenths of a percent.

A magnification of the most crowded area near Pen and Pen2 is shown in Fig. 9.5. Varying σ^2, the phase diagram changes continuously (Fig. 9.6). Two new phases, a parallel arrangement of obtuse rhombs (Rho2) and a phase built from *Sh*- and *Tr*-tiles (Shi), appear. In general, a smaller value of σ^2 simplifies the formation of complex crystals, because the double-well character of the potential is enhanced. A larger value of σ^2 on the other hand, leads to an easier formation of the hexagonal phases, since the potential approaches a conventional single-well potential shape.

The location of the stability regions can be understood from the near-neighbor configuration. Local n-fold order, i.e. a regular n-gon, is stabilized for $r_0 \approx 2\cos(\pi/n)$. The Figs. 9.4 and 9.6 confirm this for the phases Sqa ($n = 4$), Hex1 ($n = 6$), and Sig ($n = 12$). Local five-fold order (Pen, Pen2, Xi, Xi2) is found at $r_0 \approx 1.5 < 2\cos(\pi/5) = \tau \approx 1.62$ as a result of the competition with the close-packed phase Hex1. The phase Sig is intermediate to Hex1 and Sqa.

[5] We use the term 'complex', if at least one lattice constant is larger than the potential cut-off, which means that the unit cells have to be stabilized indirectly.

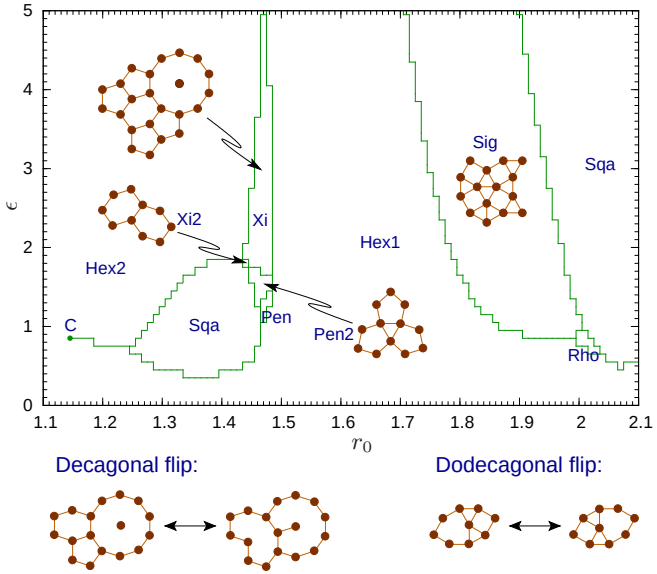

Figure 9.4: Phase diagram at $T = 0$ with $\sigma^2 = 0.02$ from relaxation simulations. Phason flips correspond to local tile rearrangements.

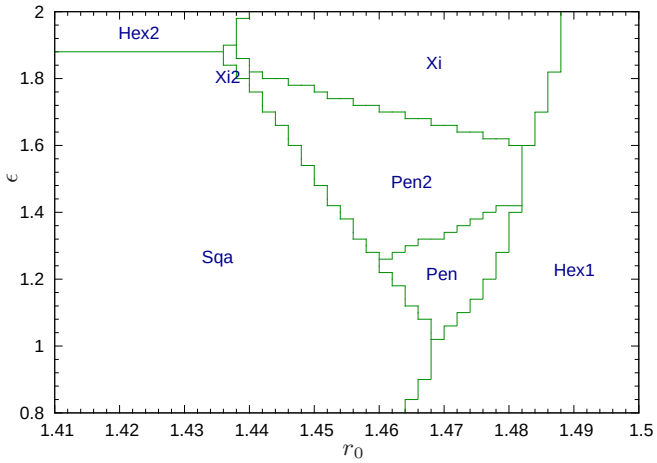

Figure 9.5: Magnified section of Fig. 9.4 near the pentagon phases.

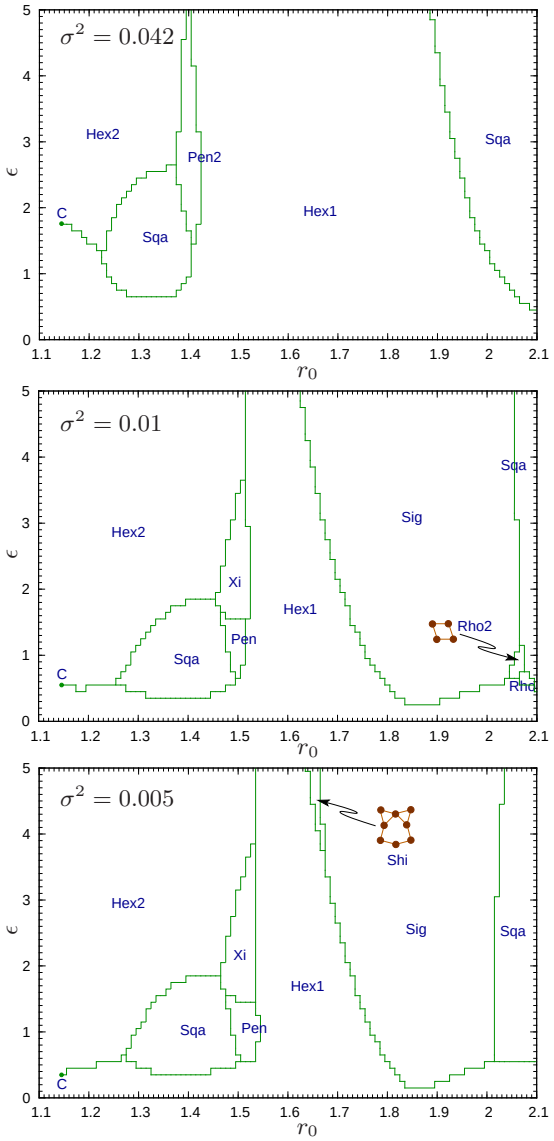

Figure 9.6: Phase diagrams of the LJG-potential for various values of σ^2.

9.3. Decagonal quasicrystal and the Xi-phase

We study the formation of the decagonal quasicrystal in detail using the parameters

$$r_0 = 1.52, \quad \epsilon = 1.8, \quad \text{and} \quad \sigma^2 = 0.02 \tag{9.2}$$

(indicated by a cross in Fig. 9.3). With these parameters, the decagonal quasicrystal grows with few defects at elevated temperatures. As we will see, upon lowering the temperature a reversible phase transition to the Xi-phase occurs. However, the approximant Xi is not the global ground state. The phase Hex2 is still more stable at low temperatures as shown in the phase diagram, Fig. 9.4. But we are not concerned with this phase, since it does not play a role in the simulations: its nucleation radius is too big. Although for smaller r_0 values the approximant Xi can be made stable down to $T = 0$, we still chose $r_0 = 1.52$, because the formation of the decagonal phase seems to be easiest and fastest there.

Let us comment on the value of σ^2. The dynamics of the complex phases is controlled by the potential hill between the minima. A high potential hill leads to a low phason flip frequency and slow phase transitions, at least in MD. On the other hand, as we have seen, a too low potential hill does not stabilize complex phases. Choosing $\sigma^2 = 0.02$ constitutes a compromise between high flip frequency and stability.

9.3.1. Phase transformation liquid – quasicrystal

The MD simulation is started in the liquid at $T = 0.7$ using 1600 particles and the NPT-ensemble. Both, periodic boundary and open boundary conditions are applied. We slowly cool down to $T = 0.4$ and then heat up again to $T = 0.7$.

The potential energy is plotted as a function of temperature in Fig. 9.7. A first order phase transition is observed during solidification/melting, including a hysteresis as a result of undercooling and superheating. In the case of open boundaries, the potential energy is higher due to the additional surface energy. Furthermore, the transition temperature is slightly higher, and the hysteresis smaller for open boundaries. In the case of periodic boundary conditions we used longer simulations to get a more accurate value for the melting temperature:

$$T_M = 0.56 \pm 0.02. \tag{9.3}$$

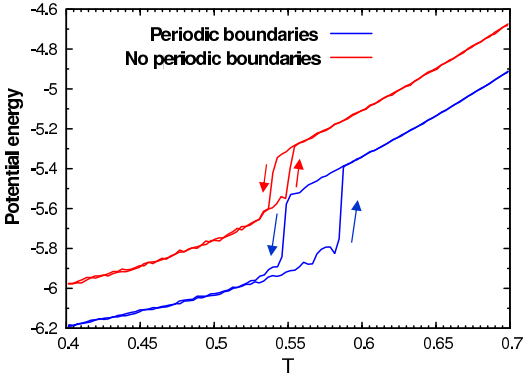

Figure 9.7: Potential energy as a function of temperature. A transition between liquid and decagonal quasicrystal is observed.

In Fig. 9.8 the volume of the system is shown. Coming from the high temperature regime, it strongly decreases due to the high thermal expansion of the liquid. At the melting point the volume jumps upwards – and then continues to fall, although the decrease is slower in the solid. In fact close to the melting point, the global minimum of the volume is observed. The behavior is known as anomalous thermal expansion.[6] Interestingly, anomalous thermal expansion has previously been observed in other two-scale potentials [33, 82].[7] Note that we do not show the volume of the system with open boundaries, since it is not well defined.

The reason for the thermal expansion during solidification is the formation of relatively open local configurations in the quasicrystal. One of them is the decagon tile D. We measure the number of decagons during the simulation run in Fig. 9.9. A few decagons are already found in the liquid, but a sharp increase occurs at the melting temperature. In the quasicrystal state the decagon number keeps increasing during the lowering of the temperature. This is an indication that the quasicrystal is not static, but changes continuously with temperature. Its structure seems to be very flexible. As expected, without periodic boundaries fewer decagons are observed.

[6] An example for a liquid with anomalous thermal expansion is water.

[7] A systematic investigation of the appearance of anomalous behavior in two-scale potentials would be interesting.

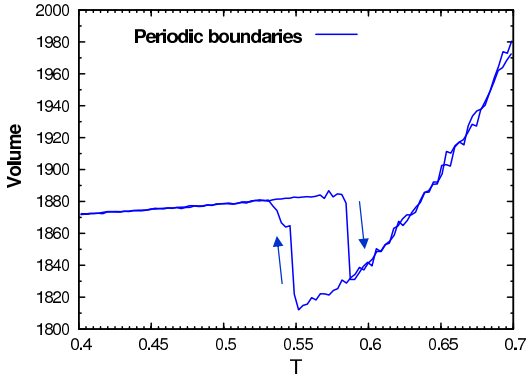

Figure 9.8: Volume as a function of temperature. The crystallization of the decagonal quasicrystal is accompanied by anomalous thermal expansion.

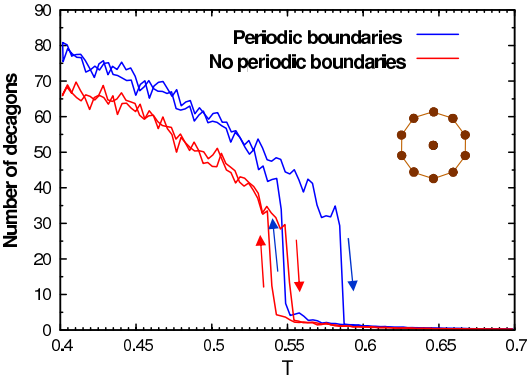

Figure 9.9: Number of decagons as a function of temperature. In the liquid only few decagons appear.

In Fig. 9.10 we show three snapshots from the cool down stage. In the first (top, left) the temperature is $T = 0.7$. Already in the liquid phase, local five-fold configurations are observed frequently. The diffraction image is isotropic. At $T_M = 0.56$ (top, right), the D-tiles (yellow) appear. An amorphous state with local decagonal order is formed rapidly. Then, multiple grains of the quasicrystal start to grow. The bigger ones increase

their size, until only one single grain remains. At $T = 0.45$ (middle, left), the decagonal symmetry is clearly visible in the diffraction image.

Three types of point defects appear in the quasicrystal as shown on the middle, right-hand side: vacancies (A), interstitials (B), and defect tiles (C). A defect tile is a tile, which does not appear in the energy ground state, i.e. it is different from the tiles shown in Fig. 9.2. The defect equilibrium density strongly decreases upon lowering the temperature. A small deformation of the tiles due to phonon motion is observed.

9.3.2. High-temperature equilibrium

We use a larger sample of 10 000 particles to study the decagonal phase in thermal equilibrium. The temperature is close to the melting temperature: $T = 0.50 = 0.9\, T_M$. Again, the system is started in the amorphous phase. Periodic boundaries and the NPT ensemble are used. After about 10^7 MD steps the initial crystallization is complete, and only one single grain remains. We continue the simulation up to $30 \cdot 10^7$ steps, healing out point defects and improving the quasiperiodicity. At the end, the sample is quenched to $T = 0$ and relaxed. We color the tiles according to the local configuration (Fig. 9.11, top). Most of the tiling is covered by the five basic tiles of the Tübingen tiling. The structure has no perfect quasicrystal order, but is in the random tiling state. Nevertheless, when viewed on an oblique angle, the (algebraic) long-range order of the quasicrystal is obvious:[8] The particles are arranged on straight lines. Their separations – short and long – follow a randomized Fibonacci sequence.

The diffraction image (Fig. 9.12, top) shows a perfect decagonal symmetry. A high number of Bragg peaks appear. Furthermore, there is a weak pattern of intrinsic diffuse scattering due to the randomness, forming yellow halos around the Bragg peaks. The innermost ring of Bragg peaks that is visible in the figure corresponds to the nearest distance $d = 3.98$ of the center of two decagon tiles. On larger scales the tiling is correlated only weakly. The radial distribution function in Fig. 9.12, bottom has sharp peaks near the minima of the potential at $r_1 = 0.95$ and $r_2 = 1.53$. A third and a fourth smaller peak are found at $r_3 = 1.79$ and $r_4 = 2.04$.

[8] Of course at finite temperature only algebraic long-range order exists in two dimensions, see Sec. 4.5.

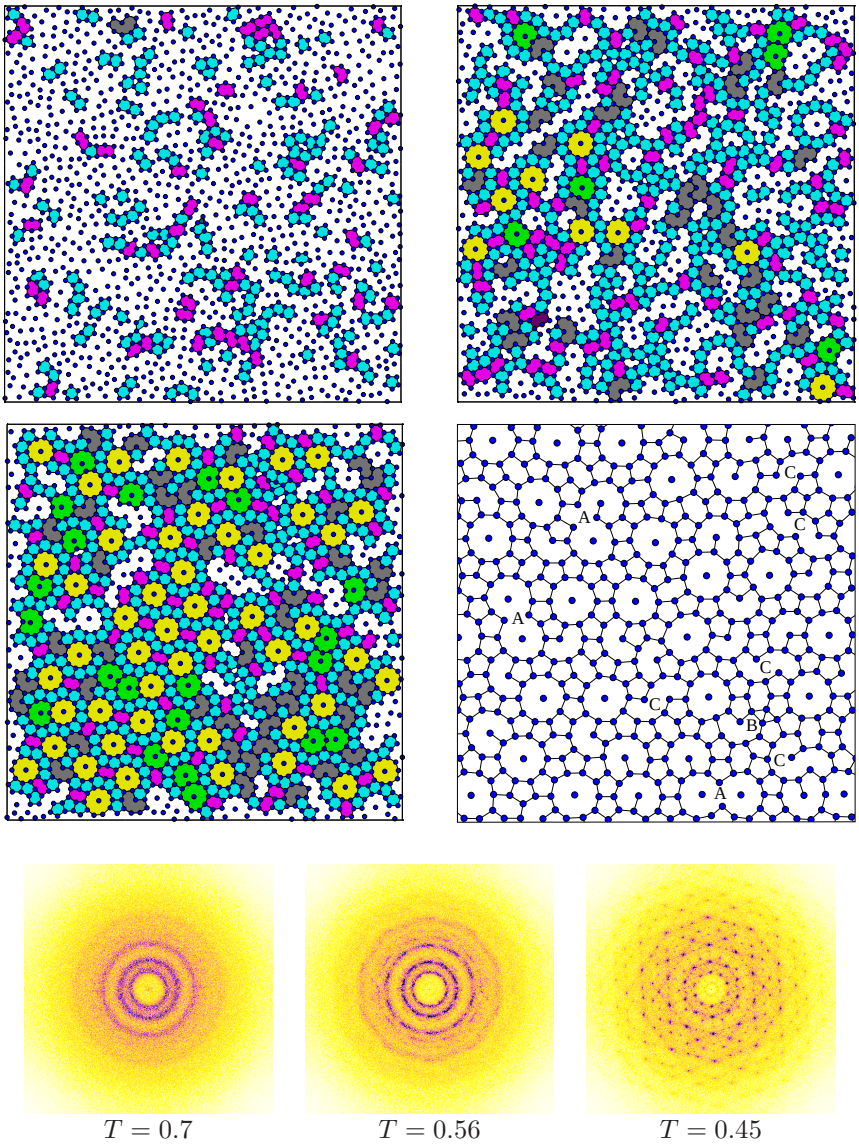

Figure 9.10: Simulation snapshots during the quasicrystal formation. See text.

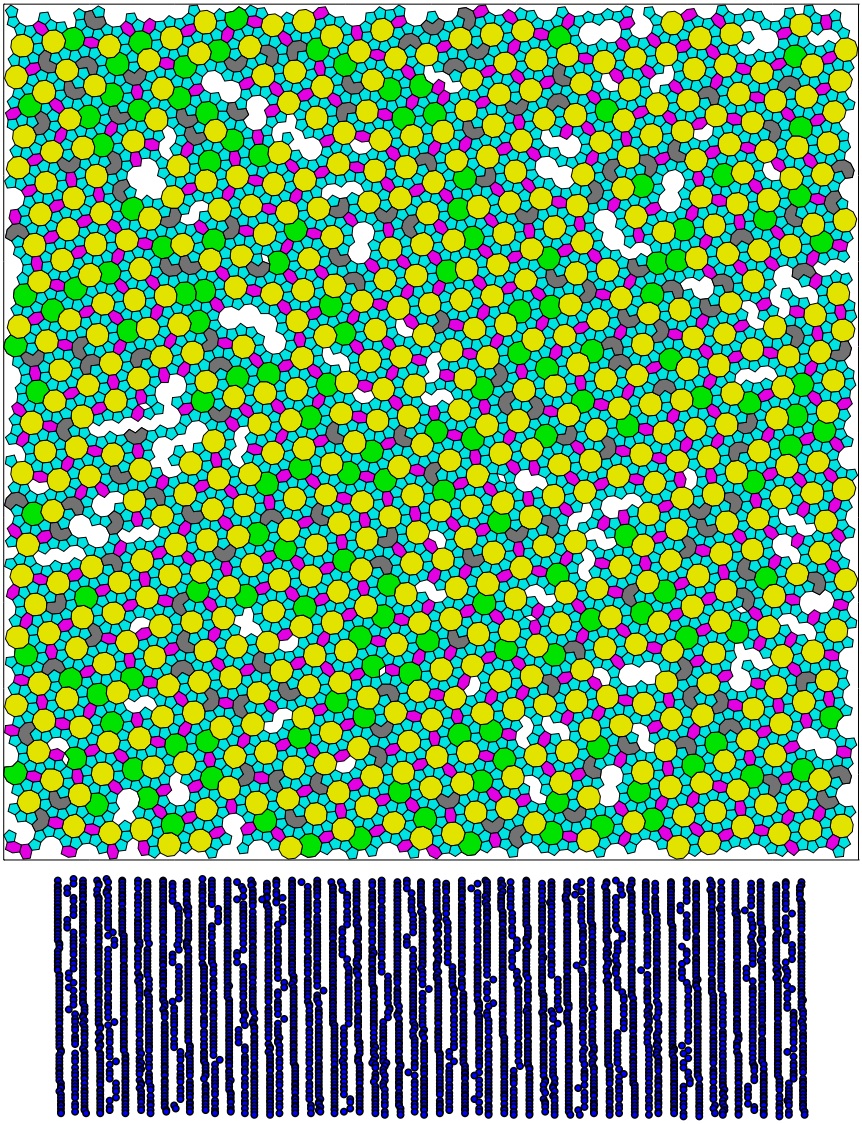

Figure 9.11: Top: Tiling of the decagonal quasicrystal, grown with MD simulation. Bottom: Oblique view of a part of the sample.

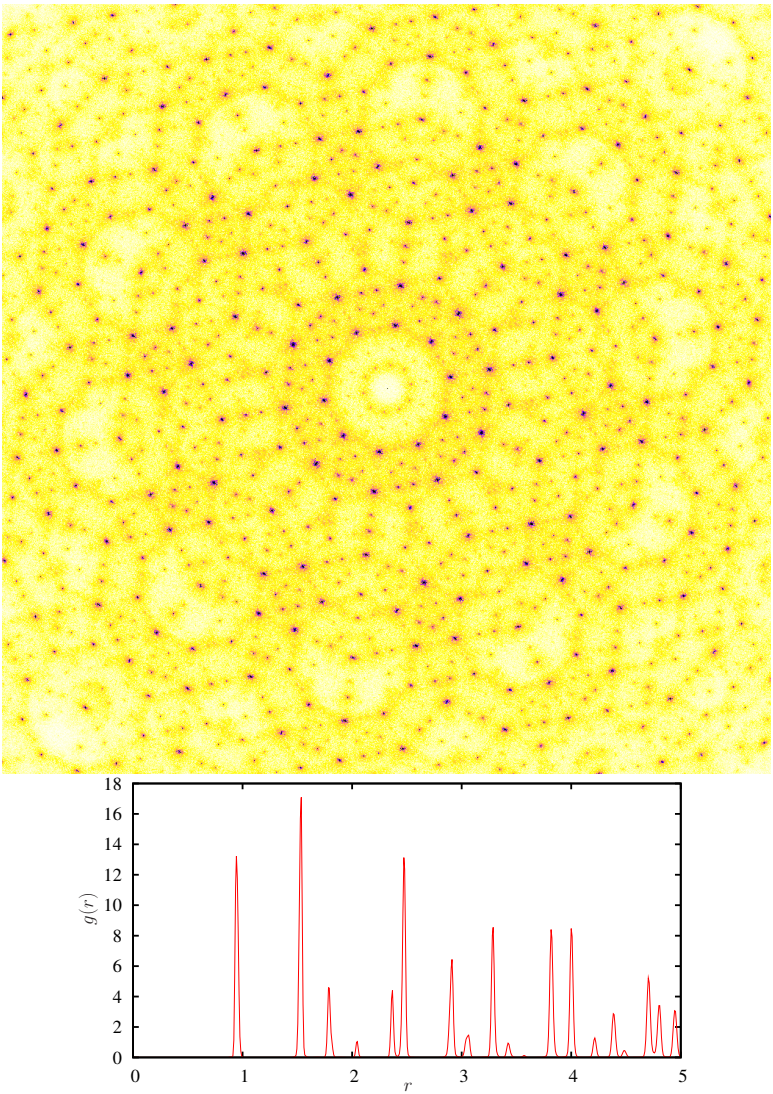

Figure 9.12: (Top) Diffraction image and (bottom) radial distribution function $g(r)$ of the decagonal quasicrystal in Fig. 9.11.

For pair potentials the potential energy E of a tiling[9] is given by the radial distribution function and the interaction potential V only:

$$E = \alpha \int g(r)V(r)\ r\mathrm{d}r, \tag{9.4}$$

with a constant α. Thus, we can determine E by looking at the peak positions in $g(r)$. Since the bonds of the tilings are drawn from the nearest neighbor connections, they correspond to the first peak at r_1. According to (9.4), this peak stabilizes single tiles, but does not prefer any arrangement of the tiles. It can be shown that the second-, third-, and fourth-nearest neighbor connections corresponding to r_2, r_3, and r_4 do not cross the boundaries of the tiles. Therefore, they also do not link neighboring tiles energetically. Further peaks at $r > 2.3$ are not important for the stabilization, because the potential has already decayed significantly. Together, this means that there are no matching rules in the tiling. The decagonal phase is stabilized completely indirectly by geometric constraints.

We calculate the potential energy of a hypothetical tiling built from a single tile only. To do so, we assign to each peak at position r_i a coordination number C_i, which is equal to the number of neighbors corresponding to that peak. For C_1, bonds contribute $1/2$ to avoid counting them twice. Additionally, N is the effective number of particles per tile: Each particle on the tile boundary contributes $2\pi/\phi$ to N. ϕ denotes the interior angle formed by the tile boundaries at the position of the particle. A particle inside the tile contributes a factor of 1. Using (9.4), the potential energy is given by

$$E = \frac{1}{N} \sum_{i=1}^{4} V(r_i)C_i. \tag{9.5}$$

A comparison of the tiles in Tab. 9.1 shows that the smallest tile, P, has the lowest potential energy, and the largest tile, D, the highest. However, a periodic tiling is of course not possible with the P-tile alone. So why is e.g. the tile D formed? To see this, we take a look at the potential energy of the decagonal phase: It is $E = -6.66$. This number is lower than the values for all tiles but the P-tile. Paradoxically, as we show later, the tiling with the highest density of D-tiles is the one with the lowest potential energy. It will turn out that this is the approximant Xi.

[9] We normalize the potential energy to the number of particles involved, i.e. it is a potential energy per particle.

Tile type	Coordination numbers C_1	C_2	C_3	C_4	Eff. particle number N	Potential energy E
P	2.5	5	0	0	1.5	-7.85
H	3	5	2	2	2	-6.44
N	4.5	8	4	2	3.5	-5.90
U	6	11	7	2	5	-5.75
D	5	10	10	0	5	-5.41

Table 9.1: Comparison of the five basic tiles. E is the potential energy of a hypothetical tiling built from a single tile only.

9.3.3. Phason flips

The particle dynamics of the quasicrystal differs significantly from what is known from simple crystals. Local rearrangements frequently occur due to phason flips. In Fig. 9.13 two simulation snapshots are shown. The starting positions of the particles are drawn as blue circles, the end positions after 10 000 MD time steps as red circles. In both cases the configuration has been quenched to $T = 0$ to remove phonon motion. It is clearly seen in the figure that only few particles have moved in-between the two snapshots. Actually, most of the end positions are not seen, because the red and blue circles overlap. We show three exemplary situations on the right-hand side of the figure: A single particle flip (top), an instantaneous, circular flip of four particles (middle), and a joint flip of two particles (bottom).

With the five basic tiles of Fig. 9.2, five flips are possible. They are shown at the bottom of Fig. 3.4. Based on the tile energies (Tab. 9.1), the total potential energy gains/losses for those flips are:

$$\Delta E(DU \rightarrow UD) = 0, \tag{9.6}$$
$$\Delta E(UN \rightarrow DHP) = -2.30, \tag{9.7}$$
$$\Delta E(UU \rightarrow DNP) = -1.98, \tag{9.8}$$
$$\Delta E(NPN \rightarrow UHP) = -0.33, \tag{9.9}$$
$$\Delta E(NHP \rightarrow HPN) = 0. \tag{9.10}$$

For the phason flips (9.7)–(9.9) the energy decreases. In general, certain flips are energetically more favorable than others. It is observed that the

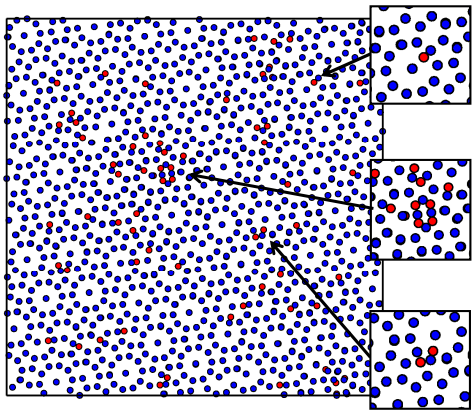

Figure 9.13: Observation of phason flips in the decagonal quasicrystal. The particle position at the beginning are shown in blue, the ones after 10 000 MD time steps in red.

largest tile on the right-hand side is larger than the largest one on the left-hand side. As a rough rule one can summarize: The formation of larger tiles (according to the sequence $P \to H \to N \to U \to D$) leads to an energy gain. This explains why the bigger tiles are formed. Of course there are also other flips, which involve defect tiles, vacancies or interstitials. However, there is no systematic way to analyze all of them.

To measure the possible flip distances and directions, we calculate the particle density autocorrelation function $G_\mathrm{a}(\boldsymbol{x}, t)$ as introduced in (4.22). We fix t at 10 000 MD steps and determine for each particle n the separation between its position at the beginning and after 10 000 steps:

$$\Delta\boldsymbol{x}_n(10\,000 \text{ steps}) = \boldsymbol{x}_n(10\,000 \text{ steps}) - \boldsymbol{x}_n(0 \text{ steps}). \tag{9.11}$$

The probability density $P(\Delta\boldsymbol{x}_n(10\,000 \text{ steps}))$, averaged over all particles and many MD steps, is identical to $G_\mathrm{a}(\boldsymbol{x}, 10\,000 \text{ steps})$. In a simple crystal G_a has a maximum at $\boldsymbol{x} = 0$ and continuously declines outwards. In the decagonal quasicrystal several maxima are observed as shown in Fig. 9.14. Each of them corresponds to a unique sequence of phason flips. Of course, the decagonal symmetry is reproduced also in G_a. Whereas the particles near the central peak have not flipped at all, the first ring of peaks corresponds to particles that have effectively flipped once. There is, in fact,

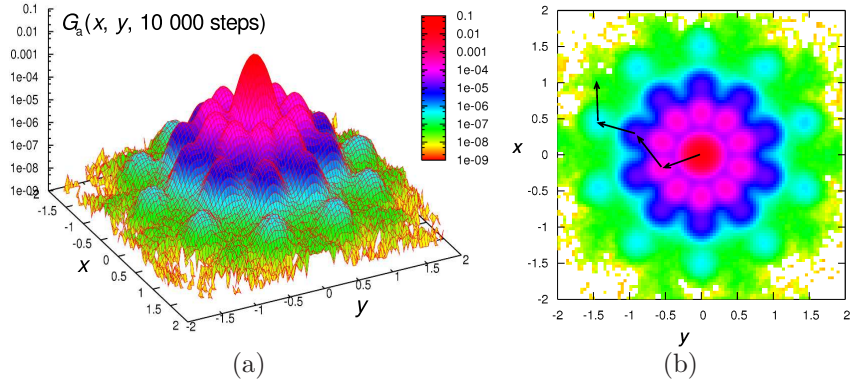

Figure 9.14: The autocorrelation function $G_a(x, y, 10000 \text{ steps})$ (a) three-dimensional and (b) in projection. Up to four consecutive flips are visible. The temperature is $T = 0.45$.

only one flip distance, which is given by the distance of the two potential minima: $\Delta x = 0.6$. The particles of the next ring have flipped two times, etc. In total, up to four consecutive flips can be spotted. However, the probability decreases exponentially with the number of flips (within the 10 000 MD steps).

Next, we determine the flip frequency as a function of temperature. The sample with 10 000 particles is simulated for 10^5 MD steps at each temperature in the interval $T \in [0.15, 0.65]$, $\Delta T = 0.01$, starting from the low temperature regime. Periodic boundary conditions are applied. A phason flip is identified as follows: If the distance of the momentary particle position from the average position – measured since the last flip – is larger than half of the flip distance, then the particle is said to have flipped. We checked in some examples that the algorithm indeed works the way intended. As a result (Fig. 9.15), an Arrhenius law is obtained. At high temperature the flip frequency ν seems to saturate slightly. At $T = 0.59$ the melting transition occurs.[10] Near the melting transition the average flip frequency is 10^{-4} per MD step and per particle. The number has to be compared with the average vibration time of a particle in its local potential minimum, which is of the order of $10 - 100$ MD steps. This

[10] Above the melting transition the determination of phason flips is meaningless.

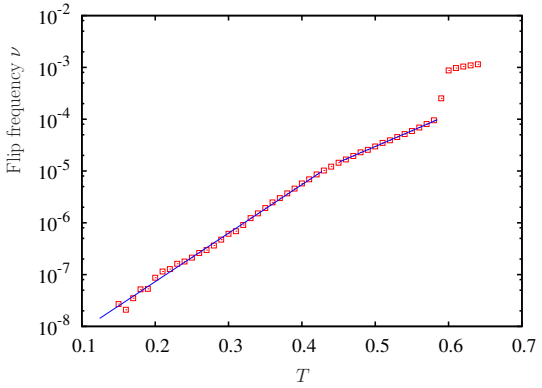

Figure 9.15: Average flip frequency as a function of temperature. At $T = 0.59$ the melting transition occurs.

means that there is one phason flip per $100 - 1000$ phonon vibrations. As an application, we can calculate the total number of phason flips that lead to the large quasicrystal of Fig. 9.11: $\nu_{\text{total}} \approx 10^8$.

9.3.4. Low-temperature transformation to the Xi-phase

From the annealing simulations at $T = 0$ we know that not the decagonal quasicrystal is the energy ground state, but the complex crystal Xi. Their potential energies are very similar: they are $E_{\text{Dec}} = -6.66$ and $E_{\text{Xi}} = -6.70$, respectively. However, because the quasicrystal has the additional freedom of local structural rearrangements by phason flips, its entropy is higher than the entropy of the Xi-phase, which has contributions by the phonon motion only. Therefore, there has to be a phase transition from the entropically stabilized quasicrystal to the energetically stabilized Xi-phase. Indeed, this is exactly what is found in the simulations, as we show now. Ample use of the hyperspace methods, introduced in chapter 2, will be necessary. We adopt the basis and notations introduced in Sec. 3.4. The general theory of elasticity of the decagonal quasicrystal has been covered in Sec. 4.3.1.

The decagonal random tiling can be embedded as a discrete de Bruijn surface in a four-dimensional hyperlattice by noting that the tiling vertices are integer multiples of four basis vectors $\boldsymbol{b}_i$, given by the basis matrix

(3.11).[11] Although the average orientation of the surface is fixed by the decagonal symmetry, phason flips lead to local fluctuations in the phason displacement $\boldsymbol{u}^{\perp}(\boldsymbol{x})$ resulting in a phason strain $\chi_{ij} = \nabla_i u_j$. According to (4.12), the phason elastic free energy density has the general form $F_{\text{phas}} = \frac{1}{2}\lambda_3\chi_1^2 + \frac{1}{2}\lambda_4\chi_2^2$, where λ_3 and λ_4 are phason elastic constants. The transformation to the phase Xi occurs by a collective rearrangement of the tiling induced by a global change of the de Bruijn surface orientation. For this to happen a huge number of phason flips is necessary, which makes the transition extremely slow.

We perform long simulations over 10^9 steps with 1600 particles and open boundaries. At intermediate temperatures, $T < 0.40$, a reversible change in the tiling is found: The D-tiles arrange preferably in a supertiling of close-packed rhombs with an edge length of 4.0. This is characteristic for the approximant Xi. However, as shown in Fig. 9.16, some defects and stacking faults are still present in the rhomb supertiling. At low temperatures, $T < 0.30$, the flip frequency is too slow to reach equilibrium with MD. Hence we turn to a Monte Carlo (MC) algorithm, which allows sampling the full temperature range from $T = 0.5$ down to zero and back up. As elementary step a random displacement inside a circle of radius 0.7 is used. The large radius allows both local relaxation and phason flips. The squared average phason strains χ_1^2, χ_2^2 are indicators of the de Bruijn surface orientation and thus order parameters for the phase transition.

We measure the phason strains as follows: (i) First, we determine the orientation of the quasicrystal. The directions of the nearest neighbor connections give the main crystallographic axis. This fixes the orientation of the basis $\{\boldsymbol{b}_i\}_i$. (ii) The hyperlattice points corresponding to the particle positions are calculate iteratively. We start at an arbitrary particle P_0. It is mapped to the hyperlattice point $(0,0,0,0)$. (iii) For each nearest neighbor P_j of P_0 we express the separation $\boldsymbol{x}_{P_j} - \boldsymbol{x}_{P_0}$ as an integer linear combination of the basis vectors $\boldsymbol{b}_i$. This maps P_j onto a hyperlattice point. (iv) We iterate, by applying the procedure to the nearest neighbors of P_j. (v) At the end, the hyperlattice points of all particles, and thus the de Bruijn surface is known. We finish by calculating χ_1^2, χ_2^2 from its average orientation. The orientation is obtained via least square fit.

The results of the MC run in Fig. 9.17 show a reversible change of χ_i^2 at

[11] The basis vectors $\boldsymbol{b}_i$ are the projections of hyperlattice basis vectors on physical space E. They are given by the two top entries in the columns of (3.11). The two bottom entries correspond to the projections on perpendicular space.

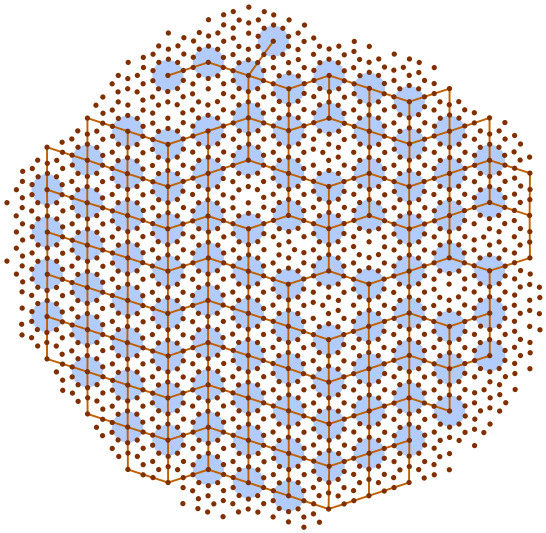

Figure 9.16: Particle configuration in MD simulation at $T = 0.30$. The D-tiles are arranged preferably in a rhomb supertiling.

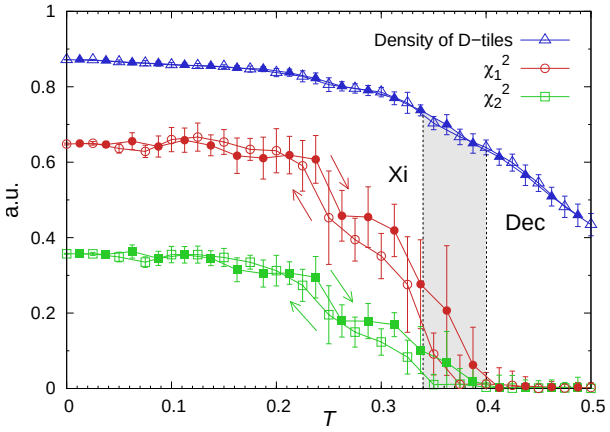

Figure 9.17: MC simulation of the phase transition between the decagonal random tiling and the approximant Xi. The data has been averaged over intermediate temperature intervals. Open symbols: cooling; full symbols: heating. The phason strains χ_i^2 and the density of D-tiles are shown.

the transition temperature

$$T_C = 0.37 \pm 0.03. \tag{9.12}$$

Above T_C, the χ_i^2 are zero, the system is the decagonal random tiling quasicrystal. Near T_C the χ_i^2 fluctuate (see the error bars) and switch for $T > T_C$ to finite values, including a small hysteresis. The system is then in the phase Xi. From the transition temperature and the energy difference given below, we get an estimation for the entropy difference per particle: $S = 0.11$. Note that no clear transition is visible in the density of D-tiles.

The applied boundary conditions are important for observing the phase transformation: With open boundary conditions the phason strain $\chi = (\chi_1, \chi_2)$ is free to fluctuate, although it will do so on a slower and slower scale with increasing system size. With periodic boundary conditions the de Bruijn surface is topologically equivalent to a torus, which means that χ is fixed and can only change via topological defects, e.g. dislocations. For similar topological reasons it is difficult to observe the phase transformation in the bulk. When no boundaries are present, it is easier to form polycrystals instead of single crystals, which can be done by local rearrangements.

Landau theory predicts a first order phase transition between quasicrystals and approximants. However, for our comparably small sample the transition is not sharp, but gradual. One possible reason are finite size effects, whose influence on the phase transition must not be neglected.

9.3.5. Stability of the approximant Xi

From the hyperspace description it follows that each approximant of the decagonal quasicrystal corresponds to a value $\chi \neq 0$. To show that the phase Xi is the energy ground state, we determine the potential energy as a function of the phason strains. We follow [100] and generate a large number of approximants with different values of $\chi = (\chi_1, \chi_2)$. Since for every value an orthorhombic approximant with phason strains arbitrarily close can be found [100], we use χ_1 and χ_2 to parameterize the approximants. In total 2601 orthorhombic approximants with 500 to 40000 particles per unit cell are generated for a sufficently fine mesh in the χ_1-χ_2-plane. Each approximant is simulated for 100 steps with MD and 100 sweeps with MC alternately, while slowly reducing the temperature from $T = 0.3$ down to $T = 0$. Periodic boundaries ensure that the phason strain cannot relax.

This way the approximant is brought into an energy minimum within the restriction of the imposed external phason strain. The MC sweeps are necessary to relax the phason strains, because the lowest energy approximant usually does not have a strictly straight, but slightly modulated de Bruijn surface. A single MC step consists of a random displacement of particles inside a ring with radius $r \in [0.50, 0.66]$, which is the flip distance of the quasicrystal.

At the end of each simulation, the potential energy is determined. The plot as a function of the phason strains in Fig. 9.18 confirms that the approximant Xi is indeed the lowest energy state at $T = 0$. It appears in two variants: parallel arrangement of the supertile rhombs connecting the D-tiles at $\chi_1 = -0.09$, $\chi_2 = -0.05$ and alternating arrangement at $\chi_1 = 0.08$, $\chi_2 = -0.02$. Because the flipping of a row of supertile rhombs does not cost energy,[12] every tiling built from the rhombs has the same energy. We do not distinguish these variants. Together they are all called 'Xi'. The quasiperiodic random tiling corresponds to the saddle point at $\chi_1 = \chi_2 = 0$. It is only metastable at $T = 0$. The phason elastic constants at zero temperature are obtained (with large error ranges) by a quadratic fit: One is positive and the other one negative:

$$\lambda_1 = 1.1, \quad \lambda_2 = -2.1. \tag{9.13}$$

High accuracy is possible by using an adapted selection of approximants with small phason strains, which we have not done. Again, the negativity of λ_2 shows that the quasicrystal is not stable at $T = 0$. The density of D-tiles and the potential energy are correlated: An increase in the number of D-tiles lowers the energy as shown in the contour plots in Fig. 9.18.

We remark that for large phason strains the decagonal symmetry is lost and there are four independent phason strains (the most general case), which means that also non-orthorhombic approximants will play a role. However, since it is not possible to increase the density of D-tiles further, the approximant Xi is also the ground state including non-orthorhombic approximants. Of course, there are also monoclinic variants of the approximant Xi.

Note that the potential energy in Fig. 9.18 is not everywhere a smooth function of the phason strains. Around the origin it is analytic, since the

[12] This is a consequence of the ideal random tiling character of the decagonal quasicrystal: a phason flip does not cost energy, if it does not change the tile types.

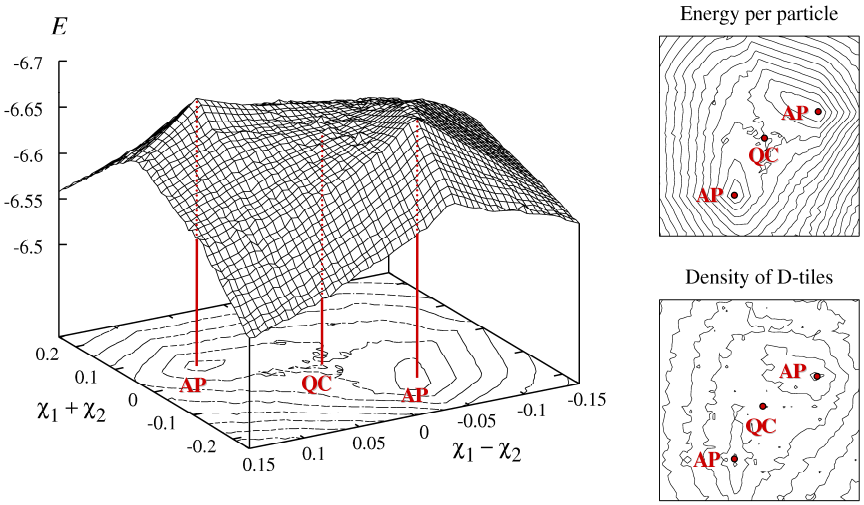

Figure 9.18: Potential energy as a function of the phason strains χ_1, χ_2 for 2601 orthorhombic approximants. Two variants of the approximant Xi (AP) have lowest energy, forming two peaks in the energy surface. (Note the reversal of the energy axis.) The quasicrystal (QC) sits on the saddle point in-between. This is also seen in the contour plots shown on the right-hand side.

quasiperiodic tiling can compensate an imposed external phason strain in a continuous manner. For larger phason strains (beyond the two peaks at the positions of the approximant Xi) there are regions, where it is planar with sharp bends. As a reason for this, phase separations in different approximants are conceivable.[13]

9.4. Dodecagonal quasicrystal I and the Sig-phase

The dodecagonal quasicrystal is found in annealing simulations over a large parameter range as shown in Fig. 9.3. From the relaxation simulations we know that at low temperatures a transformation to the Sig-phase has to occur. Hence, there are similarities to the situation for the decagonal quasicrystal. Many of the methods used there can be directly transferred

[13] A detailed investigation of the phenomenon is left for later work.

to the dodecagonal quasicrystal, but as we will see the dynamics is still quite different.

9.4.1. Growth of the dodecagonal quasicrystal

We arbitrarily choose the parameters

$$\sigma^2 = 0.02, \quad \epsilon = 2.0, \quad r_0 = 1.95. \tag{9.14}$$

This corresponds to a point in the lower middle of the phase observation region of the dodecagonal quasicrystal. The thermodynamic behavior during growth is studied using a MD simulation with 1024 particles. We cool down from $T = 1.1$ to $T = 0.4$ and heat back up. Both, periodic and open boundary conditions are applied. The potential energy as a function of temperature is shown in Fig. 9.19. At high temperature the system is in the hexagonal phase. At

$$T_C = 0.80 \pm 0.03 \tag{9.15}$$

a first order phase transition to the dodecagonal quasicrystal occurs. This is also seen in the second simulation snapshot in Fig. 9.19, which shows the situation right at the moment of the phase transition. The transition is very rapid and occurs along a front, propagating through the sample. Interestingly, the volume again behaves anomalous at the transition. The reason is the close-packing of the hexagonal phase (built from triangles only), in contrast to the dodecagonal phase (built from triangles and squares). There is not much difference between periodic and open boundaries. From the slope $\partial V/\partial T$ it is seen that the thermal expansion of the Hex-phase is larger than for the Dod-phase. The latter is almost zero.

The transformation from the hexagonal phase to the dodecagonal quasicrystal is a result of phonon instabilities. One possibility to see this are the diffraction images. In the bottom right of Fig. 9.19 they are compared for the temperatures $T = 0.85$ (above T_C) and $T = 0.65$ (below T_C). Note that strong diffuse scattering is present already in the hexagonal phase. Even far from the Bragg peaks, diffuse rings are observed. Below T_C new Bragg peaks appear at the maxima of the diffuse scattering. Therefore, the dodecagonal quasicrystal can be understood as an incommensurable, but discrete modulation of the hexagonal phase.

In order to study the dodecagonal quasicrystal close to thermal equilibrium, we simulate a larger sample of 10 000 particles over $5 \cdot 10^6$ MD

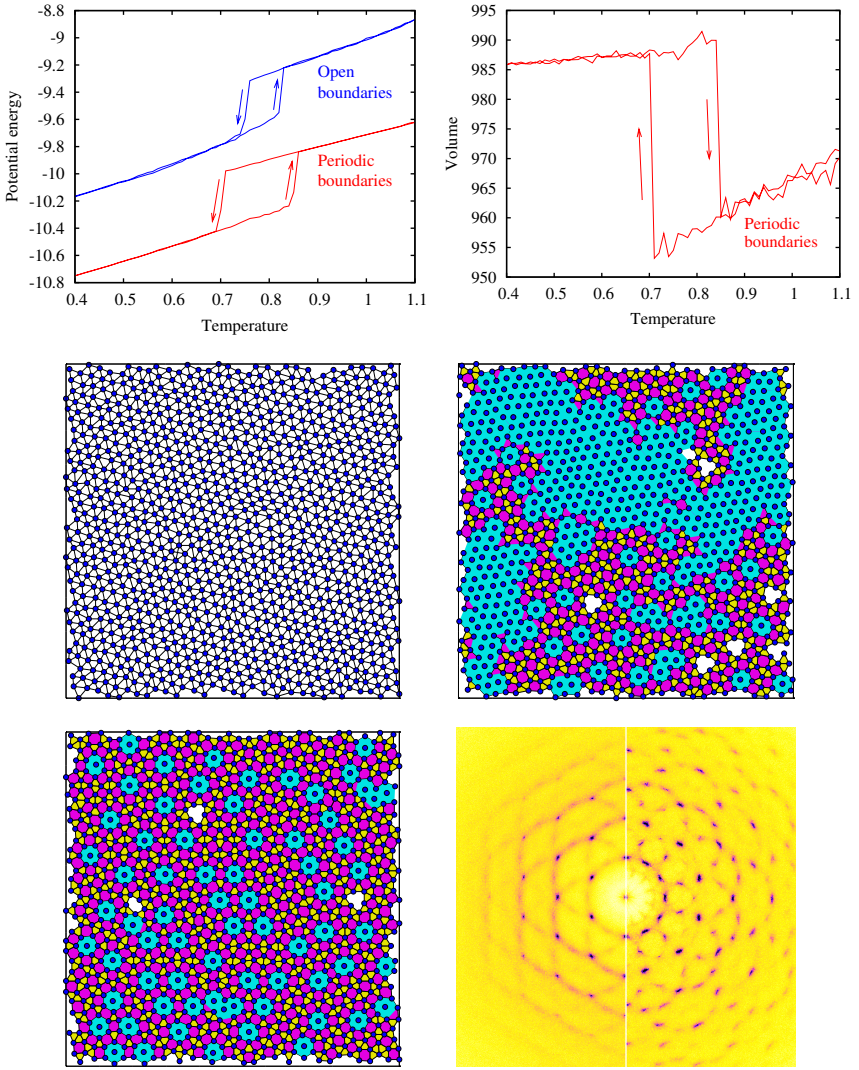

Figure 9.19: (Top) Potential energy and volume as a function of temperature. (Below) Three snapshots during different stages of the simulation. From left to right, top to bottom: $T = 1.0$, $T = 0.7$, $T = 0.4$. (Bottom right) Diffraction image at $T = 0.85$ (left-hand side) and $T = 0.65$ (right-hand side).

steps at $T = 0.5$, which is 60% of the transition temperature. The resulting tiling (Fig. 9.20) is built from the three basic tiles shown in Fig. 9.2: (Sq)are, (Tr)iangle, and (Sh)ield. We color the Tr-tiles in yellow and the Sq-tiles in magenta. The Sh-tiles are kept white. A regular hexagon of six Tr-tiles occurs repeatedly. We use cyan to distinguish it from the other triangles. The tiling has an average dodecagonal symmetry as shown in the diffraction image, although the Bragg peaks are smeared out. In fact, it seems that the dodecagonal phase is not stable at $T = 0.5$. During the simulation, small crystallites are formed locally throughout the sample as seen in the tiling. We assume that in longer simulations the crystallites continue to grow, until finally only a few of them are left. Currently we do not know, whether the quasicrystal is thermodynamically stable at higher temperatures or for other parameter values. However, since the stability region of the Sig-phase in relaxation simulations is very broad, this might well be the case.

9.4.2. Transformation to the Sig-phase via zippers

The dynamics of the dodecagonal quasicrystal is governed by phason flips, but their appearance differs from what has been observed in the decagonal quasicrystal. Whereas in the decagonal phase phason flips are possible at many places in the tiling, the phason flips of the dodecagonal phase are linked irrevocably to the Sh-tiles. A tiling of squares and triangles only would be too dense and phason flips would be impossible. Only the shields allow local rearrangements as shown at the bottom of Fig. 9.4. Since the shield is conserved in the phason flip, we can describe the phason flip dynamics as follows: The Sh-tiles move through the tiling and generate particle rearrangements along their path.

Sh-tiles are not present at zero temperature, because they are energetically unfavored. Sh-tiles are generated either during the phase transformation from the hexagonal phase or at the boundaries of the sample. At finite temperature an equilibrium density of Sh-tiles is present. Historically, the elementary process described here is well-known and is called a zipper. It has originally been studied by Oxborrow and Henley [133]. Note that the zipper is different from the usual vacancy diffusion. In the latter, no rearrangement occurs along the trajectories of the vacancies.

Since zippers are restricted to Sh-tiles, they rearrange the particles much slower than the phason flips in the decagonal quasicrystal. Neverthe-

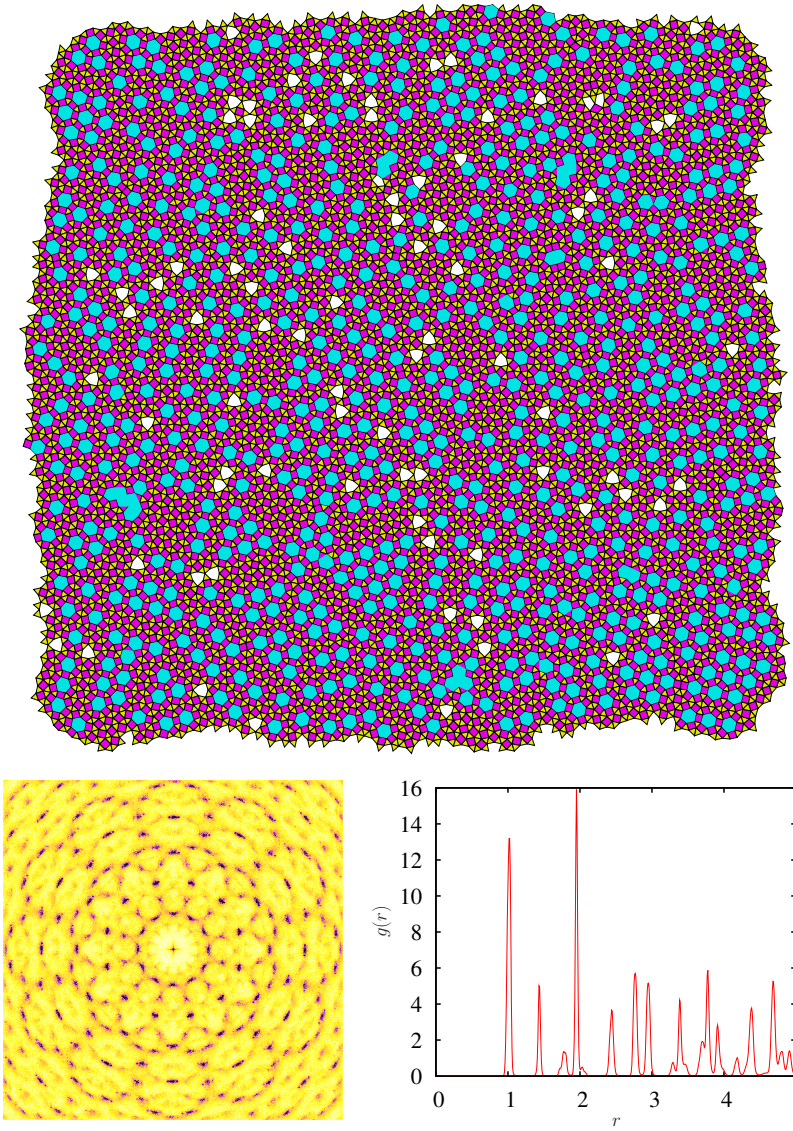

Figure 9.20: The dodecagonal quasicrystal. The basic tiles are triangle (yellow), square (magenta), a hexagon built by six triangles (cyan), and shield (white).

less, zippers are an efficient mechanism for phase transformations. For example, the small crystallites in Fig. 9.20 have grown by zippers only. One can distinguish two kinds of crystallites: (i) Crystallites without Tr-hexagons. They correspond to the Sig-phase, which is the energy ground state. (ii) Crystallites, which are a hexagonal arrangement of Tr-hexagons. They correspond to the triangles in the inflated tiling of Fig. 3.5(b). We call this phase Sig2. Its potential energy is about 1% higher at zero temperature. Why are both crystallites formed, if only the Sig-phase is energetically stable? This is understood from the following consideration: At the beginning, the dodecagonal quasicrystal grows out of the initial, amorphous sample. Neglecting the Sh-tiles, the ideal ratio of Tr-tiles to Sq-tiles in the quasicrystal is (see Sec. 3.5):

$$\#(Sq) : \#(Tr) = 0.302 : 0.698. \tag{9.16}$$

For comparison, we count 4352 triangles and 10375 triangles in the tiling of Fig. 9.20, i.e. a ratio:

$$\#(Sq) : \#(Tr) = 0.296 : 0.704. \tag{9.17}$$

The values (9.16) and (9.17) are almost identical. Furthermore, we have for the Sig-phase

$$\#(Sq) : \#(Tr) = 0.333 : 0.667 \tag{9.18}$$

and for the Sig2-phase

$$\#(Sq) : \#(Tr) = 0.273 : 0.727. \tag{9.19}$$

During a zipper motion the tile types do not change. Hence, the initial ratio (9.17) is preserved[14] and the crystal inevitably has to accept a compromise: Both phases, Sig and Sig2, are formed. The area covered by each of them is approximately equal.

The energy ground state at $T = 0$ is the Sig-phase. We now show that indeed a full transformation can be achieved in MD simulations. To find a suitable parameter set, we check several random choices. In most of them local, but not global crystallization is observed. An easy transformation is obtained with

$$\sigma^2 = 0.01, \quad \epsilon = 2.0, \quad r_0 = 1.75 \tag{9.20}$$

[14] Only at boundaries the tile type can change. It seems that the boundaries do not play a role for the large sample.

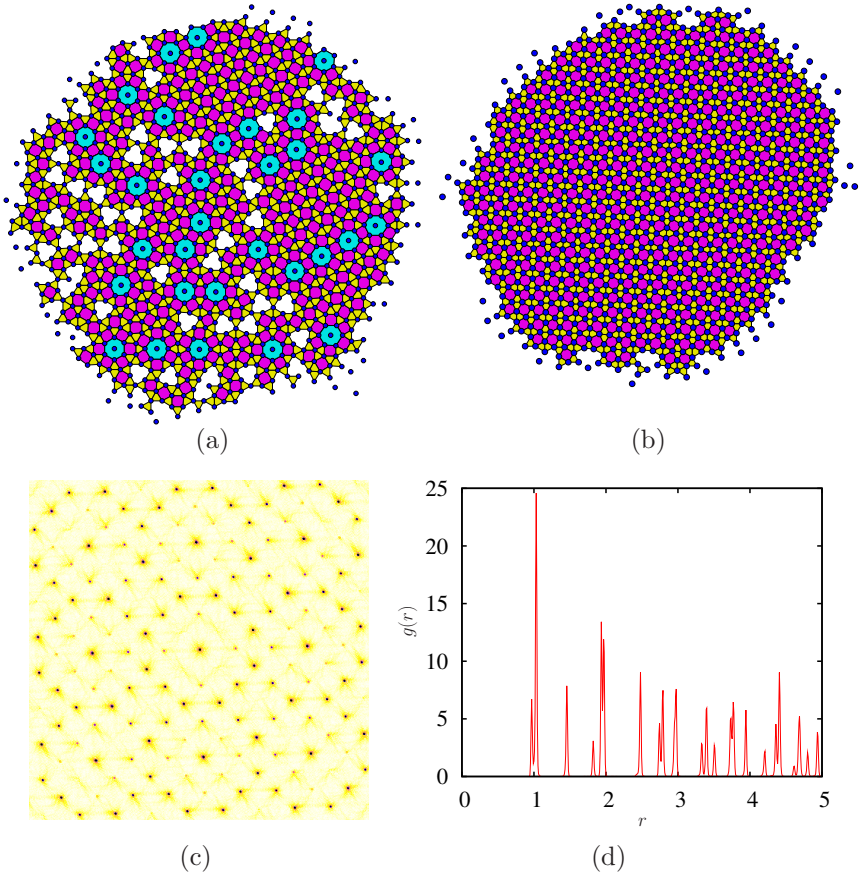

Figure 9.21: The Sig-phase as grown with the parameters $\sigma^2 = 0.01$, $\epsilon = 2.0$, $r_0 = 1.75$ at $T = 0.7$. Snapshots show the tiling after (a) 10^6 and (b) 10^8 MD steps. At the end, the sample is quenched and (c) the diffraction image plus (d) the radial distribution function are calculated. The unit cell of the Sig-phase is quadratic and contains 8 particles.

at $T = 0.7$. We use a sample of 1024 particles and open boundaries to allow the adjustment of the $\#(Sq) : \#(Tr)$ ratio. As shown in Fig. 9.21, at the beginning (after 10^6 MD steps) the sample is in the dodecagonal phase. The Sh-tile density is quite high. Solely by phason flips, a gradual structural transformation starts. After about 10^8 MD steps the crystallization is complete. A single Sig-phase has been grown. Its diffraction image shows four-fold symmetry. There is a splitting of the first peak in the radial distribution function: The bonds in between two triangles are slightly shorter than the bonds along the square edges.

9.5. Dodecagonal quasicrystal II and the Pen2-phase

Let us return to the phase diagrams in the Figs. 9.3–9.6. In total 13 phases have been found: The simple phases Hex1, Hex2, Sqa, Rho, Rho2, and the complex phases Xi, Xi2, Sig, Shi, Pen, Pen2, and the two quasicrystals. They are shown together with their densities, lattice constants, numbers of atoms per unit cell, and plane groups [65] in Tab. 9.2. Since lattice constants and densities depend on the potential parameters, we give the data for the ideal tilings at $T = 0$ with nearest neighbor distance 1.0.

What do we known about them so far? Hex1, Hex2, and Sqa are well understood and not interesting here. Rho and Rho2 are low-temperature phases. Rho is obtained by shifting every second lattice line of the high-temperature phase Hex2. Rho2 corresponds to a shearing of Hex2. A twinning of Rho2 crystallites in two orientations is often observed in simulations.[15] Xi and Sig have already been covered in the previous chapters. They are the low-temperature phases of two quasicrystals. Xi2 is difficult to grow in simulations. It seems to be only stable at low temperatures. Shi appears at high values of the parameter ϵ and low values of σ^2. We do not study the Shi-phase in detail. The phases remaining in our list are Pen and Pen2. As we will see, a randomization of their tiling occurs at high temperatures. The result is a new dodecagonal phase, termed dodecagonal quasicrystal II (Dod II) in contrast to the square-triangle phase of Sec. 9.4, which will be called dodecagonal quasicrystal I (Dod I) in the following.

[15] The transformation Hex2→Rho/Rho2 is interesting. It is triggered by phonon instabilities. We do not study it in detail here, because the phases involved are not structurally complex.

Phase	Density	Lattice constants	Atoms/u.c.	Plane group
Hex1	1.155	$a = 1.00$	1	p6m
Hex2	1.155	$a = 1.00$	1	p6m
Sqa	1.000	$a = 1.00$	1	p4m
Rho	1.051	$a = 1.00$, $b = 1.90$	2	pmg
Rho2	1.051	$a = 1.00$, $\alpha = 72°$	1	cmm
Xi	0.762	$b = 4.24$, $\alpha = 72°$	13	cmm
Xi2	0.803	$a = 1.62$, $b = 3.08$	4	pgg
Sig	1.072	$a = 2.73$	8	p4g
Shi	0.928	$a = 1.93$	3	p31m
Pen	0.898	$a = 2.62$, $b = 4.25$	10	cmm
Pen2	0.998	$a = 2.41$	5	p31m
Dec	≈ 0.76	—	∞	(10-fold)
Dod I	≈ 1.08	—	∞	(12-fold)
Dod II	≈ 0.90	—	∞	(12-fold)

Table 9.2: Structure details of the phases observed with the Lennard-Jones-Gauss potential. Five simple crystals, six complex crystals, and three quasicrystals have been found. The nearest neighbor distance is 1.0.

9.5.1. A new dodecagonal quasicrystal

For the growth of the decagonal quasicrystal and the dodecagonal quasicrystal I the second potential minimum has to be chosen deeper than the first minimum. This suggests searching for a similar ϵ parameters in the stability region of the Pen-phases. From the phase diagrams in Fig. 9.6, we find that Pen2 has a broad range of existence with $\sigma^2 = 0.042$. We choose:

$$\sigma^2 = 0.042, \quad \epsilon = 1.8, \quad r_0 = 1.42. \tag{9.21}$$

r_0 is a bit smaller than the value for the decagonal quasicrystal, σ^2 a factor of two larger. We use MD simulations to study the thermodynamic behavior of 1024 particles between $T = 0.6$ and $T = 0.1$ with periodic and open boundaries. Potential energy and volume are measured as a function of temperature (Fig. 9.22, top).

In the case of open boundaries, the system crystallizes in the dodecagonal

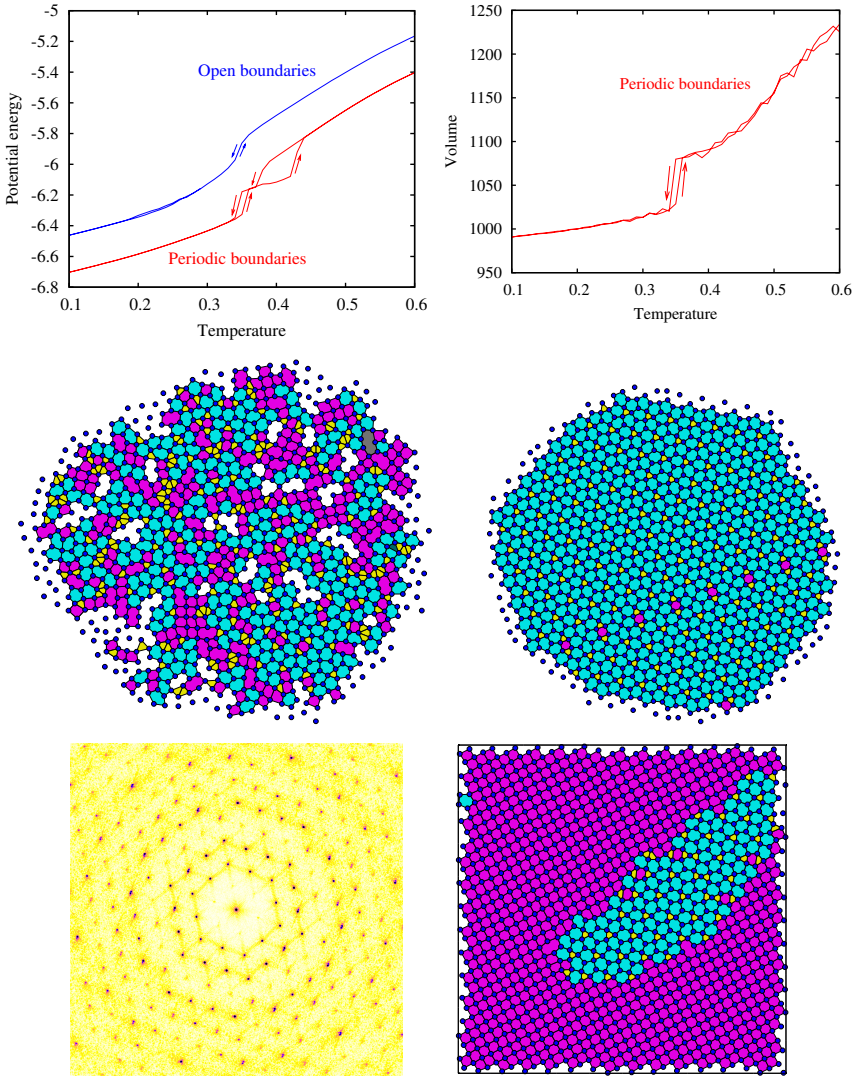

Figure 9.22: (Top) Potential energy and volume. (Middle) Different stages of the simulation: $T = 0.35$ (left) and $T = 0.1$ (right). (Bottom, left) Diffraction image of the tiling in the middle, right sub-figure. (Bottom, right) The phase transformation to Dod II does not occur with periodic boundaries, see text.

quasicrystal II at $T = 0.35$. We show a snapshot of the sample at the beginning of crystallization in Fig. 9.22 (middle, left). The tiling consists mainly of pentagons, triangles, and squares. During crystallization, the number of squares decreases, and the pentagons continuously rearrange and order. At $T = 0.28$ small crystallites of the phase Pen2 appear, and at $T = 0.27$ only two of them are left. We show the final tiling at $T = 0.10$ in Fig. 9.22 (middle, right). The two crystallites are still present at the top and bottom of the sample. They show the pentagons and triangles corresponding to Pen2. The direction of the triangles is reversed in the two crystallites. At the boundary, a line of elongated hexagons (two triangles and one square) is found. Pen2 has triangular symmetry as seen in the diffraction image (Fig. 9.22 bottom, left). Let us come back to the potential energy. There is an accelerated decrease at the melting transition. The transformation to the Pen2-phase, however, cannot be identified. Finite size effects might play a role. We also observe many tiling defects in thermal equilibrium for $0.26 < T < 0.30$, smearing out the phase transition. During the heating stage, the transitions are passed in reverse order: At $T = 0.27$ Pen2 disorders into Dod II, which then melts at $T = 0.35$.

With periodic boundaries, the situation is more complicated. We observe a new phase transformation to the phase Sqa at $T = 0.38$. It seems that the square tiling is stable at high temperatures, when the influence of the boundaries can be neglected. Upon lowering the temperature, Sqa transforms into Dod II. The transformation is difficult without the presence of defects and the system gets stuck in a mixture of Sqa and Pen2, as shown in Fig. 9.22 (bottom, right). In order to accelerate the transformation, we introduce defects by heating up the sample for a short period of time and continue cooling down from $T = 0.35$. This leads to the growth of Dod II at $T < 0.35$. We do not observe a transformation to Pen2 at low temperature. The necessary phason rearrangements are not possible with periodic boundaries. During heating, we find the transition from Dod II to Sqa at $T = 0.36$ and from Sqa to the liquid at $T = 0.43$. The volume is shown as a function of temperature in Fig. 9.22 (top, right). Surprisingly, no signature of the solidification is visible. Only at the solid-solid transformation Sqa→Dod II a volume jump with positive (normal) expansion is found. To summarize: the system passes through the following thermodynamically stable phases:

$$\text{Pen2} \overset{T_{C,1}}{\longleftrightarrow} \text{Dod II} \overset{T_{C,2}}{\longleftrightarrow} \text{Sqa} \overset{T_M}{\longleftrightarrow} \text{Liquid}.$$

The transition temperatures are:

$$T_{C,1} = 0.27 \pm 0.01, \tag{9.22}$$

$$T_{C,2} = 0.35 \pm 0.02, \tag{9.23}$$

$$T_M = 0.40 \pm 0.03. \tag{9.24}$$

9.5.2. Transformation to the Pen2-phase

We want to study the equilibrium phases Dod II, Pen2 and their transformation in detail. We use a sample of 10 000 particles with amorphous starting configuration and periodic boundary conditions. The temperature is chosen above the transition temperature: $T = 0.30$. After $3 \cdot 10^7$ MD steps the sample is quenched to $T = 0$. As usual, we draw the tiling with the nearest neighbor bonds and color the tiles according to the local particle configurations (Fig. 9.23, top). The basic tiles are the pentagon and elongated hexagon, aligned in twelve directions in a quasiperiodic random tiling. Note that the pentagons are not regular, but deformed. As a consequence of the deformation and the random tiling disorder, the radial distribution function (Fig. 9.23, bottom) of Dod II has no sharp peaks.

We repeat the simulations at $T = 0.25$, which is below the transition temperature. This time, open boundary conditions are applied. At the beginning the random tiling of Dod II is quickly formed. After 10^6 MD steps the first Pen2 crystallites appear. After 10^7 MD steps the tiling in the Fig. 9.24 (top) is obtained. Surprisingly, the crystallites approach triangular shapes and form a regular superstructure. Each of the crystallites consists of approximately 350 atoms. Whereas the crystallites have only threefold symmetry, the superstructure is a hexagonal lattice with six-fold symmetry. Neighboring crystallites are related by mirror planes. If we continue the simulations, the lattice constant of the superstructure increases. In Fig. 9.24 (bottom, left) a snapshot after $3 \cdot 10^7$ MD steps is shown. We also tried to grow Pen2 with periodic boundaries, but did not succeed. The radial distribution function of the superstructure has sharp peaks (Fig. 9.23, bottom).

The diffraction images of Dod II and the Pen2 superstructure are shown in Fig. 9.25. Dod II shows twelve-fold symmetry, but with substantial differences compared to the diffraction image of Dod I in Fig. 9.20.[16] The

[16] A few part of the diffraction image seem to have only six-fold symmetry. Finite size effects or the boundary might play a role. Further investigations are necessary.

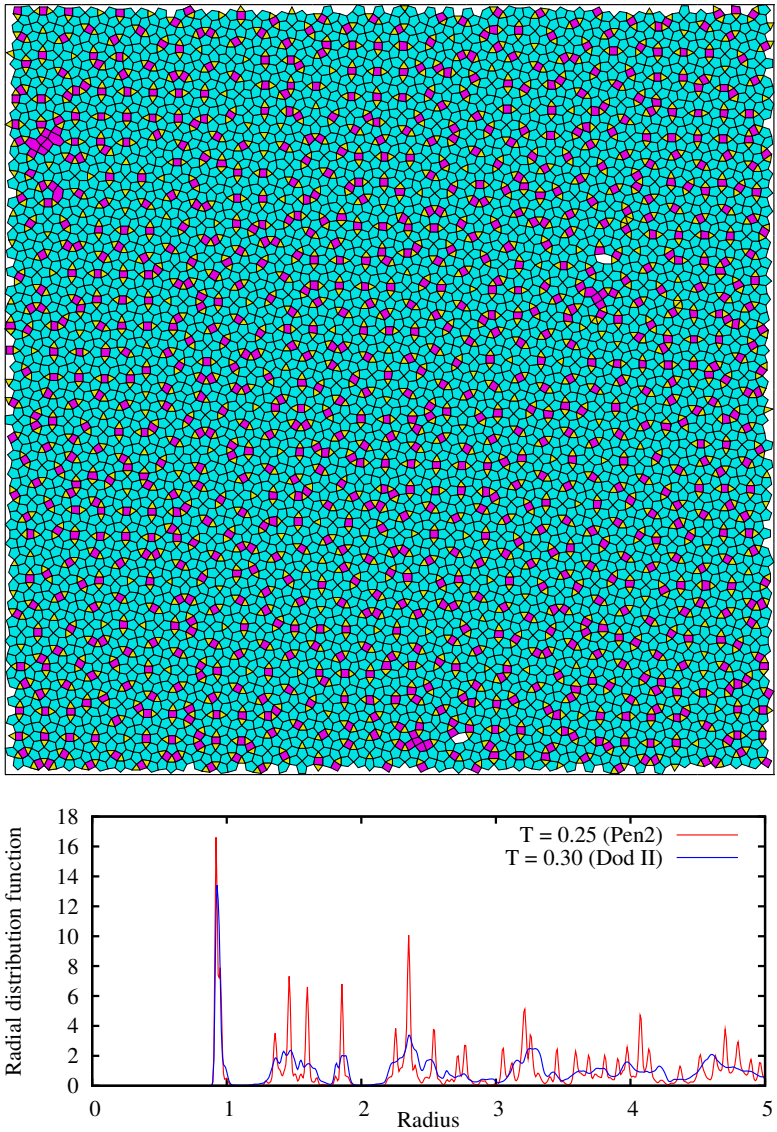

Figure 9.23: (Top) The tiling of Dod II. (Bottom) Radial distribution function.

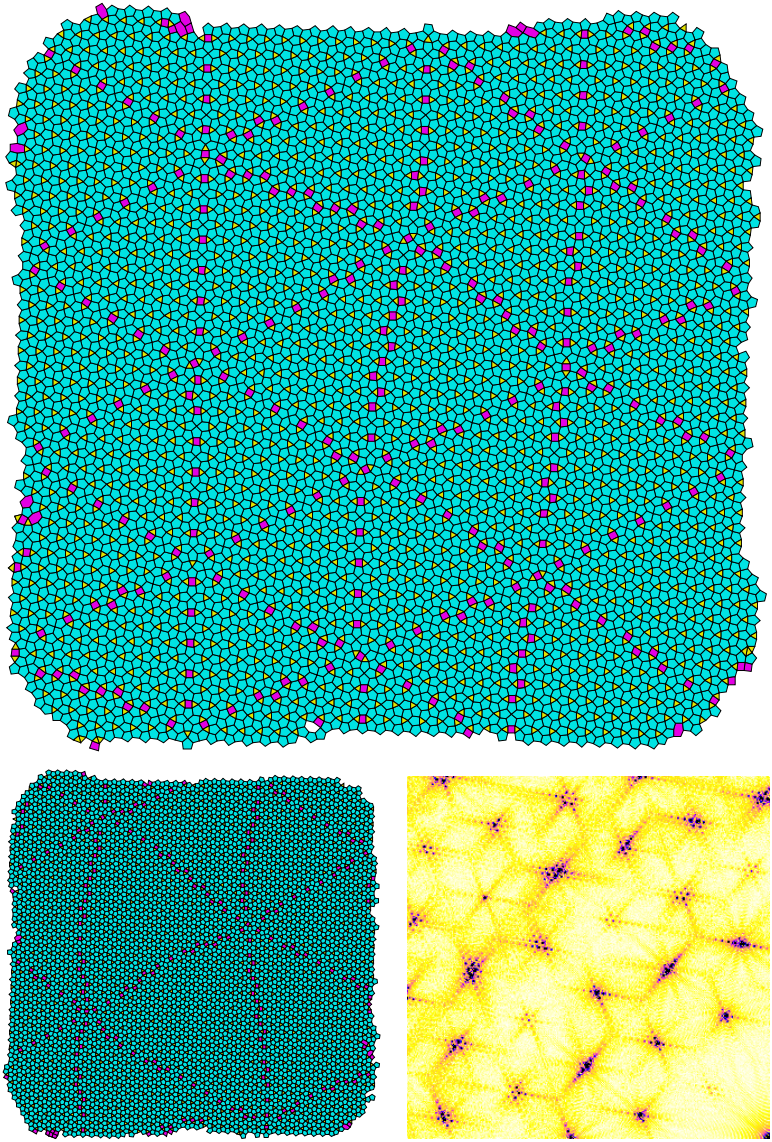

Figure 9.24: Superstructure of Pen2, see text.

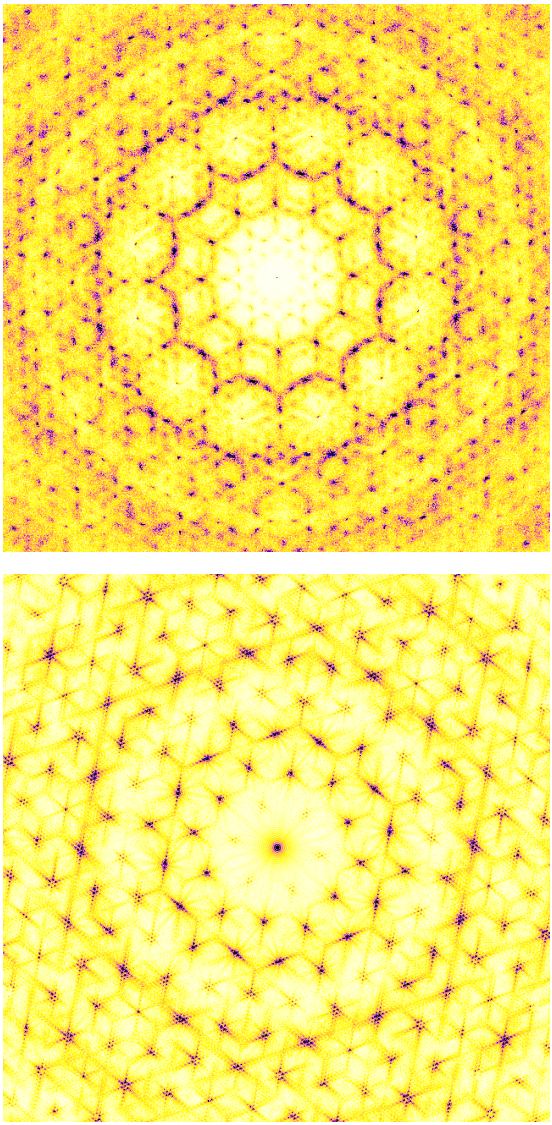

Figure 9.25: Diffraction images of Dod II (top) and the Pen2 superstructure (bottom). Notice the satellite peaks for the superstructure.

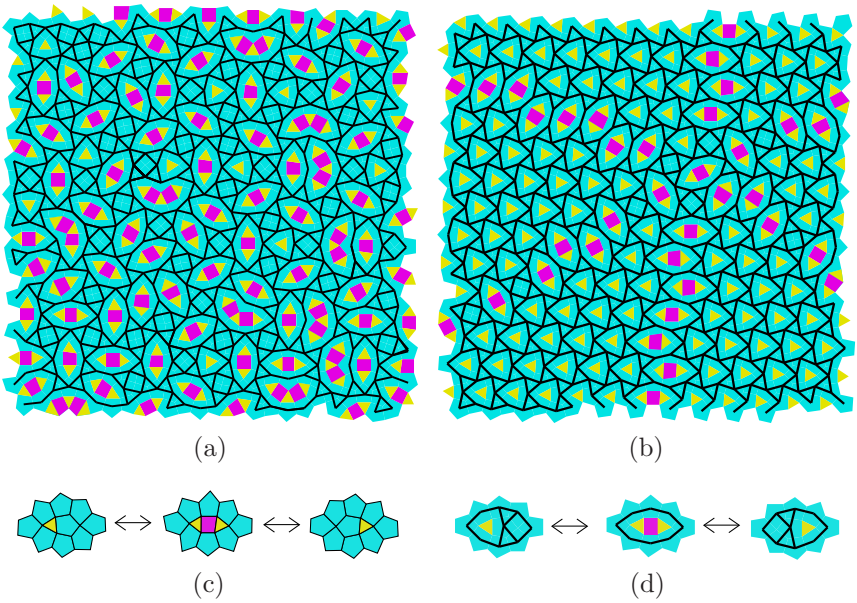

Figure 9.26: The substitution tiling is obtained by connecting the centers of the pentagons. It is a square-triangle-shield tiling. We show the substitution for the tilings found at (a) $T = 0.30$ and (b) $T = 0.25$. The phason flip of Dod II in (c) the original tiling and (d) the substitution tiling is derived from the zipper motion of the square-triangle tiling.

random tiling disorder again leads to a blurring of the Bragg peaks and a lot of diffuse scattering. The main Bragg peak positions are of course identical to the Bragg peak positions of Pen2 in Fig. 9.22. Additionally, satellite peaks show nicely that a superstructure is present. A magnification of the top left quarter of the diffraction image is shown in Fig. 9.24. We checked that the distance between the satellite peaks shrinks during the increase of the supertiling lattice constant.

9.5.3. Relation to the square-triangle-shield tiling

There is a substitution rule, which converts the Dod II tiling into a square-triangle-shield tiling and allows to describe its dynamics by a general zipper

motion. The substitution is obtained by connecting the centers of the the pentagon tiles. This directly results in a tiling which can be reduced (by adding some more lines) to squares, triangles, and shields. Fig. 9.26(a) shows the substitution for a part of the tiling in Fig. 9.23. Fig. 9.26(b) shows the substitution for a part of Fig. 9.24. The elongated hexagons are mapped onto cigar shaped tiles and the single triangles onto shields. The supertiling of Pen2 is a periodic arrangement of shields. It is identical to the tiling of the Shi-phase as introduced in Fig. 9.6.

The dynamics of Dod II is governed by phason flips, whose appearance is explained with the help of the supertiling. Let us consider an elongated hexagon plus the eight surrounding pentagons. The four central atoms, which are the vertices of the magenta square within the elongated hexagon, are very flexible. As depicted in Fig. 9.26(c), they can move collectively in pairs: If the left pair contracts and the right pair expands, then the elongated hexagon splits into a triangle on the left and a new pentagon on the right. If the right pair contracts and the left pair expands, then the triangle remains on the right. The same mechanism in the supertiling corresponds to a reduction of the cigar shaped tile into a shield, a square and two triangles (Fig. 9.26(d)). This shows: the vibration of the two pairs within the elongated hexagons generate a phason flip. The extension of a single flip to the global zipper mode works as seen in the case of Dod I.

Chapter 10.

Summary

In this thesis the influence of structural complexity on the particle dynamics and defects has been studied. We introduced the following new theoretical techniques or numerical methods:

(i) The selection method and its iterative implementation are alternative ways to generate periodic and quasiperiodic tilings from hyperspace models. They are especially useful for tilings with dislocations, because it is easy to take into account arbitrary phason strain fields. However, in the present stage the selection methods are restricted to simple models, because the atomic volumes necessary for the construction are not accessible by experiment. (Secs. 2.3 and 5.5)

(ii) A visualization software was developed for carrying out interactive molecular dynamics and Monte Carlo simulations. Two-dimensional systems are ideally suited for interactive simulations, because up to 10 000 particles can be dealt with in 'real-time' on ordinary desktop computers.[1] Furthermore, it is possible to analyze planar particle configurations easily 'by eye'. We note that interactive simulations have a useful educational purpose, because they demonstrate many basic concepts from thermodynamics and statistical physics. (Sec. 5.4)

(iii) A general theory for the structure factors of low-dimensional systems seems not to exist in the literature yet. By extending the usual phonon expansion for three-dimensional crystals to the one- and two-dimensional harmonic lattices, we have shown that low dimensionality leads to a broadening of the phonon peaks at the reciprocal lattice vectors and along the dispersion relation. The characteristic decay is given by the shape functions. (chapter 6)

[1] With 'real-time' we mean, that the typical phonon vibrations are a matter of tenths of seconds. Crystallization of simple crystal takes place within a few minutes.

The following results have been obtained for the simple model systems:

(i) *Dynamic Fibonacci chain*: We investigated the interplay of phonons and phason flips in one-dimensional systems. This was done by calculating the structure factors of various periodic and quasiperiodic chains with molecular dynamics simulations. The influence of phason flips is mainly a broadening of the characteristic peaks, edges, and branches with temperature. If the interaction potential is chosen asymmetric, dispersionless optic phonon bands split off in the dynamic structure factor. Observations in real space reveal that phason flips are concentrated along propagating phonon modes. If the chain is excited locally, new types of kink solitons and discrete breathers appear. They are closely related to the appearance of phason flips. (chapter 7)

(ii) *Tiling model for the intermetallic system AlPdMn*: We presented a simplified model for complex metallic alloy phases in this ternary system. The position of the main structural building blocks, five-fold cluster columns, are described by the help of simple tripod tilings, which allows to classify the family of Ξ-phases and the family of T-phases. The corresponding three-dimensional hyperspace model predicts enhanced structural flexibility by local rearrangements of the cluster columns via phason flips. We have shown that a direct consequence of the phason degree of freedom is the appearance of complicated partial dislocations, the metadislocations. The tilings and Burgers vectors of metadislocations were calculated. (chapter 8)

(iii) *Lennard-Jones-Gauss system*: A double-well potential reproduces typical interactions as found in elementary metals and alloys. Already in two dimensions and with identical particles, the growth of complex structures can be observed in molecular dynamics and Monte Carlo simulations. We introduced the Lennard-Jones-Gauss potential, which is a double-well potential depending on three parameters. The phase diagram as a function of the parameters is surprisingly rich, considering the simplicity of the system. It consists of 11 different phases, among them three random tiling quasicrystals: a decagonal phase (Dec) and two dodecagonal phases (Dod I and Dod II). This demonstrates that quasicrystals can appear naturally in systems with two competing nearest-neighbor dis-

tances as an attempt to maximize local particle configurations with non-crystallographic symmetry. (Secs. 9.1 and 9.2)

The quasicrystals are stabilized at elevated temperatures by the configurational entropy of the random tiling ensemble. Upon lowering the temperature, reversible transformations to complex crystals were observed for all three quasicrystals. The transformation mechanism depends on the quasicrystal phase. Locally, it has to be a rotation of the de Bruijn surface, as found for Dec. Globally, topological reasons prevent a full transformation. We find in the simulations that the formation of small crystallites (Dod I) or the growth of a periodic superstructures (Dod II) is possible. The equilibrium dynamics and the phase transformations are once more governed by phason flips. (Secs. 9.3–9.5)

Bibliography

[1] Abe, E., S. J. Pennycook, and A. P. Tsai, *Direct observation of a local thermal vibration anomaly in a quasicrystal*, Nature, **421**, 347–350 (2003).

[2] Abramowitz, M. and I. A. Stegun, *Handbook of mathematical functions* (Dover Publications, Incorporated, New York, 1965).

[3] Andersson, S., *Eine Beschreibung komplexer anorganischer Kristallstrukturen*, Angew. Chem., **95**, 67–80 (1983).

[4] Ashraff, J. A. and R. B. Stinchcombe, *Dynamic structure factor for the fibonacci-chain quasicrystal.*, Phys. Rev. B, **39**, 2670–2677 (1989).

[5] Baake, M., R. Klitzing, and M. Schlottmann, *Fractally shaped acceptance domains of quasiperiodic square-triangle tilings with dodecagonal symmetry*, Physica A, **191**, 554–558 (1992).

[6] Baake, M., P. Kramer, M. Schlottmann, and D. Zeidler, *Planar patterns with fivefold symmetry as sections of periodic structures in 4-Space*, Int. J. Mod. Phys. B, **4**, 2217–2268 (1990).

[7] Bak, P., *Phenomenological Theory of Icosahedral Incommensurate ('Quasiperiodic') Order in Mn-Al Alloys*, Phys. Rev. Lett., **54**, 1517–1519 (1985).

[8] Balanetskyy, S., G. Meisterernst, M. Heggen, and M. Feuerbacher, *Reinvestigation of the Al-Mn-Pd alloy system in the vicinity of the T- and R-phases*, Interm. (2008), in press.

[9] Bedanov, V. M., G. V. Gadiyak, and Q. Lozovik, *On a modified Lindemann-like criterion for 2D melting*, Phys. Lett. A, **109**, 289–291 (1985).

[10] Beeli, C., H. U. Nissen, and J. Robadey, *Stable Al-Mn-Pd quasicrystals*, Phil. Mag. Lett., **63**, 87–95 (1991).

[11] Beraha, L., *Modélisation des approximants de la phase icosahédrique Al-Pd-Mn et étude de leurs transformation structurales*, Ph.D. thesis, École Polytechnique, Paris (1997).

[12] Bergman, G., J. L. T. Waugh, and L. Pauling, *The Crystal Structure of the Metallic Phase $Mg_{32}(Al,Zn)_{49}$*, Acta Crystallogr., **10**, 254–259 (1957).

[13] Blüher, R., P. Scharwaechter, W. Frank, and H. Kronmüller, *First Low-Temperature Radiotracer Studies of Diffusion in Icosahedral Quasicrystals*, Phys. Rev. Lett., **80**, 1014–1017 (1998).

[14] Bohsung, J., *Defekte in Quasikristallen*, Master's thesis, Universität Stuttgart (1987).

[15] Boissieu, M., M. Boudard, R. Bellissent, M. Quilichini, B. Hennion, R. Currat, A. I. Goldman, and C. Janot, *Dynamics of the AlPdMn icosahedral phase*, J. Phys. Cond. Mat., **5**, 4945–4966 (1993).

[16] Boudard, M., M. de Boissieu, A. I. Goldman, B. Hennion, R. Bellisent, M. Quilichini, R. Currat, and C. Janot, *Optic modes in the alpdmn icosahedral phase*, Journal Phys. Cond. Matt. (1995).

[17] Bradley, A. J. and J. Thewlis, *The crystal structure of alpha-manganese*, Proc. R. Soc. London, Ser. A, **115**, 456–471 (1927).

[18] Bragg, L. and J. F. Nye, *A dynamical model of a crystal structure*, Proc. R. Soc. London, Ser. A, **A190**, 474–481 (1947).

[19] Brommer, P., *Development and Test of Interaction Potentials for Complex Metallic Alloys*, Ph.D. thesis, Universität Stuttgart (2008).

[20] Caillard, D., C. Roucau, L. Bresson, and D. Gratias, *Dislocation motion in 5-fold planes of icosahedral Al-Pd-Mn*, Acta Mater., **50**, 4499–4509 (2002).

[21] Car, R. and M. Parinello, *Unified approach for molecular dynamics and density–functional theory*, Phys. Rev. Lett., **55**, 2471–2474 (1985).

[22] Caspar, D. L. D. and E. Fontano, *Five-fold symmetry in crystalline quasicrystal lattices*, Proc. Nat. Acad. Sci. U.S.A., **93**, 14271–14278 (1996).

[23] Chen, B., X. Zeng, U. Baumeister, G. Ungar, and C. Tschierske, *Liquid Crystalline Networks Composed of Pentagonal, Square, and Triangular Cylinders*, Science, **307**, 96–99 (2005).

[24] Chisholm, M. F., S. Kumar, and P. Hazzledine, *Dislocations in Complex Materials*, Science, **307**, 701–703 (2005).

[25] Coddens, G., S. Lyonnard, and Y. Calvayrac, *Time scales and atomic species in the phason dynamics of* AlCuFe *quasicrystals*, Phys. Rev. Lett., **78**, 4209–4212 (1997).

[26] Coddens, G., S. Lyonnard, B. Hennion, and Y. Calvayrac, *Correlated Simultaneous Phason Jumps in an Icosahedral* Al-Mn-Pd *Quasicrystal*, Phys. Rev. Lett., **83**, 3226–3229 (1999).

[27] Coddens, G., S. Lyonnard, B. Hennion, and Y. Calvayrac, *Triple-axis neutron-scattering study of phason dynamics in* Al-Mn-Pd *quasicrystals*, Phys. Rev. B, **62**, 6268–6295 (2000).

[28] Crowe, D. W., *Albrecht Dürer and the regular pentagon*, in I. Hargittai (editor), *Fivefold symmetry*, pp. 465–488 (World Scientific, Singapore, 1992).

[29] Daw, M. S. and M. I. Baskes, *Semiempirical, Quantum Mechanical Calculation of Hydrogen Embrittlement in Metals*, Phys. Rev. Lett., **50**, 1285–1288 (1983).

[30] Day, C., *Colloidal particles crystallize in an increasingly wide range of structures*, Phys. Today, **59-6**, 15–17 (2006).

[31] de Boissieu, M., M. Boudard, B. Hennion, R. Bellissent, S. Kycia, A. Goldman, C. Janot, and M. Audier, *Diffuse scattering and phason elasticity in the AlPdMn icosahedral phase*, Phys. Rev. Lett., **75**, 89–92 (1995).

[32] de Bruijn, N. G., *Algebraic theory of Penrose's non-periodic tilings of the plane*, Nederl. Akad. Wetensch. Proceedings of Ser. A, **43**, 39–66 (1981).

[33] de Oliveira, A. B., P. A. Netz, T. Colla, and M. C. Barbosa, *Structural anomalies for a three dimensional isotropic core-softened potential*, J. Chem. Phys., **125**, 124503 (2006).

[34] de Wolff, P. M., *The pseudo-symmetry of modulated crystal structures*, Acta Crystallogr., **A30**, 777–785 (1974).

[35] Dilger, C., *Versetzungsbewegungen in dreidimensionalen Quasikristallen*, Master's thesis, Universität Stuttgart (1995).

[36] Donohue, J., *The structure of the elements* (Krieger Pub. Company, 1982).

[37] Doye, J. P. K. and S. C. Hendy, *On the structure of small lead clusters*, Eur. Phys. J. D, **22**, 99–107 (2003).

[38] Dzugutov, M., *Glass formation in a simple monoatomic liquid with icosahedral inherent local order*, Phys. Rev. A, **46**, R2984 R2987 (1992).

[39] Dzugutov, M., *Formation of a dodecagonal quasicrystalline phase in a simple monatomic liquid*, Phys. Rev. Lett., **70**, 2924–2927 (1993).

[40] Edagawa, K. and Y. G. So, *Experimental evaluation of phonon–phason coupling in icosahedral quasicrystals*, Phil. Mag., **87**, 77–95 (2007).

[41] Edagawa, K., K. Suzuki, and S. Takeuchi, *High Resolution Transmission Electron Microscopy Observation of Thermally Fluctuating Phasons in Decagonal Al-Cu-Co*, Phys. Rev. Lett., **85**, 1674–1677 (2000).

[42] Emery, V. J. and J. D. Axe, *One-Dimensional Fluctuations and the Chain-Ordering Transformation in* $Hg_{3-\delta}AsF_6$, Phys. Rev. Lett., **40**, 1507–1511 (1978).

[43] Engel, M., *Zur Geometrie von Phasonen und Versetzungen in Quasikristallen und ihren Approximanten*, Diplomarbeit, Universität Stuttgart (2004).

[44] Engel, M., S. Sonntag, H. Lipp, and H.-R. Trebin, *Structure factors of harmonic and anharmonic Fibonacci chains by molecular dynamics simulations*, Phys. Rev. B, **75**, 144203 (2007).

[45] Engel, M. and H.-R. Trebin, *A unified projection formalism for the Al-Pd-Mn quasicrystal Ξ-approximants and their metadislocations*, Phil. Mag., **85**, 2227–2247 (2005).

[46] Engel, M. and H.-R. Trebin, *Tiling models for metadislocations in AlPdMn approximants*, Phil. Mag., **86**, 979–984 (2006).

[47] Engel, M. and H.-R. Trebin, *Self-assembly of Monatomic Complex Crystals and Quasicrystals with a Double-Well Interaction potential*, Phys. Rev. Lett., **98**, 225505 (2007).

[48] Engel, M. and H.-R. Trebin, *Stability of the decagonal quasicrystal in the Lennard-Jones-Gauss system*, Submitted (2007).

[49] Ercolessi, F. and J. B. Adams, *Interatomic Potentials from First-Principles Calculations: the Force-Matching Method.*, Europhys. Lett., **26**, 583–588 (1994).

[50] Feuerbacher, M., S. Balanetskyy, and M. Heggen, *Novel metadislocation variants in orthorhombic Al-Pd-Fe*, Acta Mater. (2008), accepted for publication.

[51] Feuerbacher, M. and D. Caillard, *Dynamics of phason diffusion in icosahedral Al-Pd-Mn quasicrystals*, Acta Mater., **54**, 3233–3240 (2006).

[52] Feuerbacher, M., C. Thomas, J. P. A. Makongo, S. Hoffmann, W. Carrillo-Cabrera, R. Cardoso, Y. Grin, G. Kreiner, J. M. Joubert, T. Schenk, J. Gastaldi, H. Nguyen-Thi, N. Mangelinck-Noel, B. Billa, P. Donnadieu, A. Czyrska-Filemonowicz, A. Zielinska-Lipiec, B. Dubiel, T. Weber, P. Schaub, G. Krauss, V. Gramlich, J. Christensen, S. Lidin, D. Fredrickson, M. Mihalkovic, W. Sikora, J. Malinowski, S. Brühne, T. Proffen, W. Assmus, M. de Boissieu, F. Bley, J. L. Chemin, J. Schreuer, and W. Steurer, *The Samson phase beta-Mg_2Al_3, revisited*, Z. Kristallogr., **222**, 259–288 (2007).

[53] Flach, S. and C. R. Willis, *Discrete breathers*, Phys. Rep., **295**, 181–264 (1998).

[54] Florencio, J. and M. H. Lee, *Exact time evolution of a classical harmonic-oscillator chain*, Phys. Rev. A, **31**, 3231–3236 (1985).

[55] Frank, F. C. and J. S. Kasper, *Complex alloy structures regarded as sphere packings. I. Definitions and Basic Principles.*, Acta Crystallogr., **11**, 184–190 (1958).

[56] Frank, F. C. and J. S. Kasper, *Complex Alloy Structures Regarded as Sphere Packings. II. Analysis and Classification of Representative Structures*, Acta Crystallogr., **12**, 483–499 (1959).

[57] Friauf, J. B., *The crystal structure of Magnesium Di-Zincide*, Phys. Rev., **29**, 34–40 (1927).

[58] Friauf, J. B., *The crystal structures of two intermetallic compounds*, J. Am. Chem. Soc., **49**, 3107–3114 (1927).

[59] Gardner, M., *Extraordinary nonperiodic tiling that enriches the theory of tiles*, Sci. Am., **236**, 110–121 (1977).

[60] Goldman, A. I. and R. F. Kelton, *Quasicrystals and crystalline approximants*, Rev. Mod. Phys., **65**, 213–230 (1993).

[61] Greer, A. L., *Metallic glasses*, Science, **267**, 1947–1953 (1995).

[62] Grest, G. S., S. R. Nagel, A. Rahman, and J. A. Witten, *Density of states and the velocity autocorrelation function derived from quench studies*, J. Chem. Phys., **74**, 3532–3534 (1981).

[63] Hafner, J., *From Hamiltonians to Phase Diagrams* (Springer-Verlag, Berlin, 1987).

[64] Hafner, J. and M. Krajč´i, *Propagating and confined vibrational excitations in quasicrystals*, Journal Phys. Cond. Matt., **5**, 2489–2510 (1993), quasi.

[65] Hahn, T. (editor), *International Tables for Crystallography, Volume A: Space Group Symmetry* (Springer, 2002).

[66] Hargittai, I., *Fivefold symmetry* (World Scientific, Singapore, 1992).

[67] Haüy, R. J., *Essai d'une théorie sur la structure des cristaux* (Traité de cristallographie, 1784).

[68] Hayashida, K., T. Dotera, A. Takano, and Y. Matsushita, *Polymeric quasicrystal:Mesoscopic quasicrystalline tiling in ABC Star polymers*, Phys. Rev. Lett., **98**, 195502 (2007).

[69] Heggen, M., *unpublished HRTEM images*, private communications.

[70] Heggen, M., M. Engel, S. Balanetskyy, M. Feuerbacher, and H.-R. Trebin, *Structural variations in ϵ-type Al-Mn-(Pd,Fe) complex metallic alloy phases*, to appear in Phil. Mag. (2008).

[71] Heggen, M. and M. Feuerbacher, *Metadislocation arrangements in the complex metallic alloy xi'-Al-Pd-Mn*, Phil. Mag., **86**, 985–990 (2006).

[72] Henley, C. L., *Random Tiling Models*, in D. P. DiVincenzo and P. J. Steinhardt (editors), *Quasicrystals – The State of the Art*, pp. 429–524 (World Scientific, 1991).

[73] Henley, C. L., M. de Boissieu, and W. Steurer, *Discussion on clusters, phasons and quasicrystal stabilisation*, Phil. Mag., **86**, 1131–1151 (2006).

[74] Hiller, H., *The Crystallographic Restriction in Higher Dimensions*, Acta Crystallogr., **A41**, 541–544 (1985).

[75] Hiraga, K., *The structures of decagonal and quasicrystalline phases with 1.2 nm and 1.6 nm periods, studied by high-resolution electron microscopy*, in G. Chapios and W. Paciorek (editors), *Proceedings of the International Conference on Aperiodic Crystals*, pp. 341–359 (1994).

[76] Hiraga, K. and W. Sun, *The atomic arrangement of an Al-Pd-Mn decagonal quasicrystal studied by high-resolution electron microscopy*, Phil. Mag. Lett., **67**, 117–123 (1993).

[77] Hirth, J. P. and J. Lothe, *Theory of dislocations* (J. Wiley and Sons, New York, 1982).

[78] Hohenberg, P. and W. Kohn, *Inhomogeneous Electron Gas*, Phys. Rev., **136**, B864 B871 (1964).

[79] Imry, Y. and L. Gunther, *Fluctuations and physical properties of the two-dimensional crystal lattice*, Phys. Rev. B, **3**, 3939–3945 (1971).

[80] Ishii, Y., *Mode locking in quasicrystals*, Phys. Rev. B, **39**, 11862–11871 (1989).

[81] Jagla, E. A., *Phase behavior of a system of particles with core collapse*, Phys. Rev. E, **58**, 1478–1486 (1998).

[82] Jagla, E. A., *Core-softened potentials and the anomalous properties of water*, J. Chem. Phys., **111**, 8980–8986 (1999).

[83] Jancovici, B., *Infinite susceptibility without long-range order: The two-dimensional harmonic "solid"*, Phys. Rev. Lett., **19**, 20–22 (1967).

[84] Janot, C., *Quasicrystals: A Primer* (Clarendon Press, Oxford, 1994).

[85] Jarić, M. V. and D. R. Nelson, *Diffuse scattering from quasicrystals*, Phys. Rev. B, **37**, 4458–4472 (1988).

[86] Jeong, H. C. and P. J. Steinhardt, *Finite-temperature elasticity phase transition in decagonal quasicrystals*, Phys. Rev. B, **48**, 9394–9403 (1993).

[87] Kalugin, P. A. and A. Katz, *A mechanism for self-diffusion in quasicrystals*, Europhys. Lett., **21**, 921–926 (1993).

[88] Kalugin, P. A., A. Yu.Kitayev, and L. S. Levitov, *6-dimensional properties of* $Al_{0.86}Mn_{0.14}$ *alloy*, J. Physique Lett., **46**, 601–607 (1985).

[89] Katz, A. and D. Gratias, *Introduction to quasicrystals*, in E. Hippert and D. Gratias (editors), *Lectures on Quasicrystals*, pp. 187–264 (World Scientific, 1994).

[90] Katz, A. and G. Gratias, *A geometric approach to chemical ordering in icosahedral structures*, Journ. Non-Cryst. Solids, **153-154**, 187–195 (1993).

[91] Kepler, J., *Harmonices Mundi (Frankfurt 1619), Book II* (English translation by E. J. Aiton, A. M. Duncan, and J. V. Field, American Philosophical Society, 1997).

[92] Keys, A. S. and S. C. Glotzer, *How do quasicrystals grow?*, Phys. Rev. Lett., **99**, 235503 (2007).

[93] Kittel, C., *Introduction to Solid State Physics* (Wiley, 2004).

[94] Klein, H., M. Durand-Charre, and M. Audier, *Liquid-solid equilibria in the quasicrystalline regions of the Al-Pd-Mn phase diagram*, J. All. Comp., **296**, 128–137 (2000).

[95] Klein, H. and M. Feuerbacher, *Structure of dislocations and stacking faults in the complex intermetallic ξ'-(Al-Pd-Mn) phase*, Phil. Mag., **83**, 4103–4122 (2003).

[96] Klein, H., M. Feuerbacher, P. Schall, and K. Urban, *Novel Type of Dislocation in an Al-Pd-Mn Quasicrystal Approximant*, Phys. Rev. Lett., **82**, 3468–3471 (1999).

[97] Kohn, W. and L. J. Sham, *Self-Consistent Equations Including Exchange and Correlation Effects*, Phys. Rev., **140**, A1133 A1138 (1965).

[98] Koschella, U., *Zur Phason-Phonon-Kopplung in dekagonalen Quasikristallen*, Master's thesis, Universität Stuttgart (2001).

[99] Koschella, U., *Phason-elastische Energie in dekagonalen Quasikristallen*, Ph.D. thesis, Universität Stuttgart (2005).

[100] Koschella, U., F. Gähler, J. Roth, and H.-R. Trebin, *Phason elastic constants of a binary tiling quasicrystal*, J. All. Comp., **342**, 287–290 (2002).

[101] Kuo, K. H., *Mackay, anti-Mackay, double-Mackay, pseudo-Mackay, and related icoshaedral shell clusters*, Struct. Chem., **13**, 221–230 (2001).

[102] Lançon, F. and L. Billard, *Thermodynamical Properties of a Two-Dimensional Quasicrystal from Molecular Dynamics Calculations*, Europhys. Lett., **2**, 625–629 (1986).

[103] Lançon, F. and L. Billard, *Two-dimensional system with a quasi-crystalline ground state*, J. Phys. France, **49**, 249–256 (1988).

[104] Laves, F. and H. Witte, *Die Kristallstruktur des $MgNi_2$ und seine Beziehungen zu den Typen $MgCu_2$ und $MgZn_2$*, Metallwirtsch., **14**, 645–649 (1935).

[105] Laves, F. and H. Witte, *Der Einfluß von Valenzelektronen auf die Kristallstruktur ternärer Magnesiumlegierungen*, Metallwirtsch., **15**, 840–842 (1936).

[106] Leung, P. W., C. L. Henley, and G. V. Chester, *Dodecagonal order in a two-dimensional Lennard-Jones system*, Phys. Rev. B, **39**, 446–458 (1989).

[107] Leunissen, M. E., C. G. Christova, A.-P. Hynninen, C. P. Royall, A. I. Campbell, A. Imhof, M. Dijkstra, R. van Roij, and A. can Blaaderen, *Ionic colloidal crystals of oppositely charged particles*, Nature, **437**, 235–240 (2005).

[108] Levine, D., T. C. Lubensky, S. Ostlund, S. Ramaswamy, P. J. Steinhardt, and J. Toner, *Elasticity and Dislocations in Pentagonal and Icosahedral Quasicrystals*, Phys. Rev. Lett., **54**, 1520–1523 (1985).

[109] Levine, D. and P. J. Steinhardt, *Quasicrystals: a new class of ordered structures*, Phys. Rev. Lett., **53**, 2477–2480 (1984).

[110] Levine, D. and P. J. Steinhardt, *Quasicrystals. I. Definition and Structure*, Phys. Rev. B, **34**, 596–616 (1986).

[111] Lindemann, F. A., *The calculation of molecular natural frequencies*, Phys. Z., **11**, 609–612 (1910).

[112] Lipp, H., *Modellstudien zur phasonischen Flipdynamik in Quasikristallen*, Master's thesis, Universität stuttgart (2006).

[113] Lovesey, S. W., *Theory of neutron scattering from condensed matter, 1. Nuclear scattering* (Clarendon Press, Oxford, 1984).

[114] Lu, P. J. and P. J. Steinhardt, *Decagonal and Quasi-Crystalline Tilings in Medieval Islamic Architecture*, Science, **315**, 1106–1110 (2007).

[115] Lyonnard, S., G. Coddens, Y. Calvayrac, and D. Gratias, *Atomic (phason) hopping in perfect icosahedral quasicrystals AlPdMn by time-of-flight quasielastic neutron scattering*, Phys. Rev. B, **53**, 3150–3160 (1996).

[116] Mackay, A. L., *A dense non-crystallographic packing of equal spheres*, Acta Crystallogr., **15**, 916–918 (1962).

[117] Mackay, A. L., *Crystallography and the penrose pattern*, Physica, **114A**, 609–613 (1982).

[118] Makovicky, E., *800-year old pentagonal tiling from Maraghan, Iran, and the new varieties of aperiodic tiling it inspired*, in I. Hargittai (editor), *Fivefold symmetry*, pp. 67–86 (World Scientific, Singapore, 1992).

[119] Martyna, G., D. J. Tobias, and M. L. Klein, *Constant pressure molecular dynamics*, J. Chem. Phys., **101**, 4177–4189 (1994).

[120] McMahon, M. I. and R. J. Nelmes, *High-pressure structures and phase transformations in elemental metals*, Chem. Soc. Rev., **35**, 943–963 (2006).

[121] Mermin, N. D., *Crystalline Order in Two Dimensions*, Phys. Rev., **176**, 250–254 (1968).

[122] Mermin, N. D. and H. Wagner, *Absence of ferromagnetism or antiferromagnetism in one- or two-dimensional isotropic Heisenberg models*, Phys. Rev. Lett., **17**, 1133–1136 (1966).

[123] Metropolis, N., A. Rosenbluth, M. Rosenbluth, A. Teller, and E. Teller, *Equation of State Calculations by Fast Computing Machines*, J. Chem. Phys., **21**, 1087–1092 (1953).

[124] Mikeska, H. J., *Phonon peaks in the dynamic structure function of lattices without long range order*, Solid State Commun., **13**, 73–76 (1973).

[125] Mikeska, H.-J. and H. Schmidt, *Phase transition without long-range order in two dimensions*, J. Low Temp. Phys., **2**, 371–381 (1970).

[126] Mompiou, F., L. Bresson, P. Cordier, and D. Caillard, *Dislocation climb and low-temperature plasticity of an Al-Pd-Mn quasicrystal*, Phil. Mag., **83**, 3133–3157 (2003).

[127] Mori, H., *A Continued-Fraction Representation of Time-Correlation Functions*, Prog. Theor. Phys., **34**, 399–416 (1965).

[128] Mori, H., *Transport, Collective Motion, and Brownian Motion*, Prog. Theor. Phys., **33**, 423–455 (1965).

[129] Moriarty, J. A. and M. Widom, *First-principles interatomic potentials for transition-metal aluminides: Theory and trends across the 3d series*, Phys. Rev. B, **56**, 7905–7917 (1997).

[130] Naumis, G. G., C. Wang, M. F. Thorpe, and R. A. Barrio, *Coherency of phason dynamics in Fibonacci chains*, Phys. Rev. B, **59**, 14302–14312 (1999).

[131] Northby, J. A., *Structure and binding of Lennard-Jones clusters:* $13 \leq N \leq 147$, J. Chem. Phys., **87**, 6166–6177 (1987).

[132] Overhauser, A. W., *Observability of charge-density waves by neutron diffraction*, Phys. Rev. B, **3**, 3173–3182 (1971).

[133] Oxborrow, M. and C. L. Henley, *Random square-triangle tilings: A model for twelvefold-symmetric quasicrystals.*, Phys. Rev., B., **48**, 6966–6998 (1993).

[134] Paredes, R., J. L. Aragón, and R. A. Barrio, *Nonperiodic hexagonal square-triangle tilings*, Phys. Rev. B, **58**, 11990–11995 (1998).

[135] Pauling, L., *Apparent icosahedral symmetry is due to directed, multiple twinning of cubic crystals*, Nature, **317**, 512–514 (1985).

[136] Penrose, R., *The Rôle of Aesthetics in Pure and Applied Mathematical Research*, Bull. Inst. Math. and its Appl., **10**, 266–271 (1974).

[137] Penrose, R., *Pentaplexity – A class of non-periodic tilings of the plane*, Eureka, **39**, 16–22 (1978), reprinted in Math. Intell. **2**, 32-37 (1979).

[138] Pussey, P. N., W. vanMegen, P. Bartlett, B. J. Ackerson, J. G. Rarity, and S. M. Underwood, *Structure of crystals of hard colloidal spheres*, Phys. Rev. Lett., **63**, 2753–2756 (1989).

[139] Quandt, A. and M. P. Teter, *Formation of quasiperiodic patterns within a simple two-dimensional model system*, Phys. Rev. B, **59**, 8586–8592 (1999).

[140] Radons, G., *Kommensurabilitätseffekte im dynamischen Strukturfaktor des Frenkel-Kontorova-Modells*, Ph.D. thesis, Universität Regensburg (1984).

[141] Radons, G., J. Keller, and T. Geisel, *Dynamical Structure Factor of a One-Dimensional Harmonic Liquid: Comparison of Different Approximation Methods*, Z. Phys. B, **50**, 289–296 (1983).

[142] Radons, G., J. Keller, and T. Geisel, *Dynamical Structure Factor of the Frenkel-Kontorova Model*, Z. Phys. B, **61**, 339–352 (1985).

[143] Rechtsman, M., F. Stillinger, and S. Torquato, *Designed potentials via inverse methods for self-assembly*, Phys. Rev. E, **73**, 11406 (2006).

[144] Rechtsman, M. C., F. H. Stillinger, and S. Torquato, *Optimized Interactions for Targeted Self-Assembly: Application to a Honeycomb Lattice*, Phys. Rev. Lett., **95** (2005).

[145] Rechtsman, M. C., F. H. Stillinger, and S. Torquato, *Self-assembly of the simple cubic lattice with an isotropic potential*, Phys. Rev. E, **74**, 21404 (2006).

[146] Rechtsman, M. C., F. H. Stillinger, and S. Torquato, *Synthetic diamond and wurtzite structures self-assemble with isotropic pair interactions*, Phys. Rev. E, **74**, 21404 (2007).

[147] Remoissenet, M., *Waves called solitons* (Springer-Verlag Berlin, 1996).

[148] Rosenberger, F., P. G. Vekilov, M. Muschol, and B. R. Thomas, *Nucleation and crystallization of globular proteins – what we know and what is missing*, J. Cryst. Growth, **168**, 1–27 (1996).

[149] Rosenfeld, R., M. Feuerbacher, B. Baufeld, M. Bartsch, M. Wollgarten, G. Hanke, M. Beyss, U. Messerschmidt, and K. Urban, *Study of plastically deformed icosahedral* Al–Pd–Mn *single quasicrystals by transmission electron microscopy*, Phil. Mag. Lett., **72**, 375–384 (1995).

[150] Roth, J., M. Brunelli, D. Bunz, F. Gähler, J. Hahn, M. Hohl, C. Horn, J. Kaiser, R. Mikulla, G. Schaaf, J. Stelzer, and H.-R. Trebin, *IMD - A Massively Parallel Molecular Dynamics Package for Classical Simulations in Condensed Matter Physics*, in E. Krause and W. Jäger (editors), *High Performance Computing in Science and Engineering '99*, pp. 72–81 (Springer Heidelberg, 2000).

[151] Roth, J. and A. Denton, *Solid Phase Structures for the Dzugutov Pair Potential*, Phys. Rev. E, **61**, 6845–6857 (2000).

[152] Samson, S., *The Crystal Structure of the Phase* β Mg_2Al_3, Acta Crystallogr., **19**, 401–413 (1965).

[153] Schrödinger, E., *Zur Dynamik elastisch gekoppelter Punktsysteme*, Ann. Phys. (Leipzig), **349**, 916–934 (1914).

[154] Senechal, M., *Introduction to lattice geometry*, in M. Waldschmidt, P. Moussa, J.-M. Luck, and C. Itzykson (editors), *From Number Theory to Physics*, p. 476 (Springer–Verlag, Berlin, 1992).

[155] Senechal, M., *The mysterious Mr. Amann*, Math. Intell., **26**, 10–21 (2004).

[156] Shechtman, D., I. Blech, D. Gratias, and J. W. Cahn, *Metallic Phase with Long-Range Orientational Order and No Translational Symmetry*, Phys. Rev. Lett., **53**, 1951–1953 (1984).

[157] Shevchenko, E. V., D. V. Talapin, N. A. Kotov, S. O'Brien, and C. B. Murray, *Structural diversity in binary nanoparticle superlattices*, Nature, **439**, 55–59 (2006).

[158] Shindo, D. and K. Hiraga, *High-Resolution Electron Microscopy for Materials Science* (Springer-Verlag, 1998).

[159] Shoemaker, C. B. and D. P. Shoemaker, *Tetraedrisch dicht gepackte Strukturen von Legierungen der Übergangsmetalle*, Monat. Chem., **102**, 1643–1666 (1971).

[160] Shoemaker, D. P. and B. G. Bergman, *The crystal structure of a sigma phase, FeCr*, J. Am. Chem. Soc., **72**, 5793 (1950).

[161] Sinha, A. K., *Tetrahedrally close-packed transition metal alloy structures*, Prog. Mat. Sci., **15**, 79–185 (1972).

[162] Socolar, J. E. S., T. C. Lubensky, and P. J. Steinhardt, *Phonons, phasons, and dislocations in quasicrystals.*, Phys. Rev. B, **34**, 3345–3360 (1986).

[163] Sonntag, S., *Zum Strukturfaktor der dynamischen Fibonacci-Kette*, Master's thesis, Universität Stuttgart (2006).

[164] Squires, G. L., *Introduction to the theory of thermal neutron scattering* (Dover Publications Inc., New York, 1996).

[165] Stampfli, P., *A dodecagonal quasi-periodic lattice in 2 dimensions*, Helv. Phys. Acta, **59**, 1260–1263 (1986).

[166] Steinhardt, P. J. and S. Ostlund, *The Physics of Quasicrystals* (World Scientific, Singapore, 1987).

[167] Steurer, W., *Structural phase transitions from and to the quasicrystalline state*, Acta Crystallogr. Sect. A, **61**, 28–38 (2005).

[168] Steurer, W., S. I. Ben-Abraham, T. Janssen, M. Senechal, M. Baake, D. Frettlöh, R. Lifshitz, and H. Zimmermann, *What is a crystal? An ongoing discussion*, Z. Kristallogr., **222**, 308–319 (2007).

[169] Stillinger, F. H., *Lattice sum and their phase diagram implications for the classical Lennard-Jones model.*, J. Chem. Phys., **115**, 5208–5212 (2001).

[170] Sun, W. and K. Hiraga, *High-resolution transmission electron microscopy of the Al-Pd-Mn decagonal quasicrystal with 1.6 nm periodicity and its crystalline approximants*, Phil. Mag. A, **73**, 951–971 (1996).

[171] Tang, L.-H., *Random-Tiling Quasicrystal in Three Dimensions*, Phys. Rev. Lett., **64**, 2390–2393 (1990).

[172] Tang, L. H. and M. V. Jarić, *Equilibrium quasicrystal phase of a penrose tiling model*, Phys. Rev. B, **41**, 4524–4546 (1990).

[173] Trebin, H.-R., P. Brommer, M. Engel, F. Gähler, S. Hocker, F. Rösch, and J. Roth, *Simulating structure and physical properties in complex metallic alloys*, in *Proceedings of the 2nd European School in Materials Science (to appear)* (2008).

[174] Tuckerman, M. E. and G. J. Martyna, *Understanding modern molecular dynamics: techniques and applications*, J. Phys. Chem. B, **104**, 159–178 (2000).

[175] Urban, K. and M. Feuerbacher, *Structurally complex alloy phases*, J. Non-Cryst. Solids, **334 & 335**, 143–150 (2004).

[176] Wales, D. J. and J. P. K. Doye, *Global optimization by basin-hopping and the lowest energy structures of Lennard-Jones clusters containing up to 110 atoms*, Journal Phys. Chem. A, **101**, 5111–5116 (1997).

[177] Weling, F., A. Griffin, and M. Carrington, *Phonon peaks in the dynamic structure factor of a two-dimensional harmonic crystal*, Phys. Rev. B, **28**, 5296–5299 (1983).

[178] Widom, M., K. J. Strandburg, and R. H. Swendsen, *Quasicrystal Equilibrium State*, Phys. Rev. Lett., **58**, 706–709 (1987).

[179] Witte, H., *Zur Struktur und Materie der Festkörper* (Springer Verlag, Berlin, 1952).

[180] Wollgarten, M., D. Gratias, Z. Zhang, and K. Urban, *On the determination of the Burgers vector of quasicrystal dislocations by transmission electron microscopy.*, Phil. Mag. A, **64**, 819–833 (1991).

[181] Xia, Y., B. Gates, Y. Yin, and Y. Lu, *Monodispersed colloidal spheres: Old materials with new applications*, Adv. Matererials, **12**, 693–713 (2000).

[182] Yoshida, T., K. Shobu, and H. Mori, *Dynamic Properties of One-Dimensional Harmonic Liquids. I*, Prog. Theor. Phys., **66**, 759–771 (1981).

[183] Zeng, X., G. Ungar, Y. Liu, V. Percec, A. E. Dulcey, and J. K. Hobbs, *Supramolecular dendritic liquid quasicrystals*, Nature, **428**, 157–160 (2004).

[184] Zheng, X. H. and J. C. Earnshaw, *On the Lindemann criterion in 2D*, Europhys. Lett., **41**, 635–640 (1998).

List of publications

Parts of this work have been published or are currently under review:

[43] Engel, M., *Zur Geometrie von Phasonen und Versetzungen in Quasikristallen und ihren Approximanten*, Diplomarbeit, Universität Stuttgart (2004).

[45] Engel, M. and H.-R. Trebin, *A unified projection formalism for the Al-Pd-Mn quasicrystal Ξ-approximants and their metadislocations*, Phil. Mag., **85**, 2227–2247 (2005).

[46] Engel, M. and H.-R. Trebin, *Tiling models for metadislocations in AlPdMn approximants*, Phil. Mag., **86**, 979–984 (2006).

[47] Engel, M., S. Sonntag, H. Lipp, and H.-R. Trebin, *Structure factors of harmonic and anharmonic Fibonacci chains by molecular dynamics simulations*, Phys. Rev. B, **75**, 144203 (2007).

[44] Engel, M. and H.-R. Trebin, *Self-assembly of Monatomic Complex Crystals and Quasicrystals with a Double-Well Interaction potential*, Phys. Rev. Lett., **98**, 225505 (2007).

[70] Heggen, M., M. Engel, S. Balanetskyy, M. Feuerbacher, and H.-R. Trebin, *Structural variations in ϵ-type Al-Mn-(Pd,Fe) complex metallic alloy phases*, to appear in Phil. Mag. (2008).

[48] Engel, M. and H.-R. Trebin, *Stability of the decagonal quasicrystal in the Lennard-Jones-Gauss system*, Submitted (September 2007).

[173] Trebin, H.-R., P. Brommer, M. Engel, F. Gähler, S. Hocker, F. Rösch, and J. Roth, *Simulating structure and physical properties in complex metallic alloys*, in *Proceedings of the 2nd European School in Materials Science (to appear)* (2008).

Lebenslauf

Michael Engel geboren am 19. Januar 1979 in Stuttgart

Kinder:	Meike Katharina *25. Februar 2005 Anna Franziska *12. August 2006
1989 - 1998	Philipp-Matthäus-Hahn Gymnasiums in Echterdingen
1998 - 1999	Grundwehrdienst und Fernstudium der Physik an der Universität Kaiserslautern
1999 - 2004	Doppelstudium der Mathematik (Diplom) und Physik (Diplom) an der Universität Stuttgart
2001 - 2004	Stipendiat der Studienstiftung des Deutschen Volkes
seit Okt. 2004	Promotion bei Prof. Dr. Hans-Rainer Trebin, Institut für Theoretische und Angewandte Physik
Sep./Okt. 2006	Aufenthalt an der Kyushu University in Fukuoka, Japan
ab April 2008	JSPS Postdoc-Stipendium für einen Aufenthalt in Japan

Danksagung

An dieser Stelle möchte ich mich bei einigen Menschen bedanken, die auf verschiedene Weise zum Gelingen dieser Arbeit beigetragen haben.

Herrn Prof. Dr. Hans-Rainer Trebin danke ich für die freundliche Aufnahme an seinem Institut. Ich hatte die Freiheit, eigene Ideen zu entwickeln und selbständig zu arbeiten. Trotzdem konnte ich jederzeit Hilfestellungen und richtungsweisende Anleitungen erhalten.

Herrn Prof. Dr. Günter Wunner danke ich für die kurzfristige Übernahme des Mitberichts und Herrn Prof. Dr. Clemens Bechinger für die Leitung der mündlichen Doktorprüfung.

I would like to thank Prof. Dr. Takashi Odagaki for giving me the opportunity to visit his institute in Fukuoka, Japan two times and the nice introduction into the theory of glass transition.

Ich bedanke mich bei Dr. Michael Feuerbacher und Dr. Marc Heggen am Forschungszentrum Jülich für die stets reibungslose Zusammenarbeit und ihre schönen Elektronenmikroskopbilder.

Herzlich bedanken möchte ich mich bei meinem Zimmerkollegen Frohmut Rösch für die angenehme Arbeitsatmosphäre. Die Untersuchungen zur dynamischen Fibonacci-Kette wurden in Zusammenarbeit mit Steffen Sonntag und Hansjörg Lipp im Rahmen ihrer Diplomarbeiten durchgeführt.

Dank der hervorragenden Rechnerausstattung des Instituts wurden viele Aufgaben erleichtert. Jegliche Probleme wurden umgehend von Dr. Johannes Roth behoben. Dr. Franz Gähler war stets bereit, Fragen zur Theorie der Quasikristalle zu beantworten. Dr. Peter Brommer hat die Mühe auf sich genommen, das Manuskript Korrektur zu lesen.

Die Arbeit wurde nicht zuletzt auch durch das gute Arbeitsklima am Institut für Theoretische und Angewandte Physik gefördert. Darum sei an dieser Stelle den Sekretärinnen und allen Kollegen gedankt.

Meinen Eltern möchte ich für die vielfältige Unterstützung danken, die mir ein sorgenfreies Studium ermöglichte.

Diese Arbeit ist Meike und Anna gewidmet, die ihren Vater in den letzten Monaten dieser Arbeit abends häufig vermissen mußten. Ohne die tatkräftige Hilfe von Ingrid, Judit, Rolf und Richard wäre es nicht möglich gewesen, Familie und Jobs so gut unter einen Hut zu bringen.

Meiner Freundin Cosima danke ich für ihre Geduld und Liebe.

Finanzielle Förderung erfolgte von der Deutschen Forschungsgesellschaft im Rahmen des Paketantrags 36 (TR 154/24-1) sowie des EU Netzwerks “Complex Metallic Alloys”.